Synthesis and Behaviors of Aqua- and Electro-Responsive Polymers

by

Emily Frances Barker

Bachelor of Science, University of Washington, 2014

Submitted to the Graduate Faculty of the

Dietrich School of Arts and Sciences in partial fulfillment

of the requirements for the degree of

Doctor of Philosophy

University of Pittsburgh

2024

UNIVERSITY OF PITTSBURGH

DIETRICH SCHOOL OF ARTS AND SCIENCES

This dissertation was presented

by

Emily Frances Barker

It was defended on

October 19, 2023

and approved by

Jennifer Laaser, Assistant Professor, Department of Chemistry

Geoffrey Hutchison, Professor, Department of Chemistry

Sachin Velankar, Professor, Department of Chemical Engineering

Thesis Advisor/Dissertation Director: Tara Meyer, Professor, Department of Chemistry

For Pauline and Michael

Maar ik maak steeds wat ik nog niet kan om het te leren kunnen.

Vincent van Gogh

Synthesis and Behaviors of Aqua- and Electro-Responsive Polymers

Emily Frances Barker, PhD

University of Pittsburgh, 2024

Two classes of stimuli-responsive polymers were prepared and studied. The first class of materials comprised both homopolymers of and block copolymer including polyoxacyclobutane (POCB) which is known to exhibit the rare quality of cocrystallization when exposed to water. The kinetics of cocrystallization were investigated using techniques that had previously only been applied to polymer homocrystallization. It was shown that cocrystallization, while heavily influenced by diffusion effects, can still be described by standard homocrystallization theories. Block copolymers containing POCB and polyethylene oxide (PEO) were then synthesized via click chemistry to test their ability to form the hydrate as well as their ability to self-assemble. It was also established that the crystalline POCB hydrate does form for block copolymers, and that for low PEO to POCB ratios the structure of the crystal changes from spherulites to cylindrical micelles. At high temperatures the crystal melts and the block copolymers separate into aggregates/micelles with a hydrophobic core. The second class of stimuli-responsive polymers investigated were polymers bearing ionic side chains. With a long-term goal of forming layered composites whose mechanical properties could be controlled with electricity, polymer electrolytes were prepared, and their adhesion was studied. Metal substrates coated with polymers bearing both negatively and positively charged sidechains were shown to physically adhere to electrodes when an external voltage was applied. The dependence of the adhesion on environment and sample history was studied.

Table of Contents

List of Tables

List of Figures

Acknowledgements

I am beyond grateful for the opportunity I have had the past several years to work on my PhD and to develop into the scientist I am now. Such growth does not occur within one's comfort zone and I want to thank everyone who was there for me during the process. There are four people in particular who believed in me and supported me throughout who I would like to give special recognition to.

First is my advisor Tara Meyer for taking me on as a graduate student, keeping me on as a graduate student, and pushing me to develop both personally and as a scientist. I am lucky to have had such an amazing mentor to learn from and I am indebted to your endless supply of patience.

Next, I would like to thank my parents. Thank you for always cheering for me and being there for me. I looked forward every week to our Sunday crossword calls. I also especially want to thank my dad for helping me with all my science projects growing up and my mom for driving me to all the different clubs, sports practices, and music lessons that allowed me to develop my interests and taught me to believe I could achieve anything I wanted.

Finally, I wish to thank my friend and mentor Mary for always being a voice of reason when the world seemed to have gone insane, talking through with me the many challenges I faced, and encouraging me to keep my head down and focused on my goals.

1 Introduction to Dissertation

1.1 Stimuli Responsive Polymers

Unlike small molecules, which typically display the same characteristic set of properties for both one molecule and for several moles, a polymer will change properties depending on chain length, preparation, degree of folding or aggregation, branching, crosslinking, and other macromolecular traits. In otherwords,, these materials exhibit "bulk" behavior that depends directly on the interchain interactions, which can be dramatically affected by external stimuli. Small molecules, although they also respond to external stimuli, rarely exhibit cooperative behavior that one could characterize as a unique bulk materials property. Common stimuli include temperature, light, pH, salt concentration, or presence of a specific molecule[1]. This phenomenon is similar to the way proteins and other biomaterials respond to stimuli within the body, and indeed, much work in this area is inspired by biological systems.

There are multiple ways to alter a polymer's physical properties. Heating above the T_g, the T_m, or the LCST, or changing the number of crosslinks or conformation or interactions with the solvent are common ways of changing said properties[2]. Stimuli responsive polymers see use in things like drug delivery[3] and actuation[4], exhibiting a change when certain conditions are met.

The materials I investigated in the course of my PhD are unique because while the stimuli, water and electricity, are not uncommon, the manner in which they change the polymer properties are unique. Please note that the following introductions to these projects are brief and more detailed information related to precedents, approach, and rationale can be found in the specified chapters.

1.2 Water Responsive Polymers

The water responsive polymer project was undertaken in collaboration with Prof. Sachin Velankar and his research group from the Chemical and Petroleum Engineering Department at the University of Pittsburgh (Chapter 2). Polyoxacyclobutane (POCB), otherwise known as polyoxetane or polytrimethylene oxide, is a polyether with unique chemical properties. The three methylene carbons flanking each oxygen confer a relatively hydrophobic quality to the molecule, which phase separates from water at most concentrations. However, below a melting temperature of 37°C, the precise spacing of the oxygens in the polyether backbone allows a cocrystal structure between the water and the POCB to form (Fig. 1.1), despite its otherwise hydrophobic nature. This crystal structure had been originally reported in 1970[5], but only recently has the crystallization phenomenon been studied in detail[6].

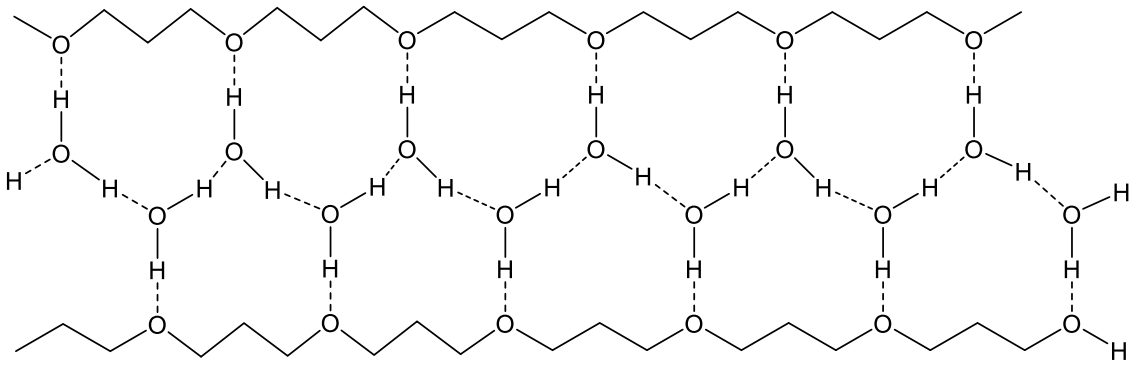

Figure 1.1: The cocrystal structure of POCB. The precise spacing of the oxygens in the polyether backbone allow for the formation of a cocrystal with water in which there is a 1:1 ratio of repeat units to water molecules

While there are a few other known polymers that cocrystallize with a small molecule, these compounds are rare, and cocrystallization with water is known only in POCB[7], linear polyethyleneimine[8], and possibly poly(1,3-dioxolane)[9-11] and of those, only POCB cocrystallizes at a biologically relevant temperature. None of the polymers that crystallize with a small molecule

have been studied kinetically or mechanistically. Polymers crystallize differently than small molecule crystals, and prior to this work, it was not known whether cocrystals crystallize in a similar manner as polymer homocrystals. Sudesna Banjeree carried out the kinetic experiments for this project and I analyzed the data collected using methods previously only used for single-component crystallization kinetics[12-13] to determine if polymer cocrystals behave similarly to polymer homocrystals.

In the context of this work, we regard water as a stimulus because the introduction of water to either the bulk phase of the polymer or a solution of the polymer in an organic solvent has a dramatic effect. Unless the temperature of the system is held very close to the melting point, visible precipitates containing crystalline regions form immediately. These crystalline materials are stable and insoluble until heated above the melting point of the hydrate.

Moving forward, in order to expand the range of potential applications for the POCB hydrate, I prepared and studied the behavior, including the interaction with water, for block copolymers combining POCB with polyethylene oxide (PEO) (Chapter 3). While the 37°C transition of the POCB cocrystal is promising for biological applications, it cannot be used directly as it either phase separates or crystallizes out. The most commonly used biocompatible, hydrophilic polymer is PEO and this makes it an ideal candidate as the hydrophilic portion of the block copolymer. I first compared methods of block copolymer synthesis to determine an optimal synthetic route, and then produced several block copolymers of various lengths and used a variety of analytical techniques to determine their supramolecular structure as well as the characterizing the crystallization behavior thereof.

Homocrystallization within block copolymers typically affects the structure, producing cylindrical micelles more frequently than the spherical micelles normally seen in self-assembly [14].

Cylindrical micelles have different rates of drug delivery than spherical micelles, and, since polymer crystals typically have amorphous regions, this could allow for interactions with small molecules for drug delivery. The ability of POCB to cocrystallize with water could significantly impact its shape as a part of a block copolymer, thus leading to increased potential as a drug delivery system. As we will see, water will have the ability to transform a structure into different forms.

1.3 Electrically Responsive Polymers

Next, we look at electrically responsive polymers. Electrically responsive polymers are particularly attractive due to the presence of electricity in our everyday lives. Examples of electrically responsive polymers include shape memory[15], color changes[16], drug delivery[17], and electrochemical actuators[18].

This project was a continuation of work done by Jeff Auletta in the Meyer group to determine the viability of ionomer films for electroadhesive applications. Electroadhesion occurs in all capacitor systems, in which the separated charges experience an attraction to each other. This process has been well documented for inorganic materials and is separated into two categories- standard coulombic attraction which describes the attraction between two capacitor plates, and Johnsen-Rahbek electroadhesion, which describes the attraction between charges at the interface of a dielectric and the capacitor plate[19]. The latter confers a lower required charge, and thus is the ideal application for biological and wearable applications.

In my project, I tested the repeatability of the adhesion effects of PEAA and studied the adhesion behavior of sodium sulfonated polystyrene-*co*-(ethylene-*b*-butylene)-*co*-styrene (SEBS)

with varying degrees of sulfonation and as well as an ionic liquid film (Chapter 4). Although electroadhesion was repeatedly observed, the behavior of the samples was found to be extremely dependent on both sample history and environmental conditions.

1.4 Final thoughts

Although these two projects involved different polymers and different stimuli, they hold in common the fact that the external stimuli are affecting interchain interactions. In the POCB/water project the external water creates crystalline order rapidly upon exposure. Although POCB, like many polymers can self-crystallize in the dry bulk form, the process is slower and requires careful thermal processing. In the electroadhesion process, the build-up of charge at the polymer surface, is used to promote strong adhesion. While polymers often exhibit some adhesive properties with other polymers and surfaces due to their ability to form a large number of individual interactions, the build-up of electrostatic charge dramatically enhances these interactions.

2 POCB kinetics

This chapter includes work done in collaboration with Sudesna Banerjee, who carried out the bulk of the characterization. My contributions include helping to develop the volumetric methodology used to characterize bulk crystallization, data analysis, particularly for the Avrami plots and Hoffman-Lauritzen plots, and manuscript writing. This chapter includes the text from our joint paper:

Liquids that Freeze when Mixed: Homogeneous Cocrystallization Kinetics of Polyoxacyclobutane–Water Hydrate; Emily F. Barker, Sudesna Banerjee, Tara Y. Meyer, and Sachin Velankar; ACS Applied Polymer Materials 2022 4 (1), 703-713; DOI: 10.1021/acsapm.1c01626.

2.1 Background on Crystallization

Crystallization both of small molecules and polymers has been studied extensively. To put our studies of the crystallization kinetics of POCB with water into context, it is useful to review some widely accepted theories of how crystallization proceeds. The two most common polymer crystallization theories are the Hoffman-Lauritzen theory of crystal growth and the Avrami model of crystallization. As we will be discussing how the kinetics of cocrystallization match the established theories of polymer crystallization, a brief review is presented.

Hoffmann-Lauritzen Regimes

One of the most common methods of describing crystal growth is through use of the Hoffman-Lauritzen (HL) theory of polymer crystal growth. In Hofmann-Lauritzen theory crystals expand via one of two processes: secondary/surface nucleation in which a new layer is added to the polymer crystal via chain folding or through addition of a new polymer chain, and lateral growth, in which the polymer expands laterally from a nucleation site. Interestingly, the difference in temperature dependance of surface nucleation (i) and lateral growth (g) can be observed in plots of undercooling vs log of growth rate[20], as the rate limiting step of the process changes as temperature changes, giving insight into the mechanism of growth. Specifically, three regimes are noted as increase in surface nucleation changes with increase in undercooling (Fig 2.1). We apply such treatment to polymer cocrystals, and thus it is necessary to expand upon these regimes and the reasoning behind them.

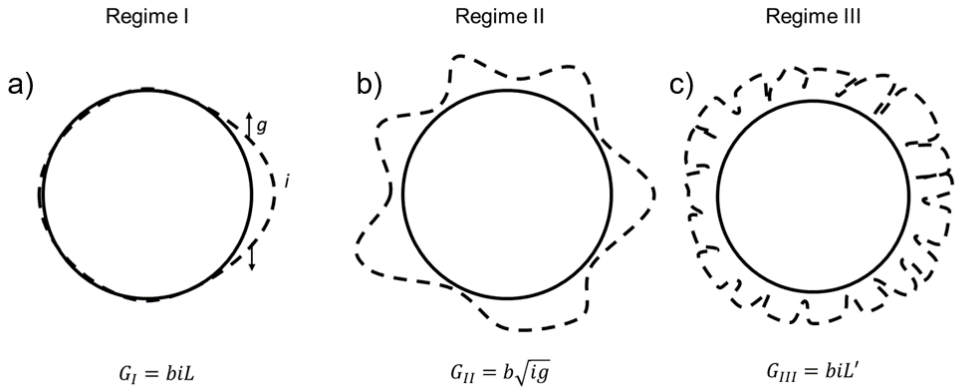

Figure 2.1: One model of the Hoffmann-Lauritzen regime growth that does not take the spherulite substructure into account in order to focus on the understanding of the regimes. In regime I (a) each nucleation event is rare and the entire surface of the crystal is covered before another nucleation event takes place. In regime II (b) both nucleation and growth are occuring on similar scales. In regime III (c) surface nucleation is so rapid there is no lateral growth contribution.

There are many sources that provide the final rates of each regime (2.1.5, 2.1.9, and 2.1.12)[12, 20-24] to explain why one sees 3 regimes in the graph of log of growth rate vs undercooling, but with regards to the reasoning behind the square root in regime II it mostly arises from the thermodynamic derivation. In the below text I thus go into further detail to expand on how one can arrive at these equations more intuitively.[25-27]

One can treat the problem as a rate problem. **A** sites on the polymer get filled in through lateral growth (g) to form the next layer of the crystal, **B**, and **A′** sites get filled in through surface nucleation (i) to form the next layer of the crystal **B** (eq. 2.1.1-2.1.4).

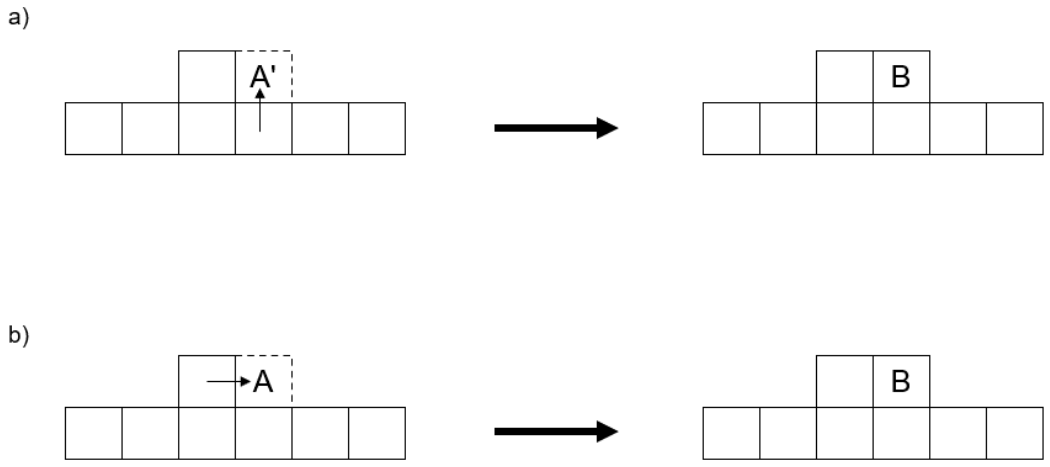

Figure 2.2: A section of a new layer of polymer crystal can either be added through surface nucleation (a) or through lateral growth (g). The empty site is given as A if it gets filled by surface nucelation and A' if it gets filled by lateral growth. Whether added via surface nucleation or lateral growth, the resulting site will be approximately the same (B) regardless..

$$A \xrightarrow{g} B \tag{2.1.1}$$

$$A' \xrightarrow{i} B \tag{2.1.2}$$

$$\frac{-dA}{dt} = g \tag{2.1.3}$$

$$\frac{-dA'}{dt} = i \tag{2.1.4}$$

Regime I

In regime I, a rare secondary nucleation event (i) occurs which allows for lateral growth (g) across the surface of the growing crystal (Fig 2.1a). Secondary nucleation is so slow that the entire surface of the crystal gets filled in through lateral growth before another nucleation event occurs, making the rate determining step the nucleation event (eq. 2.1.5). The change in **B** (the addition of the next layer of the crystal) is dependent on the rate of nucleation and the thickness (b) and persistence length (L) of the crystal.

If i << g

i is the rate-limiting step:

$$\frac{dB}{dt} = ibL \tag{2.1.5}$$

Regime II

In Regime II secondary nucleation is on the same scale as lateral growth (Fig 2.1b). A nucleation event is required for lateral growth, but since they are on the same scale, the lateral growth is not limited. Thus, we can treat the problem as follows: **A** sites get converted to the next layer **B** through lateral growth at the rate g and **A'** sites get converted to the next layer **B** at the rate i through secondary nucleation. This can be written as the equation **A + A'→2B**, which would produce a rate equation of the rate being proportional to the square root of both i and g (eq 2.1.9).

if i ≈ g

$$A + A' \rightarrow 2B \tag{2.1.6}$$

$$\frac{1}{2}A + \frac{1}{2}A' \rightarrow B \tag{2.1.7}$$

$$\frac{dB}{dt} = \left(\frac{dA}{dt}\right)^{\frac{1}{2}} x \left(\frac{dA'}{dt}\right)^{\frac{1}{2}} \tag{2.1.8}$$

$$\frac{dB}{dt} = b\sqrt{ig} \tag{2.1.9}$$

Regime III

In regime III the secondary nucleation events are occurring at such a high rate that there is virtually no time for lateral growth to occur and all spaces are being filled by secondary nucleation events (Fig 2.1c). Thus, the rate is dependent only on i (eq 2.1.12) because g is 0. The persistence length L' is given instead of L because this mechanism leads to a slightly different length.

if i ≫ g

i is the only step:

$$A \overset{g}{\nrightarrow} B \tag{2.1.10}$$

$$A' \overset{i}{\rightarrow} B \tag{2.1.11}$$

$$\frac{dB}{dt} = ibL' \tag{2.1.12}$$

It can be understood that surface nucleation is more influenced by the undercooling temperature than lateral growth, thus if one were to plot the growth rate vs degree of undercooling there will be a change in slope for regime II (Fig. 2.3) Specifically, the equation,

$$G = G_0 \beta e^{-\frac{K_g}{T\Delta T}} \tag{2.1.13}$$

where

$$K = \frac{4b\sigma\sigma_e T_m^\circ}{\Delta h_f k} \tag{2.1.14}$$

for regimes I and III and

$$K = \frac{2b\sigma\sigma_e T_m^\circ}{\Delta h_f k} \tag{2.1.15}$$

for regime II[21, 28-29]. β is the transport function related to diffusion of the polymers, σ is the surface free energy of lateral growth, σ_e is the surface free energy of a fold, T_m is the melting temperature, Δh_f is the heat of fusion per unit volume of crystal, and k is the Boltzmann constant.

For a dilute solution,

$$\beta = \frac{c^{1/3}\, kT}{h} e^{-\frac{\Delta H^*}{RT} + \frac{\Delta S^*}{R}} \tag{2.1.16}$$

where c is polymer concentration, ΔH* is the activation energy of diffusion, ΔS* is the entropy change related to diffusion, R is the gas constant, T is the temperature.

This model allows one to plot the log of the growth rate G vs 1/TΔT to produce a linearized plot where the slope of regime II is less than that of regimes I and III (Fig. 2.3).

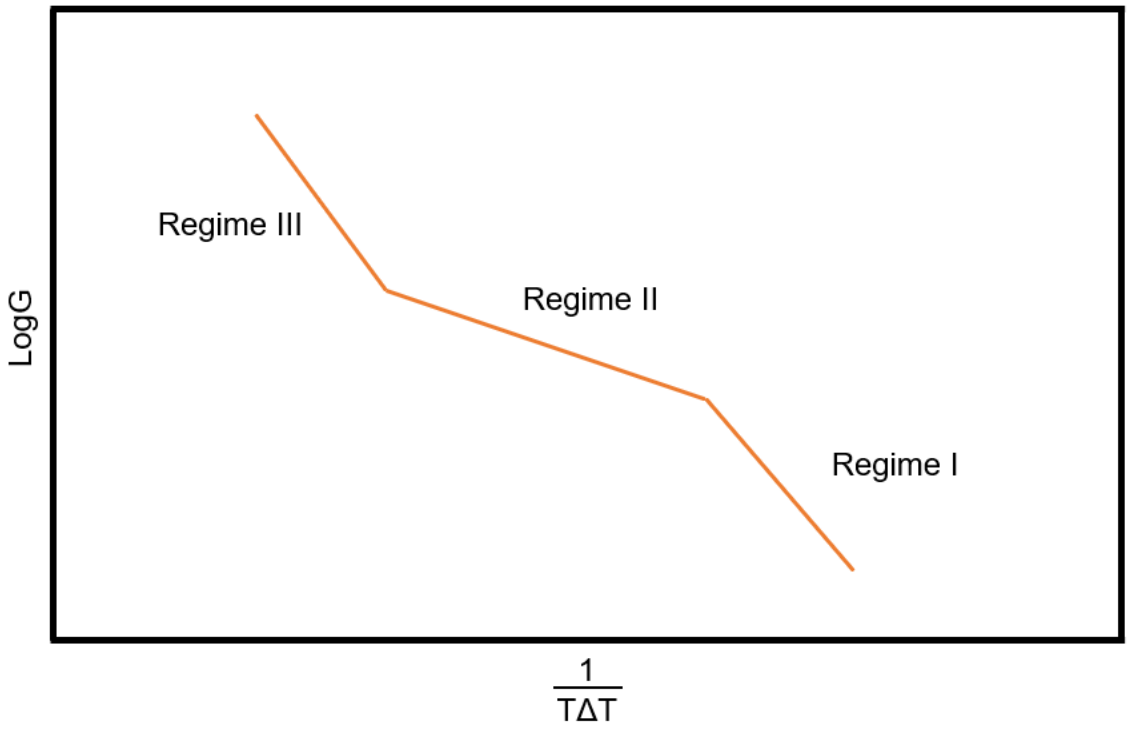

Figure 2.3: An example of the linearize plot of crystallization growth vs undercooling to highlight regime changes. Plotting the data in such a way allows one to make conclusions about the mechanism of growth.

On an atomic scale one would see that the direction of growth is not consistent with that of a sphere or circle, but rather a circle comprising many strands of lamellae (Fig. **2.4**a), each of which comprises strands of folded polymer chains (Fig. **2.4**b)[29-31].

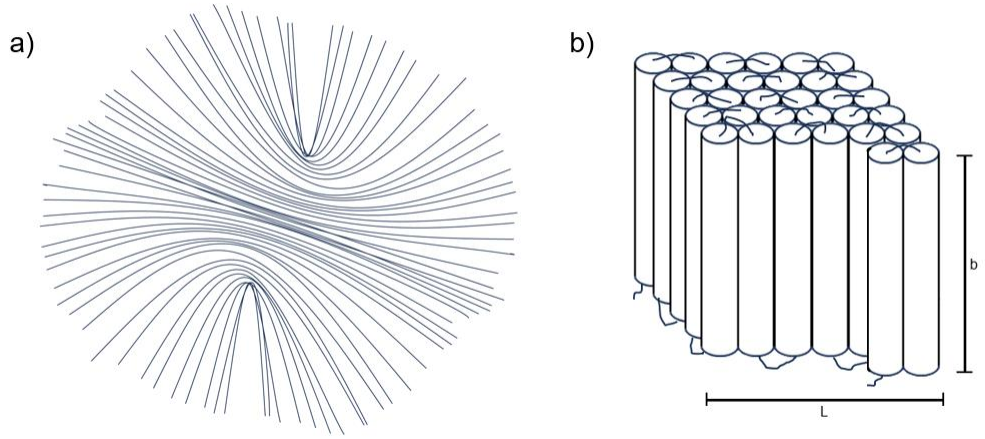

Figure 2.4: The spherulite substructure made up of many lamellae with length L and height b (a). The lamellae each contain folded polymer (b). A nucleation event would be a fold onto a new layer and growth along an already nucleated surface comprises lateral growth.

Critical radius

When a crystal is small, the free energy of crystallization is lower than the free energy of melting due to the low number of interactions between the crystallizable components. As the crystal expands, the number of interactions of the internal crystal components increases, such that the free energy of the crystal volume increases at a greater rate than the free energy of the surface. When the volume is sufficiently large, the free energy of crystallization will be larger than the free energy of melting due to the increased internal interactions of the crystal volume and crystallization will proceed. This point is known as the critical radius[32].

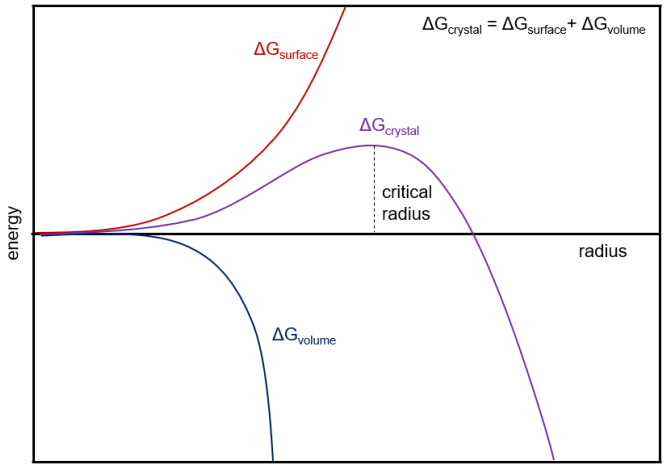

Figure 2.5: Graph showing the trends of the free energy change of surface crystallization, the free energy change of the interior volume of crystallization, and the total free energy change of crystallization, which is equal to the sum of the surface and volume crystallizations. Initially the total free energy change is positive but as the volume free energy change decreases faster than the surface free energy change changes, the total crystallization free energy change reaches a maximum known as the critical radius.

Contrary to the implication from the name, the critical radius of polymers is not a fixed diameter of a sphere, rather it takes the form of a set number of chain folds (Fig. 2.6). Zhang et. al. combined the classical crystallization theory of the critical radius with the lamellar substructure of polymer crystallites and calculated the number of chain folds that comprise the critical radius[33].

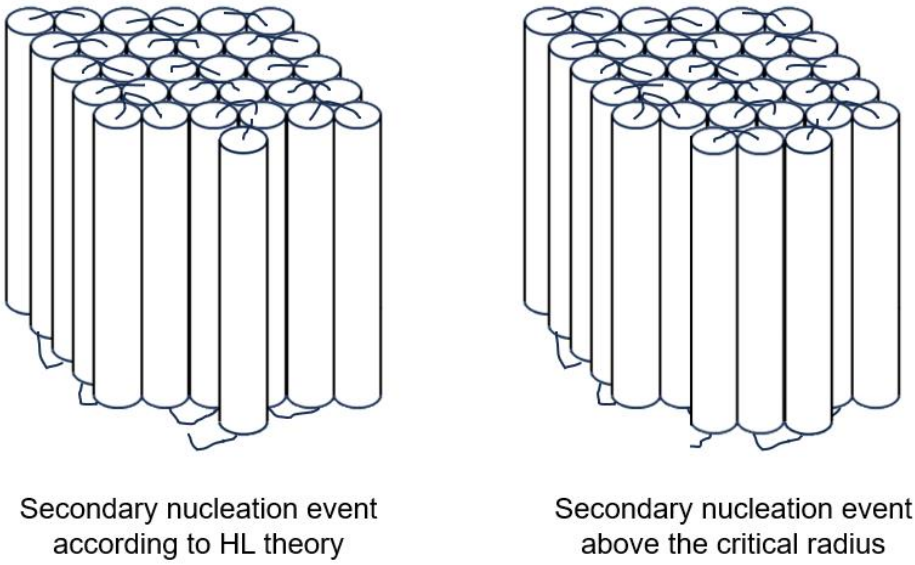

Figure 2.6: Hoffman-Lauritzen theory predicts a new secondary nucleation event is required for the next layer of crystal growth. In actuality several folds are required for a secondary nucleation event to be thermodynamically stable.

Avrami plots

JMAK theory[12] arises from a Poisson relation, as derived by Evans[34] to model the expanding circles of waves from raindrops landing in a pool of water. According to this theory, crystallization kinetics are characterized by an exponent (n) that describes the dimensionality of growth. The fraction of material crystallized, χ_c, changes as

$$\chi_c = 1 - \exp\left(-(kt^n)\right) \tag{2.1.17}$$

While the original theory required integer values for n, diffusion-controlled growth can give rise to half-integer values. As well-summarized by Lorenzo et al.[35], deviations from eq. 2.1.17 can arise for several reasons, e.g., a change in the rate of primary nucleation during the crystallization process, or an induction time for crystallization. Avrami exponents often decrease as time increases. It is also possible for a combination of diffusion-controlled nucleation and non-linear primary nucleation to yield the same exponents with differing mechanisms[36-37].

2.2 Overview

Previously[6] members of the Velankar group reported on the phase behavior of mixtures of 650 Da polyoxacyclobutane (POCB) and water. POCB, also known as polytrimethylene oxide (or glycol), polyoxetane, or poly(1,3-propanediol) has the rare ability to cocrystallize with water to form a crystalline hydrate. There are several polymers that can cocrystallize with small molecule compounds[9-11, 38-47], but cocrystallization with water is known only in POCB[7], linear polyethyleneimine[8], and possibly poly(1,3-dioxolane)[9-11]. Exclusive to POCB is its ability to cocrystallize with water near body temperature (37°C), making POCB of potential interest for medical applications. POCB also exhibits several other unusual and fascinating properties including that pure POCB has an unusually low melting temperature compared to other polyoxyalkylenes, that the melting temperature of the hydrate exceeds that of both of the individual components, and that POCB separates from water upon melting the hydrate[6]. This project moves beyond phase behavior and examines the kinetics of hydrate cocrystallization by dilatometry and by microscopic observations of spherulite growth. The central issues explored here are the dependence of cocrystallization kinetics on mixture composition and temperature.

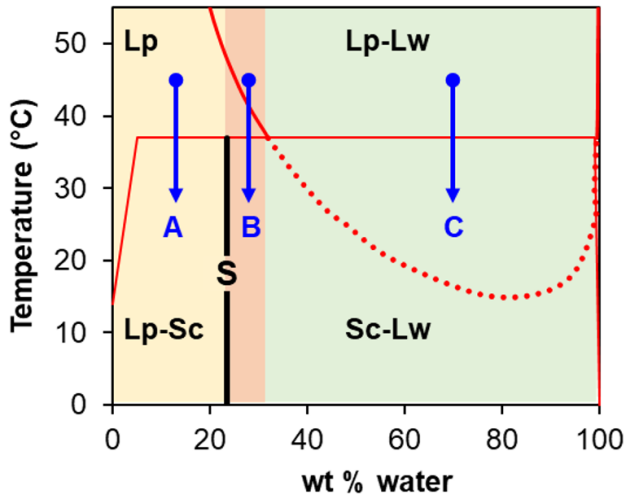

Figure 2.7: Reprinted with permission from ACS Appl. Polym. Mater. 2022, 4, 1, 703–713. Copyright 2023 American Chemical Society. Phase diagram for 650 Da POCB and water. Vertical black line labeled S indicates the composition of the cocrystal hydrate. The solid red indicates liquid-liquid coexistence between L and Lw phases. Dotted red line indicates a metastable portion of the liquid-liquid coexistence curve. Blue arrows illustrate cooling samples in three different composition regions. A: Cooling from a homogenous solution of water and polymer to form POCB/water co-crystals; B: Cooling from a phase-separated mixture through a homogeneous solution to a mixture of cocrystals in equilibrium with a solution of POCB in water; C: Cooling from a phase-separated mixture directly to a mixture of cocrystals in equilibrium with a solution of POCB in water. The left boundary of the Lp-Sc region is drawn approximately; the full phase diagram is shown in Banerjee et al[6].

While the structural and thermodynamic aspects of polymer-small molecule cocrystallization are well-studied[38-39], there is little information about the kinetics of such cocrystallization[44, 48]. As compared to the vast knowledge of crystallization kinetics of homopolymers, polymer blends, or polymer solutions[12, 30, 49], even basic questions about cocrystallization have not been tackled. For example, there is little knowledge of how cocrystallization kinetics depend on temperature, how cocrystallization proceeds with time, or how cocrystallization depends on mixture composition. In polymer crystallization from mixtures, it is well-recognized that diffusion limitations of one or both species may affect crystallization kinetics[30, 50-53]. Since cocrystallization must occur from a mixture of two species, similar diffusion

limitations may be a necessary complexity of cocrystallization. We focus on the kinetics of cooling-induced batch crystallization of POCB/water mixtures with relatively low water content (m_w < 24 wt%) where m_w is the mass percentage of water in the mixture. Low water contents are chosen for this research because, as we will discuss, it is then possible to maintain a single-phase liquid before and during the entire hydrate crystallization process.

Previously, we studied the phase behavior of POCB-water mixtures at a POCB number average molecular weight of 650 Da. Examining the corresponding phase diagram (Fig. 2.7) in detail, POCB hydrate has an isostochiometric crystal (1:1 molar ratio of repeat unit to water), corresponding to a composition of $m_w = 23.6$ wt% water[7]. For the 650 Da polymer, the melting temperature of the hydrate is $T_m = 37$°C, which is higher than both the melting temperature of pure water and pure POCB. Below 37°C, the solid crystal (S_c) coexists with either the liquid polymer-rich phase (L_p) in the region marked L_p-S_c or the liquid water-rich phase (L_w) in the region marked S_c-L_w. Above 37°C, the mixture shows either a single homogeneous liquid (L_p) or a coexistence of polymer-rich and water-rich phases (L_p-L_w). Due to the complex phase behavior, the mixture composition has important implications for batch crystallization induced by cooling and three key composition regions can be distinguished. In region A, with $m_w < 23.6\ wt\%$, a single homogeneous L_p phase exists above the melting temperature of the POCB hydrate. Cooling below T_m produces hydrate, while the coexisting L_p phase concomitantly becomes enriched in polymer as the crystallization proceeds. In region B, where the water content slightly exceeds $m_w = 23.6\ wt\%$, it is possible, depending on the initial temperature, to start crystallizing from the homogeneous L_p phase. However, as crystallization proceeds, the L_w phase becomes further enriched in water, and phase separation of the liquid phase may occur. In region C, corresponding to high m_w values, the phase-separated L_p-L_w region appears above $T = T_m$. As the hydrate

crystallizes upon cooling below T_m, both phases change in composition, until the final S_c-L_w equilibrium is reached. Regions B and C both present significant experimental challenges as phase separation requires the sample to be well-mixed to avoid density-based separation of the liquid phases due to gravity. For this reason, this first study focuses on region A only.

Even homopolymer crystallization is a complex phenomenon. A variety of factors contribute to the rate of crystallization, crystal size and shape, thermodynamic stability, and the degree of crystallinity. Two prevalent theoretical frameworks that are widely applied to the crystallization of polymers are the Johnson-Mehl-Avrami-Kolmogorov (JMAK)[12] model, which models the bulk rate of crystallization, and the Hoffman-Lauritzen (HL)[54] model for lamellar growth. It should be noted that these models each have known limitations. The JMAK model does not take into account all of the mechanics of nucleation and growth of lamellar crystals[55-56], and the HL theory does not capture all molecular aspects of polymer crystallization[54, 57-61]. Despite these limitations, these models have been shown to provide significant insight into the crystallization of polymers. One of our aims is to understand whether the cocrystallization of POCB and water can be described using these established theories.

Although the literature on the kinetics of cocrystallization of polymers with small molecules is sparse, there are some studies on these systems and other related ones that we consider relevant precedent to our current work. In particular there are several investigations that highlight potential applications for these systems, including the melting-induced delivery of encapsulated drugs[62-67] and the sequestration of impurities in water[68-70]. In related, but not fully analogous systems, studies on polymer clathrates and inclusion compounds[38-39, 43, 66, 71-72] and on the kinetics of vapor sorption of already crystallized polymers [73] are also relevant. Also important are studies on polymer-polymer cocrystallization, many of which include detailed kinetic analyses. These

investigations focus on mixtures of the same polymer but with different molecular weights[74-75], mixtures of stereoisomers[48, 76], or structurally-similar polymers [77].

2.3 Experimental

2.3.1 Materials

Polyoxacyclobutane with hydroxyl end-groups was obtained from DuPont under the trade name of Cerenol® and used without purification. The molecular weight of 650 Da was reported by the manufacturer. Our own gel permeation chromatography, using THF as solvent and polystyrene standards, gave a molecular weight of 567 Da and a dispersity of 1.8.

The glassware used to measure specific volume change was made in the glass shop at the University of Pittsburgh.

The hydrophilic fumed silica was obtained from Wacker Chemical Corporation (USA) (HDK N20) and talc (~200 mesh) was obtained from ACROS Organic.

2.3.2 Methods

Volumetric analysis of co-crystallization rates

Apparatus

Custom-made volume dilatometers (Fig. S1) were used for all measurements. The dilatometers consisted of a round-bottom flask with an approximate volume of 4 mL attached via

ground glass joint to glass tubes with an approximate length of 12 cm, an inner diameter of 1.11 mm, and an outer diameter of 7.28 mm.

Sample preparation.

Mixture compositions are be designated by m_w, the mass percentage of water in the mixture. POCB and deionized water were combined to form mixtures ranging from $m_w = 8$—-23.6 wt% water. Prior to loading samples into the dilatometers, the mixtures were heated above the melting temperature of the hydrate to achieve a homogenous liquid. An aliquot (1-2 mL) of this mixture was transferred to the custom dilatometers. The amount of material added was quantified by weight. The dilatometer was assembled and mineral oil (~ 2 mL) was added to the flask and glass tubing such that the oil meniscus at room temperature sat a few centimeters below the top of the tubing.

Volume change measurements

Using a custom sample holder (Figure 2.8), up to 5 samples were monitored simultaneously. Samples were first equilibrated for at least 15 min at 48°C to ensure that all crystals were melted. To record volume changes due to crystallization, samples were rapidly transferred from a hot bath to a cold bath maintained at a chosen crystallization temperature, T_c, in the range of 8–22°C under quiescent conditions. The experiment was photographed at 3.5 s intervals and the images were analyzed using motion tracking software to determine the position of the meniscus in the glass tubing as a function of time. The volume changes were calculated and normalized for sample weight. At the end of the experiment, the temperature was again raised to 48°C provide an accurate meniscus height corresponding to the fully molten sample. Experiments were carried out by Sudesna Banjeree.

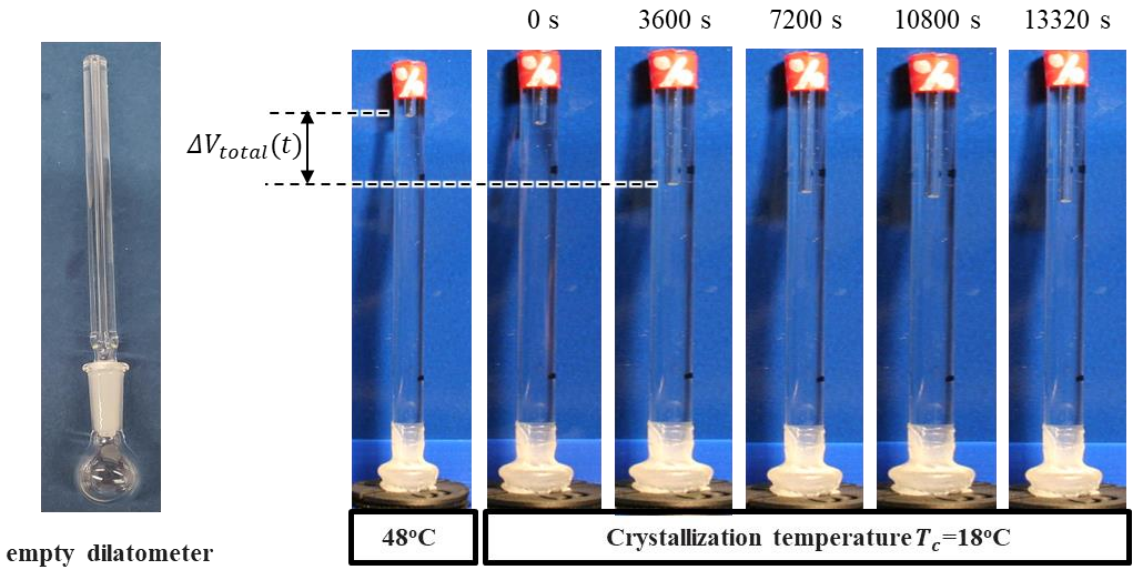

Figure 2.8: Reprinted with permission from ACS Appl. Polym. Mater. 2022, 4, 1, 703–713. Copyright 2023 American Chemical Society. Custom dilatometers were designed to fit 4 mL of liquid (POCB and water) with a capilary place thereon and filled with mineral oil to measure the volume change.

Spherulite growth rate measurements.

Each sample was first melted above 37°C and held at that temperature until the sample was a homogeneous liquid with no crystallites present. A drop of the melted liquid was placed between two glass coverslips, with the thickness regulated by 50 µm thick adhesive tape as a spacer. The sample was immediately moved to a temperature-controlled stage under a polarization microscope (Leitz Orthoplan, with a 10x objective) and images were saved at 3.5 s intervals. Experiments were carried out by Sudesna Banjeree. Due to the relatively low nucleation density, it was necessary to search across the sample to find a growing spherulite, and hence the earliest stages of spherulite growth are difficult to capture. At most sample compositions and temperatures, the spherulites were not precisely circular. To avoid difficulties in tracking the motion of a non-circular perimeter,

the growth velocity G was calculated from the evolution of area A during spherulite growth using the equations:

$$R = \sqrt{\frac{A}{\pi}} \qquad and \qquad G = \frac{dR}{dt} = \frac{1}{\sqrt{4\pi A}}\frac{dA}{dt} \tag{2.2.1}$$

Here the first equation defines the radius of an equivalent circle which has the same area as the spherulite, whereas the second relates the growth velocity G directly to the time-evolution of A. To use the above equations, spherulite images from each experiment were converted into binary form using the ImageJ software[78], and their areas A were measured. The A vs t data were then fitted to a polynomial, and R and G were then obtained from the polynomial using the above equations. Further details related to the data analysis can be found in the supporting information (Fig. S2).

2.4 Results and Discussion

2.4.1 Bulk crystallization kinetics

To understand the effects of temperature on the rate and degree of crystallization, volume changes of mixtures of POCB and water were measured in a custom volume dilatometer. Samples consisting of an 8–23.6% by weight mixture of POCB in water were topped with a layer of mineral oil. In a typical experiment, the pre-loaded dilatometer was transferred from a bath held at a temperature above the melting point (48°C) to a bath held at a fixed crystallization temperature T_c, ranging from 8–22°C.

Two stages of volume contraction were observed (Fig. 2.9a). The first occurred over the course of several minutes regardless of crystallization temperature and is associated with thermal contraction as the sample cools from 48°C to T_c. The second stage of volume contraction is due to crystallization and accelerates with decreasing T_c. The volume change due to crystallization can be isolated from the total by subtracting the thermal contraction according to eq. 2.4.1:

$$\Delta V_c(t) = -\left(\Delta V_{total}(t) - \Delta V_{tc}(t)\right) \quad 2.4.1$$

where the subscripts *tc* and *c* refer to "thermal contraction" and "crystallization", respectively. The negative sign ensures that $\Delta V_c(t)$ is presented as a positive value. The following two paragraphs describe how $\Delta V_{tc}(t)$ is estimated, using Figure 2.9a as an illustrative example.

Two methods were used to determine $\Delta V_{tc}(t)$, depending on the degree of temporal separation between the thermal contraction and the crystallization. At relatively high T_c ($T_c \geq$ 16 ℃ in Fig. 2.9a), $\Delta V_{total}(t)$ shows an unambiguous plateau after roughly 300 s. Further volume change due to crystallization occurs at times much longer than 500 s, indicating that crystallization is far slower than thermal contraction. In such cases, the data for $t <$ 500 s were fitted to a stretched exponential:

$$\Delta V_{tc} = A\left(1 - exp\left(-\left(\frac{t}{\tau}\right)^m\right)\right) \quad 2.4.2$$

Here, the fitting parameters are the magnitude of the thermal contraction, A, the time constant, τ, and the constant, m. The corresponding fits to eq. 2.4.2are shown for $T_c \geq 16\ °C$ as dashed lines in Fig. 2.9a. Typically $\tau \approx 66\ s$ and $m \approx 0.91$.

At lower T_c, crystallization is sufficiently fast that eq. 2.4.2 cannot be reliably fitted to the first 500 s of $\Delta V_{total}(t)$, i.e., there is no clear plateau in $\Delta V_{total}(t)$ before crystallization starts because the two processes occur at similar rates. In such cases, $\Delta V_{tc}(t)$ is determined by estimating

parameters in eq. 2.4.2. From the $T_c \geq 16\,°C$ data we know that parameter A, which is the magnitude of the thermal contraction, varies linearly with temperature (Fig. 2.9b), and hence the values of A below 16°C can be obtained readily by extrapolation. The parameters τ and m were found to be almost independent of T_c, and hence their average values from experiments at $T_c \geq$ 16 ℃ were adopted for $T_c <$ 16 ℃. These calculated $\Delta V_{tc}(t)$ are shown as dotted lines.

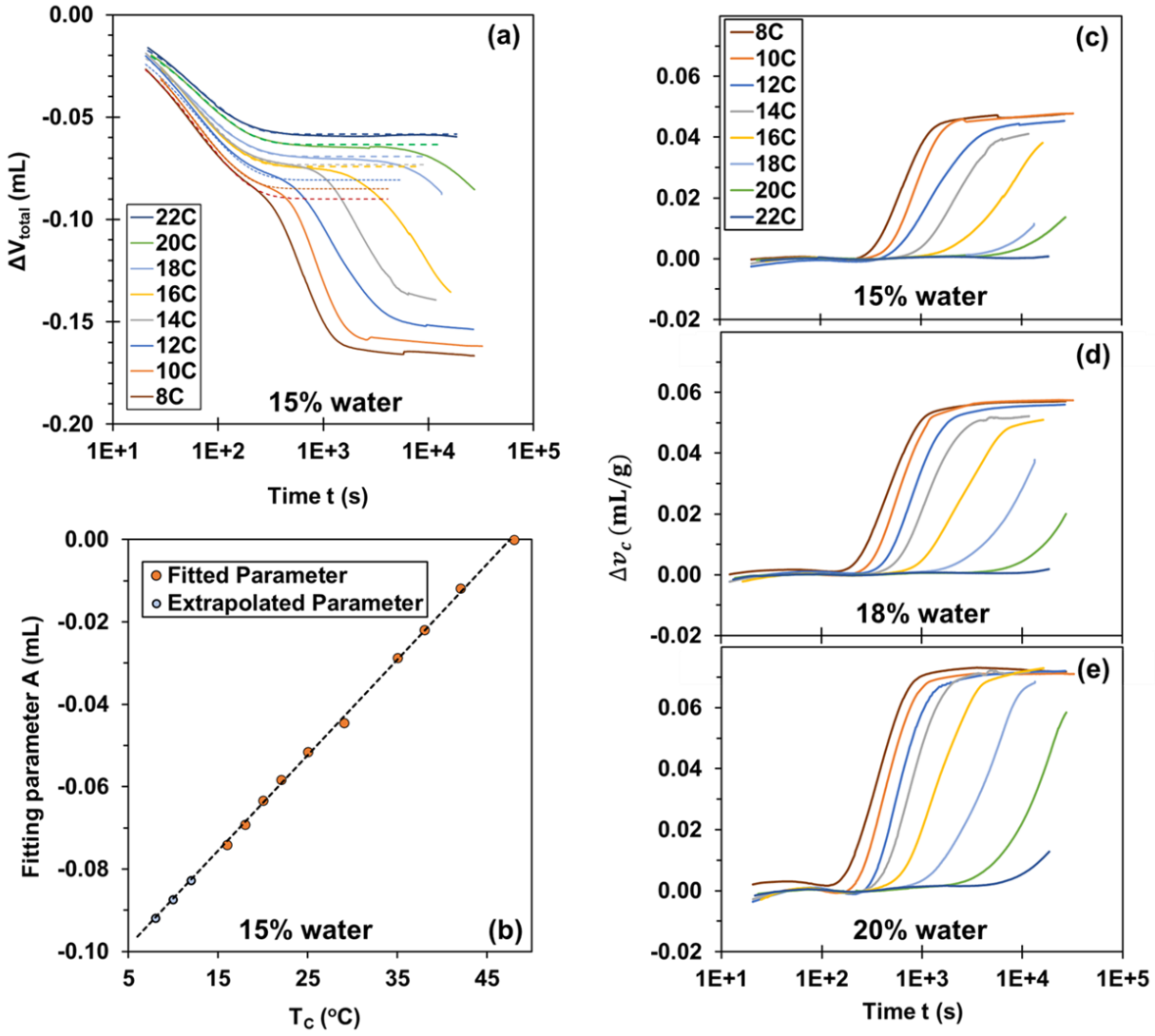

Figure 2.9. Reprinted with permission from ACS Appl. Polym. Mater. 2022, 4, 1, 703–713. Copyright 2023 American Chemical Society. Dilatometry results. a) Sample with $\boldsymbol{m_w = 15\%}$. Solid lines are experimental

measurements of $\boldsymbol{\Delta V_{total}(t)}$. Dashed and dotted lines are volume change due thermal contraction, $\boldsymbol{\Delta V_{tc}}$, see text. b) Magnitude of thermal contraction (parameter A in eq. **2.4.2**) corresponding to the data in plot (a). Filled orange circles are obtained from fitting measured data, open black circles are extrapolated from the linear fit (dashed line). c-e) Specific volume change due to crystallization for mixtures with $\boldsymbol{m_w = 15\%}$, $\boldsymbol{m_w = 18\%}$, and $\boldsymbol{m_w = 20\%}$, respectively.

Having obtained $\Delta V_{tc}(t)$, $\Delta V_c(t)$ was calculated from eq **2.4.2**. $\Delta V_c(t)$ was then normalized by sample mass to give the specific volume change of crystallization, $\Delta v_c(t)$, which is shown in Fig. 2.9c for the mixture with 15% water. The above procedure was applied at all water contents, and examples for mixtures with 18 and 20% water are shown in Fig. 2.9d and e. These calculations and normalizations were carried out by Sudesna Banjeree.

At even lower temperatures, the kinetics of crystallization were sufficiently fast that significant crystallization occurred over the same timescale as temperature equilibration. Since the crystallization is no longer isothermal, such data were not collected.

As typical for isothermal crystallization, the $\Delta v_c(t)$ vs log(t) plots of Fig. 2.9c-e are sigmoidal wherein the long-time plateau reflects the volume change Δv_c^{final} associated with complete crystallization, and the time required to approach this plateau reflects the kinetics of crystallization. For samples with relatively slow rates, crystallization did not reach completion within the time frame of data collection, and thus no plateau was observed.

We now analyze the dilatometric data quantitatively. We first examine how Δv_c^{final} changes with water content. Next, we compare the theoretical Δv_c^{final} with the experimental results and how the kinetics (as gauged by the time needed to reach a specified Δv_c) depends on composition and temperature. Finally, we visualize the $\Delta v_c(t)$ data in the form of an Avrami plot.

To obtain Δv_c^{final}, the following procedure was adopted. As it was impractical to follow all experiments to full crystallization, the 3 hr time point was selected to highlight the differences

in crystallization with water content and temperature. Fig. S4 shows the value $\Delta v_c(t)$ at $t = 3$ hr as a function of T_c. At all water contents, $\Delta v_c(3\ hr)$ increases with decreasing T_c, but plateaus at low T_c values. This behavior suggests that at sufficiently low temperatures, each sample had crystallized to its fullest extent within 3 hr, i.e., a longer crystallization time would not result in more crystallization. The low-temperature plateau value estimated from Fig. S4 is adopted as the Δv_c^{final}, and is plotted in Fig. 2.10a. At or below 10% water, Δv_c^{final} values are not reported because these samples did not crystallize fully even at the lowest temperatures and the longest times examined. Not surprisingly, the Δv_c^{final} increases with increasing water content, reflecting the fact that water is the limiting species for hydrate formation.

The experimental Δv_c^{final} was then compared with the theoretical volume change (assuming complete crystallization of all water, Δv_c^{max}), which is given as

$$\Delta v_c^{max} = \left(\frac{m_w}{\rho_w} + \frac{1 - m_w}{\rho_{POCB}}\right) - \left[\frac{\frac{m_w}{.236}}{\rho_c} + \frac{1 - \frac{m_w}{.236}}{\rho_{POCB}}\right] \qquad 2.4.3$$

where ρ_w, ρ_{POCB}, and ρ_c are the densities of the water, POCB, and crystal, respectively, and 23.6 is the mass percent of water in the crystal. Here, the first bracket is the specific volume of the liquid prior to crystallization (assuming no volume change of mixing), and the latter bracket is the sum of the volumes of the crystal and the uncrystallized POCB. The density of the crystal, estimated from dimensions of the unit cell[7], is $\rho_c = 1.176$ g/mL, whereas ρ_{POCB} =1.02 g/mL and ρ_w =1.00 g/mL. All three densities are taken as independent of temperature.

A comparison of the data with eq. 2.4.3 (solid line in Fig. 2.10a), even when water is the limiting species ($m_w < 23.6\%$), show that not all the water crystallizes and some water remains dissolved in the POCB-rich liquid phase. Note however that this judgement is acutely sensitive to any inaccuracies in ρ_c. In fact, using $\rho_c = 1.14\ g/mL$ (rather than 1.176 g/mL), brings the prediction

of eq. 2.4.2 close to the experimental results. Such a 3% error in density would occur with even a 1% deviation of the actual unit cell dimensions from the reported values. These calculations were carried out by Sudesna Banjeree.

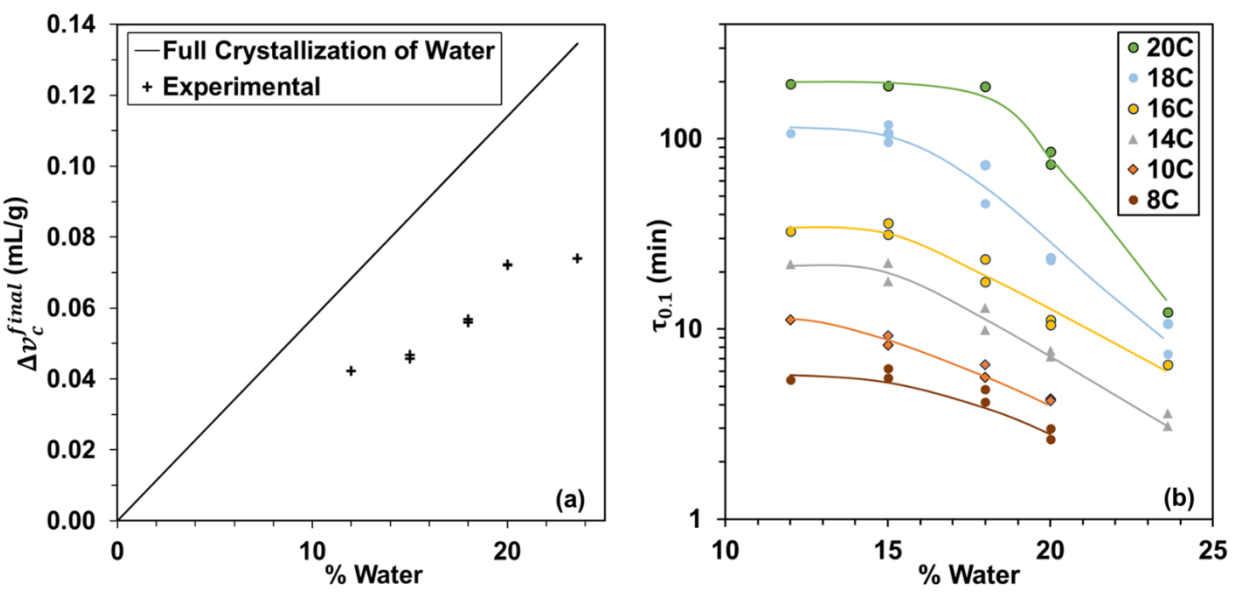

Figure 2.10. Reprinted with permission from ACS Appl. Polym. Mater. 2022, 4, 1, 703–713. Copyright 2023 American Chemical Society. a) Volume change $\boldsymbol{\Delta v_c^{final}}$ at various water contents. Solid line corresponds to full crystallization of water, eq. **2.4.2**. b) Time required for $\boldsymbol{\Delta v_c = 0.1 v_c^{final}}$, i.e., to reach 10% of the final volume change.

Turning to crystallization kinetics, we define $\tau_{0.1}$ as the time at which $\Delta v_c(t)$ reaches 10% of its final value, i.e., $\Delta v_c(t = \tau_{0.1}) = 0.1\Delta v_c^{final}$. The $\tau_{0.1}$ value provides a simple metric to judge the relative crystallization rates across all samples. Fig. 2.10b shows that $\tau_{0.1}$ increases, i.e, crystallization rate decreases, with both increasing temperature and with decreasing water content. At the lowest water contents, however, $\tau_{0.1}$ does not increase any further, i.e., crystallization becomes independent of water content. A similar analysis for $\tau_{0.5}$, i.e., the time needed for half of the final volume change, shows the same trends (Fig. S5).

Finally, moving beyond a single-number metric of $\tau_{0.1}$, we consider the details of how Δv_c evolves with time. The volume changes associated with crystallization can be described by the Avrami equation[12]:

$$\frac{\Delta v_c(t)}{\Delta v_c^{final}} = 1 - \exp\left(-(kt^n)\right) \quad 2.4.4$$

where k is the rate coefficient and n is the Avrami exponent. To test whether the Avrami equation can describe hydrate formation in this cocrystallization system, the data were plotted in the linearized form commonly used in the literature:

$$\ln\left(-\ln\left(1 - \frac{\Delta v_c(t)}{\Delta v_c^{final}}\right)\right) = n\ln(t) + \ln(k) \quad 2.4.5$$

A plot of the left-hand side of eq. 2.4.5 vs $\ln(t)$ is expected to give a straight line with a slope equal to the Avrami exponent n. Fig. 2.11 shows an example for the specific case of $m_w =$ 18% (same data as Fig. 2.9d). Similar plots for other compositions are shown in Fig. S6. As previously described by others [12, 35], such plots are highly sensitive to small errors in Δv_c early in the crystallization process, e.g., any uncertainties associated with subtracting the thermal contraction in eq. 2.4.1. Accordingly, data at very early stages $\frac{\Delta v_c(t)}{\Delta v_c^{final}} < 0.02$ are not shown in Fig. 2.11.

The data in Fig. 2.11 and Fig. S6 show approximately linear behavior early during the crystallization, with a decrease in slope at later stages consistent with past results for homopolymers [12, 35]. The early-time slopes are close to the $n = 4$ line at low T_c, and close to the $n = 2$ line at high T_c. Further, at fixed T_c, n values generally increase with increasing water content, m_w. The same conclusions are reached if the data are plotted in the Goler-Sachs form [12]

(ln ($\Delta v_c/\Delta v_c^{final}$) vs ln ($t$)), not shown. Additionally, the n values were insensitive to small changes in the value of Δv_c^{final}.

A modified Avrami analysis is sometimes adopted[35, 79] for polymer crystallization where

$$\frac{\Delta v_c(t)}{\Delta v_c^{final}} = 1 - \exp\left(-(k(t - t_{ind})^n)\right) \quad 2.4.6$$

Here the time t_{ind} is an induction time, i.e., a time delay before the crystallization starts. Induction times typically increase as T_c increases[79-81]. We reanalyzed the data using eq. 2.4.6 in two variations. In one variation, t_{ind} was selected to be 200 s, which roughly corresponds to the timescale needed for the sample to cool to within 1°C of the final temperature, T_c. This approach is based on the idea that because crystallization accelerates sharply with reducing temperature, all the crystallization must occur only after the sample temperature is close to the target T_c value. This modification reduces the n value for the fast-crystallizing samples but has no effect on the n value for slow-crystallizing samples. In the second variation, t_{ind} was set arbitrarily to $\tau_{0.1}/3$, which caused the n value to decrease in all cases. Uncertainties in what value of t_{ind} to use, or indeed whether t_{ind} should simply be set to zero, cause corresponding uncertainties in the absolute values of n. Nevertheless, the overall conclusion – that n reduces as T increases – was found to be valid, independent of choice of t_{ind}.

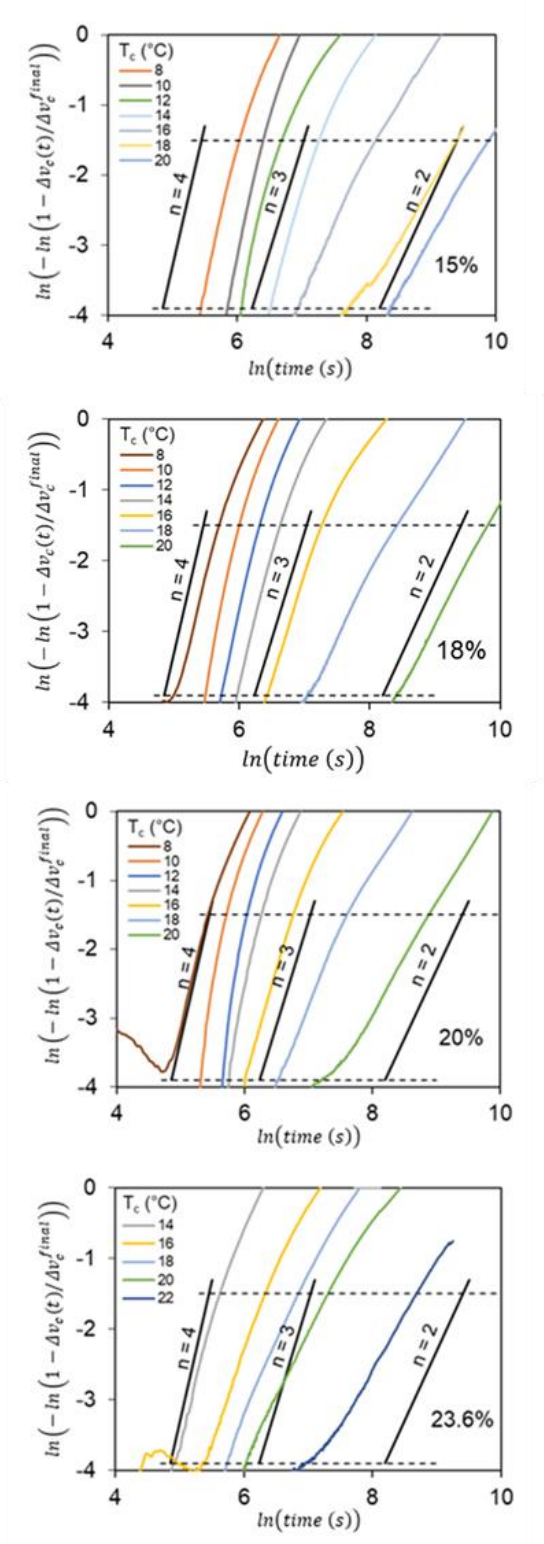

Figure 2.11. Avrami plots in the form of eq. **2.4.5** at $\boldsymbol{m_w = 15\%, 18\%, 20\%}$ and $\boldsymbol{23.6\%}$. The data are identical to Fig. 2.9d. Lower and upper dashed lines respectively correspond to $\boldsymbol{\Delta v_c / \Delta v_c^{final}}$ values of 0.02 and 0.2.

2.4.2 Spherulite Growth Velocity in Isothermal Crystallization Process

Even a cursory examination of the dilatometers during crystallization showed the presence of spherulites. The growth of these spherulites could be monitored under a polarization microscope in a film geometry. As in all polymer crystallization, one may expect that spherulite growth velocities increase significantly with decreasing temperature T_c. Further, since crystallization requires both water and POCB, one may also expect the growth velocity to depend on mixture composition. This section quantifies the dependence of spherulite growth velocity (G) on T_c at one fixed composition, and on composition at one fixed crystallization temperature.

The evolution of G with spherulite radius is shown in Fig. 2.12a at a single crystallization temperature (T_c = 14°C) for various compositions, and in Fig. 2.12b at a single composition ($m_w = 18\%$ water) for various temperatures. Example images of growing spherulites are shown above each graph. In many cases, G initially decreases as the spherulite grows. In most experiments, a steady growth velocity is reached at long times. In some experiments, before a clear steady state is reached, the growing spherulite may impinge upon another spherulite, or may grow beyond the field of view. For such samples, the last measured value of *G* is shown in Fig. 2.12a and b. We will discuss the steady velocities first, and the growth-dependent changes in G next.

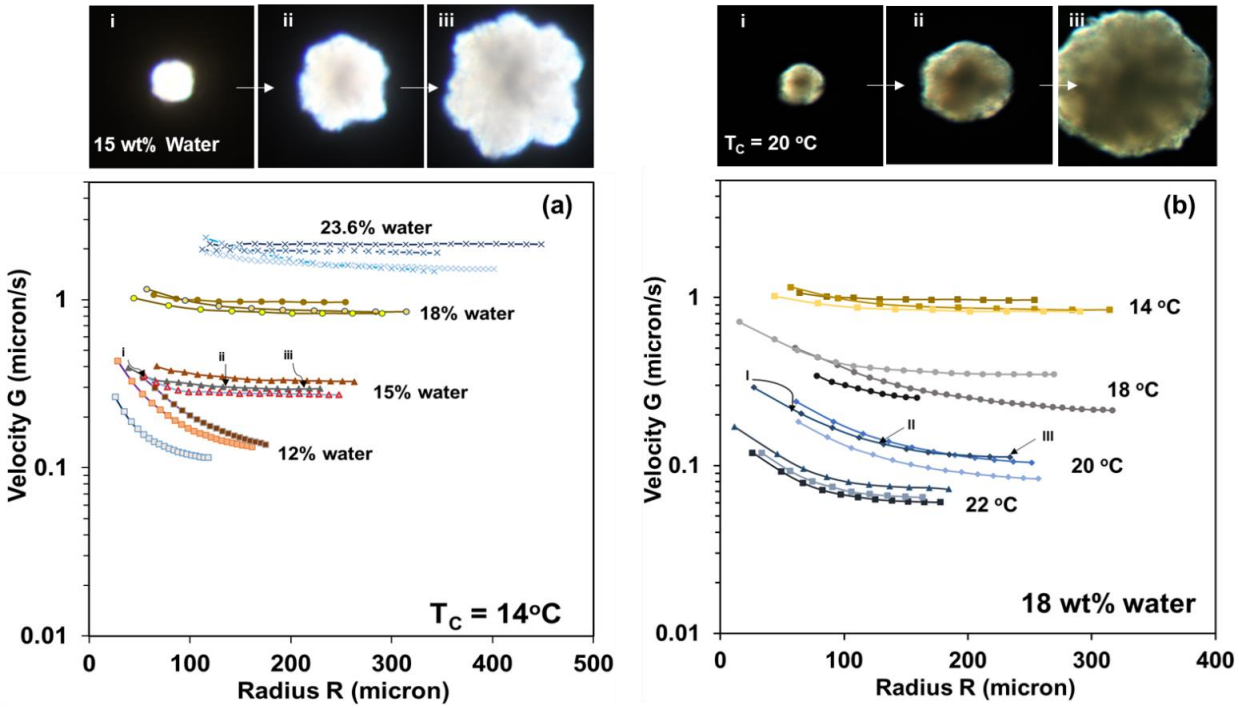

Figure 2.12. Reprinted with permission from ACS Appl. Polym. Mater. 2022, 4, 1, 703–713. Copyright 2023 American Chemical Society. Velocity during spherulite growth in POCB-water mixtures (a) of various compositions at $\boldsymbol{T_c}$ = 14°C and (b) at various temperatures $\boldsymbol{T_c}$ for a fixed composition $\boldsymbol{m_w}$ = 18 wt % water. Each experiment was conducted three times, and each run is shown separately. Example images at three stages of spherulite growth are shown above. Data collected by Sudesna Banjeree.

Fig. 2.13a shows that the steady growth velocity increases with increasing water content, and the dependence of G on m_w is almost exponential, as shown by the solid line. Fig. 2.13a also plots the bulk crystallization rate, as represented by $\tau_{0.1}^{-1}$ and $\tau_{0.5}^{-1}$, at 14°C. The slope of the dashed line is the same as of the solid line indicating that over most of the composition range, G and the bulk crystallization rate have the same composition dependence. Fig. 2.13b shows that G decreases as T_c increases. The qualitative trend is similar to the decrease in $\tau_{0.1}^{-1}$ and $\tau_{0.5}^{-1}$ with temperature (once again, the data in Fig. 2.13a are identical to those in Fig. 2.10b).

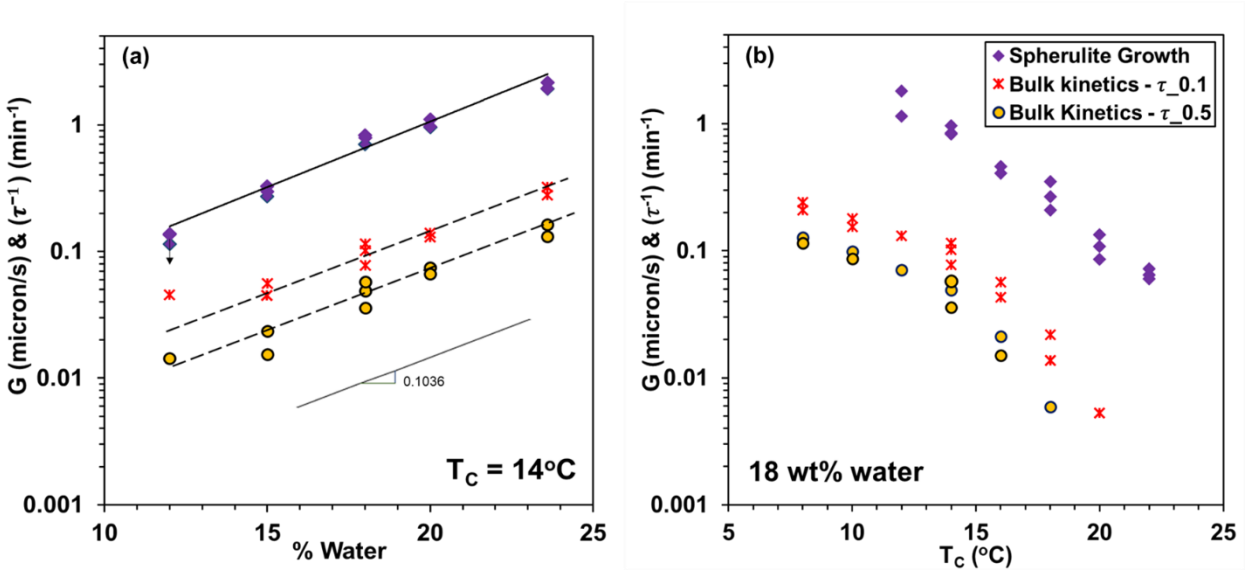

Figure 2.13. Reprinted with permission from ACS Appl. Polym. Mater. 2022, 4, 1, 703–713. Copyright 2023 American Chemical Society. Dependence of steady state growth velocity a) on composition $\boldsymbol{m_w}$ (at fixed $\boldsymbol{T_c}$ = 14°C) and on Dependence b) $\boldsymbol{T_c}$ (at fixed $\boldsymbol{m_w}$ = 18% water). The $\boldsymbol{\tau_{0.1}}$ are the same data as in Fig. **2.10**b.

The temperature dependence of growth velocity is often well-described by the Hoffman-Lauritzen theory which predicts an exponential dependence of G on $T_m/(T_c\Delta T)$ where $\Delta T = (T_m - T_c)$ is the undercooling. Fig. 2.14 plots the velocity data in the form suggested by this theory. Note that since $T_m = 310\,K$, and T_c ranges from 283-295 K, the term T_m/T_c is nearly constant and close to 1. Accordingly, the x-axis of Fig. 2.14 is nearly identical to $100/\Delta T$. The solid line is a fit to

$$\log_{10} G = A + B\frac{T_m}{T_c \Delta T} \qquad 2.4.7$$

where the temperature-coefficient $B = -0.534 \times 10^{-2}\,K^{-1}$, which is the slope of the Hoffman-Lauritzen plot, quantifies the sensitivity of the growth velocity to the undercooling. The bulk crystallization rates $\tau_{0.1}^{-1}$ and $\tau_{0.5}^{-1}$ are plotted on the same graph. At high undercooling, the data can be well-fitted with a line of slope of B (dashed line), i.e., the bulk crystallization kinetics have

roughly the same temperature dependence as the growth velocity. At low undercooling however, the $\tau_{0.1}^{-1}$ and $\tau_{0.5}^{-1}$ decreases more steeply as ΔT reduces. These results may be approximated by two straight lines (not shown) suggesting a regime change[82-85] with increasing undercooling.

The increase in temperature dependence of the $\tau_{0.1}^{-1}$ vs $\frac{T_m}{T_c \Delta T}$ data at low undercooling appears at all compositions (Fig. S7). At sufficiently large undercoolings, the data for all compositions can be approximated with the same slope of *B*. With increasing T_c, there is a transition to a higher slope, and the transition seems to occur at lower temperatures at lower water content. We speculate that this behavior may be attributable to a sharp decrease in primary nucleation rate as T_c approaches the melting temperature T_m, or as water content reduces. Notably, such a decrease in primary nucleation rate would not affect the slope of the G vs $\frac{T_m}{T_c \Delta T}$ data, which is consistent with Fig. 2.14. Alternatively, the indirect method of calculating G from volume may have somehow affected the results.

Finally, we turn to the observation from Fig. 2.12 that in many cases, G decreases during spherulite growth. In homopolymer systems under isothermal conditions[30, 86], spherulites grow at a constant radial growth velocity. However, in multicomponent systems the presence of impurities in the melt can reduce G as spherulites grow[50]. The impurities must be excluded from the crystals and, if growth is sufficiently slow, the impurities may be rejected from the spherulite altogether. This exclusion leads to the gradual build-up of a high concentration of impurity at the spherulite growth front, hence reducing G. Eventually, a steady state may be reached such that the spherulitic growth rate matches the rate at which the impurity diffuses away from the interface. The POCB-water cocrystal has 23.6 wt % water[6], corresponding to 1:1 molar ratio of monomer repeat unit to water, and therefore in all samples with $m_w < 23.6\%$ water, the excess POCB must be rejected. Excess POCB can then be viewed to have the same effect as an impurity. Moreover, lower values of m_w

require larger quantities of POCB to be rejected. Rejection of the POCB would cause a decrease in G until an eventual diffusion-limited steady-state growth is reached. The experiments agree with these expectations. Specifically, Fig. 2.12 shows that the decrease in G is much larger at low water contents, i.e., at compositions in which a larger quantity of POCB must be rejected from the crystallization mixture.

Although most samples reach a steady growth velocity in our experiments, the behavior of G at long times depends strongly on composition. For the sample with 23.6 wt% water, spherulites stop growing when they impinge on each other. However, for non-stoichiometric mixtures, we expect growth would eventually slow down because the available water is exhausted even before impingement. Such non-impinging spherulites are well-documented in the literature on crystallization of homopolymers with impurities.[30] In such cases, G must eventually reduce to zero prior to impingement. However, this corresponds to very large spherulites which are too large to be captured within the field of view of the microscope, and thus a decrease in G towards zero is not seen in Fig. 2.12.

At late stages during crystallization (beyond the times considered in the analysis here), it was observed that the spherulites sometimes showed flower-like shapes, which have also been seen previously[49, 56, 87]. Since the above analysis solely focused on the early stage spherulites, this type of shape did not affect the quantitative results presented above.

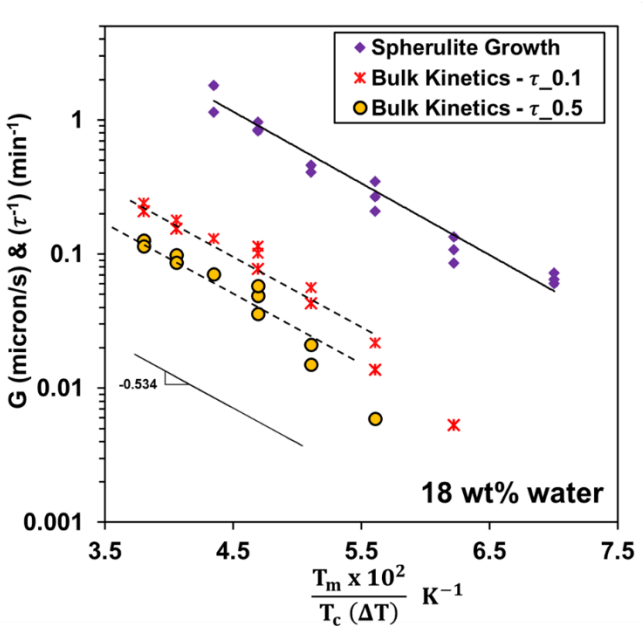

Figure 2.14. Reprinted with permission from ACS Appl. Polym. Mater. 2022, 4, 1, 703–713. Copyright 2023 American Chemical Society. Spherulite growth velocity and bulk kinetics of mixtures with $\boldsymbol{m_w}$ =18 wt% water in the form of a Hoffman-Lauritzen plot.

2.5 Summary and Conclusion

In summary, polyoxacyclobutane has the rare ability to cocrystallize with water to form a hydrate. We report the first study of the kinetics of POCB hydrate cocrystallization, and indeed the first study of cocrystallization kinetics of any polymer with a small molecule. This section is restricted to water contents below 24 wt% at which POCB-water mixtures form single phase homogeneous liquid prior to crystallization. (We further report on heterogenous mixtures containing more than 24 wt% POCB in later work:

Banerjee, Sudesna, et al. "Polymer co-crystallization from LLE: Crystallization kinetics of POCB hydrate from two-phase mixtures of POCB and water" *Polymer* (2023): https://doi.org/10.1016/j.polymer.2023.126087)

We examine the kinetics of bulk hydrate crystallization by dilatometry, and the kinetics of spherulite growth by polarization microscopy. The central issues of interest are the dependence of cocrystallization kinetics on temperature and mixture composition.

The central conclusions of this section are:

The time-evolution of the bulk kinetics can be described by the Avrami equation, though only for the initial time period as the diffusion effects of the two-component system quickly dominate the rate. The Avrami exponent reduces from roughly 4 to 2 as undercooling reduces, even for the stoichiometric mixture, suggesting that there is in fact a mechanism change in the polymer growth as the degree of undercooling changes.

The bulk crystallization rate, as quantified by the reciprocal of time needed to reach 10% crystallization, decreases exponentially as the water content reduces and decreases exponentially as ΔT^{-1} increases, where ΔT is the undercooling. At dilute water content, spherulite growth velocity reduces from a high initial value to a steady state value, reminiscent of homopolymer crystallization with impurities. This suggests that the excess POCB (as the non-limiting species) acts as an impurity, causing diffusion barriers to hydrate crystallization.

When plotting the $t_{.1}$ version of the HL plots (collected from bulk kinetic data), a regime change can be noted in a way that is in line with a change between regime 1 and regime 2. Interestingly the spherulite growth rate plot does not show that supposed regime change. This may be due to the data collection method or changes in primary nucleation.

Overall, we conclude that the well-established kinetic models in the polymer literature also apply to cocrystallization. The bulk crystallization kinetics data can be well-fitted by the JMAK model, and the temperature-dependence of spherulite growth velocity is consistent with the Hoffman-Lauritzen model. At least one other polymer is known to cocrystallize with water, and

many more cocrystallize with other small molecules, although cocrystallization kinetics have not been reported. This paper suggests that when the mixture is a homogeneous liquid prior to cocrystallization, the process resembles homopolymer crystallization. Yet, the dependence of kinetics on composition is a necessary complexity in such systems, i.e., as the mixture composition deviates from the cocrystal stoichiometry, the excess species must act as an impurity. Our ongoing work focuses on hydrate crystallization kinetics at high water contents at which POCB-water mixtures are in liquid-liquid equilibrium prior to crystallization.

3 POCB block-copolymers

3.1 Overview

3.1.1 Naming conventions

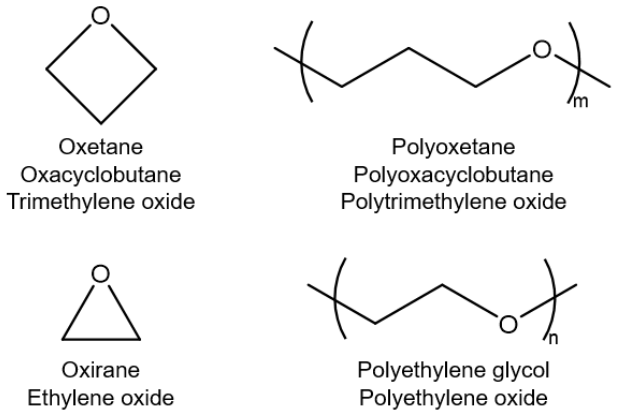

Figure 3.1: A non-exhaustive list of the names of the two block copolymer components and their corresponding mers.

Throughout this chapter the two main block components and their corresponding mers are referred to by a multitude of different names (Fig 3.1). The four-membered single-oxygen-containing heterocycle is known as oxetane, oxacyclobutane, and trimethylene oxide, while its linear polyether form is known as polyoxetane, polyoxacyclobutane (POCB), and polytrimethylene oxide. I have a slight preference for using the oxetane/polyoxetane nomenclature when discussing the reactions and syntheses thereof, and prefer to use the oxacyclobutane/polyoxacyclobutane (POCB) nomenclature when discussing the crystallization thereof, but that is not a fast rule. Trimethylene oxide/polytrimethylene oxide is rarely used except

to refer to chemicals purchased from a supplier that uses that name or to discuss a paper in which it is so named.

The three-membered single-oxygen-containing heterocycle is known as oxirane and ethylene oxide, though neither see much use in this document as this material was not handled directly. Its linear polyether form is commonly known as both polyethylene oxide (PEO) and polyethylene glycol (PEG). Historically, PEO is the term used to refer to high molecular weight forms of this polymer while PEG is the term used to refer to low molecular weight forms of this polymer, due to differing synthetic methods. In modern times the two are used interchangeably and in this section I switch between the two freely.

3.1.2 POCB synthesis

POCB can be readily prepared by the ring-opening of four-membered oxetane monomer, although this polymerization has been less studied than that of its three-membered cousin, oxirane, or the poly(THF) which is prepared from the 5-membered ring. Rose published the seminal work on POCB synthesis in 1956 using a cationic BF_3 etherate catalyst,[88] based on a few sparse prior works.[89] Many subsequent polymerizations of POCB utilize this method[90], including several foundational studies of POCB synthesis as well as numerous branched and functionalized POCB for a variety of applications[91]. The ring opening of oxetane inherently presents a greater challenge than the ring opening of oxirane due to a reduced ring-strain and a large activation energy of initiation. Various other synthetic methods have been reported to polymerize linear POCB including silyl activation, transition metal- and indium-based catalysts, hexafluoro-containing catalysts, heterogeneous catalysis, photocatalysis, bulky aluminum complexes, and acid

catalysis[92-93]. Commercial production of polyoxetane, which generally proceeds not through ring-opening but rather by condensation of diols, has included Velvetol[94] and Cerenol[95].

Of particular relevance to the current studies, cyclic ethers, including propylene oxide, can also be polymerized by initiation with an ammonium salt or alkoxide in the presence of a trialkylaluminum activator. This approach gives a defined end-group, good molecular weight control, and a narrow molecular weight distribution, although some initiation from hydride produce by chain transfer is observed[96-98]. Block copolymers of linear POCB can be produced using a variety of conventional methods[99-105], as well by coupled reactions of homopolymer blends[106-107].

3.1.3 Amphiphilic block copolymer self-assembly

Amphiphilic block copolymers (those possessing both a hydrophobic block and a hydrophilic block) display several unique and advantageous properties that can be and are exploited for practical applications, in particular drug-delivery[108-109]. Many drugs and pharmaceuticals possess high activity and effectiveness when tested *in vitro but* lose functionality *in vivo* as their hydrophobic structure limits bioavailability. Amphiphilic block copolymers help solubilize such drugs due to their tendency to self-assemble in aqueous media into macrostructures possessing an inner hydrophobic core and an outer hydrophilic shell, allowing the hydrophobic drug to associate with the hydrophobic portion while the hydrophilic portion solubilizes the structure [108, 110].

Both spherical micelles as well as cylindrical micelles are well-documented for amphiphilic block copolymers, as well as higher-order structures[109, 111]. Spherical micelles are

significantly favored to form over cylindrical micelles due to their thermodynamically stable form, however cylindrical micelles cylindrical micelles have a longer circulation time than spherical micelles in *in vivo* circulation.[14, 112-116].

Particles that possess a surface change in the layer surrounding the particle (ξ-potential) have greater stability than particles without, due to the repulsive forces that keep particles apart from each other. Micelles of PEO and polypropylene oxide (PPO) block copolymers, a structural isomer of PEO and POCB block copolymers, are known to undergo gelation at high temperatures, in which the micelles clump together[117-118], perhaps owing to its non-ionic nature.

3.1.4 Crystallization within block copolymers

Crystallization within block copolymers is a complex subject delving into the interplay of several competing forces. If the crystallization occurs below the glass transition temperature of the non-crystallizable block, the microphase structure is maintained and the crystallization occurs under confinement, which can many things about the crystallization process such as nucleation, growth, and crystal alignment[119]. When the crystallization occurs above the glass transition temperature of the non-crystallizable block, the phase segregation is maintained only if the segregation strength of the two phases is sufficiently high[120].

Very rarely do crystalline-core micelles form 1D spherical structures instead preferentially forming cylindrical micelles[121] which can be tuned to a precise, monodisperse length through crystal seeding in what is known as living crystallization-driven self-assembly (CDSA)[122-124]. Due to the co-crystallization of the POCB-water hydrate, we expect it also to tend to the formation of

cylindrical micelles, giving it advantages over related spherical polymer systems as discussed in the previous section.

3.1.5 Relationship to previous work on POCB/PEO

Two prior accounts exist of linear POCB-containing block copolymers: Bin et. al.[100] reported the successful polymerization of di- and triblock copolymers containing POCB *via* cationic polymerization and Gervais et. al.[99] reported on the successful polymerization of PEO-b-POCB block copolymers *via* anionic polymerization in the presence of triisobutyl aluminum activator, taking advantage of the large reactivity ratio difference of ethylene oxide and oxetane to produce blocky copolymers. Especially of interest are the results by Gervais and coworkers on the thermal behavior of said micelles. In particular, they noted changes in micelle size of one of their three block copolymers at the temperature associated with the crystallization of POCB with water, though they were not familiar at the time with POCB's unique ability to cocrystallize with water. It was our goal to understand if the POCB block was exhibiting cocrystallization behavior and to determine the effect on the supramolecular association of the block copolymer in water.

3.1.6 Relationship POCB/PEO Block Copolymers to Pluronics; Implications for Potential Applications

POCB/PEO block copolymers are closely related to the well-known and widely applied class of amphiphilic copolymers known as Pluronics[125]. Pluronics, which are also known as

Poloxamers, are a class of triblock copolymers that consist of three distinct blocks: a central hydrophobic polypropylene oxide (PPO) block surrounded by two water-soluble hydrophilic polyethylene oxide (PEO) blocks.

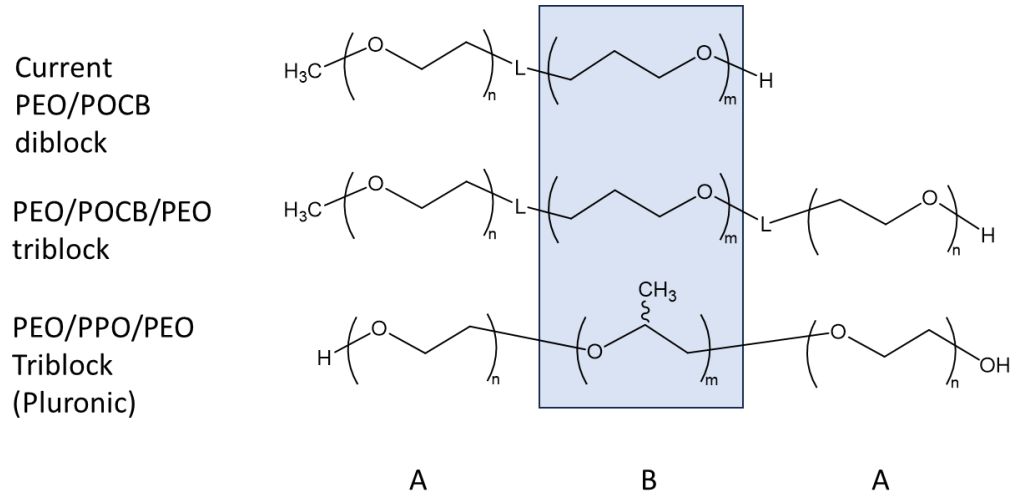

Figure 3.2: Comparison of current PEO/POCB diblock with a potential ABA triblock and the PEO/PPO/PEO triblock which are called pluronics. "L" signifies click linker group. Orientation of the blocks reflects, i.e. head-to-tail, etc., reflects the synthetic approach and would not be expected to affect properties except those that depend explicitly on the endgroup.

Pluronics exhibit a number of distinctive properties that make them especially suitable as drug-delivery agents[117, 126-130]. First, they are amphiphilic which allows them to encapsulate hydrophobic drugs and suspend them in an aqueous environment. Second, these polymers are FDA approved due to their biocompatibility, exhibiting low toxicity when used *in vivo*. Third, they exhibit a temperature-dependent gelation behavior favoring a liquid state at low temperatures and a gel-like state at higher one. This latter behavior can be exploited for drug-delivery.

Although we have initially focused on only diblock copolymers of POCB/PEO, it is clear that the triblock system PEO-*b*-POCB-*b*-PEO would be interesting to study based on their close structural relationship with pluronics (Fig. **3.2**). The oxacyclobutane repeating unit in POCB is a simple isomer of the propylene oxide repeating unit in PPO. The major difference between these

two polymers lies in their tendency to interact with water. Both are hydrophobic at higher temperatures. At lower temperatures, however, we would expect that the tendency of POCB to crystallize with water would provide new behaviors that could be exploited for applications. It would, for example, be interesting to determine the relative tendency of the PEO-*b*-POCB-*b*-PEO copolymer to interact with water vs. a hydrophobic substrate. This competition could possibly be exploited both to promote encapsulation and to control the rate of drug delivery.

3.1.7 Experimental techniques

Differential Scanning Calorimetry

Differential Scanning Calorimetry (DSC) is a useful thermal analysis technique in polymer chemistry to investigate the heat flow associated with phase transitions by measuring the difference in heat flow between a sample and a reference pan as a function of temperature, while both are subjected to a controlled heating or cooling ramp. DSC relies on the fact that different physical processes involve a change in the absorption or release of heat. The sample and reference pans are equipped with temperature sensors (thermocouples) to measure their temperatures accurately. As the experiment progresses, the instrument records the heat flow difference between the sample and reference pans required to heat the two pans to the same temperature as a function of time or temperature. By comparing the heat flow to the sample with the heat flow to the reference, DSC can detect endothermic and exothermic transitions such as melting and crystallization.

Dynamic Light Scattering

Dynamic Light Scattering (DLS) is a technique frequently employed in polymer chemistry to characterize particle size. DLS utilizes the Brownian motion of particles and their Raleigh scattering to elucidate their diffusion coefficient, and thus their size, by shining a laser through the sample and comparing the scattering pattern of the light between two time intervals. The intensity of the scattering vs time fluctuates more rapidly for smaller particles than for larger ones due to the slower diffusion of larger particles. On large time scales this plot behaves randomly, but on very small scales the plot at one time, t', is related to the plot at time t' + t. The amount of time each location on the intensity vs time plot remains "correlated" with future plots, the lag time, t, is then plotted in what is known as an autocorrelation plot. An autocorrelation function is then calculated from the autocorrelation plot, and from the decay rate a diffusion constant can be extracted. The Cumulants method or the Continuous Distribution of Relaxation Times (CONTIN) algorithm are two common ways to calculate the autocorrelation function[131]. From the diffusion constant, the hydrodynamic radius can be then calculated.

DLS has several limitations due to the indirect nature of its measurement process. To start, the autocorrelation function is best calculated for monodisperse samples between 0.3 nm and 10 μm. Further, the diffusion coefficient calculation assumes that solution is an infinitely dilute sample, which is an approximation only if the sample is sufficiently dilute. Additionally, the transformation of the diffusion constant to the hydrodynamic radius assumes the particle is a solid sphere with radius R, which may not be true for non-spherical particles and particles that interact with the water. One must also know the refractive index of the particle for particles larger than approximately 100 nm in order to view the number or volume plots instead of the intensity plot.

X-Ray Diffraction

X-Ray Diffraction (XRD) takes advantage of the fact that the crystalline spacing of atoms is on the same length-scale as x-rays, causing specific diffraction patterns when a crystalline substrate is subjected to X-ray radiation, a phenomenon known as Bragg's law. This diffraction pattern is due to the fact that the regular spacing of atoms causes light to interfere both constructively and destructively at regular intervals for certain angles at which the light interacts with the sample. The presence of diffraction in a polymer sample indicates that there is some degree of ordering in the sample, likely crystallization.

The analysis of XRD is based on the Bragg's Law equation:

$$n\lambda = 2dsin\theta \quad (2.1.1)$$

$n\lambda = 2dsin\theta$Where n is an integer, λ is the wavelength, d is the spacing distance, and theta is the incident beam angle. In single-crystal XRD, an x-ray beam is shined upon a single crystal over a range of angles. Because all the spacings are oriented the same way, results appear as a lattice, with points angled in the planes of the crystal. With powder XRD, crystals are oriented in all directions and a ring of diffraction is produced at incident angles at which any spacing is present, thus no information is present about the direction and orientation of the crystal. Polymer XRD produces similar results to powder diffraction, as the crystals within the polymer are not oriented in a single direction but instead are angled in all possible directions. With polymer XRD you might also see the presence of very broad peak which represents the amorphous portion of the polymer.

3.2 Experimental

3.2.1 Sample procedure for the synthesis of POCB and PPO from an alkoxide

Liquid alcohols (ethanol (200 proof from Decon Labs), isopropanol (Fisher Scientific), and benzyl alcohol (Mallinckrodt Chemicals) were dried via reaction with CaH_2 overnight and purified via distillation. Solid alcohols (750, 2000, and 4000 g/mol monomethyl polyethylene oxide from Sigma Aldrich or TCI) were dissolved in benzene and pre-dried via azeotropic distillation of the benzene/water azeotrope. Alkoxides were prepared by reaction of the alcohol (~20 mL in toluene (Fisher Chemical), 0.25 M) with excess sodium (Mallinckrodt Chemicals) or potassium metal (Sigma Aldrich) (Scheme 3-1). Unreacted alkali metal was quenched in water.

Assuming 100% yield of alkoxide, the dispersion in toluene (0.002 mol, 0.25 mL) was transferred to a glass bomb via syringe. Triisobutylaluminum (TIBA) (Sigma Aldrich) was added in at least 2x excess (1 mL, 1.1 M in toluene). Oxetane (thermos scientific, TCI, and Millipore Sigma) and propylene oxide (Acros) were dried via overnight stirring with CaH_2 and isolated via distillation. *Polymerization:* dried oxetane or propylene oxide was added (1.0 mL) and the sealed vessel stirred overnight either at room temperature or with heat (Scheme 3-1). The polymer was extracted twice from water with toluene.

3.2.2 General procedure for the synthesis of azide-terminated POCB (N_3-POCB)

Trimethylene oxide (oxetane), 97%, was received from Milipore-Sigma and stirred over calcium hydride overnight and subsequently vacuum-transferred to a dry Schlenk flask. *Polymerization*: N-tetrabutyl ammonium azide (TCI) (1 eq.) and triisobutyl aluminum (Sigma

Aldrich) (3 eq.) were transferred to a glass bomb via syringe and stirred. The mixture was degassed by freeze-pump-thaw (3x). Trimethylene oxide (1-3 g) was added, and the closed vessel was allowed to stir overnight at RT (Scheme 3-23-1). The reaction was quenched with MeOH (Fisher Chemical), and the solvent was removed by evaporation. The oily solid was dissolved in toluene and extracted with water (2x). After separation, the solvent was removed from the organic layer to yield the polymer as a viscous liquid (90% yield).

3.2.3 General procedure for the alkylation of PEO (PEO-alkyne)

Polyethylene glycol monomethyl ether was received from TCI and dried by dissolution in benzene followed by azeotropic distillation (12 h). The dried PEO was alkyne functionalized using methods previously described by Hiki and Kataoka[132] (Scheme 3-2). Briefly, a flame-dried rb-flask was equipped with a stir bar and charged with 3 eq. NaH (Acros). The polymer (~20 g) was dissolved in THF (80 mL) with gentle heating and transferred via syringe to the reaction vessel. Propargyl bromide (Aldrich) (0.5 M, 2 eq.), dissolved in THF (Fisher) was transferred slowly to the reaction vessel over 30 min. After stirring overnight at RT, the reaction mixture was quenched with deionized water, evaporated, and extracted into CH_2Cl_2 (Fisher). Upon removal of CH_2Cl_2 by evaporation under vacuum, the product was a yellow-white solid. Dissolving in benzene (Sigma Aldrich) followed by free-drying produced a free-flowing off-white powder. MALDI analysis was consistent with 100% substitution.

3.2.4 “Click”-reaction of POCB and PEO

N_3-POCB (1 g, 0.1 mg/mL) was combined with 10 mL dry toluene and PDTEMA (TCI) (145 µL, mmol) and degassed by freeze-pump-thaw (3x). Separately, **alkyne-PEO** (1 mol eq.), dissolved in 10 mL dry toluene was degassed by freeze-pump-thaw (3x). Note that gentle heating was required after each cycle to redissolve the alkyne-PEO. A 50 mL rb flask was charged with CuBr in a nitrogen atmosphere glovebox. Outside the box, under nitrogen, the **N_3-POCB**/PDTEMA solution was syringe-transferred to the flask containing the CuBr. Upon mixing the solution was light blue. The alkyne-PEO solution was added (Scheme 3-2). The solution became a slightly darker but still transparent blue. After stirring at RT overnight, the mixture was extracted with water (20 mL, 2x) to remove salts. Toluene was removed under vacuum to give a pale-yellow viscous liquid.

Purification: To remove PEO homopolymer, the crude mixture was dissolved in CH_2Cl_2 and treated with an equal volume of water in a separatory funnel. The aqueous layer was cloudy at this point while the CH_2Cl_2 layer was clear. Hexane was added. After mixing, the organic and aqueous layers inverted so that the organic layer was on top. The block copolymer could then be isolated from the organic layer by evaporation of the solvent. This purification was repeated 2 or 3 times as needed to remove PEO and POCB homopolymers. The PEO was present in the aqueous layer and the POCB was present as a precipitate in the organic layer.

To remove homopolymer, an extraction of water and an organic layer was performed. When the organic layer is pure DCM, all polymer extracts into the organic layer and is thus unsuitable for purification. When the organic layer is half-DCM, half-hexane, solubility is decreased sufficiently for PEO that the PEO homopolymer separates into the aqueous layer, leaving both the POCB homopolymer and block copolymer in the organic phase. When the organic

layer is 100% hexanes, solubility is further decreased such that POCB homopolymer remains in the aqueous layer and block copolymer separates into the aqueous layer. The block copolymer can be removed directly from the aqueous layer via evaporation or can be extracted from the water via DCM for easier evaporation.

3.2.5 Preparation of samples and data collection

For all measurements unless otherwise stated, polymer-water solutions were prepared directly prior to analysis and were prepared using virgin polymer.

Matrix-Assisted Laser Desorption/Ionization

Samples analyzed via MALDI were prepared using a matrix of dihydroxybenzoic acid (Acros) (DHBA) and NaI (EM Science) salt in a solution of THF. DHBA:NaI:Polymer were mixed at an approximate 40:2:10 ratio.

Differential Scanning Calorimetry

Samples analyzed via DSC were prepared by one of two methods.

Dispersed. Samples were prepared by weighing out a mass of polymer in a vial, then adding DI water in increments of 1 µL for every 1 mg of polymer until the polymer was fully dissolved/dispersed upon mixing.

Concentrated. Samples were prepared by weighing out a mass of polymer on the DSC pan, then placing DI water atop the sample in a ratio of 1 µL for every 1 mg of polymer. Measurements were taken in an open pan.

Dynamic Light Scattering

DLS was performed on a Malvern ZS90 Zetasizer and temperatures were equilibrated for 10 minutes prior to measurement. Samples were not filtered prior to measurement due to the large particle/aggregate size.

Direct dissolution. Samples for DLS analysis were prepared at 10 mg/mL in DI H_2O and vortexed until dispersed.

Evaporation method. Samples for DLS analysis were prepared by dissolution in 100 µL of DCM, addition of 1000 µL DI H_2O, and were stirred overnight until the DCM had evaporated. Samples were prepared such that the concentration would be 10 mg/mL if no H_2O had evaporated.

Atomic Force Microscopy

AFM was performed on an Asylum MFP3D with a HQ:NSC15/Al BS probe (325 kHz, 40 N/m).

Direct dissolution. Samples for AFM analysis were prepared at 1 mg/mL in DI H_2O and vortexed until dispersed.

Evaporation method. Samples for ÀFM analysis were prepared by dissolution in 100 µL of DCM, addition of 1000 µL DI H_2O, and were stirred overnight until the DCM had evaporated. Samples were prepared such that the concentration would be 1 mg/mL if no H_2O had evaporated.

Measurement. 4 µL of the solution were placed on a mica substrate and the liquid was allowed to evaporate. The stock solution of 1 mL of 1 mg/mL block copolymer was then heated in an oven to 50°C for 1 h, then 4 µL of the solution was deposited on mica in the oven and allowed to evaporate. The stock solution was brought out of the oven and allowed to cool for 1 h before 4 µL of the solution was deposited on mica at room temperature and allowed to evaporate.

Nuclear Magnetic Resonance in D_2O

NMR data were acquired on a Bruker Ultrashield 400 MHz NMR.

Direct Dissolution. Samples for NMR analysis were prepared at 10 mg/mL in D_2O and vortexed until dispersed. All samples contained undissolved materials.

Evaporation Method. Samples for NMR analysis were prepared by dissolution in 100 µL of DCM, addition of 1000 µL D_2O, and were stirred overnight until the DCM had evaporated. Samples were prepared such that the concentration would be 10 mg/mL if no D_2O had evaporated. All samples contained undissolved materials.

Measurement. The samples were equilibrated for approximately 10 minutes between each temperature change. The temperature was changed at either 5°C or 10°C increments.

Infrared Spectroscopy

FTIR was performed on a Spectrum 2 Perkin-Elmer spectrometer equipped with a universal ATR. Cooling was achieved by placing ice near or above the sample. Heating was achieved through use of a heat gun.

X-ray Diffraction

Wide-angle X-ray diffraction experiments were performed by the University Department of Chemistry x-ray expert, Dr. Steven Geib using the dispersed samples prepared for DSC (several days thereafter). Measurements were taken on a Bruker X8 Prospector Ultra Diffractometer with Apex II CCD area detector using Cu Kα radiation of 1.54178 Å wavelength and operating at 50 kV and 0.65 mA. 4 frames were collected for each sample for 210 s each.

Optical Microscopy

Optical microscopy was performed with a BH2 Olympus microscope. The microscope was calibrated with a calibration slide at 50x zoom. A sample of polymer was smeared on a glass slide. The microscope was then focused on the polymer on the glass slide. A recording was started via the microscope software and a drop of water was placed atop the polymer. The focus was adjusted due to the change in height of the polymer water mixture until crystalline growth was observed.

3.3 Results

3.3.1 POCB synthesis

Polyoxacyclobutane was initially prepared through the polymerization of oxetane from sodium and potassium isopropoxide, sodium and potassium ethoxide, and sodium benzyl alkoxide through anionic ring opening polymerization activated by triisobutyl aluminum (Scheme 3-1). Upon successful polymerization of the homopolymer, POCB was prepared from monomethyl PEO-alkoxide, also through anionic ring opening polymerization activated by triisobutyl aluminum. While successful in the production of POCB-PEO block copolymers, this method afforded poor molecular weight control due to the low solubility of alkoxides in organic solvent[105] and was discarded in favor of the more controllable click reaction.

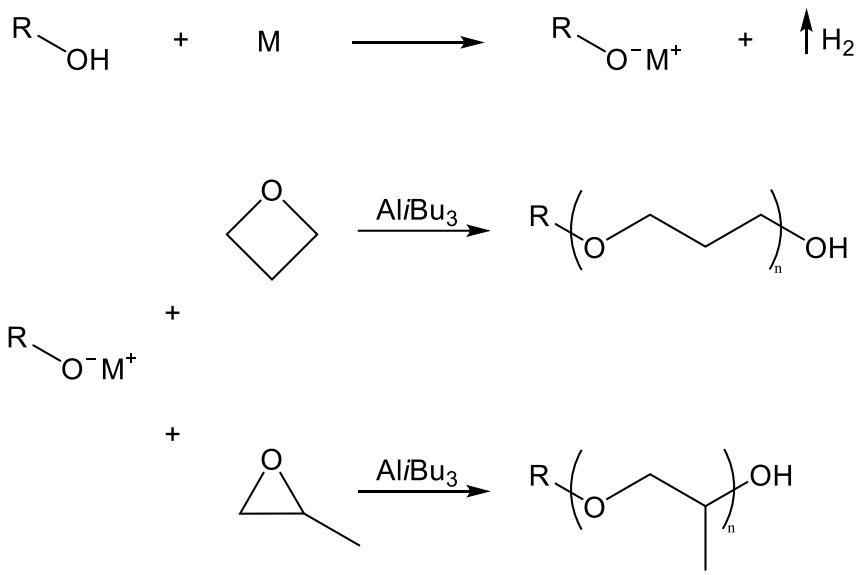

Scheme 3-1: alkoxylation of an alcohol and anionic polymerization of oxetane and methyl oxirane via from an alkoxyide via triisobutyl aluminum activation. R = monomethyl polyethylene oxide, ethanol, isopropanol, and benzyl alcohol. M = Na, K.

To prepare the samples whose characterization is described herein, the prepared blocks were coupled using an alkyne-azide click reaction. The azide functionalized POCB (**N_3-POCB**) was prepared by anionic polymerization initiated from tetrabutyl ammonium azide (Scheme 3-2).[96-97, 133] The presence of the azide group was confirmed by MALDI MS (Figure **3.4**). Detailed MALDI analysis of azido-functionalized polymers requires particular care due to the stability of N_2, which can be chemically eliminated under the MALDI ionization conditions.[134] Monomethyl-terminated PEO (M_n ca. 4000) was functionalized by coupling with propargyl bromide to give the alkyne-functionalized PEO (**alkyne-PEO**).[132, 135-137] Estimated substitution was 100% based on ^{1}H NMR spectroscopy (Fig. **3.3**) and the absence of the non-functionalized PEO in the MALDI

spectrum. (Fig. **A.25**).

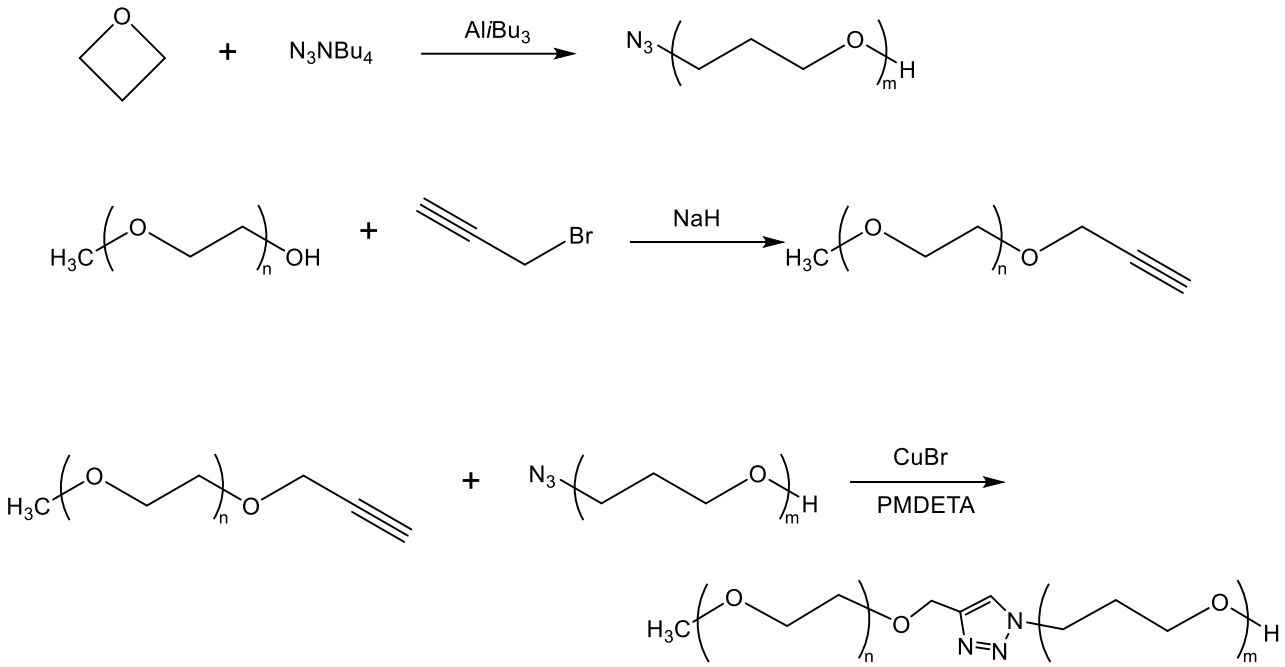

Scheme 3-2: Anionic polymerization of oxetane with tetrabutyl ammonium azide via triisobutyl aluminum activation, alkynylation of monomethyl polyethylene glycol, and copper-catalyzed click reaction of alkyne-functionallized PEG with azide-functionalized POCB to form triazole-linked PEG-POCB block copolymer.

Block copolymers of POCB and PEO were prepared by click coupling of **N_3-POCB** and **alkyne-PEO** (Scheme 3-2).[138]

3.3.2 Characterization

The ^{1}H NMR spectrum of the block copolymer shows the expected peaks for both blocks (Fig.3.3). However, this information cannot be used to confirm successful coupling of the block copolymer as the same spectrum is expected for a blend. The polymer was extracted from the homopolymers using water for the aqueous layer and a mixture of varying ratios CH_2Cl_2 for the organic layer.

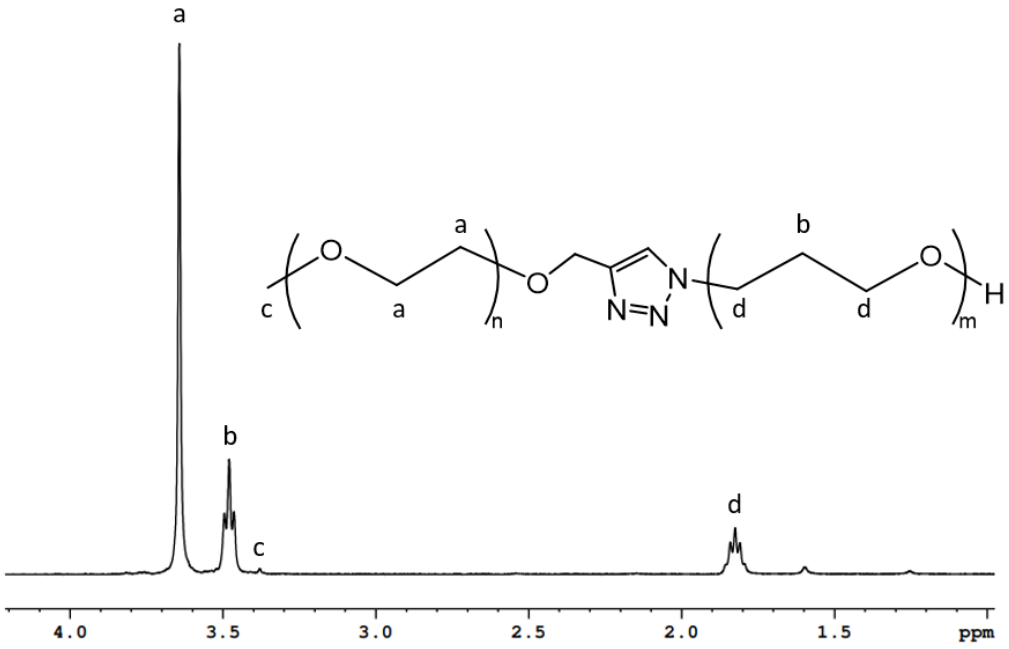

Figure 3.3: ^{1}H NMR spectrum of **Block1000** in $CDCl_3$.

MALDI analysis of the block copolymers also confirms the presence of the block copolymer (Fig. 3.4 and Fig **A.41**). Higher molecular weight species fly poorly in MALDI, thus the presence of any block copolymer peak was taken as confirmation of successful coupling. The full spectra are available in the appendix (Fig **A.29** and Fig **A.40**).

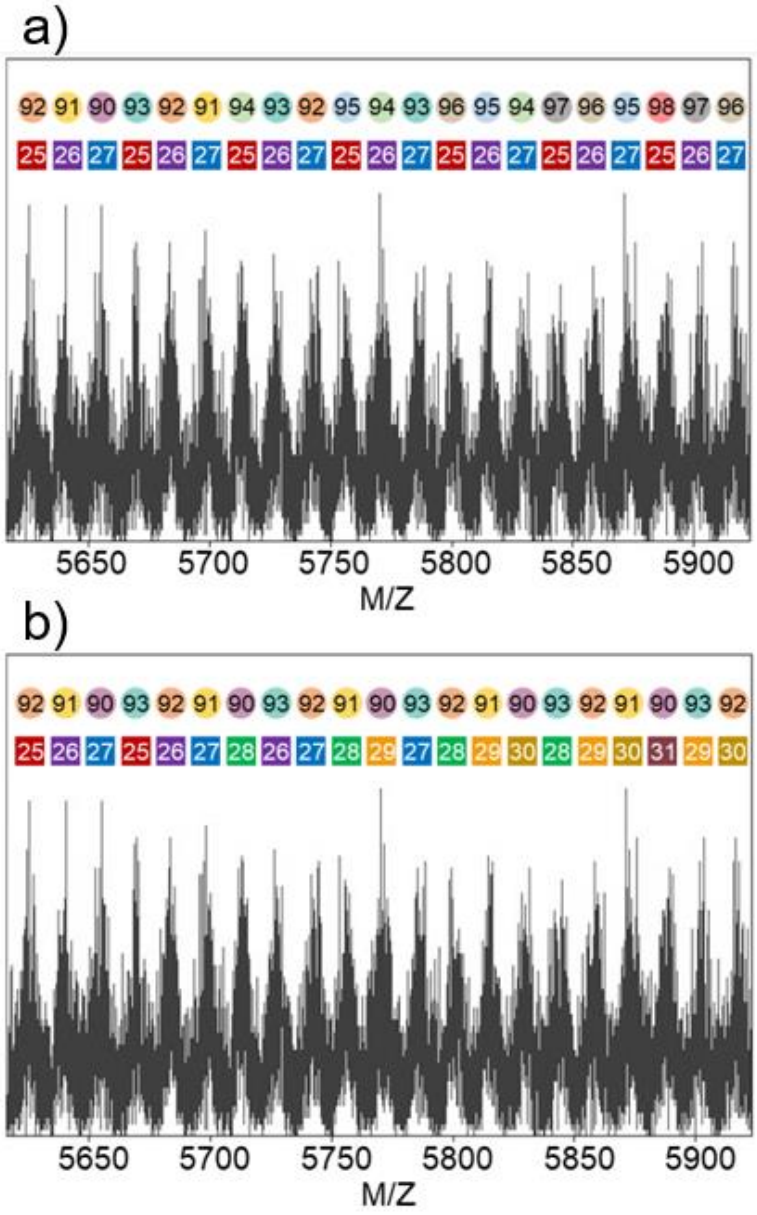

Figure 3.4: Expansion of the 5640-6000 M/z range of the MALDI spectrum of POCB-*b*-PEO (**Block1000**). Circles indicate the number of PEO units while squares indicate POCB degree of polymerization. Due to peak overlap, the same section is labled twice: (a) Labels emphasize the progression for block copolymers with POCB degrees of polymerization 25-27. (b) Labels emphase the progression of block copolymers with PEO degrees of polymerization 90-93. The full spectrum can be found in the appendix (Fig. **A.29**).

Size exclusion chromatography (SEC) also confirms a molecular weight increase (Fig. 3.5 and Fig **A.38**). The increase in molecular weight post-reaction indicates successful coupling of the

two components. The absolute molecular weight of the block copolymers was assumed to be the additive molecular weights of the two components (Table 3-1).

Table 3-1: Names and molecular weights of polymers synthesized and charactarized.

Polymer	Sample	POCB	PEO	POCB	PEO	Block	PDI	yield (%)
PEO4000a	PEO-alkyne	n/a	3839	n/a	3165	n/a	1.02	~100[b]
POCB1000a	N_3-POCB	1185	n/a	2327	n/a	n/a	1.17	54
Block1000	Block1000	1185[c]	3839[c]	2327	3165	4471	1.04	13
POCB1000b	N_3-POCB	976	n/a	1959	n/a	n/a	1.37	88
POCB2000	N_3-POCB	2324	n/a	4853	n/a	n/a	1.33	90
PEO4000b	PEO-alkyne	n/a	4095	n/a	4355	n/a	1.03	~100[b]
Block2000	Block2000	2324[c]	4095[c]	n/a	4355	8152	1.15	15.3
POCB650/Cerenol	POCB	678	n/a	942	n/a	n/a	1.58	n/a

a) SEC molecular weights are calculated vs polystyrene standards in THF; b) yield of the PEO-alkyne was determined by MALDI analysis; c) molecular weights of the blocks were derived from the homopolymer molecular weights.

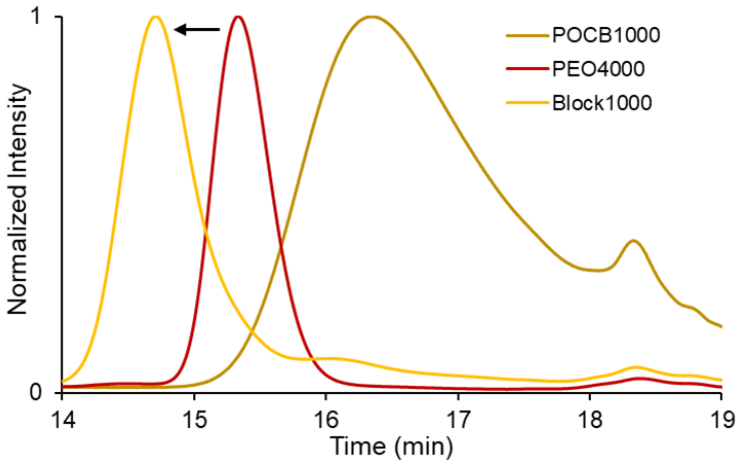

Figure 3.5: Molecular weights and dispersities of the **Block1000** and its homopolymer components, **POCB1000** and **PEO4000** as calculated from SEC in THF vs polystyrene standards.

3.3.3 Thermal Behavior

The thermal behavior of the homopolymers and the block copolymers was investigated using differential scanning calorimetry (DSC). The analysis was performed using non-hermetically sealed pans, and therefore all samples show an upward slope during the first heating cycle (Fig.3.6) that is consistent with the vaporization of water. These same samples were cooled and then heated a 2nd time. Both the cooling and 2nd heating cycles were conducted under water-free conditions due to the evaporation of water during the 1st scan.

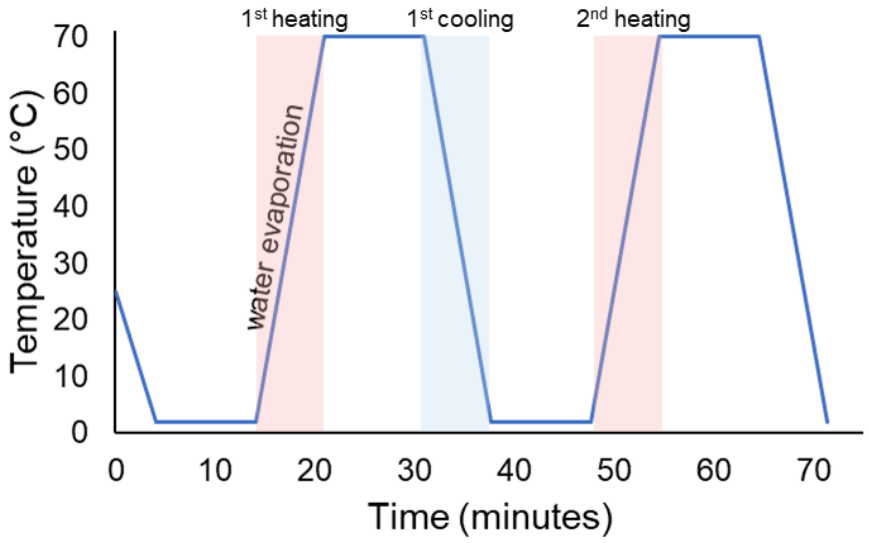

Figure 3.6: Heating cycle of thermal analysis by DCS. The heating and cooling were both performed at a rate of 10°C per minute. Water evaporation was observed during the first heating curve.

During the first heating (water-containing), all POCB homopolymers- **POCB650/Cerenol**, which was not functionalized and bore two hydroxyl end-groups, and **POCB1000** and **POCB2000** which each bore an N_3 endgroup- exhibited the expected melting transition for the water/POCB cocrystal at 37°C (Fig.3.7). The highest molecular weight POCB, **POCB2000** also had a melting peak at 14°C. The melting transition for the water/POCB cocrystal was also observed for the block

copolymers, although at a reduced temperature of 29°C, which is consistent with the presence of the PEO "contaminant." The homopolymer cocrystallization melting transition at 37°C was not present for the block copolymers.

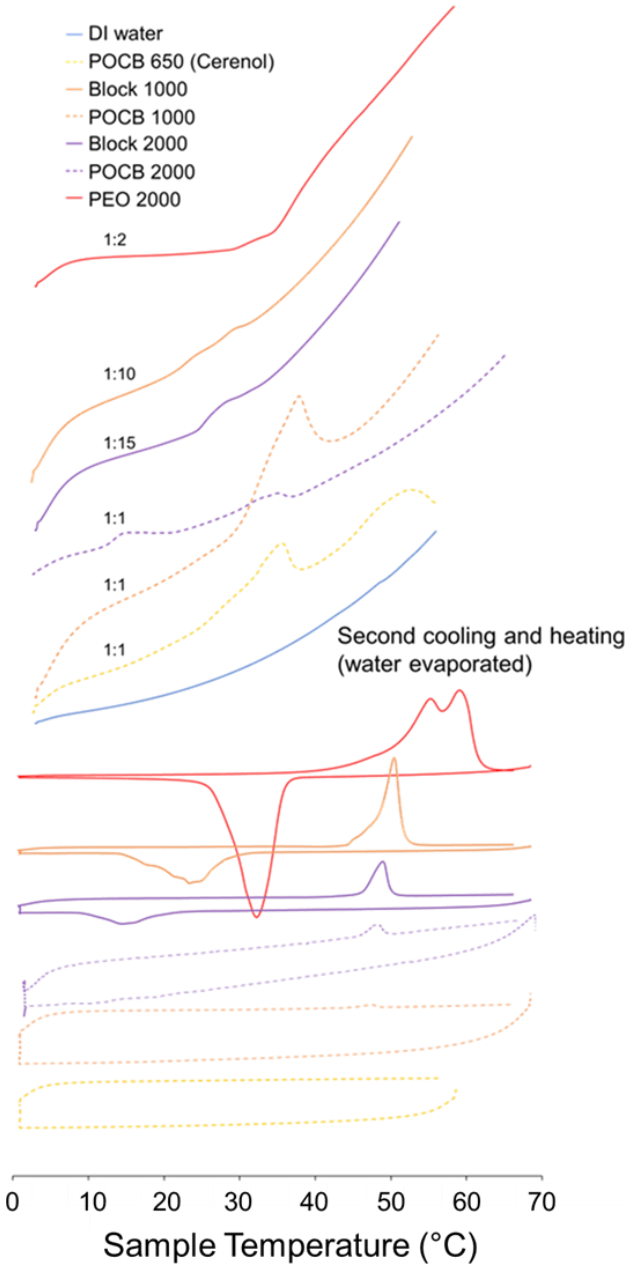

Figure 3.7: Thermal analysis of **POCB1000**, **POCB2000**, **POCB650**, **Block2000**, **Block1000**, **Block2000**, and **PEO4000** measured via DSC. The ratio of polymer to water is given above the first heating trace. Upon holding at a higher temperature the water completely evaporates and gives rise to the second cooling and heating curves (Fig **3.6**).

Upon cooling (no water present), pure PEO had crystallization peaks at 32°C and the block copolymers had a crystallization peak at 15°C for the **Block2000** and 23°C for the **Block1000** (Fig.3.7). These three peaks are all due to the crystallization of PEO. Melting of the PEO crystals is also observed for all three samples during the 2nd heating. The pure PEO had melting peaks at 55°C and 59°C and the block copolymers had melting peaks at 48°C. For the dry block copolymer melting the POCB homopolymer melting and PEO homopolymer melting peaks overlap. Neither the crystallization nor the melting peaks were observed for the pure POCB sample **POCB 650/Cerenol**, which was liquid and thus not expected to exhibit homopolymer crystallization or melting, but the solid, higher molecular weight **POCB1000** and **POCB2000** did show homopolymer crystallization. When the DSC program was adjusted to only cool to 20°C with no isothermal holding (Fig. 3.8), the melting peaks of POCB-water cocrystals were not present in the block copolymers, confirming the correspondence of the melting transition at 29°C with that of the cocrystal.

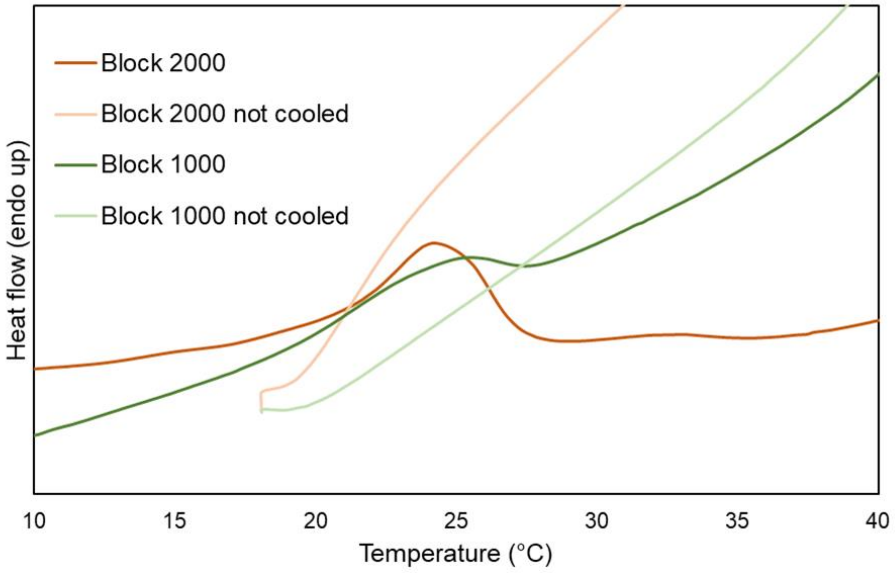

Figure 3.8: Thermal analysis of **Block2000** and **Block1000** measured via DSC The block copolymer samples were cooled to and held at 2°C for 10 minutes before heating, then were remade, cooled to 20°C, and heated again.

3.3.4 Particle size

To examine the self-assembly of the block copolymers in solution, DLS samples were prepared by direct addition of deionized water to the dry polymer (10 mg/mL). The unfiltered samples were examined at a variety of temperatures above and below the known melting point of the POCB hydrate. At low temperatures the size of the particles varied from 100 nm to 1000 nm with averages of ranging from 200-300 nm (Fig 3.9). **Block2000** exhibited more aggregation prior to heating (avg. particle sizes > 500 nm). For both block copolymers the dispersity narrows significantly with heating. For the **Block2000**, which has a longer POCB segment, there was also a significant contraction in the average size. Both block copolymers reverted back to the larger

particles with high dispersity upon recooling, which is consistent with crystals or swollen aggregates at low temperature and dehydrated aggregates at high temperatures.

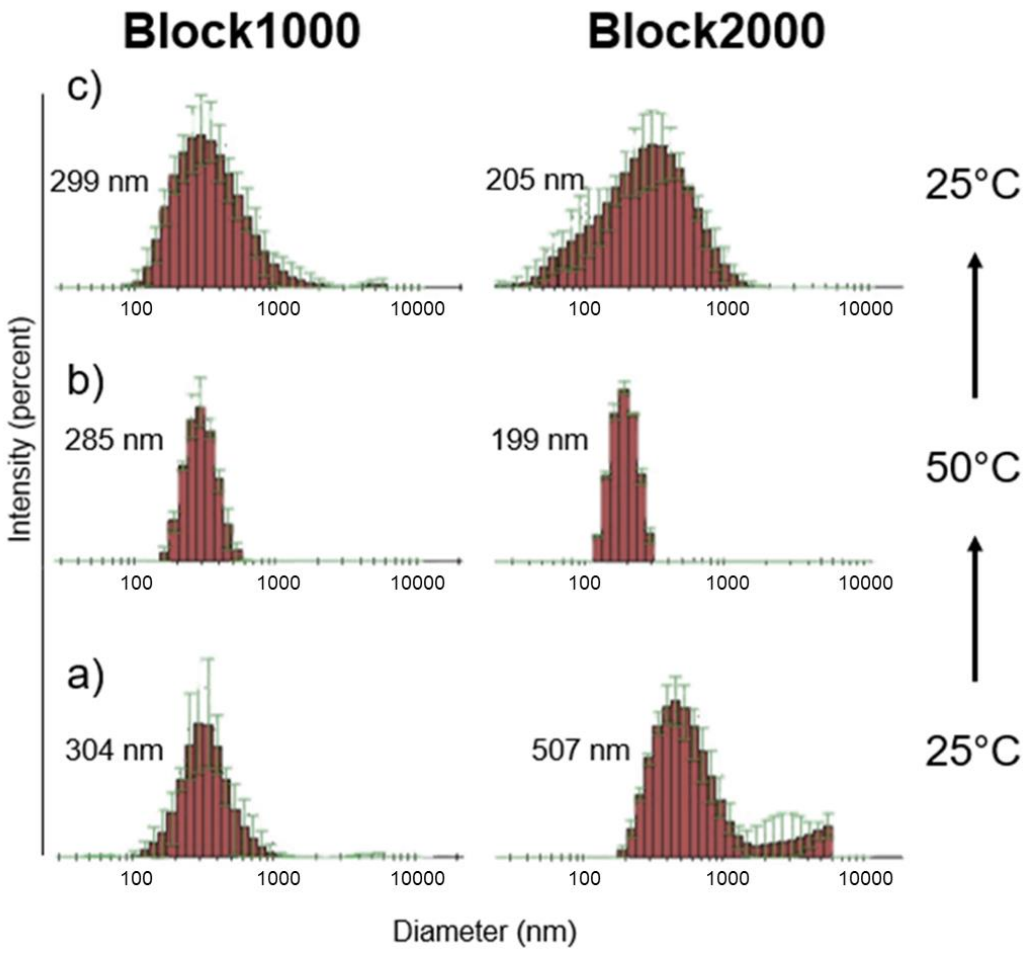

Figure 3.9: Particle size of block copolymers in water as a function of temperature. Determined by dynamic light scattering.

Particles of the two block copolymers were also prepared via the evaporation method by addition of a methylene chloride solution to water, followed by evaporation to give a 10 mg/mL suspension. There was a noticeable difference in both dispersity and size of the particles between those prepared via the evaporation method and those prepared via direct dissolution (Fig 3.10). The **Block1000** prepared by the evaporation method also exhibited a decrease in size upon heating

and an increase in size upon recooling, but at all temperatures the particles were much larger and less disperse than those prepared via the direct dissolution method. This is also true for the **Block2000** (Fig **A.45**).

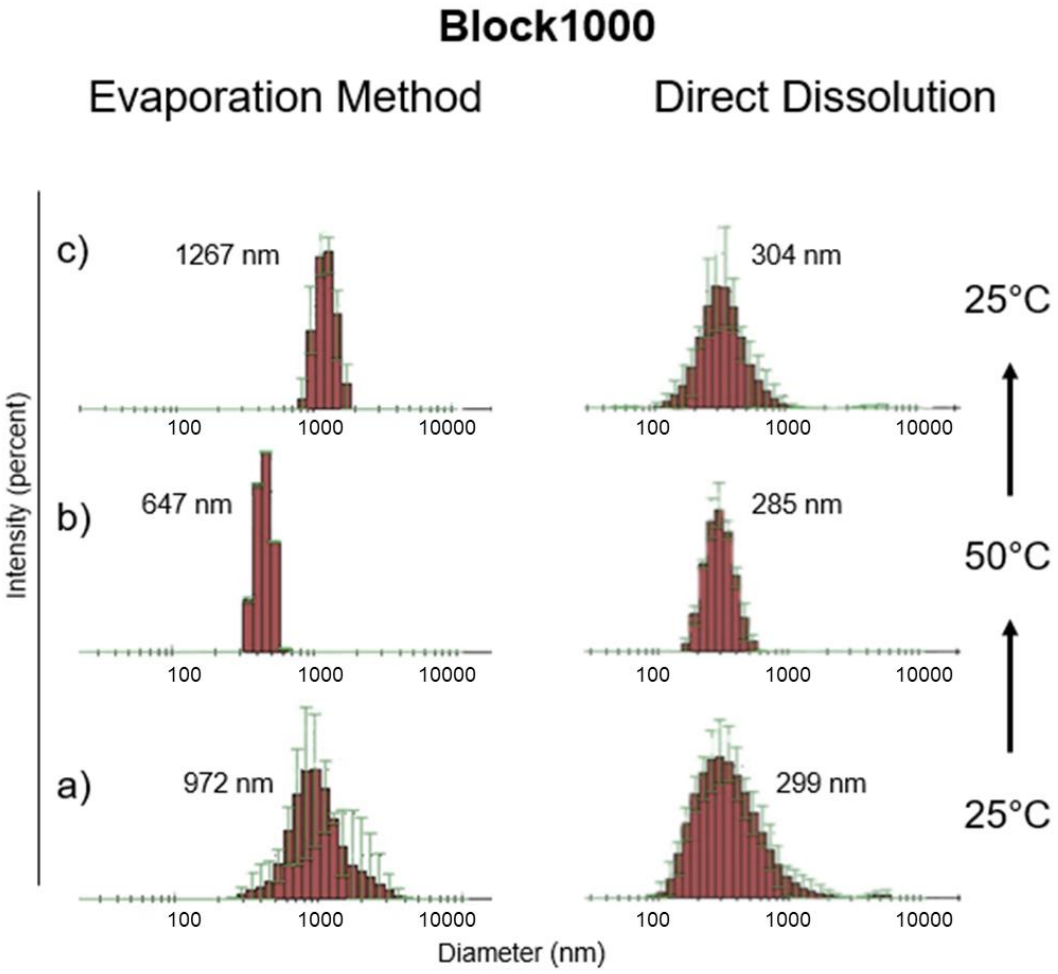

Figure 3.10: Particle size of **Block1000** in water as a function of temperature and preparation method. Determined by dynamic light scattering.

To image the particles formed in the presence of water, a suspension prepared by the evaporation method was deposited onto a mica after thermal treatment and allowed to dry. Discrete particles were only observed in the AFM for the **Block1000** (Fig 3.11). At room temperature, large spheres (~1 μm) decorated with linear crystalline structures are observed. At 50°C, the particles

become less well-defined and smaller and the linear crystalline structures disappear. Upon recooling, the particles do not return to the exact morphology observed before heating but rather appear as particles and aggregates with well-defined internal patterns, likely of the crystallization of the phase segregated POCB and PEO components.

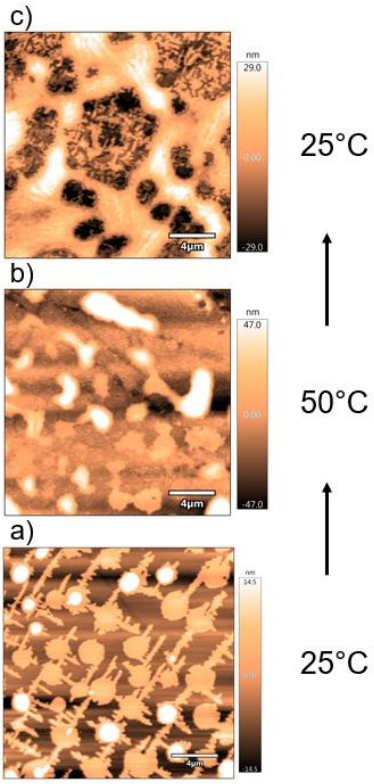

Figure 3.11: nanoscale imaging of the **Block1000** prepared through the evaporation method using atomic force microscopy.

3.3.5 Solution Phase NMR studies

Before discussing the NMR data collected in D_2O, it is important to review what is known about the phase behavior of POCB. Previous studies on low molecular weight POCB (M_n = 650) have demonstrated that at temperatures above the melting point of the hydrate mixtures of polymer

with less than 20% water give homogeneous solutions, which when cooled yield a mixture of the crystallized hydrate and a polymer-rich solution[6]. At lower polymer concentrations, phase separation into polymer-rich and water-rich phases is observed above T_m. Cooling eventually leads to the polymer hydrate in the presence of a water-rich phase. It is important to note that the polymer rich phase, especially for samples of higher molecular weights, includes water-swollen solids. The phase behavior of the POCB is relevant because solution phase NMR spectroscopy will necessarily provide information only on the freely tumbling liquid phase materials. Materials such as the POCB hydrate and the polymer-rich phase that is mostly solid will not be visible in the NMR spectra.

Interestingly, the aqueous ^{1}H NMR spectra of both the block copolymers and POCB homopolymer indicate the presence of more than one type of environment for the water-soluble components (non-soluble components are clearly present in these samples as well). In particular, both the α and β-protons of the POCB show two signals in most circumstances, with the α hydrogen triplet exhibiting the most significant shift, from 3.57 to 3.46 ppm (Figures **A.27** and **A.44**). Moreover, the ratio of these two peaks favors the upfield peak for samples with a longer POCB chain. Prior work on the related Pluronics system, a structural isomer of the block copolymers studied, suggests that this upfield shift is consistent with a decrease in the degree of association of POCB with water[117].

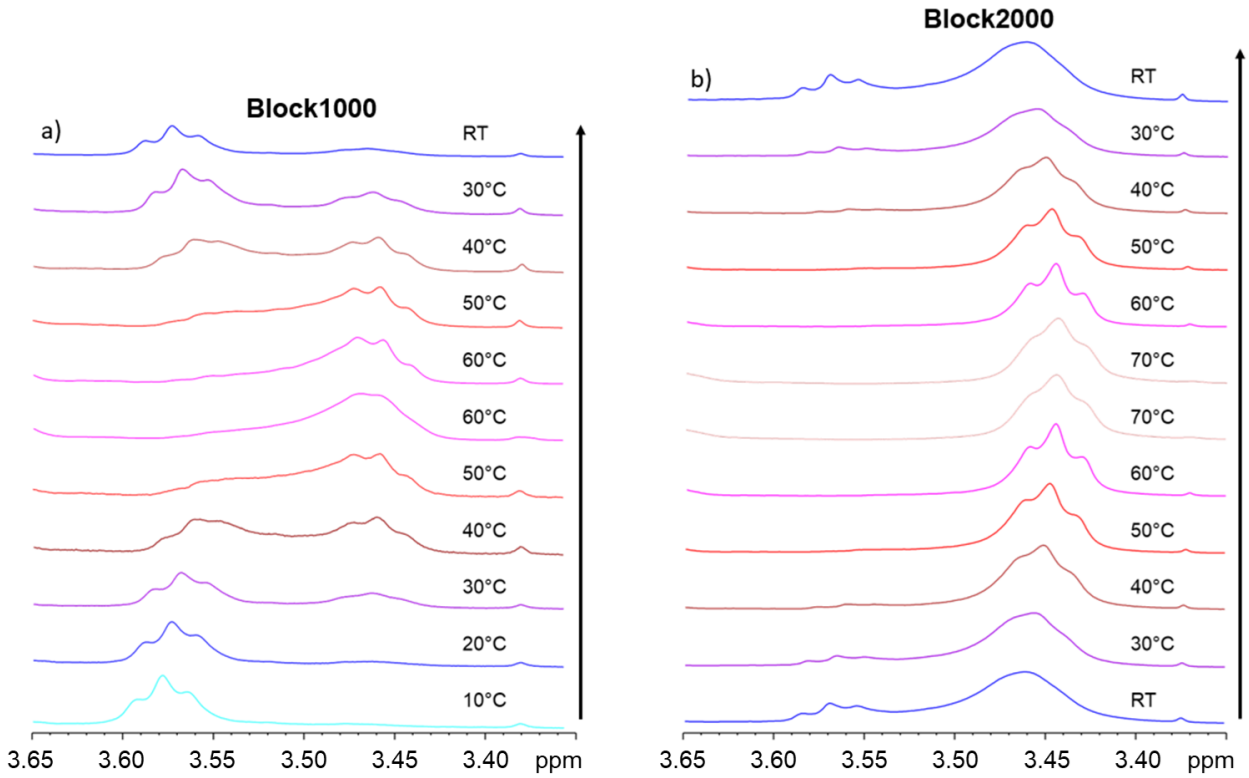

Figure 3.12: 3.35 to 3.65 ppm region of the POCB ^{1}H NMR spectrum (α proton peaks) upon heating and recooling of a) the **Block1000**; and b) the **Block2000**.

The ratio of these two peaks is also affected by heating and by the initial preparation method. Upon heating, there is a significant increase in the upfield peak in all samples. For the block copolymers this is clearly an equilibrium process wherein the original peak ratio is reestablished after cooling (Fig 3.12). The homopolymers, while they did exhibit the upfield shift upon heating, did not fully revert to their preheating ratios under these conditions (3.13). The interpretation of this behavior is challenging because of the low solubility of POCB in water; significant precipitate was always present (cloudy samples).

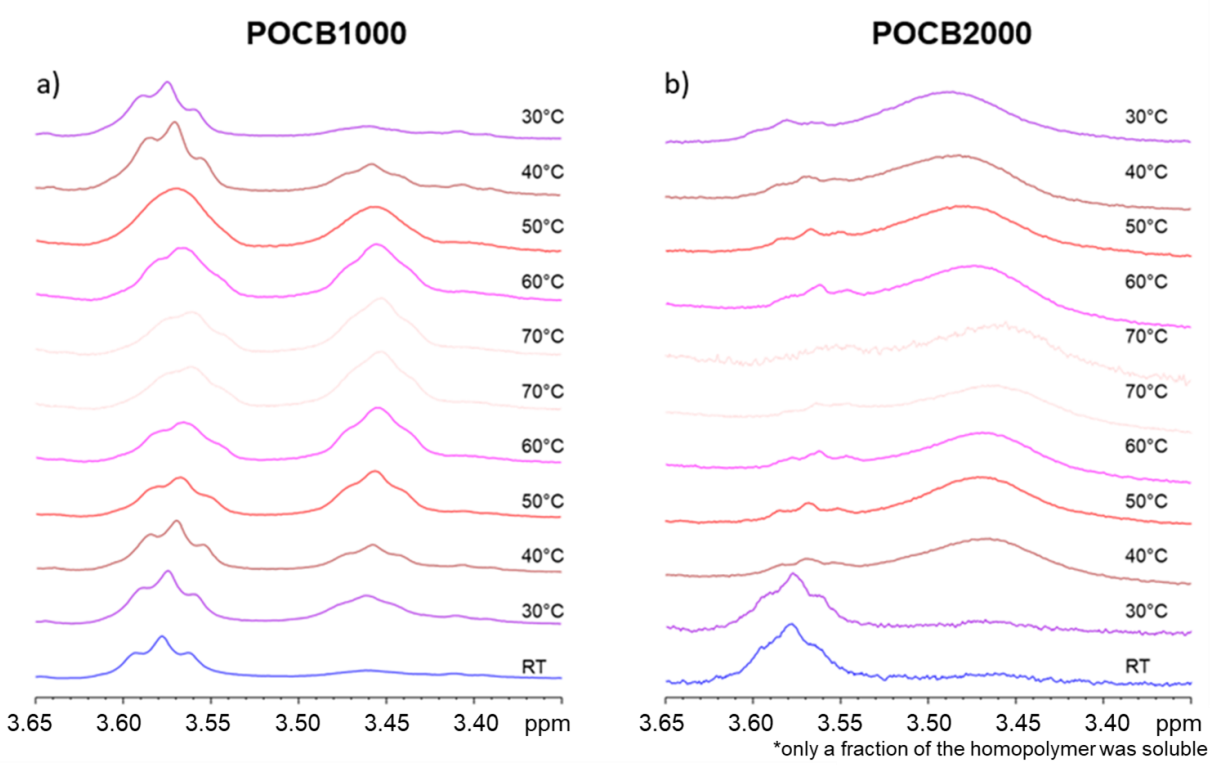

Figure 3.13: 3.35 to 3.65 ppm region of the POCB ^{1}H NMR spectrum (α proton peaks) upon heating and recooling of a) the **POCB1000**; and b) the **POCB2000**.

Initially, a non-equilibrium ratio of the two species was observed when the block copolymers were prepared by the evaporation method. More of the species associated with the downfield peak is originally present relative to the ratio observed in samples prepared by direct dissolution. Upon heating and cooling, however, the ratio reverts to that observed both before and after heating for the direct dissolution samples (Fig 3.14).

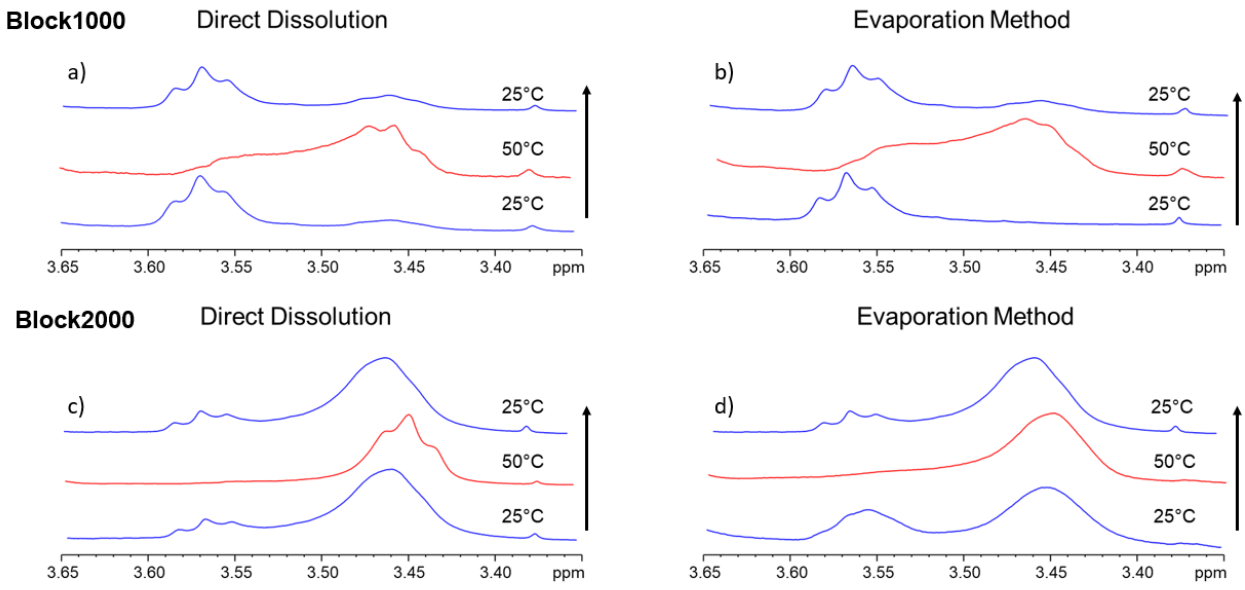

Figure 3.14: 3.35 to 3.65 ppm region of the POCB ^{1}H NMR spectrum (α proton peaks) upon heating and recooling of a) the **Block1000** prepared through direct dissolution; b) through the evaporation method; c) the **Block2000** prepared through direct dissolution; and d) prepared through the evaporation method.

3.3.6 FTIR analysis

In an effort to ascertain if POCB in the block copolymers were capable of forming hydrate cocrystals with water, IR data were acquired for both the block copolymers and their homopolymer components. It is known from the earliest studies on POCB, that the POCB polymer hydrate exhibits a unique IR signature in region associated with O-H stretching. Distinct bands are observed at 3481, 3376, 3332, and 3210 cm^{-1} (Fig. **3.15**), as reported by Makino et. al[139 5, 139]. In contrast with free water, which exhibits a broad absorption from 2750 to 3750 cm^{-1}, the cocrystal confines the water to specific environments that exhibit narrow absorption peaks (Fig 3.16). Although vibrational modes associated with POCB are also affected by the cocrystallization, these

bands are not as useful in this case as they are masked by the peaks associated with the PEO for samples of the block copolymer.

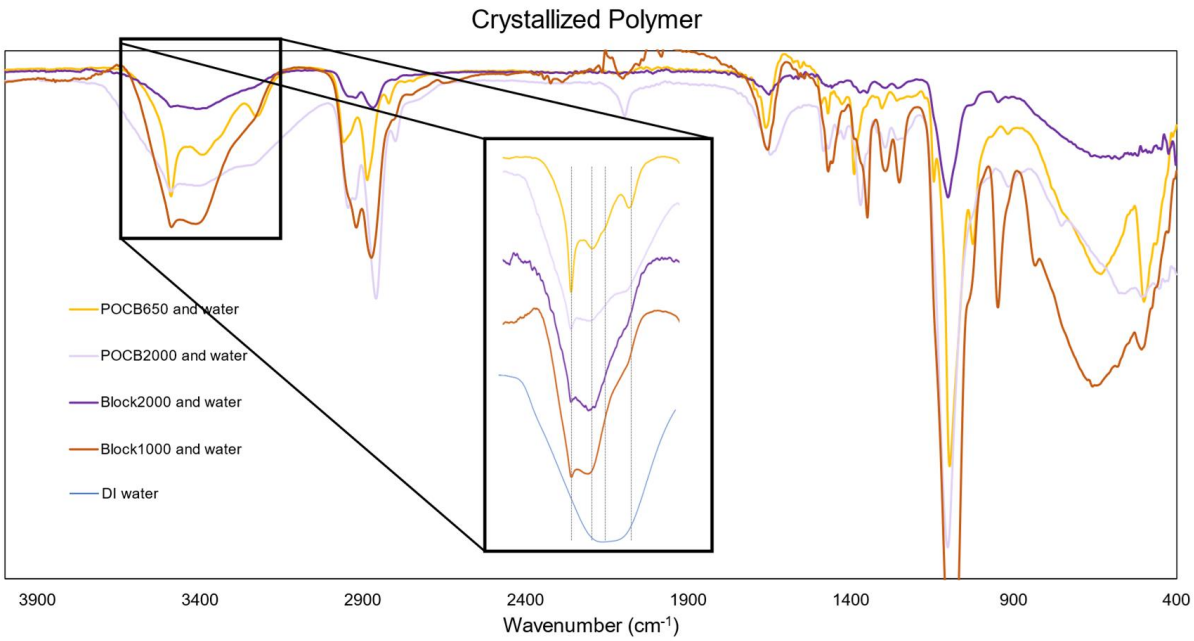

Figure 3.15: Infrared absorbance spectrum of POCB and POCB-PEO block copolymers in a hydrated, cocrystalline state in the presence of liquid water. DI water was partially subtracted from all spectra. The OH stretching region is enlarged and compared with DI water to emphasize the change in the OH bonding due to crystllization. Grey lines added to show the four OH stretching peaks

Analysis of the samples was performed by preparing a highly concentrated mixture of POCB or block copolymer with water and placing it directly on the ATIR sensor, cooling or heating as necessary. In all samples where POCB was present, the pattern of distinct water peaks were visible in the OH stretching region. Upon heating, those signals disappeared for both the homopolymers and the block copolymers, consistent with the loss of crystallinity. It is important to note that these samples also contain free water and that the spectra shown are the result of a subtraction of the free water spectrum from the original data.

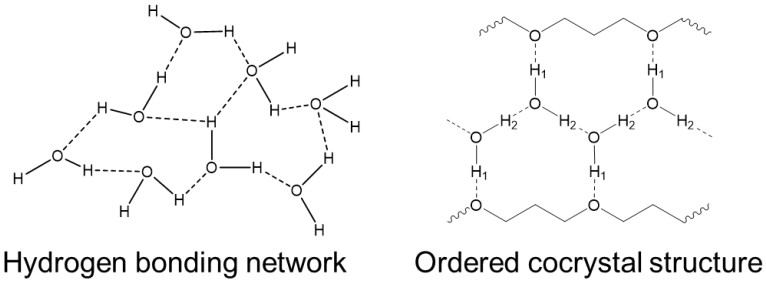

Figure 3.16: Hydrogen bonding of pure water vs water trapped in the POCB-water hydrate.

3.3.7 XRD analysis

The presence of the POCB hydrate cocrystal in both of the block copolymer samples was further confirmed by x-ray scattering. X-ray data were collected for each block-water hydrate and its homopolymer-water hydrate analogue at both 2°C and 50°C. For all samples at 2°C, the hydrate showed peaks at 14.4 degrees and 24.8 degrees (Fig 3.17a), consistent with hydrate crystallization[6]. AT 2°C, the **Block1000** also exhibited peaks consistent with that of PEO crystallization, which may be due to the low water content of the sample that allowed for XRD analysis and may not be representative of a dispersion in water. The **POCB2000** at 2°C also exhibited a peak at 21 degrees, consistent with that of solid polymer crystallization[6] (Fig 3.17b). Neither the hydrate peak nor the solid crystalline POCB were present for any of the samples at 50°C and only amorphous polymer peaks were present.

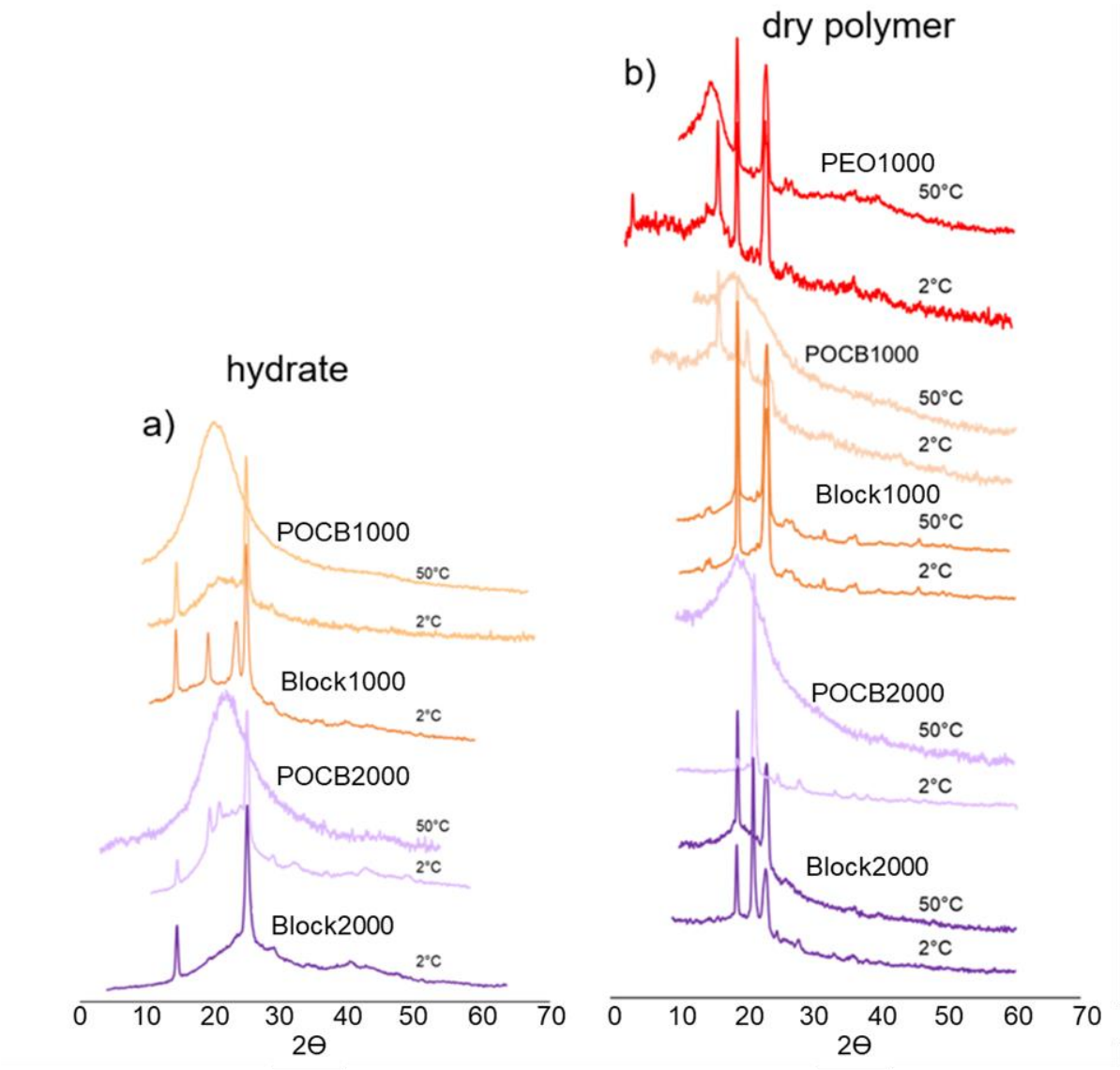

Figure 3.17: a) Wide-angle X-ray diffraction patterns of POCB-hydrate measured at 2°C and 50°C and POCB-PEO block copolymer hydrate measured at 2°C and b) wide-angle X-ray diffraction patterns of pure POCB, pure POCB-PEO block copolymer, and pure PEO measured at 2°C and 50°C (Cu Kα radiation of 0.154 nm wavelength).

3.3.8 Optical microscopy

Crystallization was also observed by optical microscopy for the block copolymers (Fig. 3.18). The **Block2000** sample exhibited slow-growing spherulites approximately 5 minutes after

additions of water to the solid. The **Block1000** sample formed a network of cylindrical structures approximately 15 minutes after the addition of water. The spherulite morphology observed for the **Block2000** sample is surprisingly similar to that observed in our earlier studies on homopolymer POCB samples[140]. The cylindrical morphology is consistent with crystallization driven self-assembly of polymers with a high amorphous:crystallizable block ratio[141].

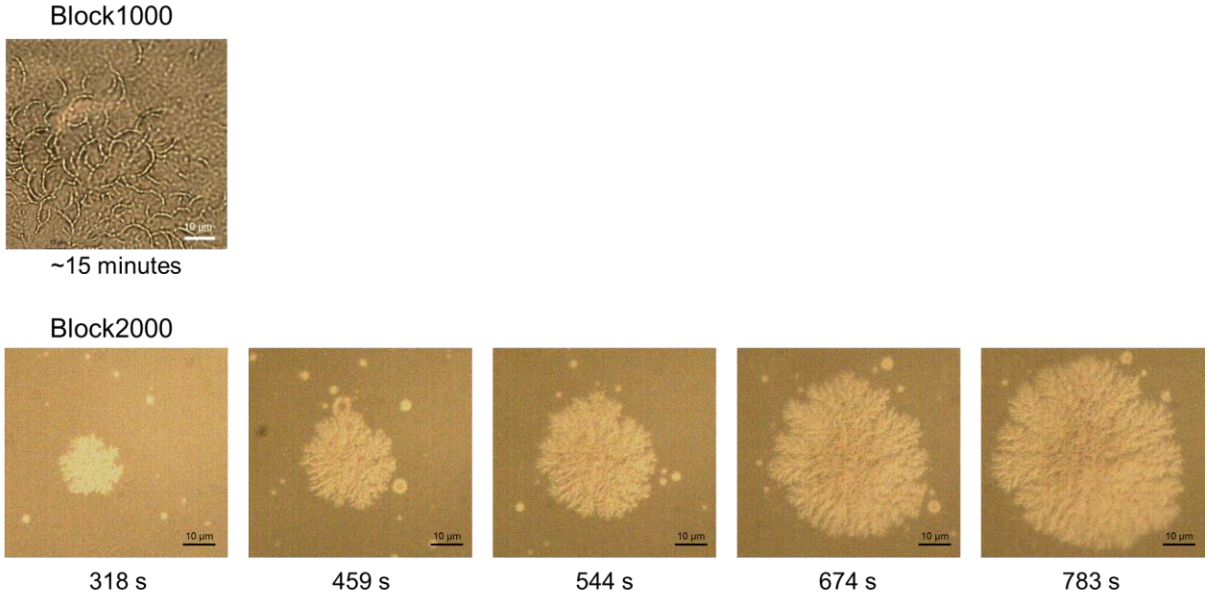

Figure 3.18: Images at 50x of the **Block1000,** forming cylindrical crystals, and **Block2000,** forming traditional spherulites

3.4 Discussion and Conclusions

The POCB block copolymer behavior can be grouped into two distinct categories: the cocrystallization behavior with water and the phase behavior upon heating. Looking at the

cocrystallization behavior, one can reasonably conclude based on the XRD data, the FTIR data, and the DSC data that the POCB block of the block copolymer does cocrystallize with water. Further, optical microscopy suggests that the block copolymer has access to 1D cylindrical micellular morphology at high PEO:POCB ratios and typical spherulitic growth at moderate PEO:POCB ratios.

The next portion discusses the phase behavior upon heating, which more challenging to interpret. Ma et. al.[117] showed the micellization of the related Pluronics system can be tracked *via* NMR. The PPO peaks they observed undergo a similar upfield shift as the POCB peaks, which they attribute to the micellization, though more broadly to the disassociation of the PPO with the water and preferential association with itself during the course of micellization. A reasonable interpretation of the POCB block copolymer system would be that it is also undergoing disassociation from water, and that may be indicative of micellization.

Ultimately however, both the **Block1000** and the **Block2000** showed evidence of heavy aggregation that may have decreased with temperature *via* DLC analysis. The **Block1000** indicated interesting particle formation according to AFM analysis from particles formed *via* the evaporation method, though that likely has little bearing on the question of phase behavior in water as the samples were evaporated to dryness. No particles present via AFM imagining were similar to what Gervais et. al. observed, despite identical preparation methods. Two of the three polymers they had synthesized were not accompanied by AFM images, perhaps indicative of there not being any distinct particles, similar to what we saw with our block copolymers. The particles they did observe on the 3000:3000 g/mol PEO:POCB can be rationally assumed to not contain water due to the preparation method. Further, with the trend that the smaller the PEO:POCB ratio, the more spherulitic the growth, and the larger the PEO:POCB ratio, the more micellular the growth, one

would expect the cocrystal structures if measured by Gervais et. al. to be typical spherulites. Via XRD analysis we know dry **Block1000** exhibits primarily PEO crystallization and that is perhaps what they had observed with their 3000:3000 PEO-POCB block copolymer, though that does contradict the particle size decrease they reported of the particles in water as measured by DLS.

The DLS data we collected suggests the particles form large aggregates, larger than that of a micelle, that shrink to some degree and decrease in dispersity upon heating. The size of these aggregates is heavily dependent on preparation method. It would not be unreasonable to suggest that these aggregates are composed of POCB-water cocrystals at low temperature and form aggregates of micelles/phase separated species at high temperatures.

Tentatively we can begin to paint a picture of what we suspect is occurring with the block copolymer in water (Fig3.19. 3.19). With cooling below 29°C and time, polymer crystallization occurs; either in the classic spherulitic structure if the POCB content is sufficiently high, or as cylindrical micelles if the PEO content is sufficiently high to prevent lamellar stacking present in spherulitic growth. With heating above 29°C, the cocrystal melts and the core excludes water, potentially forming spherical that remain aggregated with neighboring former-crystals.

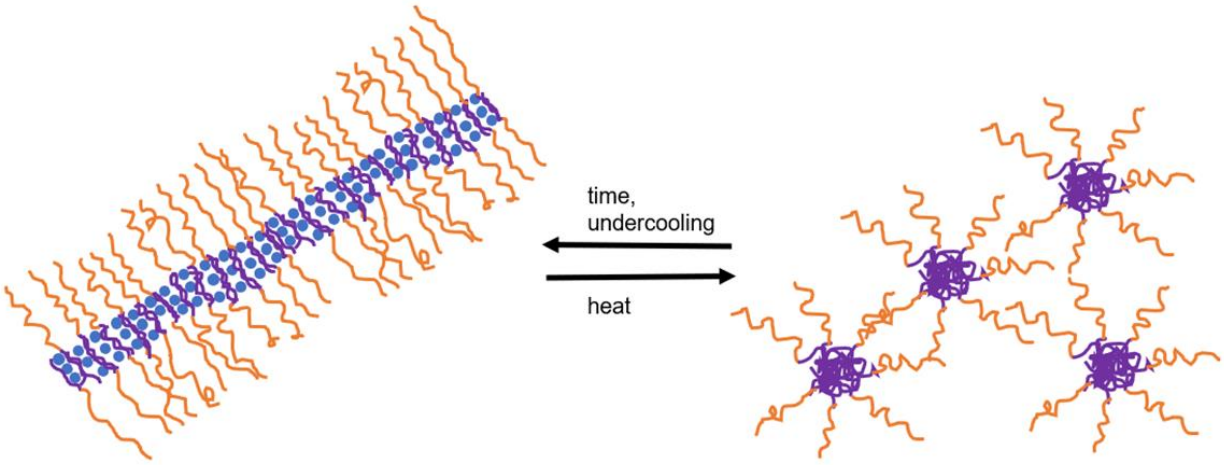

Figure 3.19: Tentative phase behavior of PEO-POCB block copolymers in water

4 Electroadhesion in ionomers

4.1 Overview

Although electrostatic attractions were first described by Coulomb in 1784, we have not yet fully exploited the phenomenon for electroadhesion applications. It is well-known that the stored opposite charges in capacitor plates experience electrostatic attractive forces toward each other, but this knowledge has been primarily utilized to ensure the physical separation of the charged plates that is required for capacitor functionality. Electrostatic chucks, in contrast, directly utilize the electrostatic forces in a capacitor-like system to hold a flat substrate, such as a silicon wafer, in place for processing. The field of electroadhesion, however, still has applications that have yet to be actualized and details that have yet to be described. My project focuses on the development of novel electroadhesive ionomeric materials for the eventual goal of producing layered stimuli-responsive composites that modulate their stiffness from flexible-to-rigid through a low-voltage input. Electrically-stimulated variable-moduli materials would allow the development of a broad range applications from electrically stiffening fabrics to robotics to prosthetics. Various obstacles inherent in ionomer electroadhesion, such as humidity dependence, plastic surface contacts, and electrochemical changes, have impeded the development of these materials. We are working to understand and create solutions to these obstacles.

4.1.1 Previous work in the group

This project evolved out of a desire to produce a tunable stimuli-responsive material that can alter its mechanical properties through the input of electricity. Many stimuli responsive materials exist that respond to heat, pH, and added chemicals to change properties such as their phase, solubility, color, and drug encapsulation.[142-144] There are, however, few examples of materials that undergo changes in their mechanical properties in response to electricity. While shaping and tuning the mechanical properties of a polymer through stimuli such as heat or chemical mixing are far from unknown processes, the development of a system that changes its mechanical properties in response to a low voltage input would allow for the development of previously unexplored material applications. For example, a polymer that requires an extremely high melt temperature would be unsuitable for molding to the skin, while a low-voltage electricity-responsive polymer would not perturb the bodily pain response. Chemical additives are also not ideal as they tend to induce irreversible changes and are limited to materials safe for general use. Electrically-stimulated materials would, in contrast, be reversible, easily utilized, and accessible for the general population.

The Meyer group was the first to design a material that could switch from a flexible solid to a rigid one through the input of electricity while maintaining a defined 3D structure and could do so reversibly[145-147]. The responsive material consisted of polymer bearing coordinating substituents doped with a metal that, under bulk electrolysis, could undergo changes in oxidation state. The metal ions exhibited oxidation-state dependent coordination and the hydrogel-based materials responded to these changes in crosslink density by changes in mechanical properties. Although this approach was effective, as a reversible switch between high and low moduli was observed, the diffusion-controlled bulk-electrolysis in the hydrogels was extremely slow.

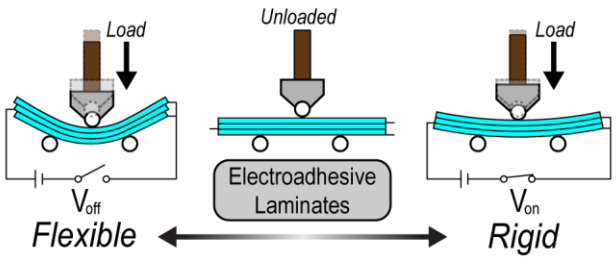

Figure 4.1: : Previous work with PEAA showed that switching between unbonded and bonded would produce stacks with different moments of inertia that resulted in a change in flexibility

In order to create a more rapid stimuli response to change a material's mechanical properties, Jeff Auletta from the Meyer group worked to develop a 2nd generation system that could control the mechanical properties of a composite system using a completely different mechanism, electroadhesion. The idea was to create a construct of stacked polymer layers and exploit electroadhesion to reversibly weld the layers into a single multi-ply unit (Figure 4.1). Bonding the layers together altered the effective thickness of the material and altered the moment of inertia. The bending stiffness of the composite was thus controlled by the application of a potential. The material that was used in this case was poly(ethylene-*co*-acrylic acid) (PEAA) and the variable studied was the counterion, which was changed between K^+, tetramethyl ammonium (TMA), tetraethyl ammonium (TEA), and tetrapropyl ammonium (TPA). This system worked well, especially as a first test, but there were some issues, namely that the system was extremely dependent on humidity and that full bonding was never observed due to arcing at higher voltages and other potential unknown problems (Figure 4.2). Additionally, the electroadhesion was never measured directly, making it such that the cause of change in flexural rigidity could not be determined.

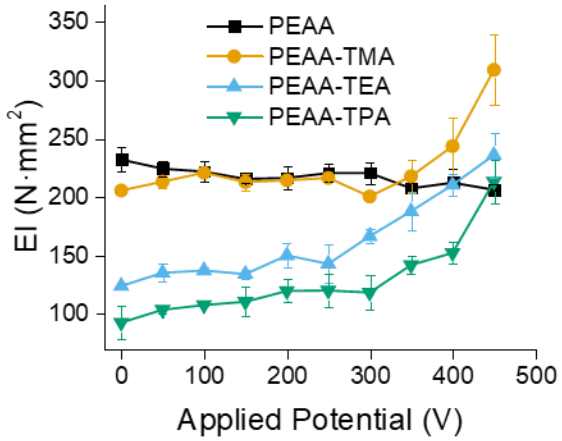

Figure 4.2: PEAA flexural moduli of multilayer systems under applied potentials, carried out by Jeff Auletta. PEAA by itself shows no apparent change in flexuaral moduli with increase in applied potential, but with the trimethl-, ethyl-, and propyl- amine salts the modulus increased with increased potential. Note that this is for the 3-point bending test shown in Figure 4.1.

4.1.2 Current Work

The next phase of the project was to systematically study the factors influencing ionomer electroadhesion. A new polymer, sulfonated poly(styrene-*b*-ethylene-*ran*-butylene-*b*-styrene) (sSEBS), was chosen to study as a variable ratio of ion groups to polymer backbone could easily be added post-polymerization. It also has been extensively studied in the fuel cell world due to its relative availability, functionalizibility, and high ion exchange capacity compared to industrial standard Nafion.[148] SEBS is manufactured on the industrial scale and the sulfonation process involves commonly used reagents that can be altered in concentration to produce varying sulfonation degrees. Herein, we will discuss the results of our systematic exploration of the factors influencing electroadhesion in sulfonated SEBS.

4.1.3 Electroadhesive theory

Electrostatic chucks hold charges apart with a dielectric layer. When the electroadhesive has a nonconductive dielectric between the charged plates (Figure 4.3), the system behaves as two parallel plate capacitors with a capacitance and Coulombic force that is dependent on the distance between the two electrodes ($\mathbf{d_d}$) and the electric permittivity of the dielectric between them[149]. The force relationship of two charged parallel plates is well-known and given in equation 1.1, where **F** is the force, **A** is the surface area of the plates, $\mathbf{\varepsilon_0}$ is the vacuum permittivity, $\mathbf{\varepsilon_r}$ is the dielectric constant of the material between charged plates, **V** is the applied potential, and **d** is the distance between charges. The derivation is provided in Appendix A1.

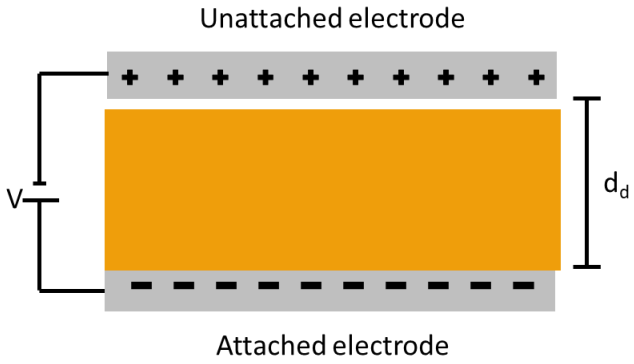

Figure 4.3: A coulombic electroadhesive- the dielectric spacer in the middle is non-polarizable and so the electrostatic force is entirely dependent on the distance between the two metal plates.

$$\boldsymbol{F} = \frac{\boldsymbol{A\epsilon_0\epsilon_r}}{\mathbf{2}}\left(\frac{\boldsymbol{V}}{\boldsymbol{d}}\right)^{\mathbf{2}} \qquad 4.1$$

When the electroadhesive dielectric is conductive, the charges involved in electroadhesion are the ones separated by a gap ($\mathbf{d_g}$) between the dielectric and the unattached electrode (Figure 4.4). The gap system can be modeled as the second of two leaky capacitors in series (Figure 1.5), and it is

known that the potential across the second capacitor behaves as the potential across a voltage divider[149] (Equation 4.2) and thus the overall force equation becomes Equation 4.3. This force is typically referred to as the Johnsen-Rahbek force.[150] Many studies have been done on both the Coulombic and JR electroadhesives[151-161], but our work would be the first to utilize ionomers, which have an exceptionally low starting modulus compared to other electroadhesive materials.

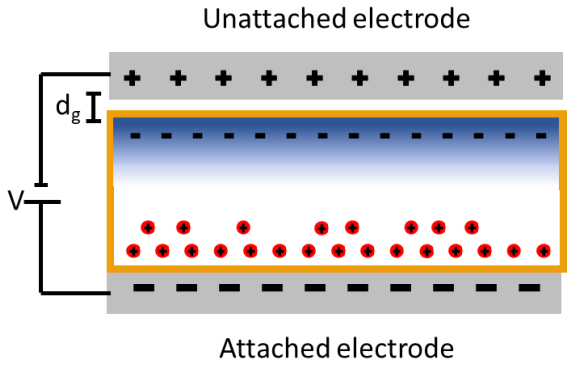

Figure 4.4: A Johnsen-Rahbek electroadhesive- the dielectric spacer is polarizable, leading to interfacial charges, and so the electrostatic force is instead dependent on the distance between the electric plate and the dielectric interface.

$$\boldsymbol{V_g} = \frac{\boldsymbol{R_g}}{\boldsymbol{R_d} + \boldsymbol{R_g}} \qquad 4.2$$

$$\boldsymbol{F} = \frac{\boldsymbol{A\epsilon_0\epsilon_r}}{\boldsymbol{2}}\left(\frac{\boldsymbol{R_g}}{\boldsymbol{R_d} + \boldsymbol{R_g}}\frac{\boldsymbol{V}}{\boldsymbol{d_g}}\right)^{\boldsymbol{2}} \qquad 4.3$$

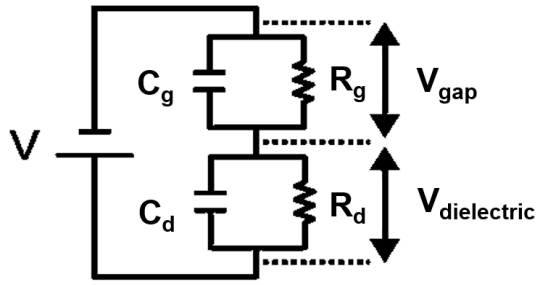

Figure 4.5: Equivalent circuit diagram of two leaky capacitors in series. C_g is the gap capacitance, C_d is the dielectric capacitance, R_g is the gap resistance, and R_d is the dielectric resistance.

4.1.4 Ionomer structure

Ionomers are considered poly-(ions) that generally have less than 15-20 mol% ions[162] and it is well known that all poly-(ions) and ionomers adsorb water from the surrounding atmospheric humidity. Ionomers with a block structure, and random copolymer ionomers with longer block lengths, are known to segregate due to unfavorable mixing interactions. This behavior means there will typically be segregated segments of high ionic clustering, surrounded by non-ionized moieties, and segments of non-polar regions. The ionic and non-polar segments may arrange themselves in high-order block geometries such as lamellar or cylindrical or may simply exist as disordered nano- or microphase separated regions. Work by Weiss and Fitzgerald[163] was fundamental in describing this three-phase morphology of sulfonated SEBS polymers, proving the block microdomains existed on an order of 10-30 nm and the ionic cluster microdomains existed on an order of 2-4 nm. A recent review of sulfonated SEBS by Elabd et al[164] provides a good overview on other research of the known properties and morphologies of sulfonated SEBS.

The nature of the non-polar and ionic segments can affect the properties of the ionomer. The ionic nature influences the cluster strength, and the nature of non-polar segment affects

mechanical and thermal properties as well. A common variation of the ionic group is between carboxylate ions, which aggregate weakly, and sulfonate ions, which aggregate strongly. The most important comparison of the hydrophobic backbone is between hydrocarbon-based ionomers and perfluorocarbon-based ionomers because both have important industrial usage, though other backbone types have been explored in the research.[165-166] It is well understood that perfluorocarbon backbones experience no induced-dipole effects and therefore possess a higher melt-processability than polymers with a hydrocarbon backbone. A combination of these two components can be used to effectively explain the melt behaviors of different ionomers. Based on the above understanding, one would expect a carboxylate analog of Nafion to have high melt-processability, which it does.[167] Nafion itself and hydrocarbon acrylates are also easily processable. Sulfonated hydrocarbon ionomers however, have poor or non-existent melt-processability due to the combined effects of the strong ion group as well as the stiff hydrophobic backbone.

Hydrated ionomers are often challenging to understand because the hydrated structure is not crystalline but is a dynamic or mobile system that is difficult to measure. For example, small-angle X-ray scattering (SAXS) is useful in measuring ordered structure but difficult for measuring the number of waters attached to an ion group.[148, 168-169]

Ionomers have a strong affinity toward water and will adsorb moisture from the atmosphere. The hydration of ionic groups decreases the attraction of the ionic clusters by forming barriers between the ion pairs. This decrease in cluster strength results in better flow of the polymers and causes a decrease in the glass transition temperature (T_g) and mechanical properties. The decrease in cluster strength also means that the more ionic groups added to the ionomer, the less resistive the material becomes. For fuel cell applications it is thought that this is due to charge movement either from an electro-osmotic pressure or from a diffusion-based system due to

electrochemical redox reactions at the electrodes.[170] Research in molecular dynamic modeling has also been useful in categorizing the morphology of hydrated ionomers.[170-171]

4.2 Results and Discussion

4.2.1 Polymer synthesis

Poly(Styrene-*b*-ethylene-*ran*-butylene-*b*-styrene) was donated by Kraton Corporation and the styrene moieties were sulfonated to varying degrees through the commonly used reaction of acetyl sulfate with the SEBS polymer[172] (Scheme 4-1). Because the solubilities of acetic anhydride and sulfuric acid (the components of acetyl sulfate) are poor in the relatively non-polar solvents that dissolve SEBS polymer, the optimal range of reagents ratios was found experimentally. The ultimate procedure called for a range of 3 to 7 times the moles of acetic anhydride to styrene groups, which were then reacted for 2 hours in DCM at reflux, during which time a polymer precipitate formed.

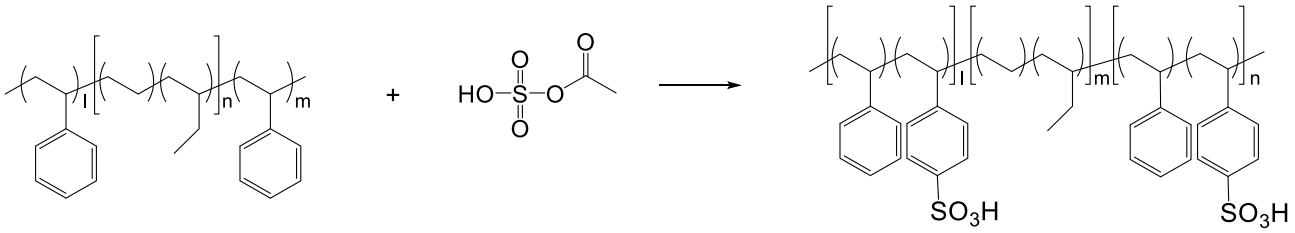

Poly(styrene-*b*-(ethylene-*ran*-butylene)-*b*-styrene) (SEBS)

Acetyl sulfate

Sulfonated SEBS (sSEBS)

Scheme 4-1: Sulfonation of SEBS polymer

The acidic proton was replaced with a sodium ion using an equivalent molar ratio of sodium methoxide to original acid (Scheme4-2). While solid phase ion exchange of dried polymer in an aqueous sodium hydroxide solution was originally tested, it was replaced due to the ease of the organic base one-pot synthesis method which also allowed for higher degree of system control.

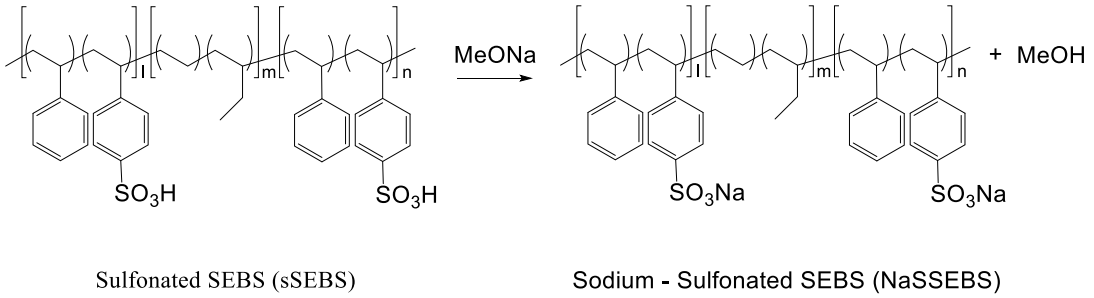

Scheme 4-2: Sodium exchange of sulfonated SEBS polymer

4.2.2 Naming convention and polymer description

Ionomers are named in the following fashion: SEBS-SX% where X is the degree of sulfonation in mole percent. The unmodified SEBS polymer is 30% styrene groups by mass and the sulfonation degree refers specifically to the mole percent of modified styrene groups. It is important to note that a polymer with a high degree of sulfonation according to this convention will still have a relatively low ion content with respect to the mass of the polymer.

The degree of sulfonation was determined by elemental analysis (EA). Additionally, two sulfonations of SEBS were verified through Gran plot titrations. For an EA-based sulfonation degree of 34%, titration showed its percent sulfonation to be 30% and for an EA-based sulfonation degree of 47%, titration showed its percent sulfonation to be 43%. These values are in fairly good accordance. It is possible that due to the solid nature of the polymer during titration, not all

sulfonate sites were accessible for protonation and thus causing the difference in degree of sulfonation. Table 4-1 lists the polymers made and their corresponding degree of sulfonation.

Table 4-1: Sulfonated SEBS polymers

Sample Name	Degree of Sulfonation (%)[a]
SEBS-S34%	34%
SEBS-S46%	46%
SEBS-S68%	68%
SEBS-S60%	60%
SEBS-S77%	77%
SEB-S63%	63%
SEBS-S88%	88%
SEBS-S75%	75%

[a]Degree of sulfonation determined through elemental analysis

4.2.3 Depositing thick films onto aluminum electrodes

Deposition process

For the purpose of this project, the processing goal was to produce smooth, flat films that were well-attached to a ¾-inch aluminum electrode, referred to in this document as the "attached electrode". It is important to note that the use of the word film in this context refers to thick films that will have bulk properties as well as surface properties. Film smoothness was also extremely important as smoothness has a direct impact on the gap distance and contact properties of electroadhesive materials.

For both film production and later testing it was necessary to expose the samples to controlled humidity conditions. This "conditioning" was accomplished by sealing the samples in

a closed container with a series of salt solutions known to establish and maintain a constant relative humidity (RH).[173-174]

A facile method for pressing smooth sulfonated-styrene based ionomers was developed that involves wetting the polymer with water to act as a natural plasticizer then pressing at 125 ºC on an aluminum hot press. The method developed here was designed for small scale batches and utilized the natural adsorption of water by ionomers in a high-humidity (85% RH) chamber, but a scale up to a much larger, similar system could be easily accomplished. Solution casting is challenging for these polymers as it requires complicated solvent systems that vary depending on the degree of ionization.[175]

Directly using ionomer water uptake for sulfonated SEBS processing is highly beneficial because it allows for plasticizer-free and solvent-free thermal processing of a polymer that is otherwise not melt-processable. A plasticizer-free ionomer such as sulfonated SEBS is necessary for many membrane applications, such as fuel cells, where added chemicals could potentially interact and interfere with the reaction system. In addition, plasticizers reduce mechanical properties, which may or may not be a desired characteristic, and are sometimes also considered a health concern. It has been well known that water decreases the mechanical properties of polyelectrolytes[176], but utilizing this property for the purpose of producing ionomer SEBS films appears to have not before been studied previously. The only challenge in this method is that processing steps must be repeated to allow adequate time for the polymer to reach a stable and reproducible conformation. The films formed for this study were said to have reached this state when they were visibly smooth and had no apparent feature changes between subsequent processing.

The ultimate protocol to press smooth NaSSEBS films involved conditioning the amorphous polymer in an 85% RH chamber for several days until visibly wetted with no change in appearance. The weights of the polymers were recorded to 0.2 ± 0.01 g and were pressed onto an aluminum electrode at 1 lb of pressure at 125 ºC (lower temperatures do not yield smooth samples) between two glass slides with aluminum spacers on each side. They were then reconditioned in the 85% RH chamber either overnight or until visibly wetted and were subsequently re-pressed following the same method. If two presses did not result in a smooth sample, more pressing following the same method were performed until either the sample appeared very smooth or until there was no change in smoothness. Multiple presses were necessary due to evaporation effects to allow the polymer to stabilize.

Our prior efforts at producing electrode-bound thick films, which were lengthy and involved a combination of casting and heat pressing, did not lead to films that were uniform and well-attached to the electrode (Figure 4.6). Two batches of polymer were utilized to develop the film processing protocol: SEBS-S46% and SEBS-S35%. First attempts involved hot pressing dried amorphous polymer at 125ºC, 300 ºC, and 400 ºC with no apparent flow. Solution casting was also tested with poor surface characteristics. Higher pressing pressures were also tested, using polycarbonate as a pressing surface. Residual DMSO, however, partially dissolved the polycarbonate but also allowed the sample to flow. The final method of hydrated processing was investigated at this point (Figure 4.7).

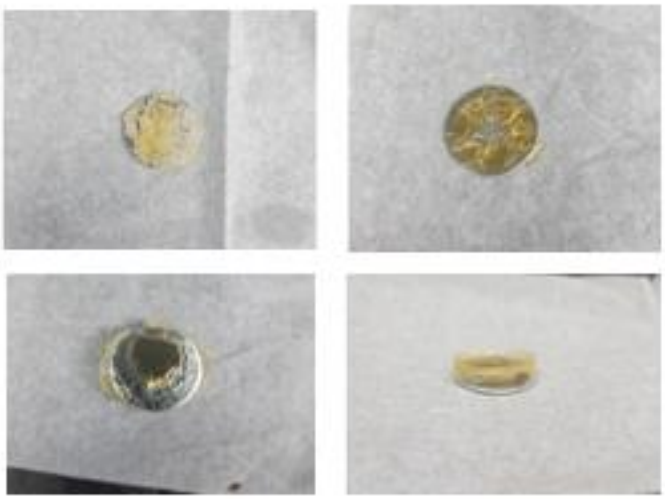

Figure 4.6: Poorly bonded films produced by solution casting.

Figure 4.7: Well-bonded film prepared by thermal processing.

Film Morphology Characterization

Attempts to characterize the block morphology of the sulfonated SEBS polymer were mainly unsuccessful. Transmission electron microscopy (TEM) has been reported as a characterization method for sulfonated SEBS in the literature but our initial attempts (with the help

of microscopist Tom Harper, University of Pittsburgh) to microtome the films were unsuccessful. tapping mode atomic force microscopy (AFM) as well as scanning electron microscopy (SEM) did not give meaningful data as to the morphology of the sample either. Energy dispersive X-ray spectroscopy (EDS) exhibited strange effects in which the signals for each atom present in the SEBS molecule decreased over time as the electron beam was applied, which could indicate chemical changes at the surface of the polymer.

Due to the difficulty of characterizing these films, each film was prepared with the same amount of polymer each time and in the same conditions to mitigate morphological disparities between samples.

4.2.4 Electroadhesion friction testing

The experimental goal was to examine the frictional electroadhesive force, as that would mimic the forces present in the bilayer composite structure. A custom instrument was utilized to provide both a method of inputting potential to the system and to measuring force. The collection and interpretation of that data is given in this section.

A 3-point bending instrument was constructed by Professor William C. Clark of the Mechanical Engineering and Materials Science Dept. of the University of Pittsburgh and Dr. Jeff Auletta. I later modified the instrument with the help of Dr. Auletta to instead measure the shear friction electroadhesive force of the prepared film (Figure **4.24**). The entire apparatus is enclosed and maintained at a humidity within 2% RH of the conditioning humidity using dry N_2 gas. A 16-bit immobile load cell measured the friction force of a 5/8-inch unattached electrode sliding across

the film. A 50 g weight was added above the attached electrode to ensure proper starting contact. The load cell output and current are monitored before and during the application of the potential to the bound and free electrodes. The sample is subjected to a brief charging period (45 s) before the platform on which the bound electrode is mounted is moved away from the load cell for an appropriate duration to ensure complete separation of the film and the unattached electrode (usually 30 s). This process collects a force vs. applied force curve as shown in Figure **4.8**. The static friction forces for each trial are then plotted vs. applied potential.

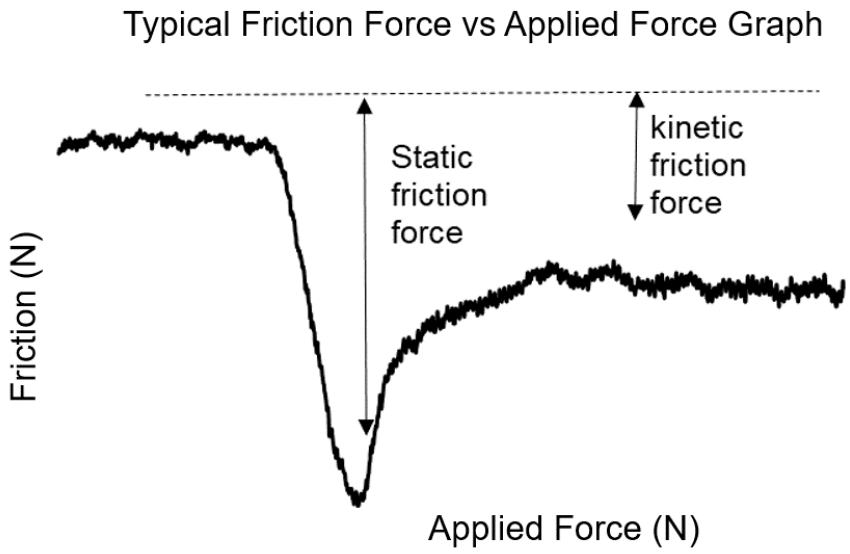

Figure 4.8: Typical friction vs applied force curve

Initially, friction testing was performed to measure the sliding forces of an electroadhesive laminate directly. During the course of this testing, large deviations from the expected trends predicted by equation 1.3 of the measured electroadhesive forces were observed. It became apparent that there were mitigating effects occurring during testing. The following experiments and ensuing discussion provide an explanation to these trends.

Variation of cathode and anode placement

Electroadhesive testing was conducted on polished aluminum unattached electrodes and S75% polymer films conditioned at 43% RH, starting at 0 V, running three trials on each sample, and then increasing the applied potential by 50 V and continuing to run three trials for every potential. Each trial consisted of a 45 s charging step followed by a 30 s pulling step, after which the potential was turned off and the sample was reset. The same test was repeated for polished and unpolished unattached aluminum electrodes and for films in which the anode was attached to the polymer and for films in which the cathode was attached to the polymer. The average of each trial for a given potential were plotted in Figures 4.9 and 4.10.

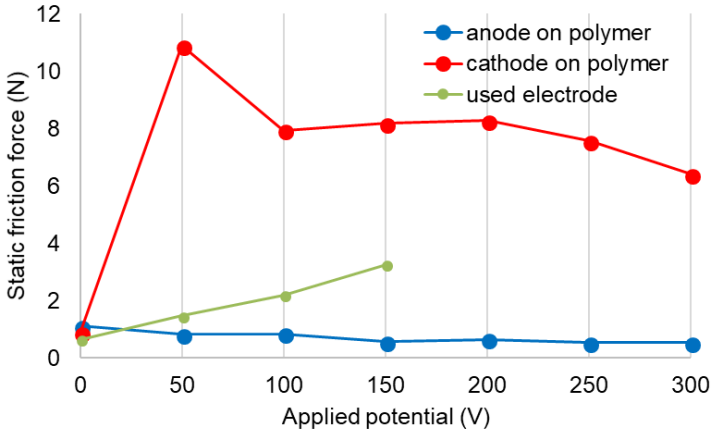

Figure 4.9: The anodic polymer (blue) gives no electroadhesive force response while the cathodic polymer (red) has an electroadhesive force response (Al electrode, polished, 43% RH, S75%). When the electrode previously used as the anode is subsequently used as the cathode (green), a diminished force response relative to a virgin cathode was observed.

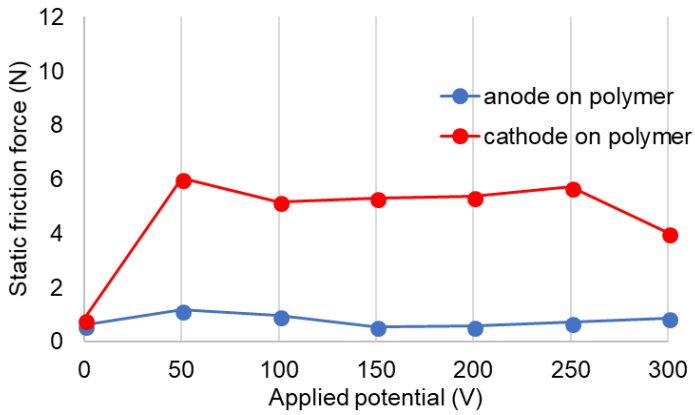

Figure 4.10: The anodic polymer gives no electroadhesive force response while the cathodic polymer has an electroadhesive force response (Al electrode, unpolished, 43% RH, S75%)

Figure 4.11: When the polymer is the anode, there is significantly more discoloration of the sample bound to the electrode than when the polymer is the anode (the degree of difference somewhat minimized due to lighting issues in these photographs). Both samples show some coating of the unattached electrode.

The difference between the electroadhesion when the direction of charge flow was reversed was striking. While the unattached electrode required over 10 N of force to completely speparate from the polymer film that was acting as the cathode, there was no significant adhesion when the

anode was on the polymer, and there was a stark physical change to the anodic polymer film after electroadhesion friction testing (Figure 4.11). The film became darkened where contact with the unattached electrode had been made and it exhibited a 'tacky' feeling to the touch. There was also evidence of a coating on the unattached aluminum electrode, despite its relatively short contact time. These differences provide substantial evidence that the sulfonated SEBS polymer undergoes some sort of decomposition, likely oxidation as the changes observed are greatest when the unattached electrode is positively polarized. While we do not completely understand the nature of the degradation, it is likely hydroxide radical catalyzed degradation of the polymer.[177-179] It is also of note that there is slight discoloration of the cathodic polymer film (Figures 4.11) as well as the anodic unattached electrode, but the discoloration was less apparent and did not appear to be present throughout the entire depth of the polymer film as was the case for the anodic film. This observation is in accordance with the theory that the sulfonated SEBS polymer oxidizes, as one would expect slight oxidation to occur at the contact point with the unattached electrode as the gap capacitor system experiences leakage current.

To determine whether the significant visible change in the unattached electrode when the polymer was the anode was the reason that no static friction force was observed, the used electrode (with coating present as shown) was placed on a fresh polymer sample conditioned at 43% RH and was run where the electrode was now the anode, and the polymer was the cathode. While the static friction force was diminished, it still exhibited a force-voltage response, and a current was present. The formation of a passivating layer on the aluminum may also be contributing to reduced electroadhesion in addition to the passivation of the polymer. However, anodic unattached electrodes form a passivating layer to a much lower degree than cathodic unattached electrode (Figure 4.9), and since there is still current and a force-voltage response even with significant

aluminum passivation, it is clear that the passivation of the electrode is not the largest factor affecting the adhesion.

Variation of increasing or decreasing potential change on a sample

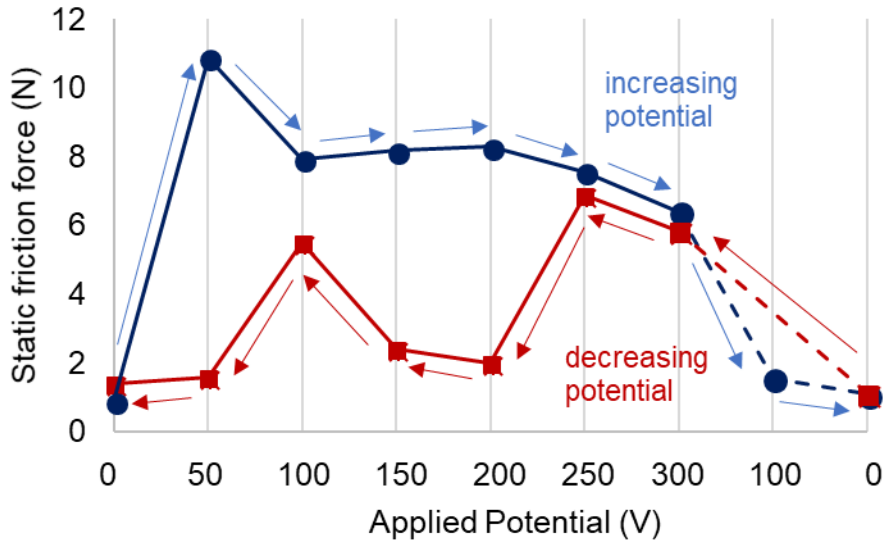

Figure 4.12: The adhesion pattern differs significantly when the sample is first charged at a high potential than when the potential is increased at each step (Al electrode, polished, 43% RH, S75%).

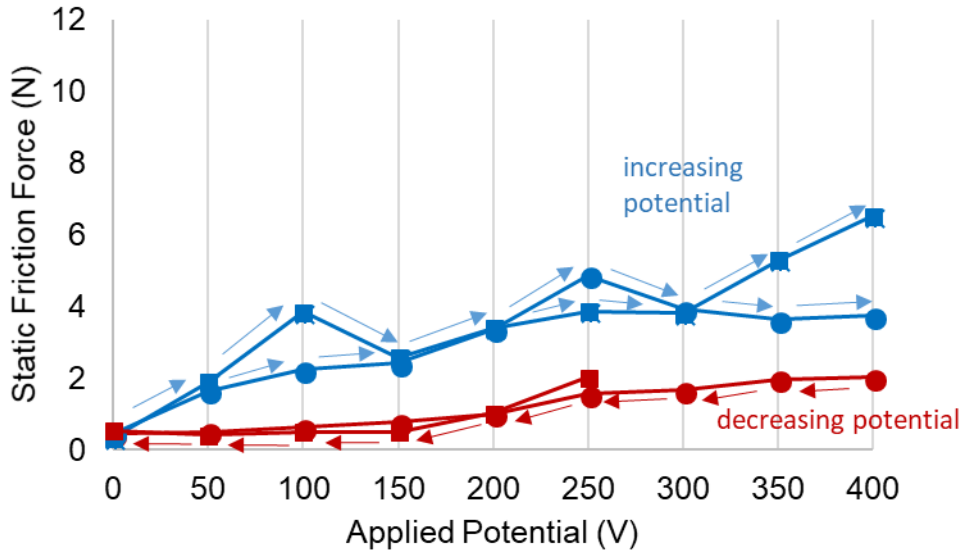

Figure 4.13: The same differences in the step-direction, increasing vs. decreasing, are seen when the humidity is lowered and a brass electrode is used (Brass electrode, polished, 23% RH, S75%).

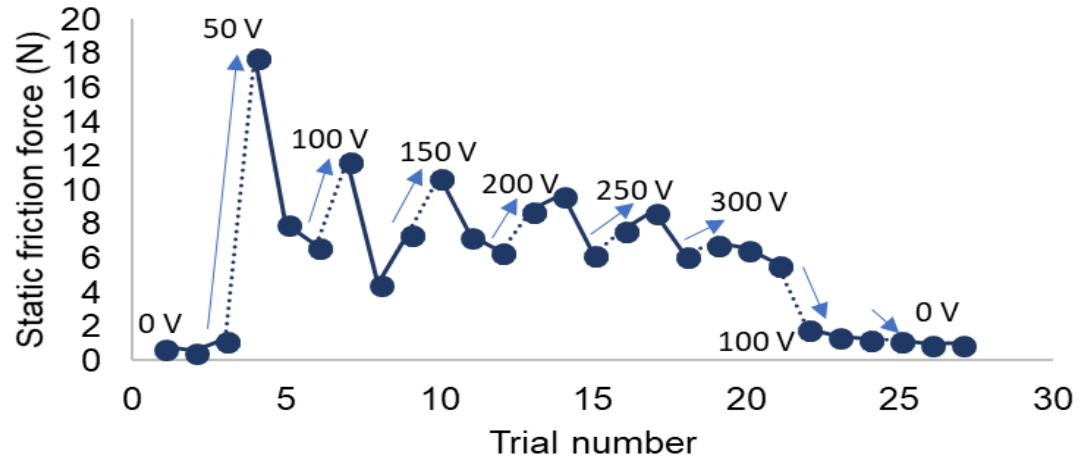

Figure 4.14: Plot of each measurement of Figure **4.12** in a series (acquired in a single session on a single sample). Each set of data (between arrows) consisted of three runs at specific potential. The arrows indicate each stepwise increase of the voltage by 50 V. Typically a spike in electroadhesion is observed immediately after the voltage is increased. (Al electrode, polished, 43% RH, S75%).

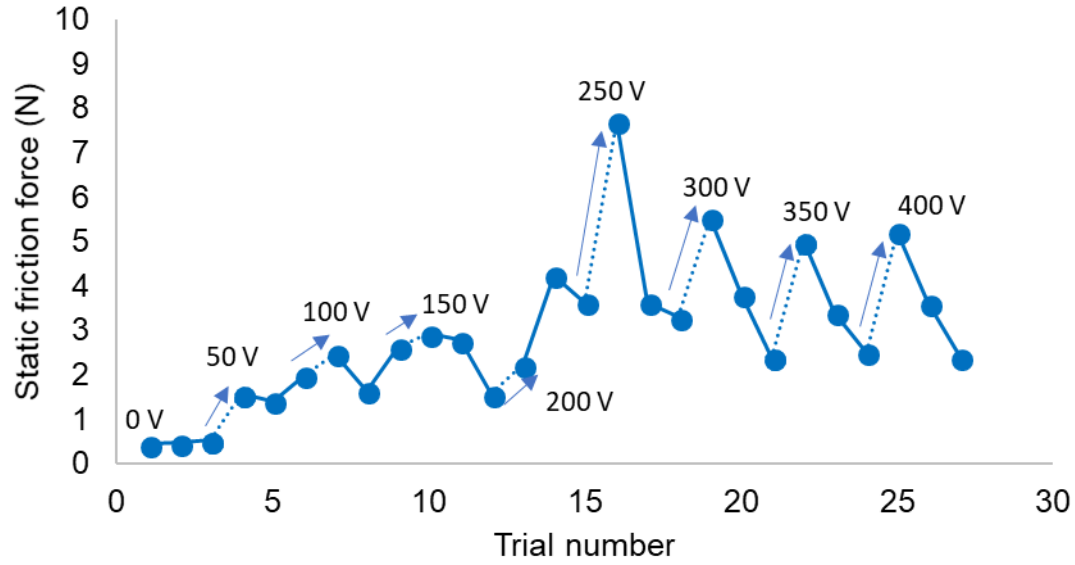

Figure 4.15: Plot of each measurement of Figure **4.13** in a series (acquired in a single session on a single sample). Each set of data (between arrows) consisted of three runs at specific potential. The arrows indicate each stepwise increase of the voltage by 50 V. Typically a spike in electroadhesion is observed immediately after the voltage is increased. (Brass electrode, polished, 23% RH, S75%).

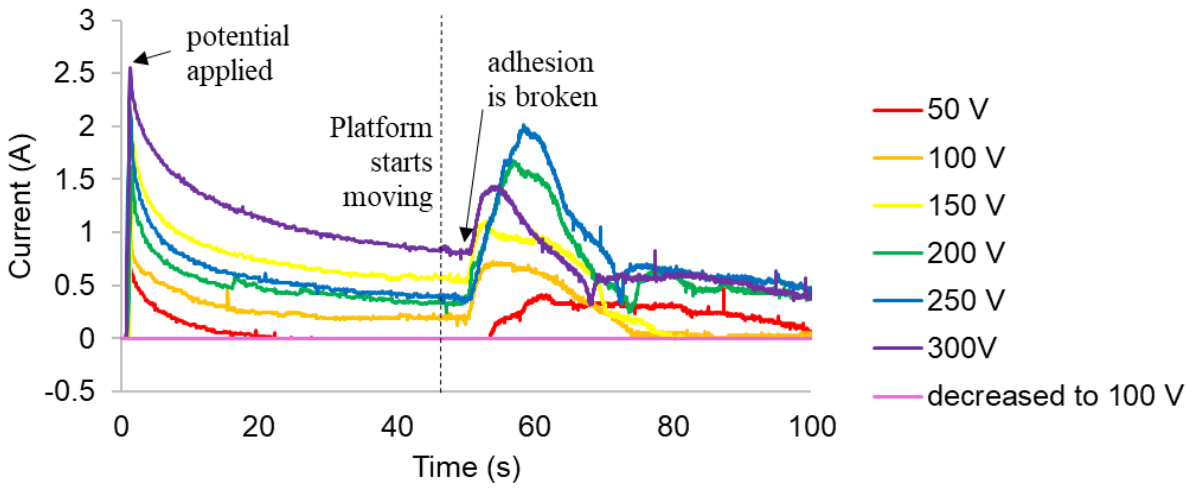

Figure 4.16: Representative current data (first run of every potential) for electroadhesive testing. Current generally increases with applied potential but is not restored when decreased to 100 V after a large amount of current has been applied (Al, polished, 43% RH, S75%). Potential is applied at the beginning of the experiment, the platform starts moving 46 seconds into the experiment, and the electroadhesion between the polymer and the electrode is broken shortly after. There is a renewed spike in current as the unadhered electrode jumps to a fresh location on the polymer.

Electroadhesive testing was conducted on S75% polymer films conditioned at 23% RH and 43% RH starting at 0 V, running three trials on each sample, and then increasing the applied potential by 50 V and continuing to run three trials at every new increased potential. The same electroadhesive testing method was conducted on fresh polymer films that were also conditioned at 23% RH and 43% RH starting at 400 V, running three trials on each sample, and then decreasing the applied potential by 50 V and continuing to run three trials at every new lowered potential. Each trial consisted of a 45 second charging step followed by a 30 second pulling step, after which the potential was turned off and the testing apparatus was reset. The average of the force responses of the three trials at a given potential were plotted in Figures 4.12 and 4.13. Examples of the force response for each trial are given in Figures 4.14 and 4.15.

There was a hysteresis of the electroadhesive force observed that gives additional insight into the effect the oxidation of the polymer is having on the electroadhesion. Starting at a low

potential and raising the potential in a stepwise fashion systematically increases adhesion, while starting at a high potential and stepping down gives adhesive forces that are substantially lower. This effect is explained by the formation of the passivating layer, which blocks ion movement. Higher currents are present at higher potentials due to Ohm's law, causing there to be a greater and faster buildup of the oxidized passivating layer when starting from a higher potential than there was when starting at a lower potential. The greater buildup of the oxidized layer causes the charge separation to be greater for the films that started at a high potential and decreased by 50 V compared to the films that started at a low potential and increased by 50 V. There was significant variance between trials at the same potential due to variance in the thickness of the oxidized layer and placement of the unattached electrode. Generally, as subsequent trials were conducted at a given applied potential, the first trial at a potential would have the largest force response that would then decrease with the number of trials. Occasionally, the second or third trial at a given potential would have the largest force response, which is likely due to the placement of the unattached electrode onto a portion of the polymer film previously untouched and thus without significant oxidation layer accumulation to prevent charge flow at the gap.

The current was recorded for the sample at 43% RH as it was exposed to stepwise increases of applied potential of 50 V (Figure 4.16). The current generally increased with increasing applied potential, congruent with Ohm's law. When the potential was reduced to 100 V after repeated trials at higher potentials, there was no current present above the detection threshold minimum. We hypothesize that the charge was unable to flow due the insurmountable contact resistance at that potential because of the oxidized layer.

Increasing the applied potential in smaller steps

To test the hypothesis of the formation of an oxidative layer that inhibits further adhesion response, electroadhesive testing was conducted on polished aluminum unattached electrodes and S75% polymer films conditioned at 43% RH, starting at 0 V, running three trials on each sample, and then increasing the applied potential by only 5 V and continuing to run three trials for every potential. Each trial consisted of a 45 second charging step followed by a 30 second pulling step, after which the potential was turned off and the sample was reset. The average of the three trials was plotted in Figure 4.17. The electroadhesive force as the potential increased also increased, but the increase was greatly muted compared to the testing done with high potential step. It was observed that the force response from the low step increases of potential only reached an average force of around 1.5 N, even with 50 V of applied potential, compared to the average force reached at 50 V when starting with 50 V of around 11 N (Figure 4.12). Even when testing the small incrementation of potential, however, there was significant variation between each trial at a given potential.

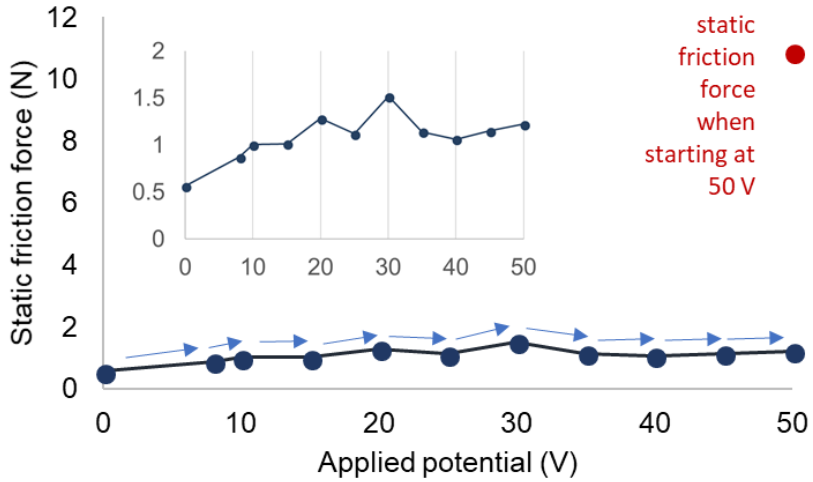

Figure 4.17: Low potential step increase (Al electrode, polished, 43% RH, S75%). Compared to the static friction force acchieved when the test is started at 50 V (11 N), when the voltage is slowly

ramped up the maximum force reached is 1 N at 50 V. We speculate that the amount of current applied over many runs led to the formation of a passivating layer.

The difference of electroadhesive force at 50 V when incrementing the potential by 5 V, compared to starting at 50 V directly and incrementing the potential by 50 V, is consistent with the formation of an oxidized layer. Over the course of many trials, the oxidized layer is slowly built up, distancing the charges at the interface of the dielectric and the unattached electrode and thus diminishing the electrostatic interactions. It may appear on first examination to be surprising that starting at a higher applied potential of 50 V had a greater electroadhesive force response than when starting at a low applied potential and increasing the potential up to 50 V, because the trend shown in Figures 4.12 and 4.13 exhibit the opposite effect, where starting with a large potential of 300 V produces a decreased force response than the force response of 300 V arrived at by starting with a potential of 50 V and then increasing the applied potential by 50 V over the course of several trials. This apparent discrepancy can be explained because 50 V of applied potential provides significant current to the system and, while an oxidized layer does form, the current never reaches 0 and therefore the charge buildup at the interface never equilibrates with the gap distance before the potential is substantially increased again. In fact, the unequilibrated oxidized layer likely serves to provide a barrier against leakage current which causes the capacitance, and thus the force, at the higher potential to be increased. On the other hand, when the potential is increased slowly, the oxidized layer builds up at an equilibrated rate to the increase in potential, such that there is always a gap potential close to 0. There is some variation in the expected electroadhesion which is likely due to partial placement of the unattached electrode onto a less oxidized polymer area.

Variation of sulfonation degree

The dependence of the electroadhesive force on the sulfonation degree was also investigated. A 63% sulfonated SEBS polymer and an 88% sulfonated SEBS polymer were converted into films and the force response of each at varying humidities was measured. Each polymer was pressed onto aluminum electrodes (the attached electrode) and conditioned in humidity chamber of 43, 23, and 7% relative humidities. The system was then charged for 30 seconds at a given potential and the unattached electrode was pulled across the polymer film for 13 seconds several times. The average of each measurement was taken and plotted in Figure 4.18 and an example of the force response to an applied potential of each trial is shown in Figure 4.19.

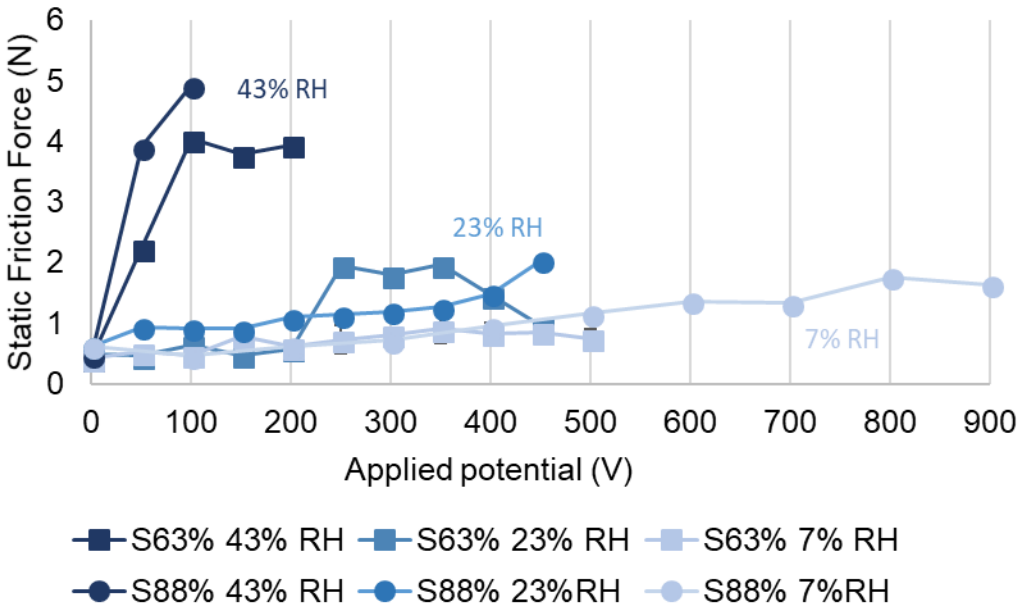

Figure 4.18: Variation in sulfonation degree and relative humidity (brass electrode, polished, varying RH). The relative humidity had a significant impact in the force of attraction- the 43% RH had a maximum of 4 N for the 63% sulfonated sample at 100 to 200 V, and 5 N for the 88% sulfonated sample at 100 V. The 23% relative humidity samples were a lot lower- The maximum friction force was 2 N at 250 to 350 V for the 63% sulfonated sample and also 2 N at 450 V for the 88% sulfonated sample. The 7% RH samples maxed out at 0.5 V for the 64% sulfonated sample at 500 V and 1.5 N at 900 V for the 88% sulfonated sample.

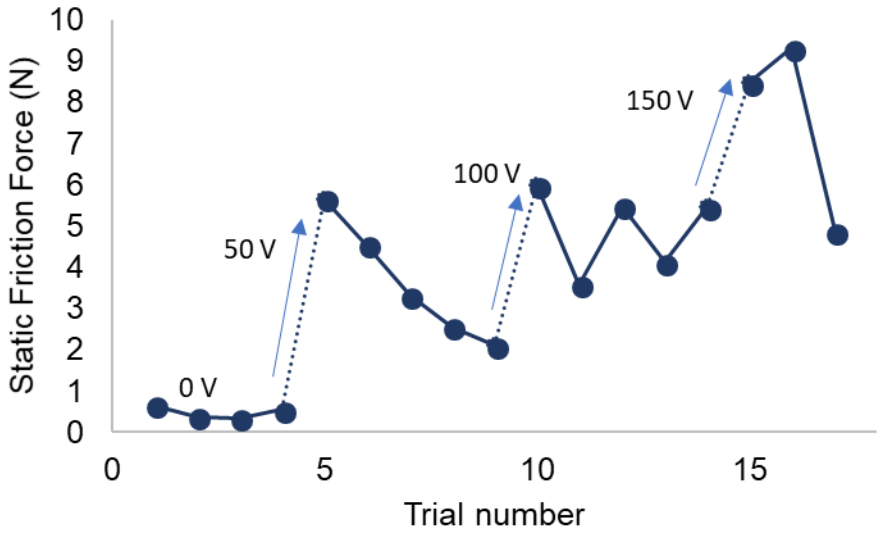

Figure 4.19: Each trial number for a set of data given in Figure **4.18** at a given potential and then increasing by 50 V. There is a spike in electroadhesion initially which then tends to decrease with repeated trials. (Al electrode, polished, 43% RH, S88%).

Due to the formation of the passivating layer, it was challenging to extract information about how the degree of sulfonation affects the electroadhesion. The two degrees of sulfonation compared were both of sufficient dielectric conductivity to allow for electroadhesion to be observed. There is a clear difference between the electroadhesive forces of the varying relative humidities. The films with the highest water content have the highest electroadhesion response, due to the increased dielectric conductivity and the films with the lowest water content have the lowest electroadhesion response. Additionally, the minimal force response of the 7% relative humidity sample shows that the force of these samples is primarily dependent on the Johnsen-Rahbek gap system instead of the Coulombic electrode system between the dielectric polymer film.

While the general electroadhesive force trend shown by the averages goes up fairly consistently with increasing applied potential, there is again significant variation of the measured force of the different trials at the same potential, especially for films with a high electroadhesive potential response. Generally, the adhesive force of the first trial at a given potential is large and then decreases with increased trials at that potential, though there are occasional exceptions to this rule. This trend can be explained by the oxidation effects. Slight misalignment of the unattached electrode can cause large variations due to the gap distance variations of fresh sites.

Variation of unattached electrode surface roughness

The electroadhesive force was measured using S75% polymer samples with a polished unattached aluminum electrode and a cleaned unpolished aluminum electrode. The polished aluminum electrode had a large-scale roughness average (5x magnification) of 170 ± 70 nm and had a small-scale roughness average (10x magnification) of 86 ± 3 nm. The unpolished aluminum electrode had a large-scale roughness average (5x magnification) of 500 ± 100 nm and a small-scale roughness average (10x magnification) of 370 ± 50 nm. At each potential, the polymer underwent three trials at that potential before the potential was changed. Each trial consisted of a 45 second charging step followed by a 30 second pulling step, after which the potential was turned off and the testing apparatus was reset. The averages of each of the three trials were taken and plotted in Figure **4.20**.

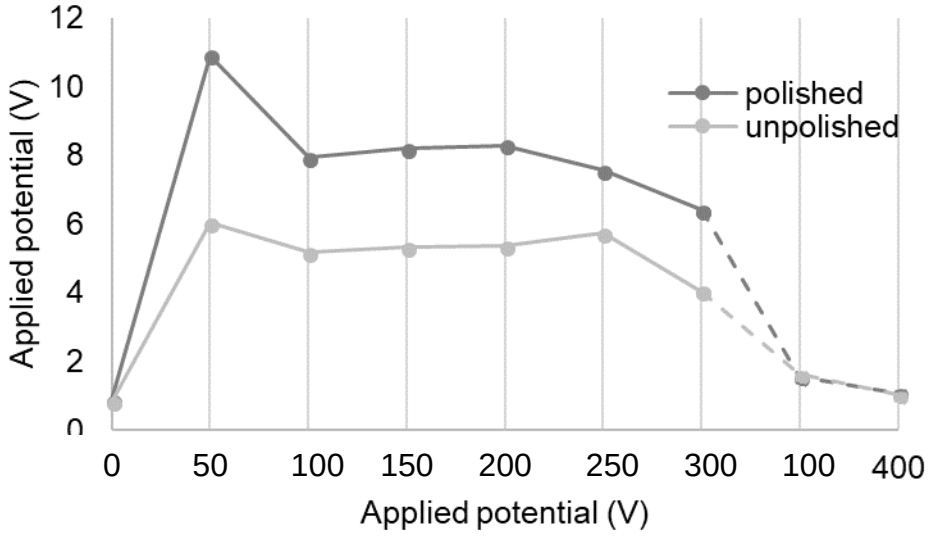

Figure 4.20: Variation in surface roughness of unattached electrode (Al, 43% RH, S75%). The difference in electroadhesion shows the dependence on gap distance and shows that the polymer does not conform perfectly to the electrode surface.

The results of this experiment show that the polymer film is not perfectly conforming to the surface of the electrode and that the roughness of the aluminum surface has an effect on electroadhesion. The greater the surface roughness of the polymer, the lower the electroadhesive force was due to an increased gap distance between the charges.

For both electrodes, after reaching an applied potential of 300 V the applied potential was decreased, first to 100 V then to 0 V. At each potential the polymer film was tested three times. Notably, the force exhibited at 100 V was significantly less than the force exhibited at 100 V earlier in the testing for both films, and they decreased to a similar force. This hysteresis of the electroadhesive response further demonstrates the effects of the buildup of an oxidized hydrophobic layer on the surface of the film. Significant charge flow occurs between the dielectric's surface and the unattached electrode after many trials at high potentials. Thus, there

will be a larger effective gap distance, due to the oxidized layer, after many trials than at the beginning of the experiment.

The static friction force at 0 V was similar both before and after testing, showing that no significant tribological effects were influencing the testing.

4.2.5 Discussion of oxidation effects on adhesion

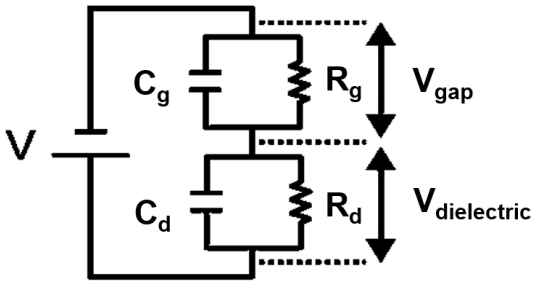

Figure 4.21: Equivalent circuit of system. V is the applied potential, C_g is the gap capacitance, C_d is the dielectric capacitance, R_g is the gap resistance, R_d is the dielectric resistance, V_{gap} is the potential across the gap between the unattached electrode and the polymer film, and $V_{dielectric}$ is the potential across the polymer film.

The charging of the polymer-electrode system can be modeled as an electrolytic capacitor and the equivalent circuit is shown in Figure 4.21. There appeared to be disagreements in the literature about the mathematical model of this circuit[152, 157, 180-181], and so the time-dependent force equation of this system was derived (Appendix A2) and shown in equation 2.1 where **F** is the electroadhesive force, **A** is the total surface area of each charged plate, $\boldsymbol{\varepsilon_0}$ is the vacuum permittivity, $\boldsymbol{\varepsilon_g}$ is the gap dielectric constant, $\boldsymbol{\varepsilon_d}$ is the polymer film's (the dielectric material's) bulk dielectric constant, $\mathbf{G_g}$ is the gap conductance (equals $\mathbf{1/R_g}$ where $\mathbf{R_g}$ is the gap resistance), $\mathbf{G_d}$ is the dielectric conductance (equals $\mathbf{1/R_d}$ where $\mathbf{R_d}$ is the dielectric resistance), **V** is the applied potential, $\mathbf{d_g}$ is the gap distance, $\mathbf{d_d}$ is the dielectric thickness, and **t** is time.

$$F = \frac{A\epsilon_0}{2}\left[\epsilon_g\left(\frac{G_d}{G_d+G_g}\frac{V}{d_g}\right)^2 + \epsilon_d\left(\frac{G_g}{G_d+G_g}\frac{V}{d_d}\right)^2\right]\left(1 - e^{-\frac{G_d+G_g}{A\epsilon_0\left(\frac{\epsilon_g}{d_g}+\frac{\epsilon_d}{d_d}\right)}t}\right)^2 \quad (2.1)$$

$$F = \frac{A\epsilon_0}{2}\epsilon_d\left(\frac{V}{d_d}\right)^2 \quad (2.2)$$

$$F = \frac{A\epsilon_0}{2}\epsilon_g\left(\frac{G_d}{G_d+G_g}\frac{V}{d_g}\right)^2 \quad (2.3)$$

On a large timescale and when the dielectric material has no conductance, equation 2.1 simplifies to equation 2.2, which is the expected force equation for electrodes acting as parallel plate capacitors (equation 1.1). On a large time scale, when the change in current approaches 0 (after approximately 30 to 45 s according to Figure 4.16), and when the dielectric material has conductance, charge will build up at the gap capacitor system and the force dependence on the dielectric capacitor will become insignificant due to the much higher distance between charges, and thus the force equation will simplify to equation 3, which is the expected force equation for a capacitor between a resistive divider (equation 1.3).

Any changes in the force of the ionomer electroadhesive will be due only to variations in the variables of equation 2.3, and thus this equation will be used to show why the buildup of an oxidized layer at the surface of the polymer film is consistent with the measured electroadhesion. The applied potential, given no other mitigating effects, should have a second order effect on the electroadhesive force according to equation 2.3. However, while the applied potential changes over the course of the overall friction test, the measured electroadhesive force does not always increase as the potential increases, much less increase by a squared dependency, and often decreases when the electroadhesion is measured repeatedly at the same potential. Additionally, the

electroadhesive force displaces hysteresis, as the path taken to reach an applied potential will affect the electroadhesion. Therefore, other factors included in equation 2.3 must be neutralizing the effects of the applied potential.

The factors that could be causing this diminished force voltage dependency are the surface area of the polymer, the conductivity of the gap, the conductivity of the dielectric, the gap distance, and the dielectric constant. First, while the surface area of the polymer may change slightly with increased plasticization, this effect was shown to be minimally present (section 2.4.5). The conductivity of the gap could be increasing to cause this effect, as an increase in gap conductivity would result in fewer charges built up at the interface, but current measurements show that the conductivity of the system is actually decreasing, not increasing (Figure 4.16). A plausible theory is that there is a decrease in conductivity of the dielectric polymer film due to some change in the bulk material. However, it is unlikely the bulk dielectric is undergoing such changes. The results in section 2.4.1 suggest that redox reactions to the bulk material prevent any electroadhesive force from occurring. Other changes, such as dielectric breakdown, increase the material's conductivity instead of decreasing it. The dielectric constant of the bulk material is not relevant to the gap system force equation, and the dielectric constant of the gap is not going to decrease as it is the dielectric constant of air which has an approximate value of unity. Thus, the only other factor that could cause the electroadhesive force to diminish is to increase the effective distance of charges at the gap. This could be due to tribological surface variations, but as shown in section 2.5.5, this is unlikely.

The buildup of a non-conducting layer at the interface then is not only the sole factor remaining that could explain why the force response of these materials displays such irregularities, it also does explain the force responses perfectly. The electroadhesive force tends to increase on

average with increase applied potential, but that force response will be lowered if there has already been a large current flow through the material. For high potential step increases, the pre-existing buildup of the non-conducting layer can initially block some current by decreasing the gap conductance and thus slow the buildup of the non-conducting layer while also forcing the charges further apart (but not so far apart that there is no gap potential). For low potential step increases, the non-conducting layer is allowed to equilibrate to a state where there is no current flow, preventing any oxidation, but also to a state where there is no potential across the gap, and thus no adhesion. The buildup of a passivating non-conducting layer also explains the trends between trials at the same potential. There tends to be an increase in electroadhesion when the potential is initially increased (for large potential steps) that diminishes over time. Sometimes there are cases where this rule does not hold true, such as where the potential increases greatly on the second or third trial instead, and this can be easily explained by offset of the unattached electrode onto a fresh location of the polymer that lacks the buildup of the oxidized layer. Figure 4.22 below illustrates this process.

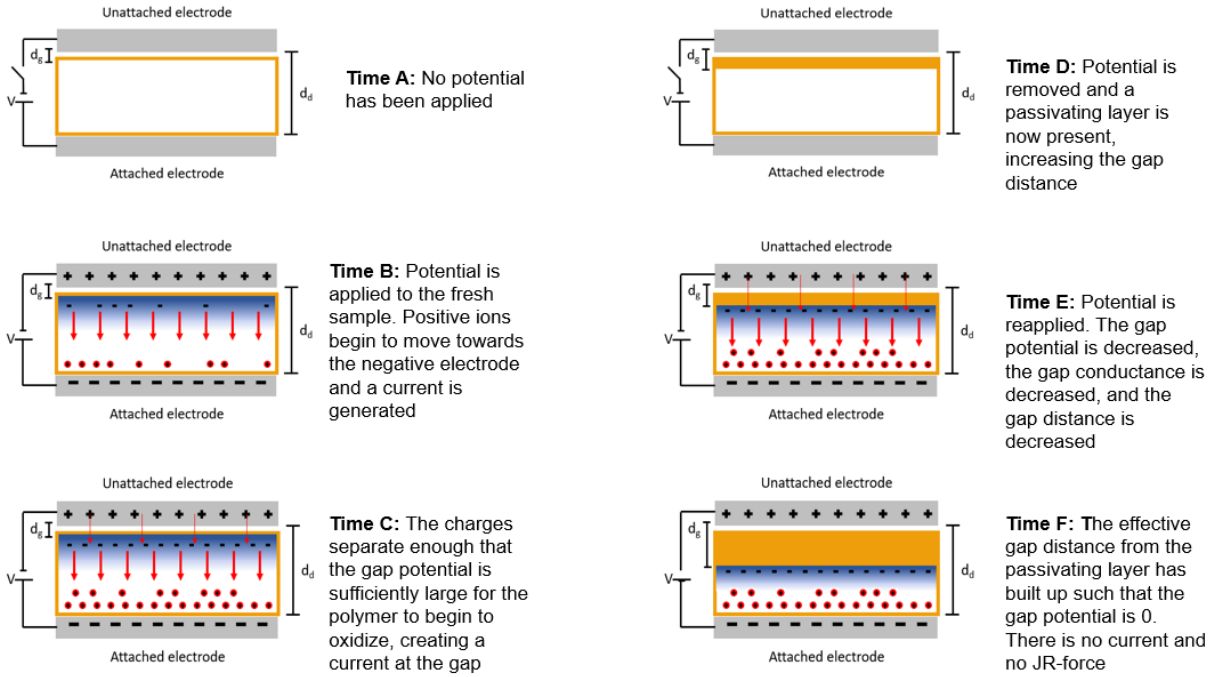

Figure 4.22: The formation of the oxidized passivating layer. Time A: the dielectric is in its virgin state. Time B: ions begin to flow towards the interface, creating a charge differential. Time C: the charge differential is sufficient that an electrostatic force between the electrodes creates sticking, but the polymer also begins to oxidize. Time D: the potenial is removed but unlike the virgin material, a passivating layer is present. Time E: charge is applied and a charge differential begins to appear, creating an attractive force. Unlike Time B and C, however, the passivating layer is present and decreases the attractive force. At time F, the passiving layer has built up sufficiently that the gap distance prevents JR attractive force.

4.3 Experimental

4.3.1 Materials

SEBS polymer G1652 MU was gifted from Kraton Corporation and used as provided. It was characterized via SEC (Table 5.1). Acetic anhydride, sulfuric acid, DCM, DCE, were received from Fisher and used as provided.

Table 5.1 Characterization of SEBS polymer using SEC

Mn	Mw	Dispersity
58.7 kDa	59.6 kDa	1.015

4.3.2 Naming scheme

Polymers are named in the following format: SEBS-SX%, where the X is the percent sulfonated.

4.4 Conclusion

Ionomer electroadhesion was observed and characterized. Unfortunately, more work is needed to produce a stable electroadhesive film, however the experiments and analysis performed provide useful insight into the development of ionomer electroadhesives. Relevant equations have been derived, protocols for determining the efficacy of an ionomer electroadhesive have been

developed, and a problem with ionomer electroadhesives has been analyzed and can be easily spotted in future materials. Additionally, sulfonated SEBS is an often-studied material for energy transfer and energy storage applications and the work done thus far can offer useful insights in that field.

4.4.1 Sulfonation of SEBS polymer

SEBS polymer (5 g) was dissolved in DCM (Table 5.2) at 40 ºC under nitrogen. In a separate rb flask, DCM (Table 5.2) was chilled under purging conditions on ice for 10 minutes. Acetic anhydride was then added in 1.2 molar excess to the sulfuric acid. The solution was stirred with purging for 10 minutes. The sulfuric acid was then added, and the solution was purged for an additional 10 minutes. This solution was transferred to the SEBS solution flask via canula transfer. After 2 hours the reaction was removed from heat and isopropanol was added to dissolve the precipitated polymer. The solution was chilled to 0° C and 25% sodium methoxide in methanol was added in slight excess to neutralize the acid. Each batch was then dried and washed 3x with water before being dried in a vacuum oven at 60 ºC.

4.4.2 Determination of the degree of sulfonation

Elemental analysis, performed by Atlantic Microlab, was the main method of determining sulfur content. Table 5.3 shows the received mass percent sulfur of each sample and a sample calculation for converting grams of sulfur to mole percent sulfonation is given as follows:

Table 5.2: Sulfonation reaction conditions

Sulfonation degree	DCM of SEBS (mL)	DCM of acetyl sulfate (mL)	SEBS (g)	Acetic anhydride (mL)	Sulfuric acid (mL)	Isopropanol (mL)	Sodium methoxide 25% in methanol (mL)
SEBS-S34%	100	150	5.1	3.4	1.4	0	10
SEBS-S42%	100	150	5.0	6.5	3.1	0	15
SEBS-S68%	100	150	5.0	4.9	2.3	30	20
SEBS-S60%	100	150	5.0	8.2	3.8	50	60
SEBS-S77%	100	150	5.0	11.4	5.4	100	125
SEBS-S65%	400	600	20.0	19.6	9.2	300	42
SEBS-S94%	400	600	20.0	45.7	21.5	550	115
SEBS-S75%	800	1200	40.0	42.3	18.4	200	165

4.92% and 4.85%. Average: 4.887%

Mass % S from EA:

4.92% and 4.85%. Average: 4.887%

Moles sulfonate groups:

$$0.044887 \text{ g S x } \frac{1 \text{ mol}}{32.066 \text{ g}} \text{ S x } \frac{1 \text{ mol} -SO_3Na}{1 \text{ mol S}} = 1.52 \text{ x } 10^3 \text{ mol } -SO_3Na$$

Mass unsulfonated polymer:

$$1 \text{ g sulfonated SEBS} - 0.04887 \text{ g S x } \frac{\frac{103.053 \text{ g}}{\text{mol}} -SO_3Na}{\frac{32.066 \text{ g}}{\text{mol}} \text{S}} \text{ x} \frac{1 \text{ mol} -SO_3Na}{1 \text{ mol S}} =$$

0.843 g unsulfonated SEBS

Moles styrene (30 wt% of unsulfonated polymer):

$$\frac{0.843 \text{ g SEBS x } 0.30 \frac{\text{g styrene}}{\text{g SEBS}}}{104.152 \frac{\text{g}}{\text{mol}} \text{styrene}} = 2.43 \text{ x } 10^{-3} \text{ mol styrene}$$

Mol % sulfonation:

$$\frac{1.52 \text{ x } 10^{-3} \text{ mol } -\text{SO3Na}}{2.43 \text{ x } 10^{-3} \text{ mol styrene}} \text{ x } 100\% = 63\%$$

Table 5.3: Degree of sulfonation calculated from elemental analysis

Mass % S (1)	Mass % S (2)	Percent sulfonation
2.89	No duplicate	34%
3.73	No duplicate	46%
5.25	5.15	68%
4.75	4.64	60%
5.86	5.76	77%
4.92	4.85	63%
6.40	6.52	88%
5.62	5.65	75%

Additionally, the first two sulfonation percentages were verified through Gran plot titrations. A solution of nitric acid (0.1000 M) and a solution of sodium nitrate (1.000 M) were prepared. A solution of sodium hydroxide (0.09734 M) was prepared and standardized against the nitric acid solution. Solid polymer (0.1006 g and 0.0711 g) was cryomilled then stirred in an acidic solution (200 mL, 0.100 M HNO_3, 0.0100 M $NaNO_3$). pH was monitored using a pH probe. Base was added using a 1000 μL micropipetter in 1000 μL increments near the beginning and end points and 100 μL increments near the equivalence point. After each addition of base the pH was allowed to stabilize before recording.

The results were plotted using standard Gran plots (Figure **4.23**) and the difference in volume of base added at the x-intercept was used to determine the moles of sulfonate groups. The

mass of the sulfonate groups was subtracted from the total polymer mass and the percent sulfonation was determined through a similar calculation as for elemental analysis.

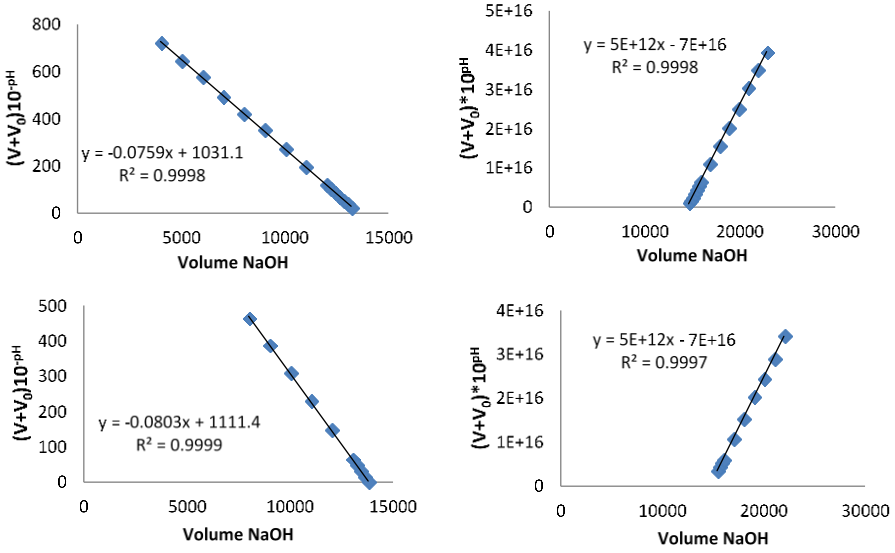

Figure 4.23: a) the strong acid function of the first sulfonated SEBS b) the strong base function of the first sulfonated SEBS c) the strong acid function of the second sulfonated SEBS d) the strong base function of the second sulfonated SEBS

4.4.3 Humidity Conditioning

Several grams of various salts were added to screw-top plastic containers (500 mL) and were slightly wetted to form highly saturated salt slurries. Each salt caused the humidity of the chamber to remain at a different controlled humidity. A stand was placed over each slurry in the container to allow samples to be placed in the chamber. When a sample had equilibrated in a specific humidity environment it was said to have been conditioned to that humidity. Humidities were verified with a hygrometer.

Table 5.4: salt content of controlled humidity chambers

Salt	LiBr	LiCl	KCH_3COOH	K_2CO_3	KCl
Relative humidity (%)	7	12	23	43	85

5.5 Film and electrode preparations

Dried sulfonated SEBS polymers were conditioned in an 85% RH humidity chamber for several days until visible water adsorption had occurred. A sample of polymer (0.2 g) was then placed onto a ¾-inch circular aluminum disk (0.25 mm thickness) between two glass slides with aluminum spacers (0.25 mm thickness) on both ends of the slides. The slides were pressed at 125 ºC under 1 lb of pressure for 2 minutes and then removed and allowed to briefly cool. The pressed polymer on the electrode was then reconditioned at 85% RH for one day, or less if visible water adsorption had occurred. The pressing and conditioning cycle was then repeated one or two times until samples were smooth. The films were then attached to copper tape and mounted on glass slides.

To make polished brass electrodes copper wire was soldered to 5/8-inch brass electrodes. The electrodes were then polished with 0.3 μm alumina and 0.05 μm alumina until shiny. The electrodes were then mounted on glass slides. To make polished aluminum electrodes, 5/8-inch aluminum electrodes were polished with 0.3 μm alumina for 10 minutes. To make unpolished aluminum electrodes, 5/8-inch aluminum electrodes were washed with soap and water. Surface roughness of both polished and unpolished aluminum electrodes were measured with optical

profilometry (Table 5.5). Electrodes were then mounted onto glass slides for placement into the testing apparatus. The electrodes were placed on an elevated glass mount to prevent the attached wire from interfering with the ability of the electrode to lay flat against the polymer.

Table 5.5: Surface profilometry results

		unattached electrode	
magnification	Location on electrode	polished anode	unpolished anode
5X	Location 1	--	768
	Location 2	100	535
	Location 3	247	537
	average	173.5	536
10X	Location 1	82.752	453
	Location 2	85.594	345
	Location 3	88.873	326
	average	85.74	375
50X	Location 1	90.146	484
	Location 2	83.921	274
	Location 3	89.589	219
	average	87.885	326

		unattached electrode	
magnification	Location on electrode	polished anode	unpolished anode
5X	Location 1	--	768
	Location 2	100	535
	Location 3	247	537
	average	173.5	536
10X	Location 1	82.752	453
	Location 2	85.594	345
	Location 3	88.873	326
	average	85.74	375
50X	Location 1	90.146	484
	Location 2	83.921	274
	Location 3	89.589	219
	average	87.885	326

magnification	Location on electrode	unattached electrode polished anode	unattached electrode unpolished anode
5X	Location 1	--	768
	Location 2	100	535
	Location 3	247	537
	average	173.5	536
10X	Location 1	82.752	453
	Location 2	85.594	345
	Location 3	88.873	326
	average	85.74	375
50X	Location 1	90.146	484
	Location 2	83.921	274
	Location 3	89.589	219
	average	87.885	326

4.4.4 Testing apparatus and measurement

The entire apparatus (Figure 4.24) is enclosed and maintained at a desired humidity using dry N_2 gas and monitored via hygrometer. A 16-bit immobile load cell measured the friction force of a 5/8-inch brass electrode sliding across the film. The positive electrode was generally attached to the unattached electrode and the negative electrode was generally attached beneath the film. A 50 g weight was added to ensure proper starting contact. The film slid when a motor moved the film away from the load cell. A program was written in C++ to simultaneously automate the movement of the rig through an Arduino and to collect data from the load cell. The load cell output and leakage current are monitored before and during the application of the potential to the bound and free electrodes. The program starts with a 5 second baseline reading, then a specified charging period occurs (generally 30 s), at the start of which the desired potential is manually toggled. After

the charging period, the platform on which the bound electrode is mounted moves away from the load cell for a specified pull period. After the duration of the pulling period, the potential is manually toggled off and the platform then resets itself. The reset causes slack between the load cell and the mount for the electrode, and the apparatus is manually reset between runs.

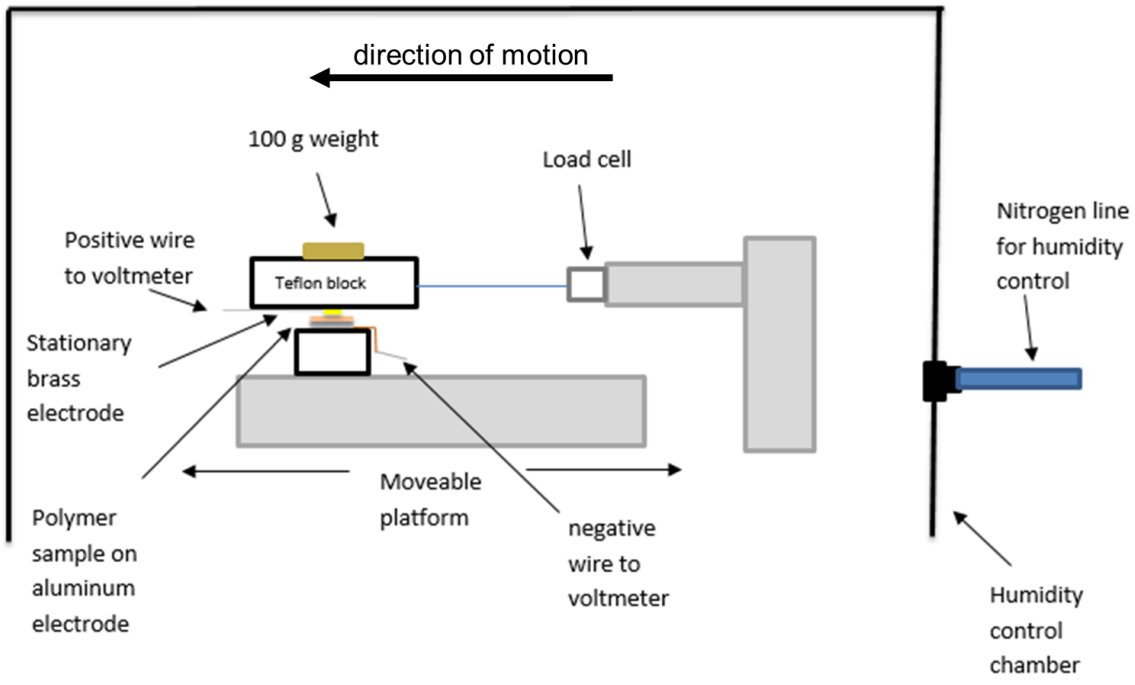

Figure 4.24: Shear testing apparatus. The film-electrode-on-glass slide sample was secured onto the testing apparatus, which sits above a movable platform.A second electrode, attached to a glass slide, was secured to an upper teflon block and placed atop the film. Contact was ensured by the placement of a 100 g brass weight atop the teflon block. Both electrodes were attached to a wire allowing for the addition of a current. At the start of the testing the moveable platform was pulled by a motor, and the force of the friction was measured by the load cell attached to the teflon block atop the upper electrode.

4.4.5 Raw data interpretation methodology

Data was output as load cell response vs. pull time in mS and the load cell response was converted to newtons through a load cell calibration. The force calculated is the static friction force using a load-cell calibration curve calculated by Jeff Auletta.

5 Future Directions

5.1 Crystallization Kinetics of POCB

Further studies have been conducted by the Velankar group to understand heterogeneous POCB-water cocrystallization[182] and work is in progress to understand the cocrystallization kinetics of POCB and water at varying molecular weights. However mechanistically there is still more work to be done with regards to developing a firm grasp of the molecular structures of the cocrystals. SAXS may be useful here to further investigate the structures. DSC could also potentially be used instead of dilatometers, which may help to monitor crystallization particularly at low temperatures, but is challenging due to possible loss of water.

5.2 POCB block copolymers

Moving forward on this project would consist of several goals, including further characterization, easier synthetic routes to allow for a greater range of products to be produced, preparation of the crystals to create monodisperse 1D cylinders, production of materials that do no aggregate, and the design of materials that can more seamlessly transition between the crystallized and micellized state, if possible. For the additional characterization small-angle X-ray scattering (SAXS) to measure the microphase separation would be interesting. To produce monodisperse, controlled length cylindrical micelles through living crystallization-driven self-assembly by seeding the crystallization with crystal fragments produced by sonication, for example.

A wider range of block ratios to make a phase diagram would also be ideal, but would require fine-tuning the synthesis to make it less time consuming. If one were to continue further with these specific block copolymers produced via click chemistry for medical applications, further synthetic methods would also have to be investigated to ensure the absence of copper. However, it may make the most sense to copolymerize the PEO-POCB block copolymers via the anionic ring-opening polymerization of both PEO and POCB together in the presence of triisobutyl aluminum activator, as previously performed by Gervais and coworkers[183]. While a click reaction has its advantages in that there are no by-products in the reaction, it is known that there are often poor yields for high molecular weight polymers unless the reaction conditions have been perfectly optimized[184], and it would be more time-effective to prepare the molecule the Gervais method. To perform a reaction from gaseous ethylene oxide, a student would be advised to receive training from a lab experienced in such reactions. This reaction setup should in theory reduce purification times and allow for a larger range of molecular weight ratios to be produced.

To produce distinct micelles above the melting temperature of the block copolymers instead of aggregates. The first attempt at this should be with making triblocks (PEO-POCB-PEO) as that is what has been successfully done for Pluronics micelles[185-186]. A triblock even for the same number of hydrophilic moieties is significantly more prone to micellization than a diblock[187]. Adjusting the preparation method (evaporation method, decreased concentration, etc), but while keeping the solution above the melting temperature may also help.

5.3 Electroadhesive materials

Limited studies in the literature regarding the oxidative degradation of polystyrene sulfonic acid and other polymer electrolytic membranes (PEMs) have yet to provide a definite oxidative degradation mechanism, though it is likely through the formation of a hydroxyl radical and could involve the complete dissociation of the styrene group[179]. Other studies point toward the dissolved electrode membrane as a catalyst for PEM degradation, and that carbons in PEMs could withstand potentials lower than 1.1 kV upon the removal of such catalytic metals.[177] One potential direction to further this study is to determine the cause of degradation.

Overall, there is leakage current present in both the sulfonated SEBS and the PEAA electroadhesives, and therefore moving forward oxidative protection of the film must be looked into. Using an antioxidant and using a more inert electrode are potential solutions, though the most practical would be a thin layer coating of an insulator covering the dielectric polymer.

With this type of work, one must keep in mind that almost all electronic components, such as batteries, have had years of fine-tuning to be of functional use, and still exhibit imperfect recharging. Thus, moving forward, one must have tempered expectations on how much progress can be made in the topic during one PhD, and anyone this project should not be aiming for perfection but rather for improvement.

6 Bibliography

1.Wei, M.; Gao, Y.; Li, X.; Serpe, M. J., Stimuli-responsive polymers and their applications. *Polymer Chemistry* **2017,** *8* (1), 127-143.

2.Yan, D.; Wang, Z.; Zhang, Z., Stimuli-responsive crystalline smart materials: from rational design and fabrication to applications. *Accounts of Chemical Research* **2022,** *55* (7), 1047-1058.

3.Wells, C. M.; Harris, M.; Choi, L.; Murali, V. P.; Guerra, F. D.; Jennings, J. A., Stimuli-responsive drug release from smart polymers. *Journal of functional biomaterials* **2019,** *10* (3), 34.

4.Zheng, Q.; Xu, C.; Jiang, Z.; Zhu, M.; Chen, C.; Fu, F., Smart actuators based on external stimulus response. *Frontiers in Chemistry* **2021,** *9*, 650358.

5.Kakida, H.; Makino, D.; Chatani, Y.; Kobayashi, M.; Tadokoro, H., Strutural Studies of Polyethers [-(CH2)mO-]n. VIII. Polyoxacyclobutane Hydrate (Modification I). *Macromolecules* **1970,** *3* (5), 569-578.

6.Banerjee, J.; Koronaios, P.; Morganstein, B.; Geib, S. J.; Enick, R. M.; Keith, J. A.; Beckman, E. J.; Velankar, S. S., Liquids That Freeze When Mixed: Cocrystallization and Liquid–Liquid Equilibrium in Polyoxacyclobutane–Water Mixtures. *Macromolecules* **2018,** *51* (8), 3176-3183.

7.Kakida, H.; Makino, D.; Chatani, Y.; Kobayashi, M.; Tadokoro, H., Strutural studies of polyethers [-(CH2) mO-] n. viii. polyoxacyclobutane hydrate (modification i). *Macromolecules* **1970,** *3* (5), 569-578.

8.Chatani, Y.; Kobatake, T.; Tadokoro, H., Structural studies of poly (ethylenimine). 3. Structural characterization of anhydrous and hydrous states and crystal structure of the hemihydrate. *Macromolecules* **1983,** *16* (2), 199-204.

9.Sasaki, S.; Takahashi, Y.; Tadokoro, H., Structural studies of polyformals. II. Crystal structure of poly-1,3-dioxolane: Modification II1. *Journal of Polymer Science: Polymer Physics Edition* **1972,** *10* (12), 2363-2378.

10.Alamo, R.; Fatou, J. G.; Guzmán, J., Crystallization of polyformals: 1. Crystallization kinetics of poly(1,3-dioxolane). *Polymer* **1982,** *23* (3), 374-378.

11.Benkhira, A.; Franta, E.; Francois, J., Polydioxolane in aqueous solutions. 1. Phase diagram. *Macromolecules* **1992,** *25* (21), 5697-5704.

12.Mandelkern, L., *Crystallization of polymers: volume 2, kinetics and mechanisms*. Cambridge University Press: 2004.

13.Armitstead, K.; Goldbeck-Wood, G.; Keller, A., Polymer crystallization theories. In *Macromolecules: Synthesis, Order and Advanced Properties*, Springer Berlin Heidelberg: Berlin, Heidelberg, 1992; pp 219-312.

14.MacFarlane, L.; Zhao, C.; Cai, J.; Qiu, H.; Manners, I., Emerging applications for living crystallization-driven self-assembly. *Chemical Science* **2021,** *12* (13), 4661-4682.

15.D'Elia, E.; Ahmed, H. S.; Feilden, E.; Saiz, E., Electrically-responsive graphene-based shape-memory composites. *Applied Materials Today* **2019,** *15*, 185-191.

16.Nucara, L.; Greco, F.; Mattoli, V., Electrically responsive photonic crystals: a review. *Journal of Materials Chemistry C* **2015,** *3* (33), 8449-8467.
17.Bansal, M.; Dravid, A.; Aqrawe, Z.; Montgomery, J.; Wu, Z.; Svirskis, D., Conducting polymer hydrogels for electrically responsive drug delivery. *Journal of Controlled Release* **2020,** *328,* 192-209.
18.Kong, L.; Chen, W., Carbon Nanotube and Graphene-based Bioinspired Electrochemical Actuators. *Advanced Materials* **2014,** *26* (7), 1025-1043.
19.Sogard, M. R.; Mikkelson, A. R.; Nataraju, M.; Turner, K. T.; Engelstad, R. L., Analysis of Coulomb and Johnsen-Rahbek electrostatic chuck performance for extreme ultraviolet lithography. *Journal of Vacuum Science & Technology B: Microelectronics and Nanometer Structures Processing, Measurement, and Phenomena* **2007,** *25* (6), 2155-2161.
20.Clark, E. J.; Hoffman, J. D., Regime III crystallization in polypropylene. *Macromolecules* **1984,** *17* (4), 878-885.
21.Sanchez, I. C.; DiMarzio, E. A., Dilute solution theory of polymer crystal growth: Fractionation effects. *Journal of Research of the National Bureau of Standards. Section A, Physics and Chemistry* **1972,** *76* (3), 213.
22.Hillig, W., A derivation of classical two-dimensional nucleation kinetics and the associated crystal growth laws. *Acta Metallurgica* **1966,** *14* (12), 1868-1869.
23.Zhang, M. C.; Guo, B.-H.; Xu, J., A review on polymer crystallization theories. *Crystals* **2016,** *7* (1), 4.
24.Lauritzen Jr, J. I., Effect of a finite substrate length upon polymer crystal lamellar growth rate. *Journal of Applied Physics* **1973,** *44* (10), 4353-4359.
25.Hoffman, J. D.; Guttman, C. M.; DiMarzio, E. A., On the problem of crystallization of polymers from the melt with chain folding. *Faraday Discussions of the Chemical Society* **1979,** *68,* 177-197.
26.Hoffman, J. D., Role of reptation in the rate of crystallization of polyethylene fractions from the melt. *Polymer* **1982,** *23* (5), 656-670.
27.Gates, D.; Westcott, M., Kinetics of polymer crystallization-II. Growth régimes. *Proceedings of the Royal Society of London. A. Mathematical and Physical Sciences* **1988,** *416* (1851), 463-476.
28.Hillig, W. B., A derivation of classical two-dimensional nucleation kinetics and the associated crystal growth laws. *Acta Metallurgica* **1966,** *14* (12), 1868-1869.
29.Hoffman, J. D.; Davis, G. T.; Lauritzen, J. I., The Rate of Crystallization of Linear Polymers with Chain Folding. In *Treatise on Solid State Chemistry: Volume 3 Crystalline and Noncrystalline Solids*, Hannay, N. B., Ed. Springer US: Boston, MA, 1976; pp 497-614.
30.Crist, B.; Schultz, J. M., Polymer spherulites: A critical review. *Progress in Polymer Science* **2016,** *56,* 1-63.
31.Keller, A., Polymer crystals. *Reports on progress in Physics* **1968,** *31* (2), 623.
32.Boistelle, R.; Astier, J., Crystallization mechanisms in solution. *Journal of crystal growth* **1988,** *90* (1-3), 14-30.
33.Zhang, S.; Han, J.; Gao, Y.; Guo, B.; Reiter, G.; Xu, J., Determination of the Critical Size of Secondary Nuclei on the Lateral Growth Front of Lamellar Polymer Crystals. *Macromolecules* **2019,** *52* (19), 7439-7447.
34.Evans, U., The laws of expanding circles and spheres in relation to the lateral growth of surface films and the grain-size of metals. *Transactions of the Faraday Society* **1945,** *41,* 365-374.

35.Lorenzo, A. T.; Arnal, M. L.; Albuerne, J.; Müller, A. J., DSC isothermal polymer crystallization kinetics measurements and the use of the Avrami equation to fit the data: Guidelines to avoid common problems. *Polymer Testing* **2007,** *26* (2), 222-231.
36.Pradell, T.; Crespo, D.; Clavaguera, N.; Clavaguera-Mora, M., Diffusion controlled grain growth in primary crystallization: Avrami exponents revisited. *Journal of Physics: Condensed Matter* **1998,** *10* (17), 3833.
37.Mandelkern, L., Crystallization kinetics of homopolymers:
bulk crystallization; mathematical formulation. In *Crystallization of Polymers: Volume 2, Kinetics and Mechanisms*, Cambridge University Press: 2004.
38.Tarallo, O., *Encyclopedia of Polymer Science and Technology*. 2002.
39.Guenet, J.-M., *Polymer-solvent molecular compounds*. Elsevier: 2010.
40.Malik, S.; Rochas, C.; Schmutz, M.; Guenet, J. M., Syndiotactic Polystyrene Intercalates from Naphthalene Derivatives. *Macromolecules* **2005,** *38* (14), 6024-6030.
41.Dasgupta, D.; Malik, S.; Thierry, A.; Guenet, J. M.; Nandi, A. K., Thermodynamics, Morphology, and Structure of the Poly(vinylidene fluoride)−Ethyl Acetoacetate System. *Macromolecules* **2006,** *39* (18), 6110-6114.
42.Tarallo, O.; Petraccone, V.; R. Albunia, A.; Daniel, C.; Guerra, G., Monoclinic and Triclinic δ-Clathrates of Syndiotactic Polystyrene. *Macromolecules* **2010,** *43* (20), 8549-8558.
43.Point, J. J.; Coutelier, C., Linear high polymers as host in intercalates. Introduction and example. *Journal of Polymer Science: Polymer Physics Edition* **1985,** *23* (1), 231-239.
44.Paternostre, L.; Damman, P.; Dosière, M., Metastabilities of lamellar crystals of molecular complexes. *Polymer* **1998,** *39* (19), 4579-4592.
45.Delaite, E.; Point, J. J.; Damman, P.; Dosiere, M., Two allotropic forms for the poly(ethylene oxide)-resorcinol molecular complex. *Macromolecules* **1992,** *25* (18), 4768-4778.
46.Wagner, J. F.; Dosière, M.; Guenet, J. M. In *Temperature-Concentration Phase Diagram of PEO-Urea*, Macromolecular Symposia, Wiley Online Library: 2005; pp 121-124.
47.Belfiore, L. A.; Lee, C. K.; Tang, J., The influence of competitive interactions on multiple eutectic phase behavior in poly (ethylene oxide) molecular complexes. *Polymer* **2003,** *44* (11), 3333-3346.
48.Xie, L.; Li, X.-j.; Xiong, Y.-z.; Chen, Q.; Xie, H.-b.; Zheng, Q., Can classic Avrami theory describe the isothermal crystallization kinetics for stereocomplex poly (lactic acid)? *Chinese Journal of Polymer Science* **2017,** *35* (6), 773-781.
49.Wunderlich, B., *Macromolecular Physics V2*. Elsevier: 2012; Vol. 2.
50.Mandelkern, L., Crystallization kinetics of polymer mixtures. In *Crystallization of Polymers: Volume 2, Kinetics and Mechanisms*, Cambridge University Press: 2004.
51.Cao, M.; Xu, J. T.; Dong, Q.; Fu, Z. S.; Fan, Z. Q., Crystallization kinetics and morphology of iso-PP/ethylene-propylene-b-copolymer/ethylene-propylene-r-copolymer ternary blends. *Iranian Polymer Journal (English)* **2009,** *18* (5 (107)), -.
52.Hwang, J. C.; Chen, C.-C.; Chen, H.-L.; Yang, W.-C. O., Analysis of two-stage crystallization kinetics for poly (ethylene terephthalate)/poly (ether imide) blends. *Polymer* **1997,** *38* (16), 4097-4101.
53.Huang, J.-W.; Chang, C.-C.; Kang, C.-C.; Yeh, M.-Y., Crystallization kinetics and nucleation parameters of Nylon 6 and poly (ethylene-co-glycidyl methacrylate) blend. *Thermochimica acta* **2008,** *468* (1-2), 66-74.
54.Zhang, M. C.; Guo, B.-H.; Xu, J., A review on polymer crystallization theories. *Crystals* **2017,** *7* (1), 4.

55.Piorkowska, E.; Galeski, A.; Haudin, J.-M., Critical assessment of overall crystallization kinetics theories and predictions. *Progress in Polymer Science* **2006,** *31* (6), 549-575.
56.Bruna, P.; Crespo, D.; González-Cinca, R.; Pineda, E., On the validity of Avrami formalism in primary crystallization. *Journal of Applied Physics* **2006,** *100* (5), 054907.
57.Zhang, S.; Han, J.; Gao, Y.; Guo, B.; Reiter, G. n.; Xu, J., Determination of the critical size of secondary nuclei on the lateral growth front of lamellar polymer crystals. *Macromolecules* **2019,** *52* (19), 7439-7447.
58.Kundagrami, A.; Muthukumar, M., Continuum theory of polymer crystallization. *The Journal of chemical physics* **2007,** *126* (14), 144901.
59.Sanchez, I. C.; DiMarzio, E. A., Dilute solution theory of polymer crystal growth: a kinetic theory of chain folding. *The Journal of Chemical Physics* **1971,** *55* (2), 893-908.
60.Sadler, D. M., New explanation for chain folding in polymers. *Nature* **1987,** *326* (6109), 174-177.
61.Sadler, D. M.; Gilmer, G. H., Selection of lamellar thickness in polymer crystal growth: a rate-theory model. *Physical Review B* **1988,** *38* (8), 5684.
62.Rodrigues, M.; Baptista, B.; Lopes, J. A.; Sarraguça, M. C., Pharmaceutical cocrystallization techniques. Advances and challenges. *International Journal of Pharmaceutics* **2018,** *547* (1), 404-420.
63.Nugrahani, I.; Utami, D.; Ibrahim, S.; Nugraha, Y. P.; Uekusa, H., Zwitterionic cocrystal of diclofenac and l-proline: structure determination, solubility, kinetics of cocrystallization, and stability study. *European Journal of Pharmaceutical Sciences* **2018,** *117*, 168-176.
64.Padrela, L.; Rodrigues, M. A.; Tiago, J. o.; Velaga, S. P.; Matos, H. A.; de Azevedo, E. G., Insight into the mechanisms of cocrystallization of pharmaceuticals in supercritical solvents. *Crystal Growth & Design* **2015,** *15* (7), 3175-3181.
65.Sarceviča, I.; Orola, L. n.; Nartowski, K. P.; Khimyak, Y. Z.; Round, A. N.; Fábián, L., Mechanistic and Kinetic Insight into Spontaneous Cocrystallization of Isoniazid and Benzoic Acid. *Molecular Pharmaceutics* **2015,** *12* (8), 2981-2992.
66.Zhong, Z.; Guo, C.; Yang, X.; Guo, B.; Xu, J.; Huang, Y., Drug molecule diflunisal forms crystalline inclusion complexes with multiple types of linear polymers. *Crystal Growth & Design* **2016,** *16* (3), 1181-1186.
67.Qiu, S.; Lai, J.; Guo, M.; Wang, K.; Lai, X.; Desai, U.; Juma, N.; Li, M., Role of polymers in solution and tablet-based carbamazepine cocrystal formulations. *CrystEngComm* **2016,** *18* (15), 2664-2678.
68.Xanthopoulou, M.; Giliopoulos, D.; Tzollas, N.; Triantafyllidis, K. S.; Kostoglou, M.; Katsoyiannis, I. A., Phosphate removal using polyethylenimine functionalized silica-based materials. *Sustainability* **2021,** *13* (3), 1502.
69.Thakur, A. K.; Nisola, G. M.; Limjuco, L. A.; Parohinog, K. J.; Torrejos, R. E. C.; Shahi, V. K.; Chung, W.-J., Polyethylenimine-modified mesoporous silica adsorbent for simultaneous removal of Cd(II) and Ni(II) from aqueous solution. *Journal of Industrial and Engineering Chemistry* **2017,** *49*, 133-144.
70.Tang, Y.; Li, M.; Mu, C.; Zhou, J.; Shi, B., Ultrafast and efficient removal of anionic dyes from wastewater by polyethyleneimine-modified silica nanoparticles. *Chemosphere* **2019,** *229*, 570-579.
71.Bhatnagar, V., Clathrates of urea and thiourea. *Journal of Structural Chemistry* **1968,** *8* (3), 513-529.

72.Harada, A.; Li, J.; Kamachi, M., Double-stranded inclusion complexes of cyclodextrin threaded on poly (ethylene glycol). *Nature* **1994,** *370* (6485), 126-128.
73.Manfredi, C.; Del Nobile, M.; Mensitieri, G.; Guerra, G.; Rapacciuolo, M., Vapor sorption in emptied clathrate samples of syndiotactic polystyrene. *Journal of Polymer Science Part B: Polymer Physics* **1997,** *35* (1), 133-140.
74.Balijepalli, S.; Schultz, J.; Lin, J., Phase behavior and morphology of poly (ethylene oxide) blends. *Macromolecules* **1996,** *29* (20), 6601-6611.
75.Jiang, X.; Li, T.; Hu, W., Understanding the Growth Rates of Polymer Cocrystallization in the Binary Mixtures of Different Chain Lengths: Revisited. *The Journal of Physical Chemistry B* **2015,** *119* (30), 9975-9981.
76.Pal, S.; Nandi, A. K., Cocrystallization mechanism of poly (3-hexyl thiophenes) with different amount of chain regioregularity. *Journal of Applied Polymer Science* **2006,** *101* (6), 3811-3820.
77.Datta, J.; Nandi, A. K., Cocrystallization mechanism of vinylidene fluoride-tetrafluoroethylene copolymers with different copolymer composition. *Macromolecular Chemistry and Physics* **1998,** *199* (11), 2583-2588.
78.Schneider, C. A.; Rasband, W. S.; Eliceiri, K. W., NIH Image to ImageJ: 25 years of image analysis. *Nature Methods* **2012,** *9* (7), 671-675.
79.Iwamatsu, M., Direct numerical simulation of homogeneous nucleation and growth in a phase-field model using cell dynamics method. *The Journal of chemical physics* **2008,** *128* (8), 084504.
80.Deshpande, V.; Jape, S., Isothermal crystallization kinetics of anhydrous sodium acetate nucleated poly (ethylene terephthalate). *Journal of applied polymer science* **2010,** *116* (6), 3541-3554.
81.Inoue, M., Crystallization and melting of copolymers of polyoxymethylene. *Journal of Applied Polymer Science* **1964,** *8* (5), 2225-2238.
82.Hoffman, J. D.; Frolen, L. J.; Ross, G. S.; Lauritzen Jr, J. I., On the growth rate of spherulites and axialites from the melt in polyethylene fractions: regime I and regime II crystallization. *Journal of research of the National Bureau of Standards. Section A, Physics and chemistry* **1975,** *79* (6), 671.
83.Lauritzen Jr, J. I.; Hoffman, J. D., Extension of theory of growth of chain-folded polymer crystals to large undercoolings. *Journal of applied Physics* **1973,** *44* (10), 4340-4352.
84.Rice, S. A., *Advances in chemical physics. Volume 128*. Wiley [etc.]: New York, 2004.
85.Allen, R. C.; Mandelkern, L., On regimes I and II during polymer crystallization. *Polymer Bulletin* **1987,** *17* (5), 473-480.
86.Keith, H. D.; Padden, F. J., A Phenomenological Theory of Spherulitic Crystallization. *Journal of Applied Physics* **1963,** *34* (8), 2409-2421.
87.Couder, Y.; Maurer, J.; González-Cinca, R.; Hernández-Machado, A., Side-branch growth in two-dimensional dendrites. I. Experiments. *Physical Review E* **2005,** *71* (3), 031602.
88.Rose, J. B., 111. Cationic polymerisation of oxacyclobutanes. Part I. *Journal of the Chemical Society (Resumed)* **1956,** (0), 542-546.
89.Farthing, A. C.; Reynolds, R. J. W., Synthesis and properties of a new polyether: Poly-3,3-bis(chloromethyl)-1-oxabutene. *Journal of Polymer Science* **1954,** *12* (1), 503-507.
90.Dreyfuss, M. P.; Dreyfuss, P., In *Encyclopedia of Polymer Science and Technology*, Mark, H. F. B., N; Overberger, C G; Menges, G; Kroschwitz, J I, Ed. United States, 1987; Vol. 10, p 653.
91.Parzuchowski, P.; Mamiński, M. Ł., Poly-(3-ethyl-3-hydroxymethyl)oxetanes—Synthesis and Adhesive Interactions with Polar Substrates. *Polymers* **2020,** *12* (1), 222.

92.González, C. C.; Bello, A.; Pereña, J. M., Oligomerization of oxetane and synthesis of polyterephthalates derived from 1,3-propanediol and 3,3′-oxydipropanol. *Die Makromolekulare Chemie* **1989,** *190* (6), 1217-1224.
93.Desai, H.; Cunliffe, A. V.; Stewart, M. J.; Amass, A. J., Synthesis of narrow molecular weight distribution α,ω-hydroxy telechelic polyoxetane by the activated monomer mechanism. *Polymer* **1993,** *34* (3), 642-645.
94.Velvetol: The sustainable alternative to petrochemicals https://www.chemanager-online.com/en/products/velvetol-sustainable-alternative-petrochemicals.
95.Webwire Putting Science to Work: DuPont™ Cerenol™ Made From 100% Renewable Resources. https://www.webwire.com/ViewPressRel.asp?aId=38211.
96.Labbé, A.; Carlotti, S.; Billouard, C.; Desbois, P.; Deffieux, A., Controlled High-Speed Anionic Polymerization of Propylene Oxide Initiated by Onium Salts in the Presence of Triisobutylaluminum. *Macromolecules* **2007,** *40* (22), 7842-7847.
97.Billouard, C.; Carlotti, S.; Desbois, P.; Deffieux, A., "Controlled" High-Speed Anionic Polymerization of Propylene Oxide Initiated by Alkali Metal Alkoxide/Trialkylaluminum Systems. *Macromolecules* **2004,** *37* (11), 4038-4043.
98.Schmitt, B.; Stauf, W.; Müller, H. E., Anionic Polymerization of (Meth)acrylates in the Presence of Cesium Halide−Trialkylaluminum Complexes in Toluene. *Macromolecules* **2001,** *34* (6), 1551-1557.
99.Gervais, M.; Forens, A.; Ibarboure, E.; Carlotti, S., Anionic polymerization of activated oxetane and its copolymerization with ethylene oxide for the synthesis of amphiphilic block copolymers. *Polymer Chemistry* **2018,** *9* (19), 2660-2668.
100.Luan, B.; Yuan, Q.; Pan, C.-Y., Synthesis and Characterization of Poly(trimethylene oxide)-block-Polystyrene and Poly(trimethylene oxide)-block-Polystyrene-block-Poly(methyl methacrylate) by Combination of Atom Transfer Radical Polymerization (ATRP) and Cationic Ring-Opening Polymerization (CROP). *Macromolecular Chemistry and Physics* **2004,** *205* (15), 2097-2104.
101.Vandenberg, E. J.; Robinson, A. E., Coordination Polymerization of Trimethylene Oxide. In *Polyethers*, American Chemical Society: 1975; Vol. 6, pp 101-119.
102.Kanazawa, A.; Aoshima, S., Cationic Terpolymerization of Vinyl Ethers, Oxetane, and Ketones via Concurrent Vinyl-Addition, Ring-Opening, and Carbonyl-Addition Mechanisms: Multiblock Polymer Synthesis and Mechanistic Investigation. *Macromolecules* **2017,** *50* (17), 6595-6605.
103.Diaz, C.; Ebrahimi, T.; Mehrkhodavandi, P., Cationic indium complexes for the copolymerization of functionalized epoxides with cyclic ethers and lactide. *Chemical Communications* **2019,** *55* (23), 3347-3350.
104.Mørkeseth, H.; Sørensen, S. H. *Fremstilling av TPEG, og herding og karakterisering av TPEG-baserte polymermatriser*; 824643246X; 2020.
105.Penczek, S.; Cypryk, M.; Duda, A.; Kubisa, P.; Słomkowski, S., Living ring-opening polymerizations of heterocyclic monomers. *Progress in Polymer Science* **2007,** *32* (2), 247-282.
106.Oguni, N.; Kamachi, M.; Stille, J. K., Spontaneous Cohabitory Anionic Polymerization of Vinylidene Cyanide and Cationic Polymerization of Cyclic Ethers on Mixing the Two Monomers at 25°. *Macromolecules* **1974,** *7* (4), 435-439.

107.Crivello, J. V.; Fan, M., Catalysis of ring-opening and vinyl polymerizations by dicobaltoctacarbonyl. *Journal of Polymer Science Part A: Polymer Chemistry* **1992,** *30* (1), 31-39.
108.Adams, M. L.; Lavasanifar, A.; Kwon, G. S., Amphiphilic block copolymers for drug delivery. *Journal of Pharmaceutical Sciences* **2003,** *92* (7), 1343-1355.
109.Rösler, A.; Vandermeulen, G. W.; Klok, H.-A., Advanced drug delivery devices via self-assembly of amphiphilic block copolymers. *Advanced drug delivery reviews* **2012,** *64*, 270-279.
110.Alexandridis, P.; Lindman, B., *Amphiphilic block copolymers: self-assembly and applications*. Elsevier: 2000.
111.Holder, S. J.; Sommerdijk, N. A., New micellar morphologies from amphiphilic block copolymers: disks, toroids and bicontinuous micelles. *Polymer Chemistry* **2011,** *2* (5), 1018-1028.
112.Geng, Y.; Dalhaimer, P.; Cai, S.; Tsai, R.; Tewari, M.; Minko, T.; Discher, D. E., Shape effects of filaments versus spherical particles in flow and drug delivery. *Nature nanotechnology* **2007,** *2* (4), 249-55.
113.Zhang, K.; Fang, H.; Chen, Z.; Taylor, J.-S. A.; Wooley, K. L., Shape Effects of Nanoparticles Conjugated with Cell-Penetrating Peptides (HIV Tat PTD) on CHO Cell Uptake. *Bioconjugate Chemistry* **2008,** *19* (9), 1880-1887.
114.Zhang, K.; Rossin, R.; Hagooly, A.; Chen, Z.; Welch, M. J.; Wooley, K. L., Folate-mediated cell uptake of shell-crosslinked spheres and cylinders. *Journal of Polymer Science Part A: Polymer Chemistry* **2008,** *46* (22), 7578-7583.
115.Harada, A.; Kataoka, K., Supramolecular assemblies of block copolymers in aqueous media as nanocontainers relevant to biological applications. *Progress in Polymer Science* **2006,** *31* (11), 949-982.
116.Petzetakis, N.; Dove, A. P.; O'Reilly, R. K., Cylindrical micelles from the living crystallization-driven self-assembly of poly (lactide)-containing block copolymers. *Chemical Science* **2011,** *2* (5), 955-960.
117.Ma, J.-h.; Guo, C.; Tang, Y.-l.; Liu, H.-z., 1H NMR Spectroscopic Investigations on the Micellization and Gelation of PEO−PPO−PEO Block Copolymers in Aqueous Solutions. *Langmuir* **2007,** *23* (19), 9596-9605.
118.Hopkins, C. C.; de Bruyn, J. R., Gelation and long-time relaxation of aqueous solutions of Pluronic F127. *Journal of Rheology* **2019,** *63* (1), 191-201.
119.Hamley, I. W., Crystallization in Block Copolymers. In *Interfaces Crystallization Viscoelasticity*, Springer Berlin Heidelberg: Berlin, Heidelberg, 1999; pp 113-137.
120.Loo, Y.-L.; Register, R. A.; Ryan, A. J., Modes of crystallization in block copolymer microdomains: breakout, templated, and confined. *Macromolecules* **2002,** *35* (6), 2365-2374.
121.Schmelz, J.; Karg, M.; Hellweg, T.; Schmalz, H., General pathway toward crystalline-core micelles with tunable morphology and corona segregation. *ACS nano* **2011,** *5* (12), 9523-9534.
122.Wang, X.; Guerin, G.; Wang, H.; Wang, Y.; Manners, I.; Winnik, M. A., Cylindrical block copolymer micelles and co-micelles of controlled length and architecture. *science* **2007,** *317* (5838), 644-647.
123.Gilroy, J. B.; Gädt, T.; Whittell, G. R.; Chabanne, L.; Mitchels, J. M.; Richardson, R. M.; Winnik, M. A.; Manners, I., Monodisperse cylindrical micelles by crystallization-driven living self-assembly. *Nature chemistry* **2010,** *2* (7), 566-570.
124.McGrath, N.; Patil, A. J.; Watson, S. M. D.; Horrocks, B. R.; Faul, C. F. J.; Houlton, A.; Winnik, M. A.; Mann, S.; Manners, I., Conductive, Monodisperse Polyaniline Nanofibers of

Controlled Length Using Well-Defined Cylindrical Block Copolymer Micelles as Templates. *Chemistry – A European Journal* **2013,** *19* (39), 13030-13039.
125.Kabanov, A. V.; Batrakova, E. V.; Alakhov, V. Y., Pluronic® block copolymers as novel polymer therapeutics for drug and gene delivery. *Journal of controlled release* **2002,** *82* (2-3), 189-212.
126.Altinok, H.; Yu, G.-E.; Nixon, S. K.; Gorry, P. A.; Attwood, D.; Booth, C., Effect of Block Architecture on the Self-Assembly of Copolymers of Ethylene Oxide and Propylene Oxide in Aqueous Solution. *Langmuir* **1997,** *13* (22), 5837-5848.
127.Su, Y.-l.; Wang, J.; Liu, H.-z., Formation of a Hydrophobic Microenvironment in Aqueous PEO−PPO−PEO Block Copolymer Solutions Investigated by Fourier Transform Infrared Spectroscopy. *The Journal of Physical Chemistry B* **2002,** *106* (45), 11823-11828.
128.Wanka, G.; Hoffmann, H.; Ulbricht, W., Phase Diagrams and Aggregation Behavior of Poly(oxyethylene)-Poly(oxypropylene)-Poly(oxyethylene) Triblock Copolymers in Aqueous Solutions. *Macromolecules* **1994,** *27* (15), 4145-4159.
129.Wu, G.; Zhou, Z.; Chu, B., Water-induced micelle formation of block copoly(oxyethylene-oxypropylene-oxyethylene) in o-xylene. *Macromolecules* **1993,** *26* (8), 2117-2125.
130.Yang, Y.-W.; Deng, N.-J.; Yu, G.-E.; Zhou, Z.-K.; Attwood, D.; Booth, C., Micellization of Diblock and Triblock Copolymers in Aqueous Solution. New Results for Oxyethylene/ Oxybutylene Copolymers E38B12 and E21B11E21. Comparison of Oxyethylene/Oxybutylene, Oxyethylene/Oxypropylene, and Oxyethylene/Alkyl Systems. *Langmuir* **1995,** *11* (12), 4703-4711.
131.Russo, P., A Practical Minicourse in Dynamic Light Scattering. https://macro.lsu.edu/howto/, 2012. https://macro.lsu.edu/howto/DLS_Minicourse/DLS_Minicourse.pdf.
132.Hiki, S.; Kataoka, K., Versatile and Selective Synthesis of "Click Chemistry" Compatible Heterobifunctional Poly(ethylene glycol)s Possessing Azide and Alkyne Functionalities. *Bioconjugate Chemistry* **2010,** *21* (2), 248-254.
133.Carlotti, S.; Billouard, C.; Gautriaud, E.; Desbois, P.; Deffieux, A., Activation Mechanisms of Trialkylaluminum in Alkali Metal Alkoxides or Tetraalkylammonium Salts / Propylene Oxide Controlled Anionic Polymerization. *Macromolecular Symposia* **2005,** *226* (1), 61-68.
134.Li, Y.; Hoskins, J. N.; Sreerama, S. G.; Grayson, S. M., MALDI−TOF Mass Spectral Characterization of Polymers Containing an Azide Group: Evidence of Metastable Ions. *Macromolecules* **2010,** *43* (14), 6225-6228.
135.Goswami, L. N.; Houston, Z. H.; Sarma, S. J.; Jalisatgi, S. S.; Hawthorne, M. F., Efficient synthesis of diverse heterobifunctionalized clickable oligo (ethylene glycol) linkers: potential applications in bioconjugation and targeted drug delivery. *Organic & biomolecular chemistry* **2013,** *11* (7), 1116-1126.
136.Stone, R.; Qi, B.; Trebatoski, D.; Jetti, R.; Bandera, Y.; Foulger, S.; Mefford, O., A versatile stable platform for multifunctional applications: synthesis of a nitroDOPA–PEO–alkyne scaffold for iron oxide nanoparticles. *Journal of Materials Chemistry B* **2014,** *2* (30), 4789-4793.
137.Lu, C.; Zhong, W., Synthesis of propargyl-terminated heterobifunctional poly (ethylene glycol). *Polymers* **2010,** *2* (4), 407-417.
138.Ochs, J.; Veloso, A.; Martínez-Tong, D. E.; Alegria, A.; Barroso-Bujans, F., An Insight into the Anionic Ring-Opening Polymerization with Tetrabutylammonium Azide for the Generation of Pure Cyclic Poly(glycidyl phenyl ether). *Macromolecules* **2018,** *51* (7), 2447-2455.

139.Makino, D.; Kobayashi, M.; Tadokoro, H., Structural Studies of Polyethers, [–(CH2)m–O–]n. VII. Infrared Spectra of Polyoxacyclobutane. *The Journal of Chemical Physics* **1969,** *51* (9), 3901-3916.
140.Barker, E. F.; Banerjee, S.; Meyer, T. Y.; Velankar, S., Liquids that Freeze when Mixed: Homogeneous Cocrystallization Kinetics of Polyoxacyclobutane–Water Hydrate. *ACS Applied Polymer Materials* **2022,** *4* (1), 703-713.
141.Hsiao, M.-S.; Yusoff, S. F. M.; Winnik, M. A.; Manners, I., Crystallization-driven self-assembly of block copolymers with a short crystallizable core-forming segment: controlling micelle morphology through the influence of molar mass and solvent selectivity. *Macromolecules* **2014,** *47* (7), 2361-2372.
142.Lendlein, A.; Shastri, V. P., Stimuli-Sensitive Polymers. *Advanced materials* **2010,** *22* (31), 3344-3347.
143.De las Heras Alarcón, C.; Pennadam, S.; Alexander, C., Stimuli responsive polymers for biomedical applications. *Chemical Society Reviews* **2005,** *34* (3), 276-285.
144.Stuart, M. A. C.; Huck, W. T.; Genzer, J.; Müller, M.; Ober, C.; Stamm, M.; Sukhorukov, G. B.; Szleifer, I.; Tsukruk, V. V.; Urban, M., Emerging applications of stimuli-responsive polymer materials. *Nature materials* **2010,** *9* (2), 101-113.
145.Auletta, J. T.; LeDonne, G. J.; Gronborg, K. C.; Ladd, C. D.; Liu, H.; Clark, W. W.; Meyer, T. Y., Stimuli-Responsive Iron-Cross-Linked Hydrogels That Undergo Redox-Driven Switching between Hard and Soft States. *Macromolecules* **2015,** *48* (6), 1736-1747.
146.Harris, R. D.; Auletta, J. T.; Motlagh, S. A. M.; Lawless, M. J.; Perri, N. M.; Saxena, S.; Weiland, L. M.; Waldeck, D. H.; Clark, W. W.; Meyer, T. Y., Chemical and Electrochemical Manipulation of Mechanical Properties in Stimuli-Responsive Copper-Cross-Linked Hydrogels. *ACS Macro Letters* **2013,** *2* (12), 1095-1099.
147.Calvo-Marzal, P.; Delaney, M. P.; Auletta, J. T.; Pan, T.; Perri, N. M.; Weiland, L. M.; Waldeck, D. H.; Clark, W. W.; Meyer, T. Y., Manipulating Mechanical Properties with Electricity: Electroplastic Elastomer Hydrogels. *ACS Macro Letters* **2012,** *1* (1), 204-208.
148.Elabd, Y. A.; Napadensky, E.; Walker, C. W.; Winey, K. I., Transport properties of sulfonated poly (styrene-b-isobutylene-b-styrene) triblock copolymers at high ion-exchange capacities. *Macromolecules* **2006,** *39* (1), 399-407.
149.Shultz, C. D.; Peshkin, M. A.; Colgate, J. E. In *Surface haptics via electroadhesion: Expanding electrovibration with Johnsen and Rahbek*, 2015 IEEE World Haptics Conference (WHC), 22-26 June 2015; 2015; pp 57-62.
150.Johnsen, A.; Rahbek, K., A physical phenomenon and its applications to telegraphy, telephony, etc. *Electrical Engineers, Journal of the Institution of* **1923,** *61* (320), 713-725.
151.Abraham Simpson, C.; Sarah, B., A comparison of critical shear force in low-voltage, all-polymer electroadhesives to a basic friction model. *Smart Materials and Structures* **2017,** *26* (2), 025028.
152.Shim, G. I.; Sugai, H., Dechuck Operation of Coulomb Type and Johnsen-Rahbek Type of Electrostatic Chuck Used in Plasma Processing. *Plasma and Fusion Research* **2008,** *3*, 051-051.
153.Krahn, J.; Menon, C., Electro-dry-adhesion. *Langmuir* **2012,** *28* (12), 5438-5443.
154.Mullenbach, J.; Peshkin, M.; Colgate, J. E., eShiver: Lateral Force Feedback on Fingertips through Oscillatory Motion of an Electroadhesive Surface. *IEEE Transactions on Haptics* **2016,** *PP* (99), 1-1.
155.Asano, K.; Hatakeyama, F.; Yatsuzuka, K., Fundamental study of an electrostatic chuck for silicon wafer handling. *IEEE Transactions on Industry Applications* **2002,** *38* (3), 840-845.

156.Jeonghoon, Y.; Jae-Seok, C.; Sang-Joon, H.; Tae-Hyun, K.; Sung Jin, L. In *Finite element analysis of the attractive force on a Coulomb type electrostatic chuck*, Electrical Machines and Systems, 2007. ICEMS. International Conference on, 8-11 Oct. 2007; 2007; pp 1371-1375.
157.Qin, S.; McTeer, A., Wafer dependence of Johnsen–Rahbek type electrostatic chuck for semiconductor processes. *Journal of Applied Physics* **2007,** *102* (6), 064901.
158.Sogard, M. R.; Mikkelson, A. R.; Nataraju, M.; Turner, K. T.; Engelstad, R. L., Analysis of Coulomb and Johnsen-Rahbek electrostatic chuck performance for extreme ultraviolet lithography. *Journal of Vacuum Science & Technology B* **2007,** *25* (6), 2155-2161.
159.Cao, C.; Sun, X.; Fang, Y.; Qin, Q.-H.; Yu, A.; Feng, X.-Q., Theoretical model and design of electroadhesive pad with interdigitated electrodes. *Materials & Design* **2016,** *89*, 485-491.
160.Shintake, J.; Rosset, S.; Schubert, B.; Floreano, D.; Shea, H., Versatile Soft Grippers with Intrinsic Electroadhesion Based on Multifunctional Polymer Actuators. *Advanced Materials* **2016,** *28* (2), 231-238.
161.Kanno, S.; Kato, K.; Yoshioka, K.; Nishio, R.; Tsubone, T., Prediction of clamping pressure in a Johnsen-Rahbek-type electrostatic chuck based on circuit simulation. *Journal of Vacuum Science & Technology B* **2006,** *24* (1), 216-223.
162.Tant, M. R.; Mauritz, K. A.; Wilkes, G. L., *Ionomers: synthesis, structure, properties and applications*. Springer Science & Business Media: 2012.
163.Weiss, R.; Sen, A.; Willis, C.; Pottick, L., Block copolymer ionomers: 1. Synthesis and physical properties of sulphonated poly (styrene-ethylene/butylene-styrene). *Polymer* **1991,** *32* (10), 1867-1874.
164.Elabd, Y. A.; Hickner, M. A., Block Copolymers for Fuel Cells. *Macromolecules* **2011,** *44* (1), 1-11.
165.Chikashige, Y.; Chikyu, Y.; Miyatake, K.; Watanabe, M., Poly (arylene ether) ionomers containing sulfofluorenyl groups for fuel cell applications. *Macromolecules* **2005,** *38* (16), 7121-7126.
166.Schuster, M.; Kreuer, K.-D.; Andersen, H. T.; Maier, J., Sulfonated poly (phenylene sulfone) polymers as hydrolytically and thermooxidatively stable proton conducting ionomers. *Macromolecules* **2007,** *40* (3), 598-607.
167.Mauritz, K. A.; Moore, R. B., State of Understanding of Nafion. *Chemical Reviews* **2004,** *104* (10), 4535-4586.
168.Tierney, N. K.; Register, R. A., Ion hopping in ethylene− methacrylic acid ionomer melts as probed by rheometry and cation diffusion measurements. *Macromolecules* **2002,** *35* (6), 2358-2364.
169.Serpico, J. M.; Ehrenberg, S. G.; Fontanella, J. J.; Jiao, X.; Perahia, D.; McGrady, K. A.; Sanders, E. H.; Kellogg, G. E.; Wnek, G. E., Transport and Structural Studies of Sulfonated Styrene−Ethylene Copolymer Membranes. *Macromolecules* **2002,** *35* (15), 5916-5921.
170.Jang, S. S.; Molinero, V.; Çağın, T.; Goddard, W. A., Nanophase-Segregation and Transport in Nafion 117 from Molecular Dynamics Simulations: Effect of Monomeric Sequence. *The Journal of Physical Chemistry B* **2004,** *108* (10), 3149-3157.
171.Devanathan, R.; Venkatnathan, A.; Dupuis, M., Atomistic Simulation of Nafion Membrane: I. Effect of Hydration on Membrane Nanostructure. *The Journal of Physical Chemistry B* **2007,** *111* (28), 8069-8079.
172.Elabd, Y. A.; Napadensky, E., Sulfonation and characterization of poly(styrene-isobutylene-styrene) triblock copolymers at high ion-exchange capacities. *Polymer* **2004,** *45* (9), 3037-3043.

173.Rockland, L. B., Saturated salt solutions for static control of relative humidity between 5° and 40° C. *Analytical Chemistry* **1960,** *32* (10), 1375-1376.
174.Greenspan, L., Humidity fixed points of binary saturated aqueous solutions. *Journal of research of the national bureau of standards* **1977,** *81* (1), 89-96.
175.Lundberg, R. D.; Makowski, H. S., Solution behavior of ionomers. I. Metal sulfonate ionomers in mixed solvents. *Journal of Polymer Science: Polymer Physics Edition* **1980,** *18* (8), 1821-1836.
176.Schaaf, P.; Schlenoff, J. B., Saloplastics: processing compact polyelectrolyte complexes. *Advanced Materials* **2015,** *27* (15), 2420-2432.
177.Wu, J.; Yuan, X. Z.; Martin, J. J.; Wang, H.; Zhang, J.; Shen, J.; Wu, S.; Merida, W., A review of PEM fuel cell durability: Degradation mechanisms and mitigation strategies. *Journal of Power Sources* **2008,** *184* (1), 104-119.
178.Büchi, F. N.; Gupta, B.; Haas, O.; Scherer, G. G., Study of radiation-grafted FEP-G-polystyrene membranes as polymer electrolytes in fuel cells. *Electrochimica Acta* **1995,** *40* (3), 345-353.
179.Mattsson, B.; Ericson, H.; Torell, L. M.; Sundholm, F., Degradation of a fuel cell membrane, as revealed by micro-Raman spectroscopy. *Electrochimica Acta* **2000,** *45* (8), 1405-1408.
180.Watanabe, T.; Kitabayashi, T.; Nakayama, C., Relationship between electrical resistivity and electrostatic force of alumina electrostatic chuck. *Japanese journal of applied physics* **1993,** *32* (2R), 864.
181.Stuckes, A. D. Some theoretical and practical considerations of the Johnsen-Rahbek effect *Proceedings of the IEE - Part B: Radio and Electronic Engineering* [Online], 1956, p. 125-131. http://digital-library.theiet.org/content/journals/10.1049/pi-b-1.1956.0128.
182.Banerjee, S.; Gresh-Sill, M.; Barker, E. F.; Meyer, T. Y.; Velankar, S. S., Polymer co-crystallization from LLE: Crystallization kinetics of POCB hydrate from two-phase mixtures of POCB and water. *Polymer* **2023,** *282*, 126087.
183.Gervais, M.; Labbé, A.; Carlotti, S.; Deffieux, A., Direct Synthesis of α-Azido,ω-hydroxypolyethers by Monomer-Activated Anionic Polymerization. *Macromolecules* **2009,** *42* (7), 2395-2400.
184.Pickens, C. J.; Johnson, S. N.; Pressnall, M. M.; Leon, M. A.; Berkland, C. J., Practical Considerations, Challenges, and Limitations of Bioconjugation via Azide–Alkyne Cycloaddition. *Bioconjugate Chemistry* **2018,** *29* (3), 686-701.
185.Kadam, Y.; Yerramilli, U.; Bahadur, A.; Bahadur, P., Micelles from PEO-PPO-PEO block copolymers as nanocontainers for solubilization of a poorly water soluble drug hydrochlorothiazide. *Colloids Surf B Biointerfaces* **2011,** *83* (1), 49-57.
186.Wang, Y.; Li, Y.; Zhang, L.; Fang, X., Pharmacokinetics and biodistribution of paclitaxel-loaded pluronic P105 polymeric micelles. *Archives of Pharmacal Research* **2008,** *31* (4), 530-538.
187.Panagiotopoulos, A. Z.; Floriano, M. A.; Kumar, S. K., Micellization and Phase Separation of Diblock and Triblock Model Surfactants. *Langmuir* **2002,** *18* (7), 2940-2948.

Appendix A Characterization

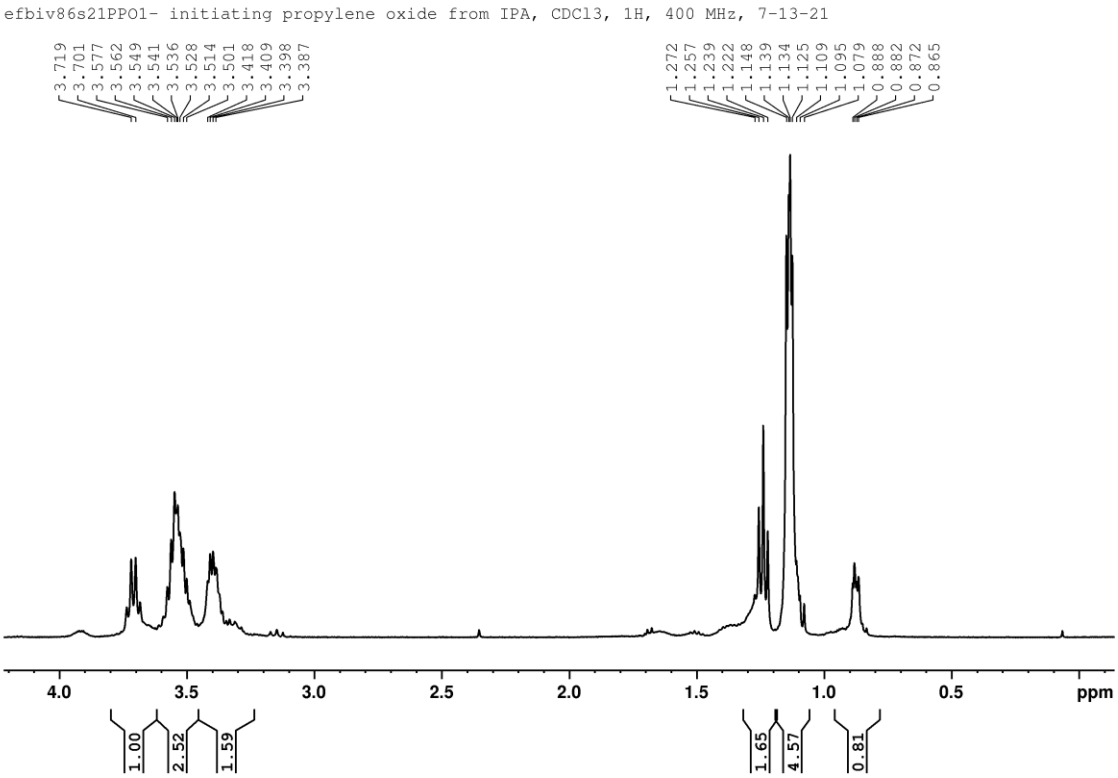

Figure A.1: PPO from IPA ^{1}H

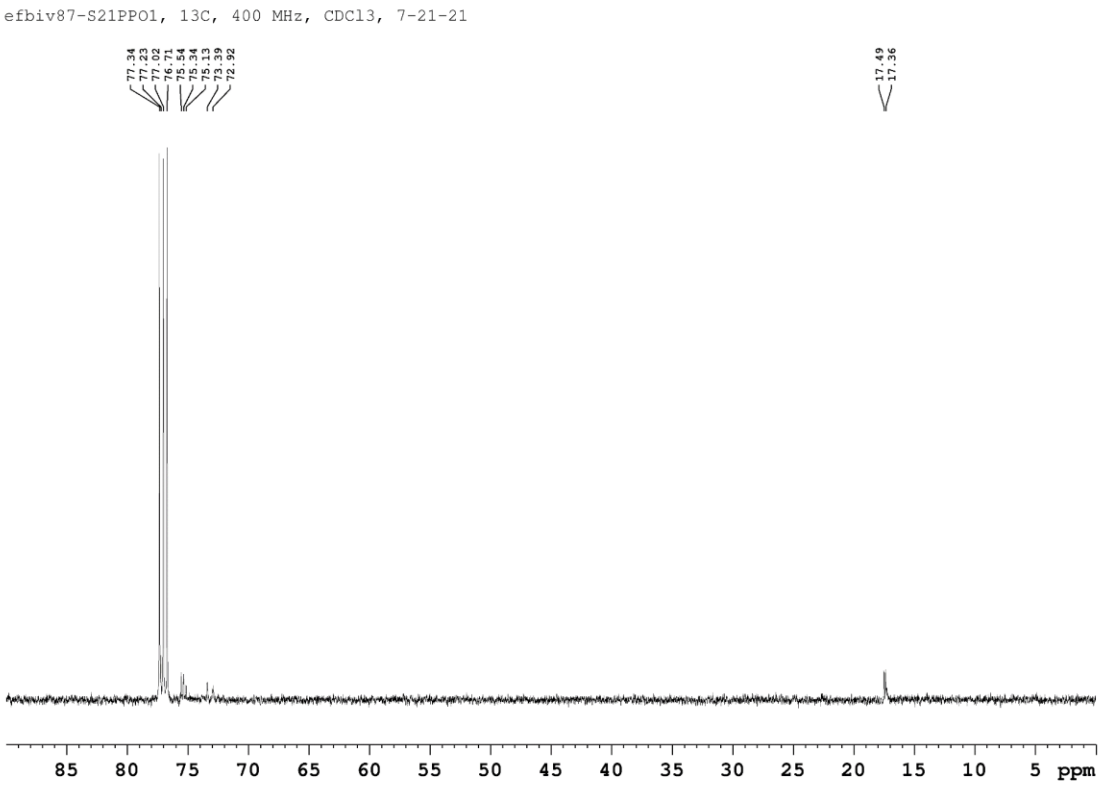

Figure A.2: PPO from IPA ^{13}C

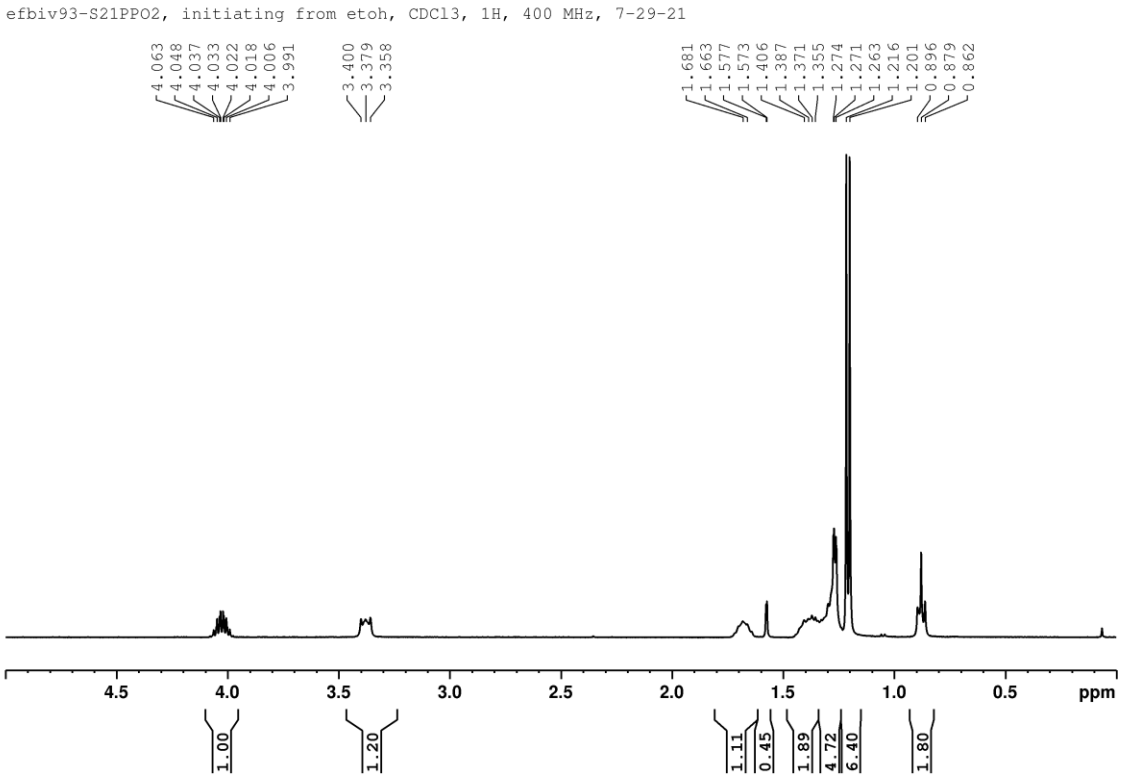

Figure A.3: PPO from EtOH, failed reaction, ^{1}H

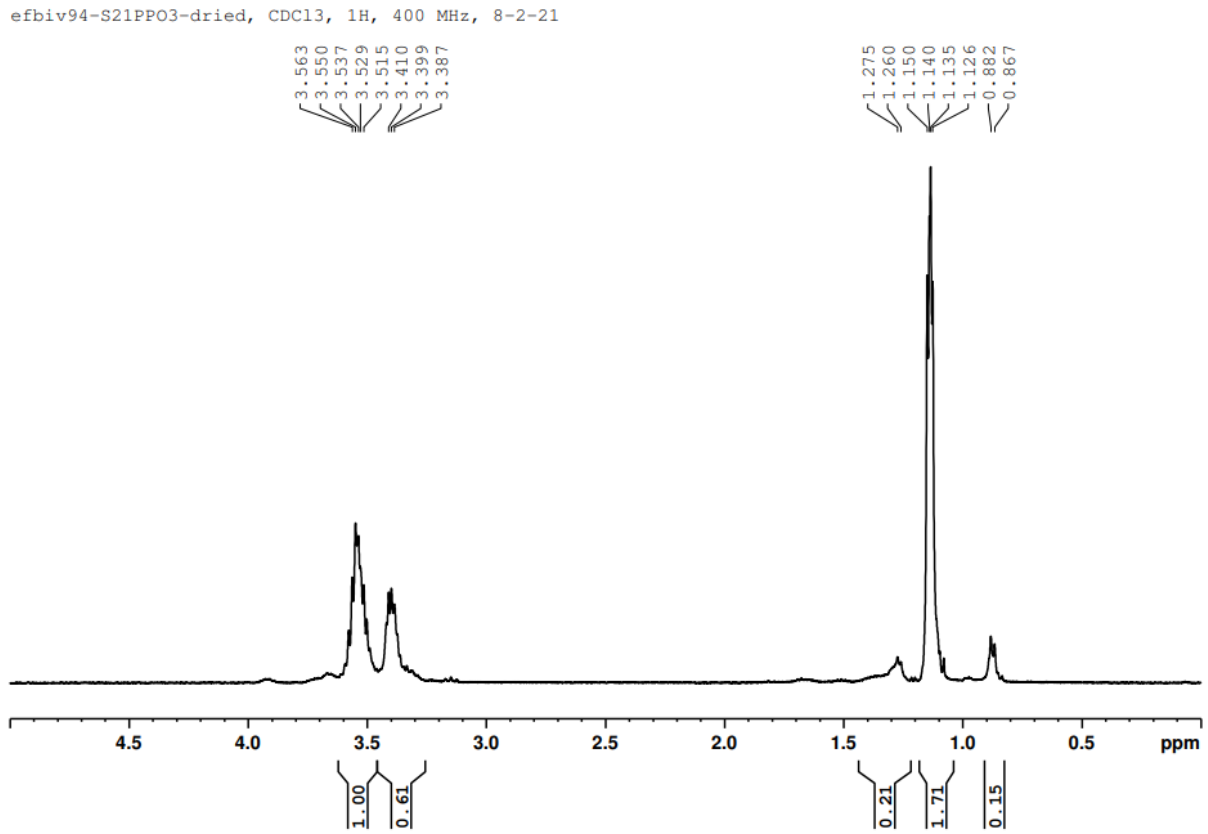

Figure A.4: PPO from EtOH ^{1}H

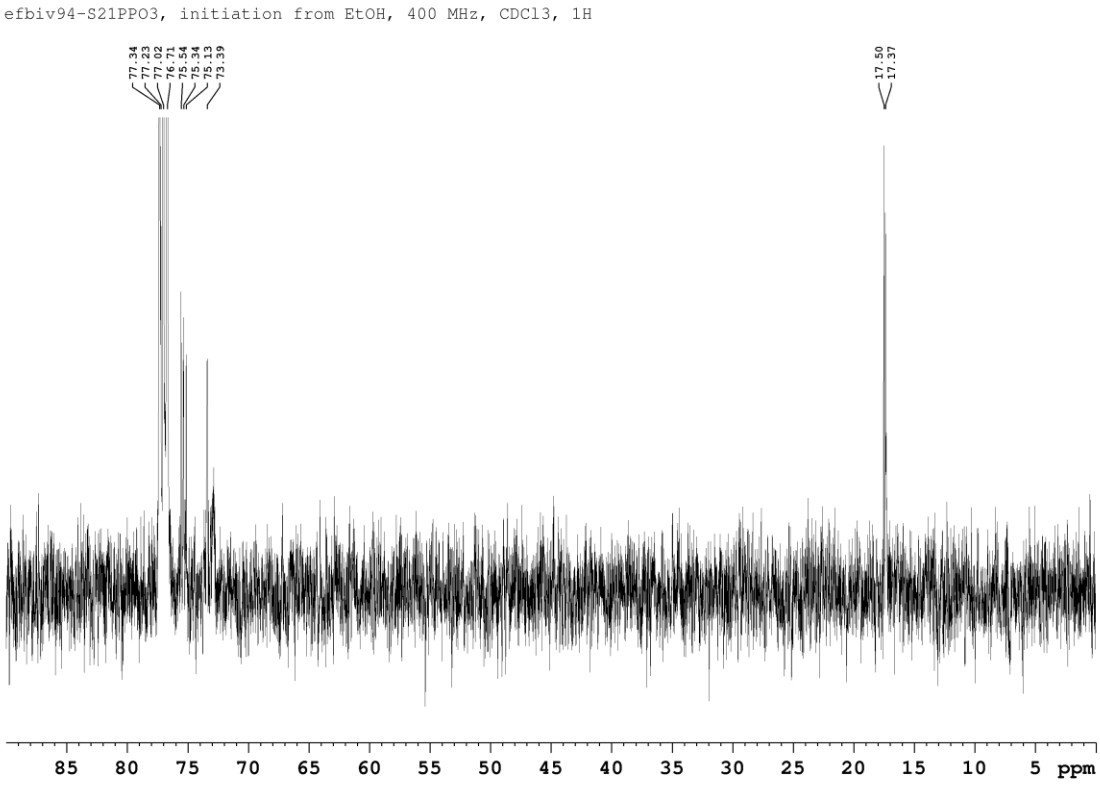

Figure A.5: PPO from EtOH ^{13}C

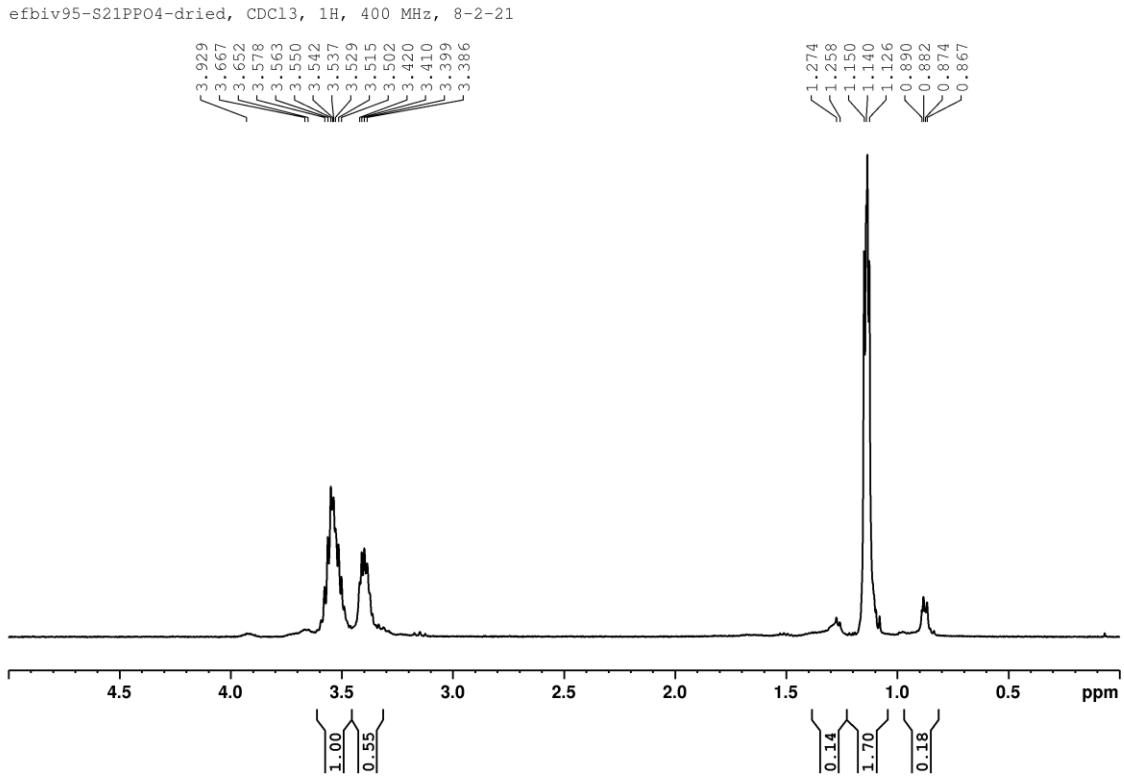

Figure A.6: PPO from an alcohol

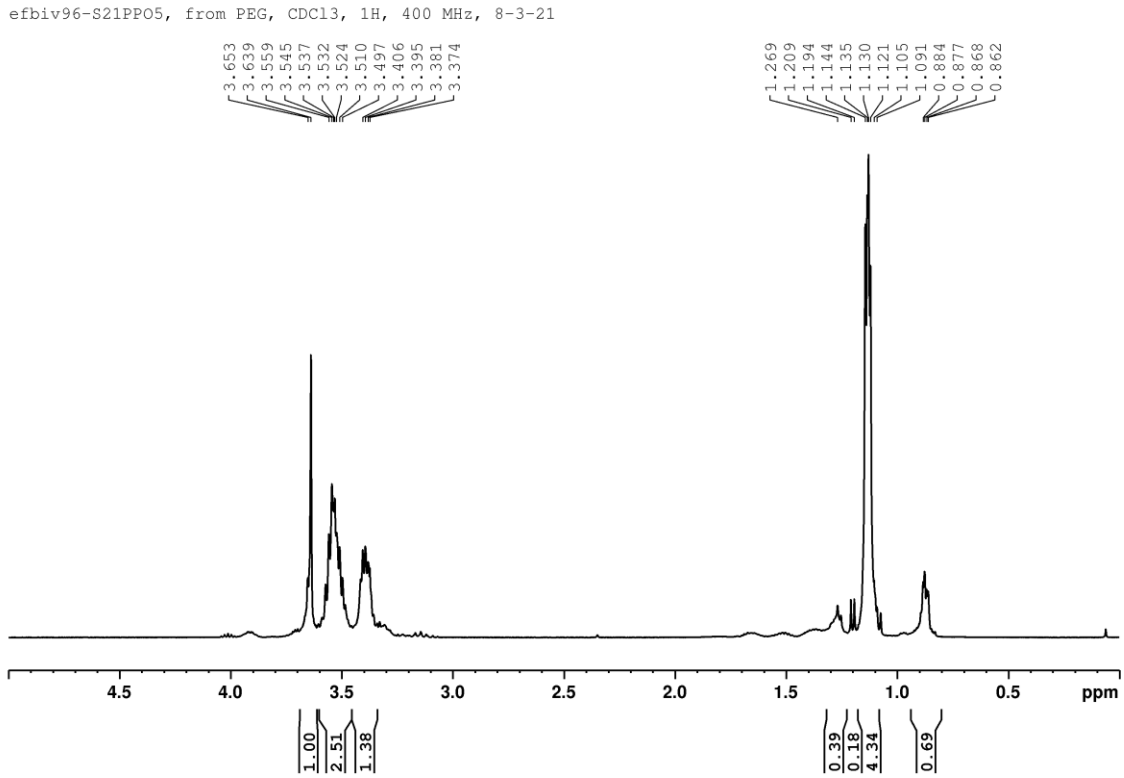

Figure A.7: PPO from PEO-OH

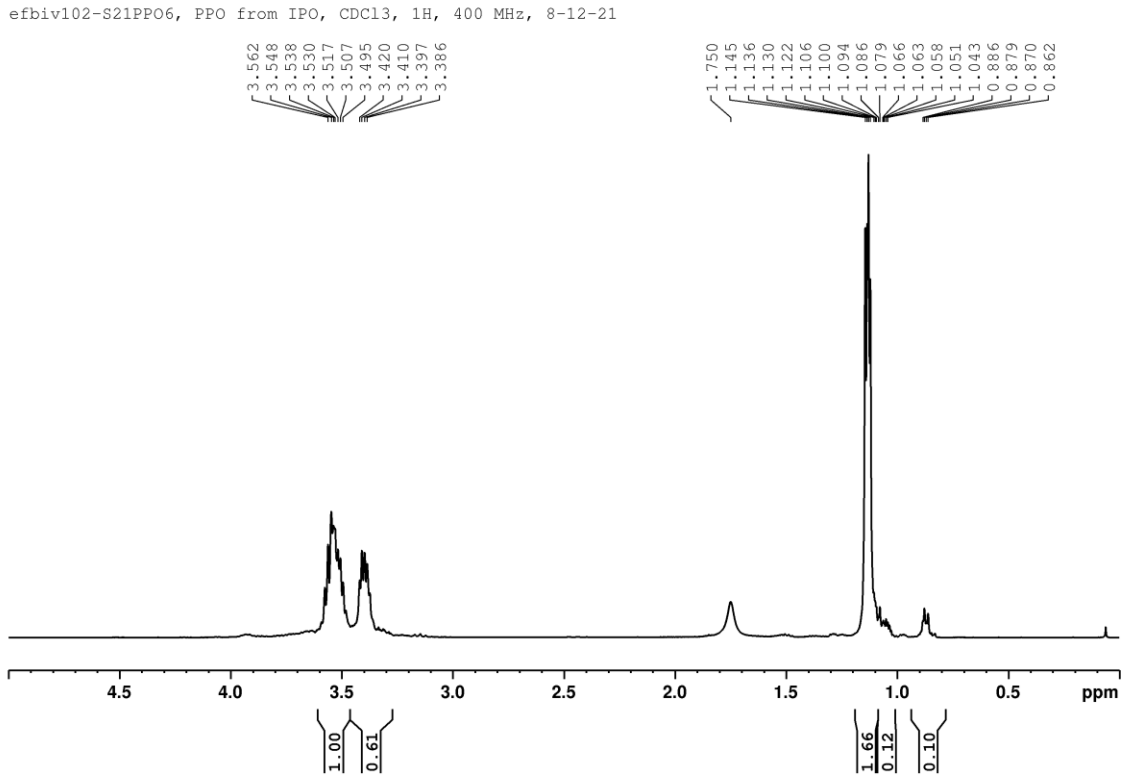

Figure A.8: PPO from IPO ^{1}H

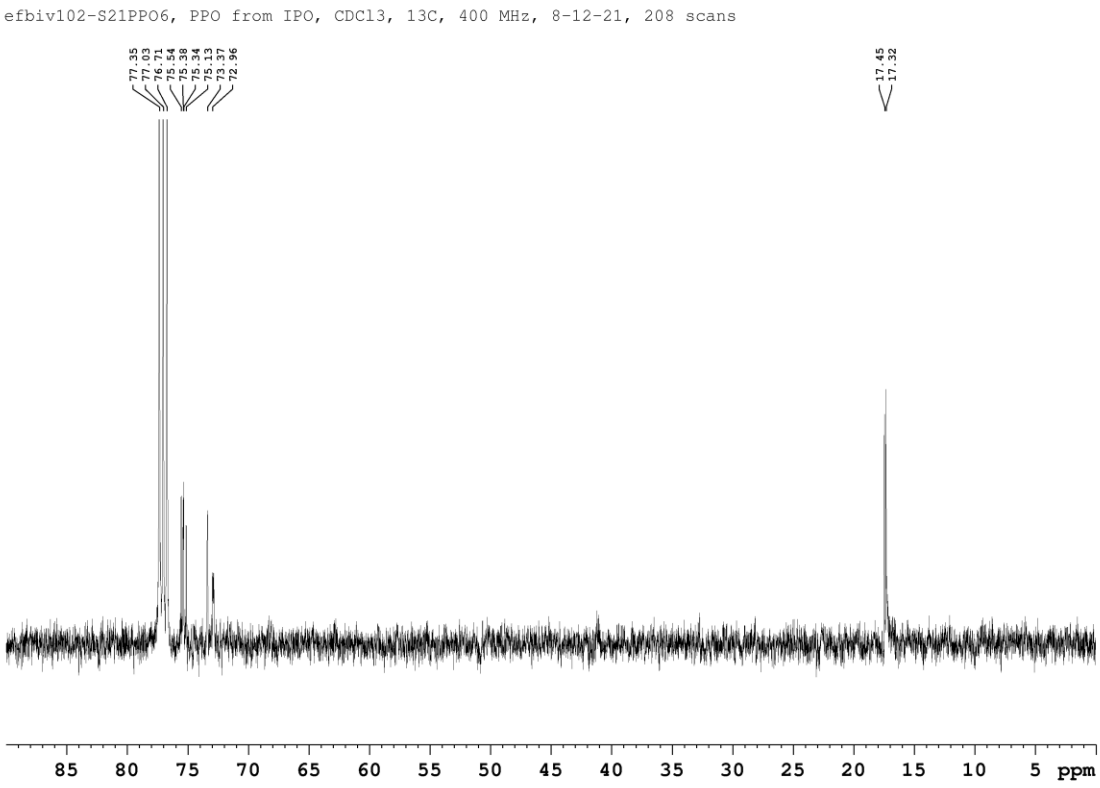

Figure A.9: PPO from IPO ^{13}C

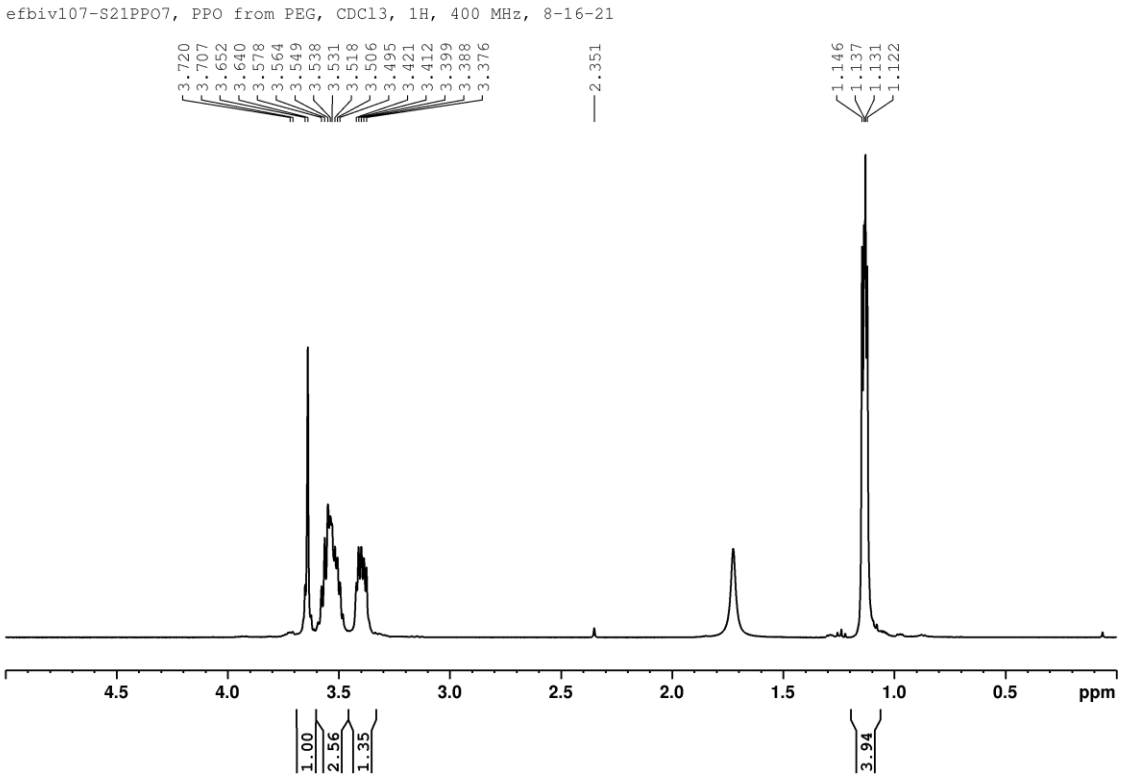

Figure A.10: PPO from PEG-Na ^{1}H

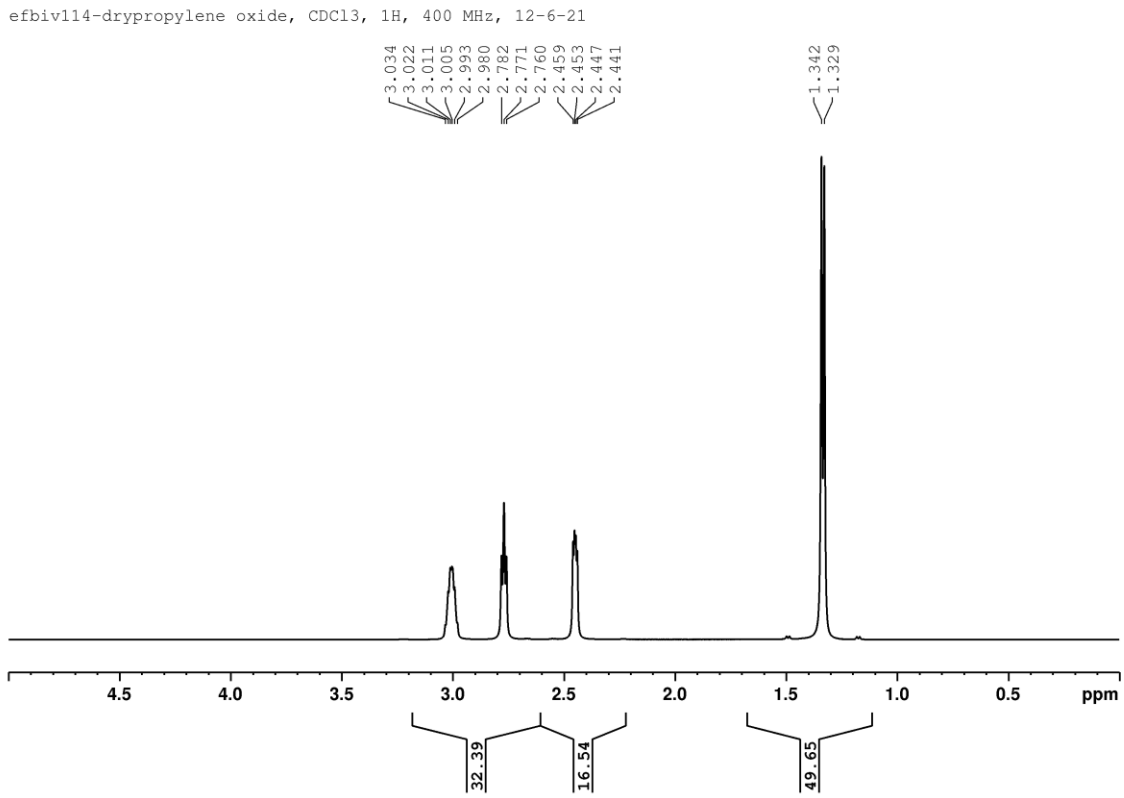

Figure A.11: propylene oxide starting material

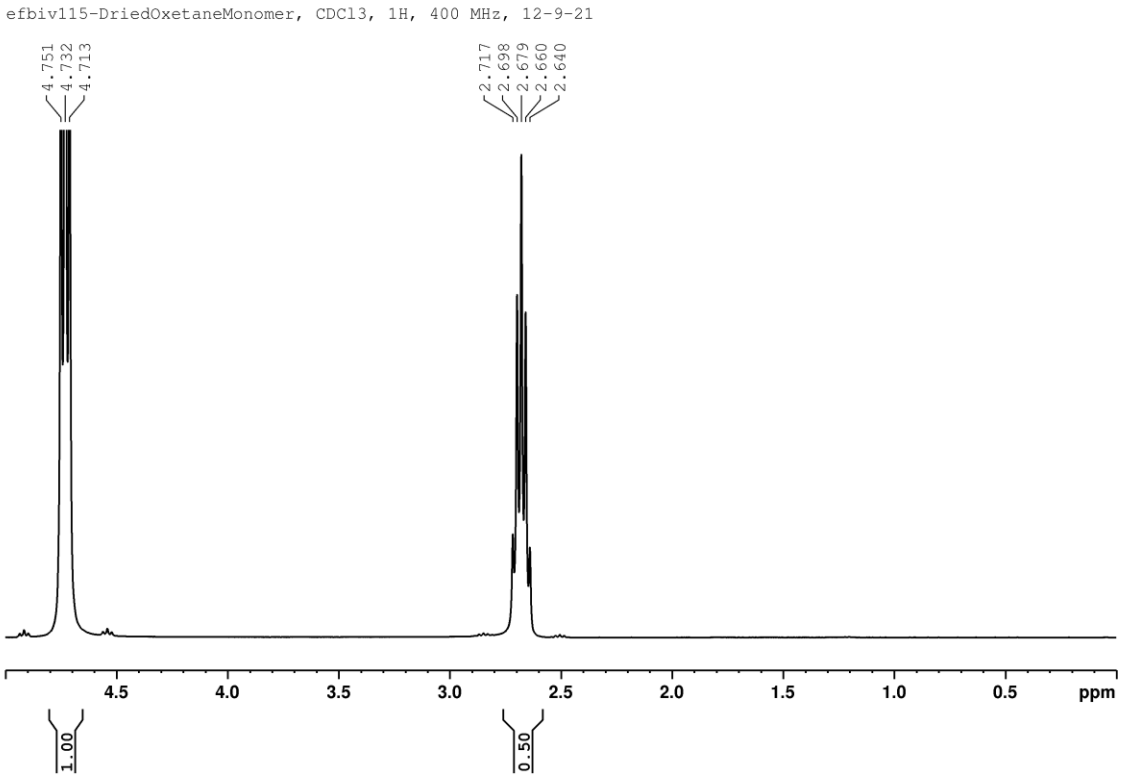

Figure A.12: Oxetane monomer

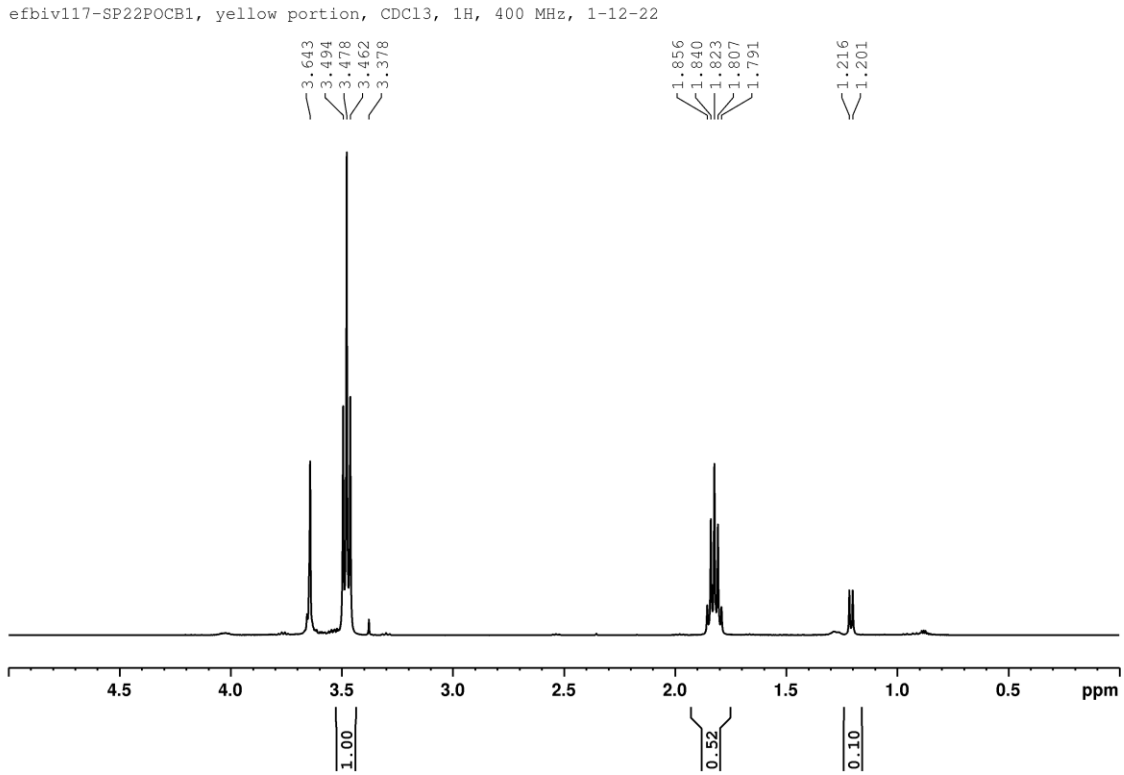

Figure A.13: POCB from an alkoxide

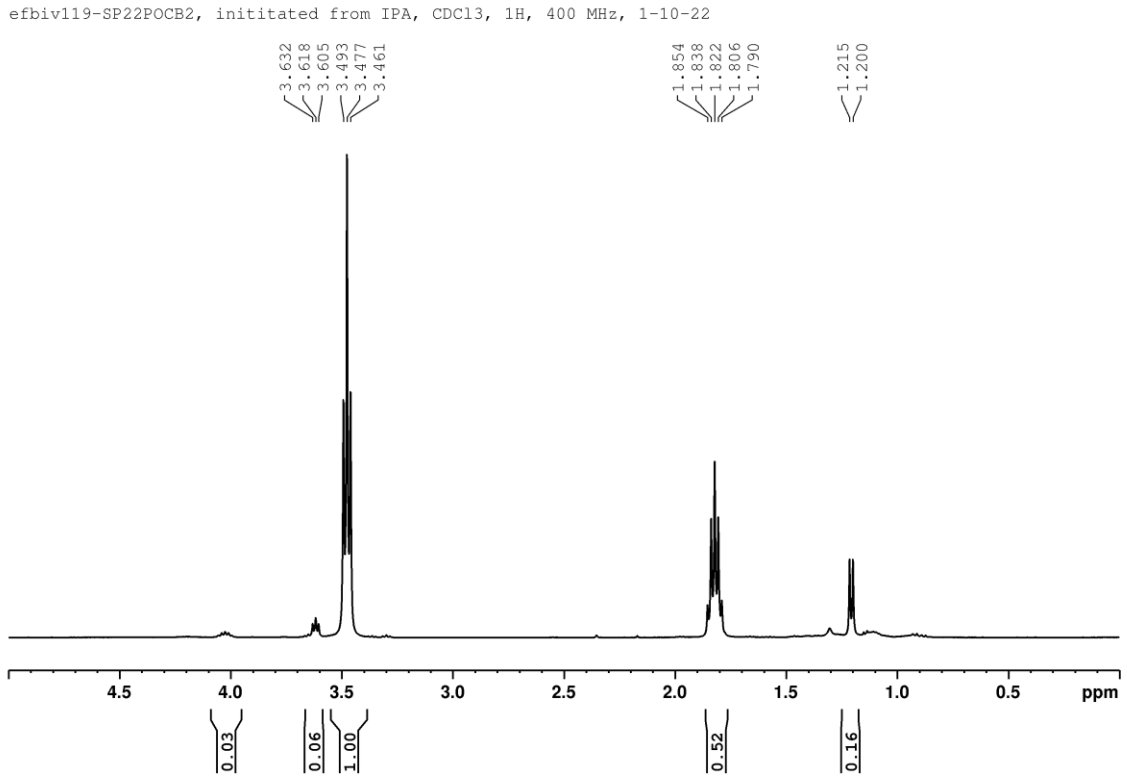

Figure A.14: POCB from IPO

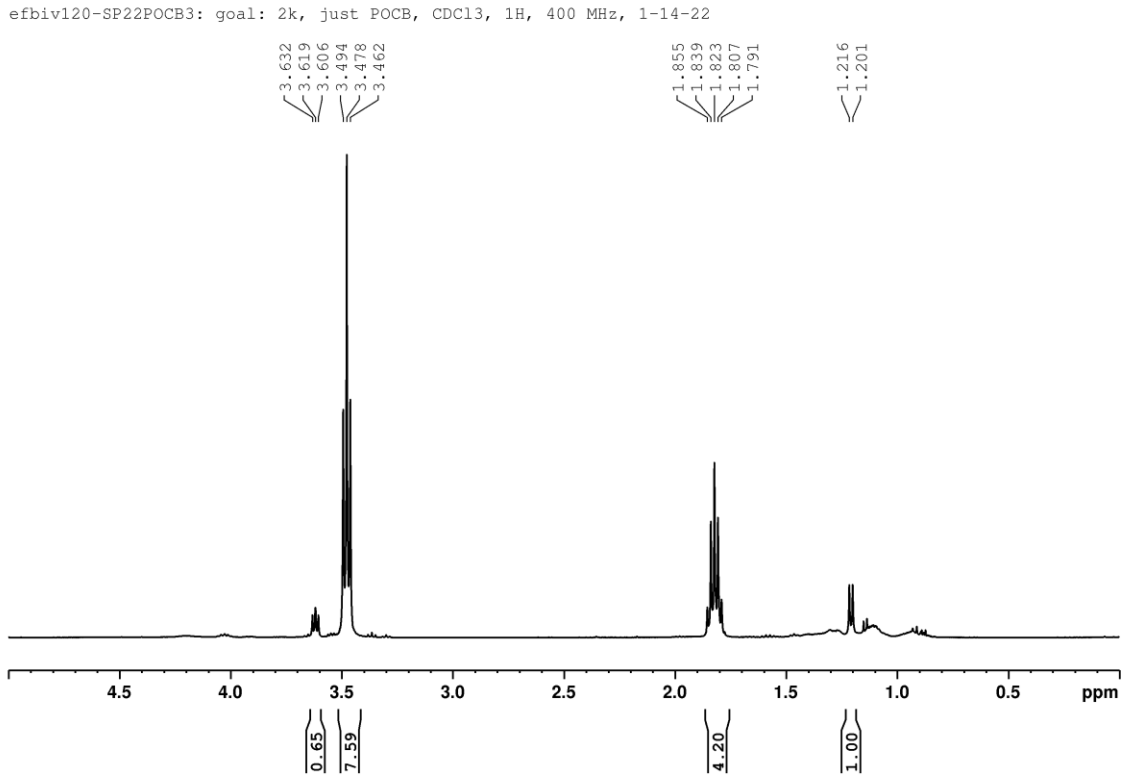

Figure A.15: POCB from an alkoxide

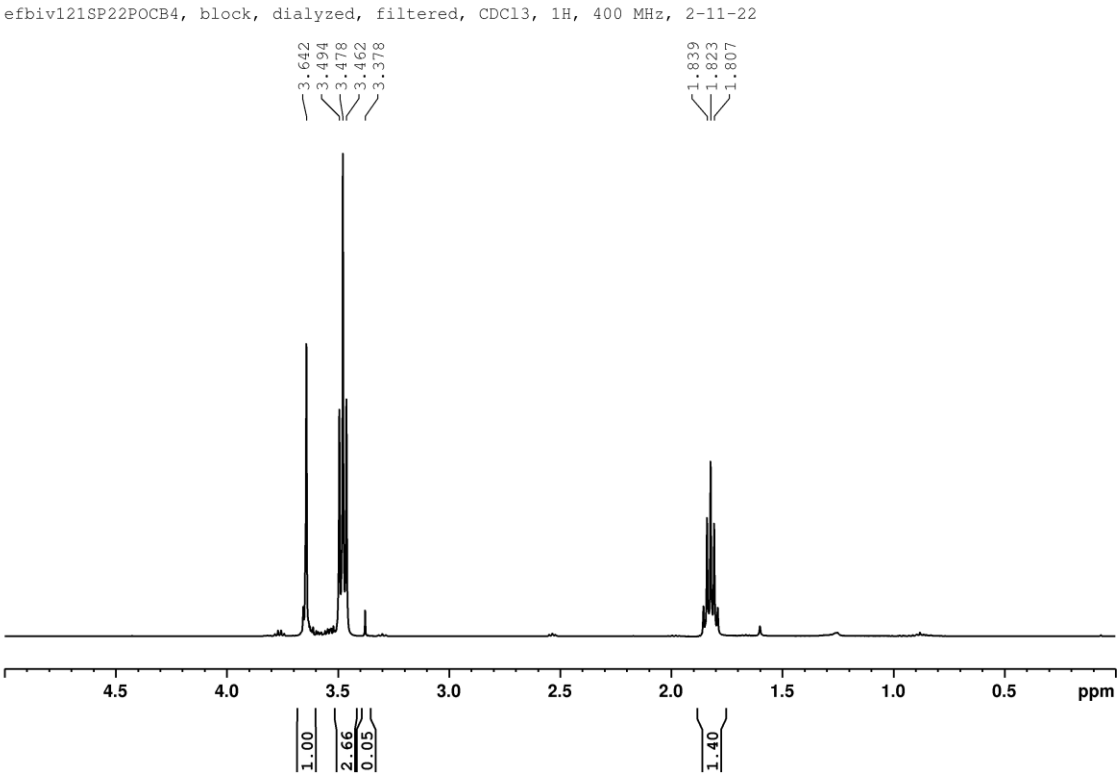

Figure A.16: POCB from PEO-Na

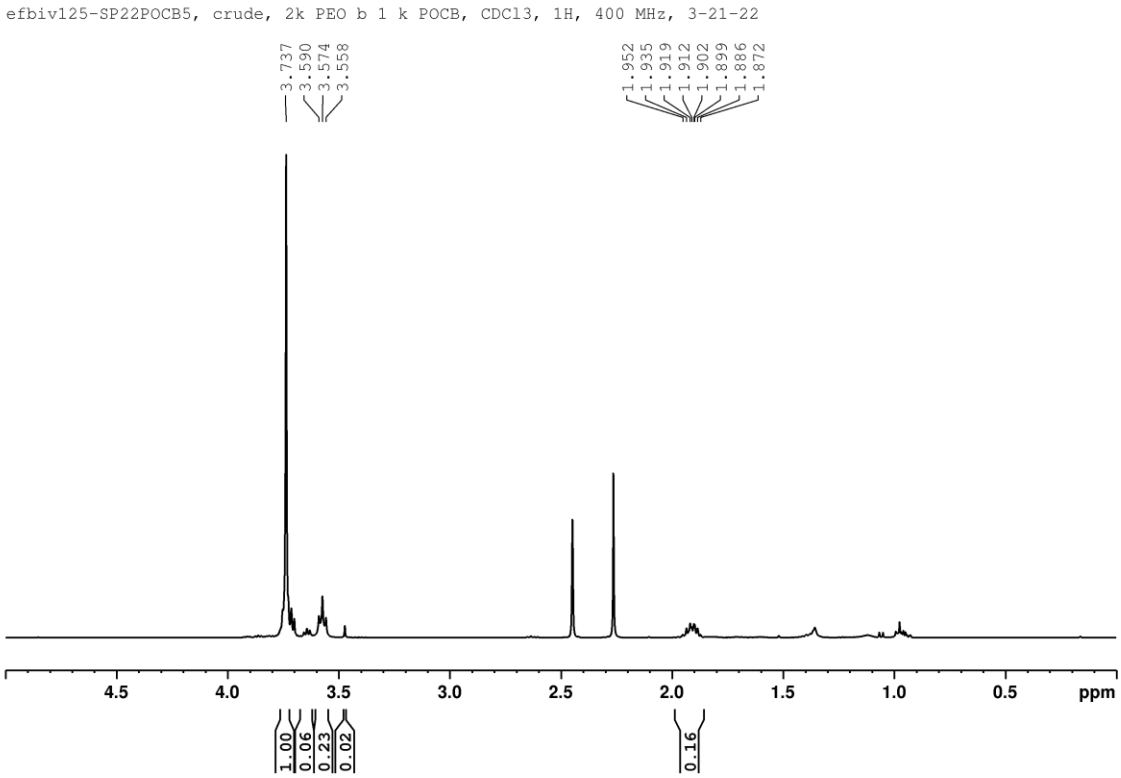

Figure A.17: POCB from PEONa

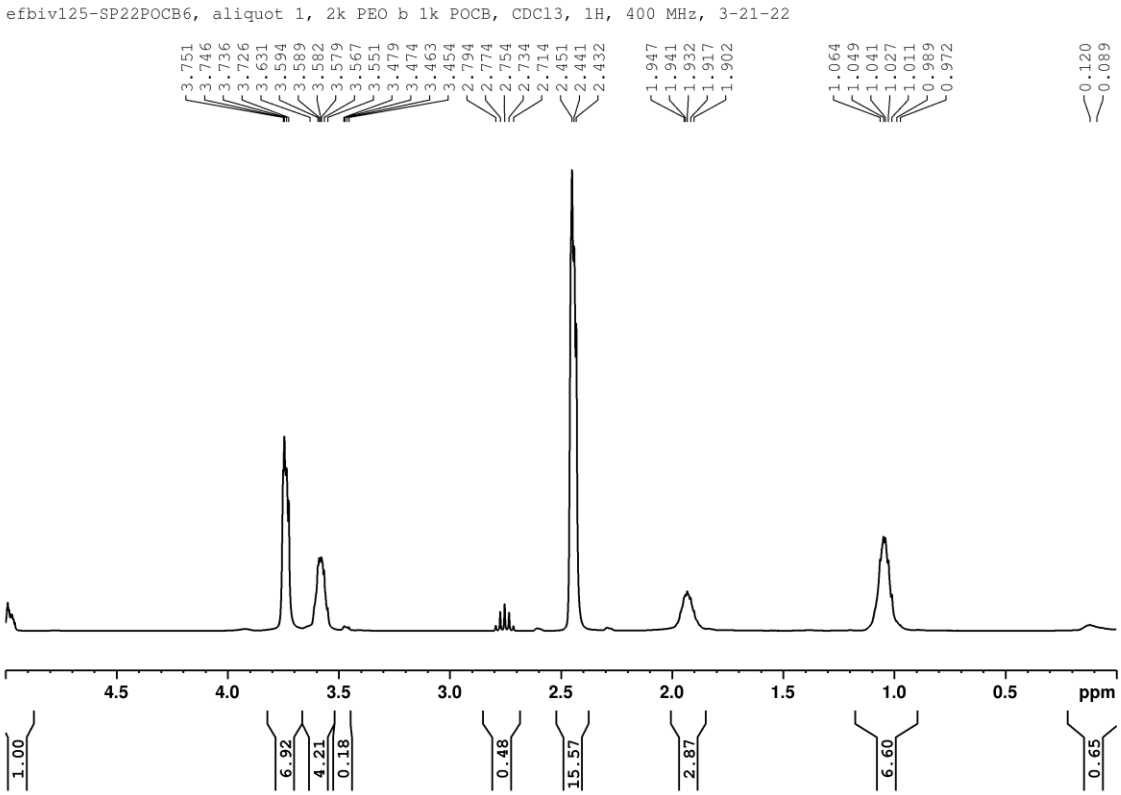

Figure A.18: POCB from PEONa test reaction aliquot

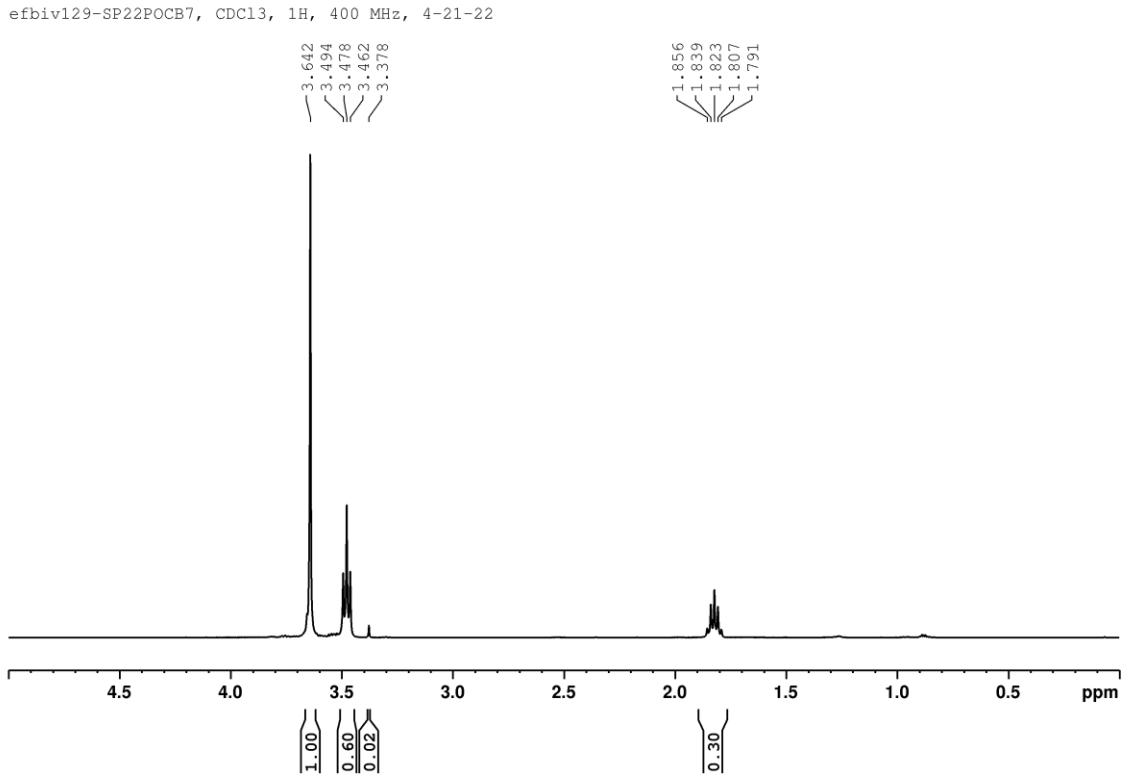

Figure A.19: POCB from PEONa

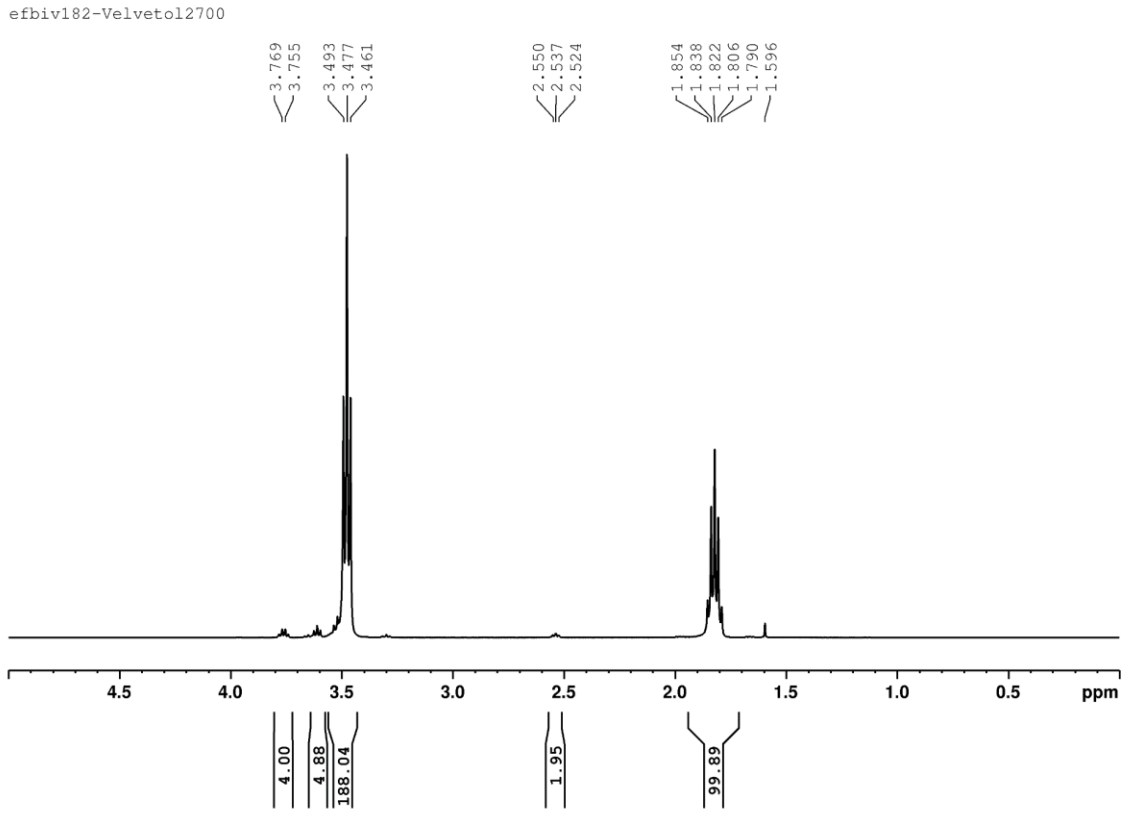

Figure A.20: Velvetol (produced by Allessa)

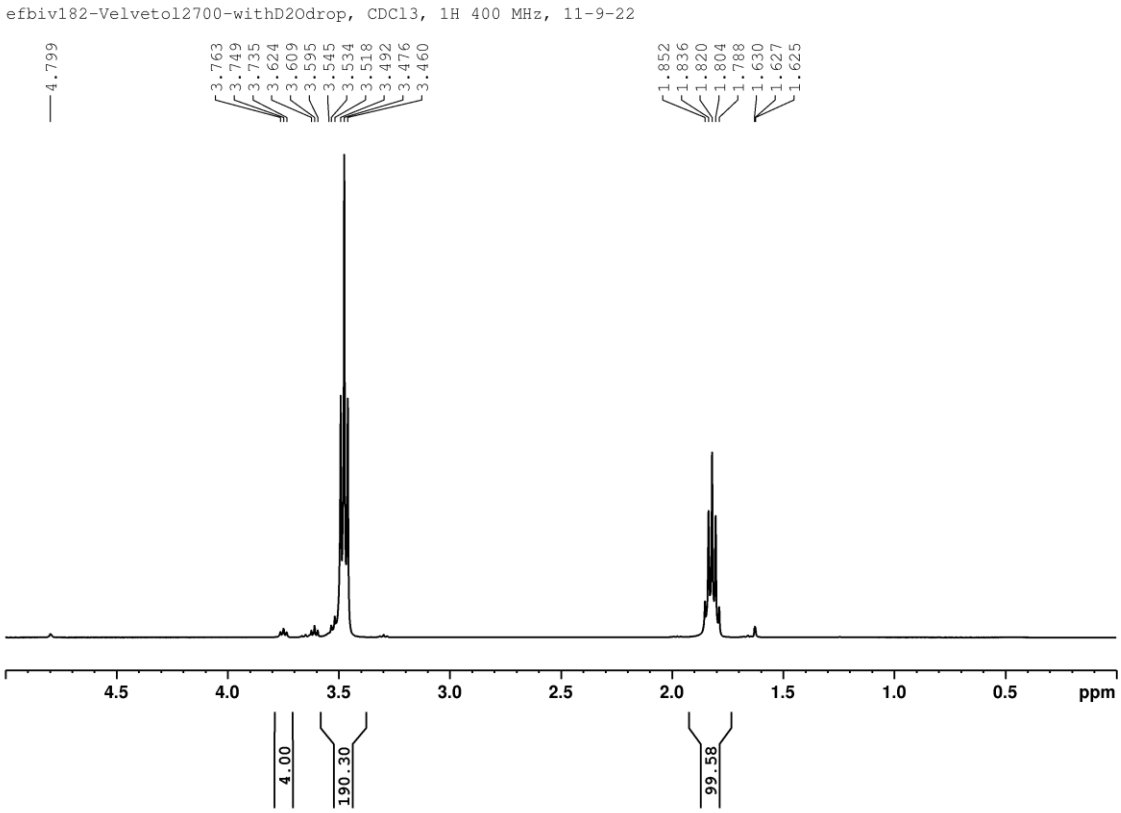

Figure A.21: Velvetol with a drop of D_2O. The peak at 2.55 disappears.

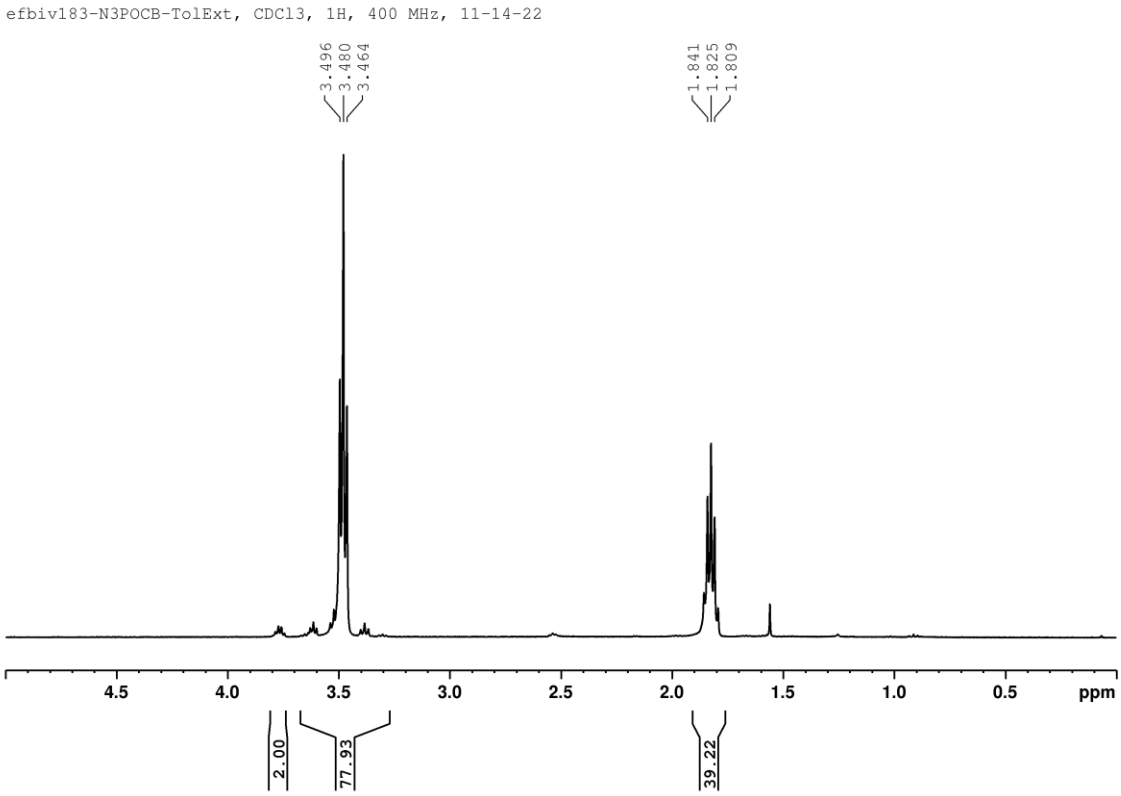

Figure A.22: N_3POCB (POCB1000), the one that is part of **Block1000.**

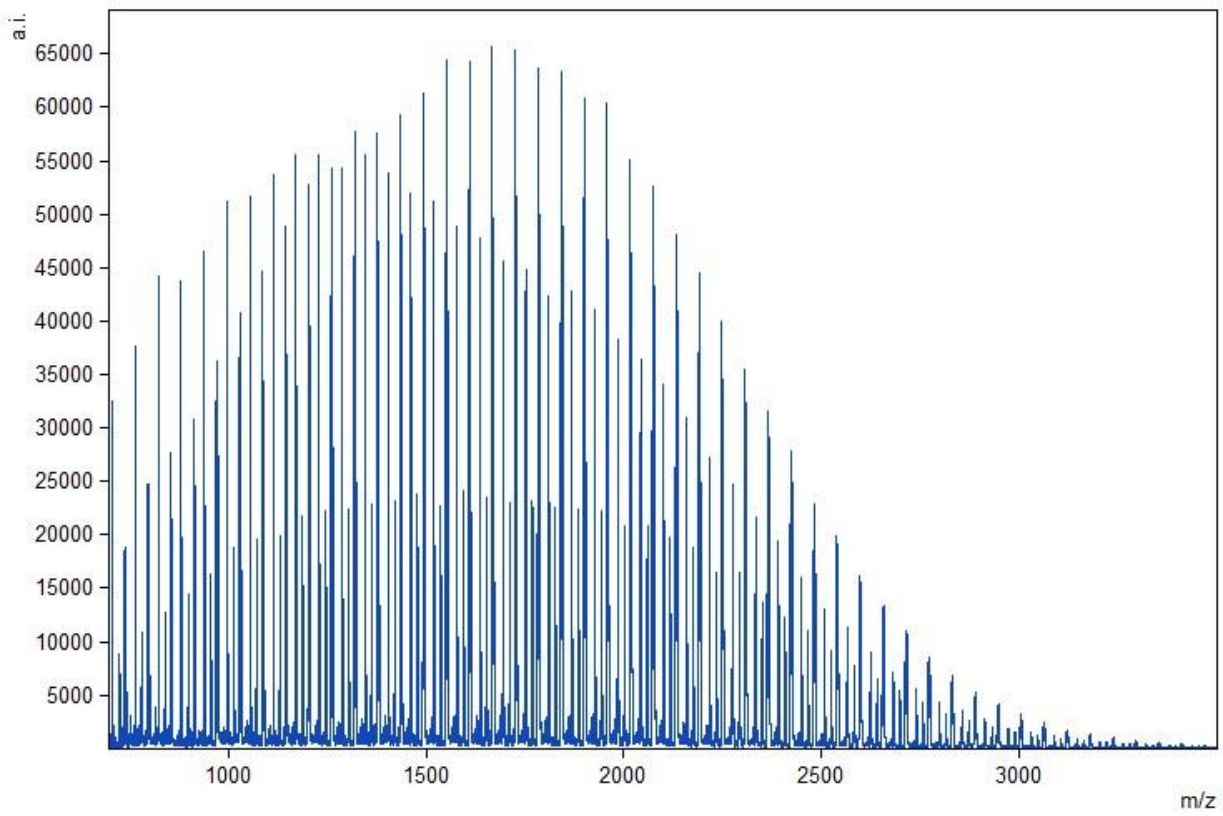

Figure A.23: POCB1000 (183). The different groupings of peaks represent the N_3-, the N^+-, and the de-azidated form of the molecule[134].

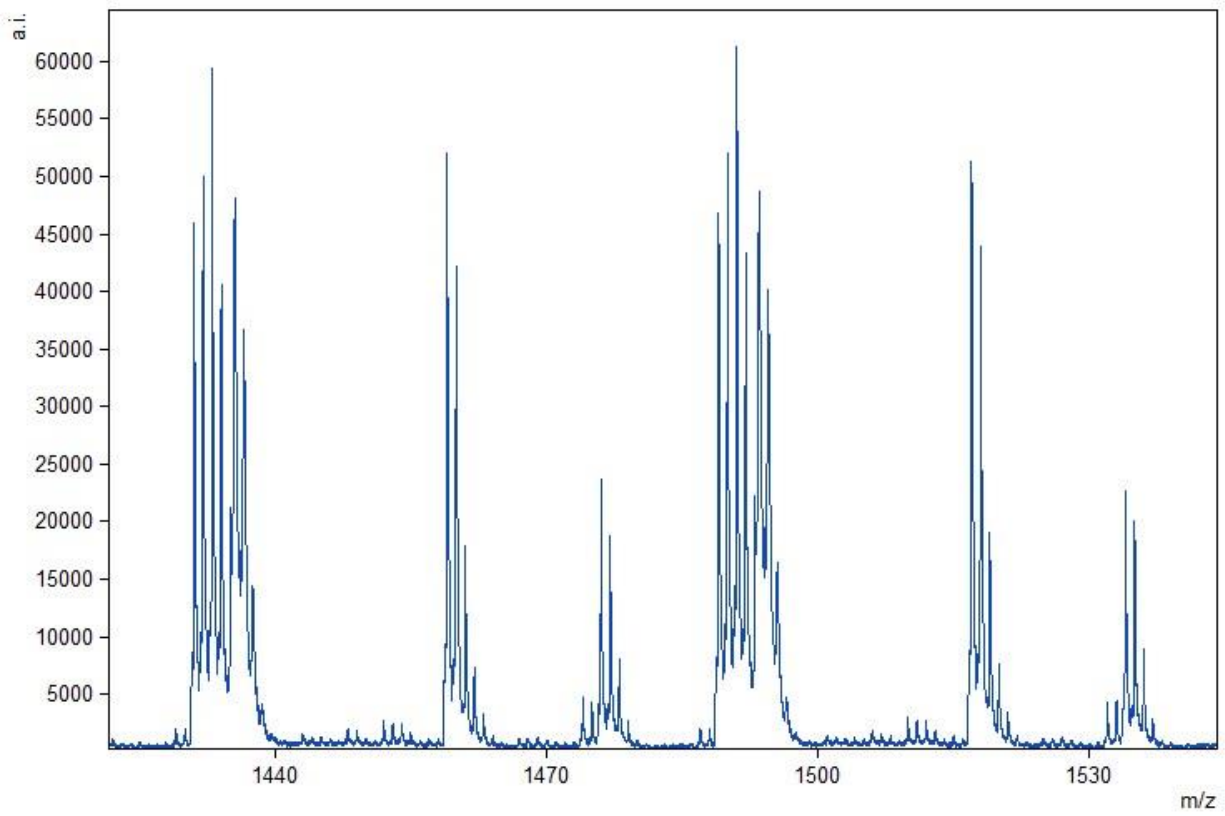

Figure A.24: POCB1000 (183), zoomed. The different groupings of peaks represent the N_3-, the N^+-, and the de-azidated form of the molecule[134].

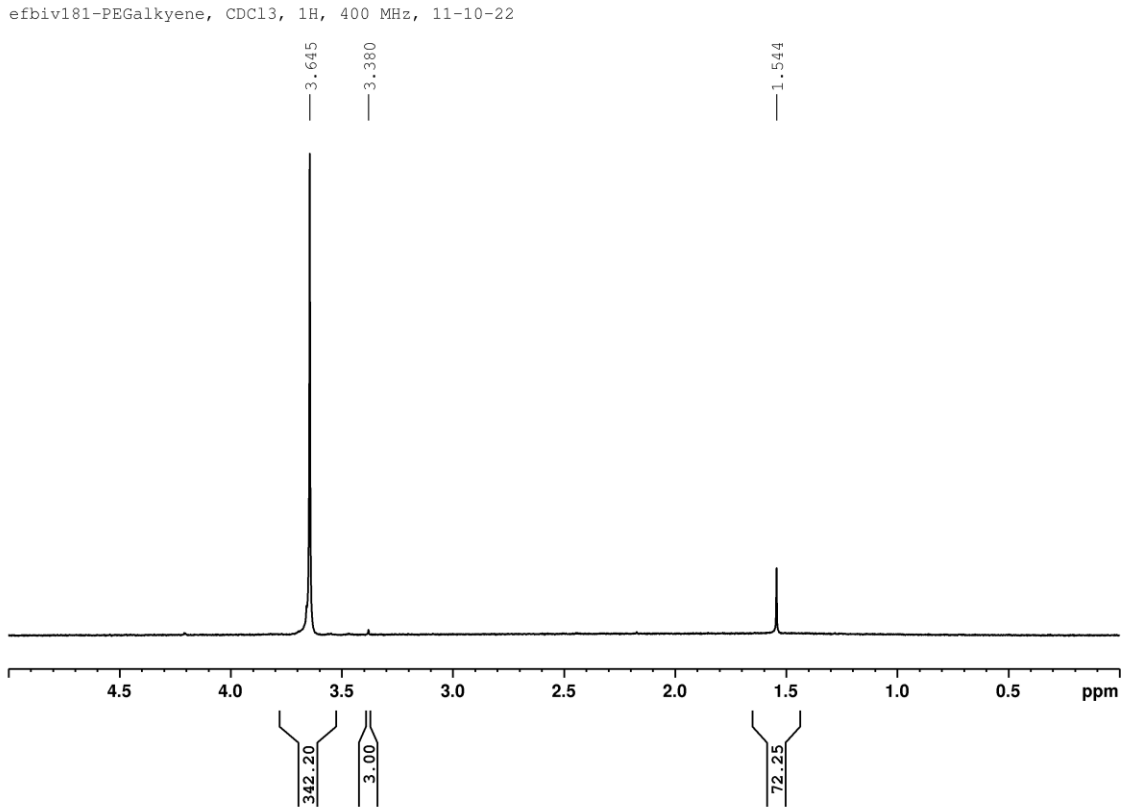

Figure A.25: ^{1}HNMR of PEGalkyne, PEO4000, the one that is part of **Block1000**

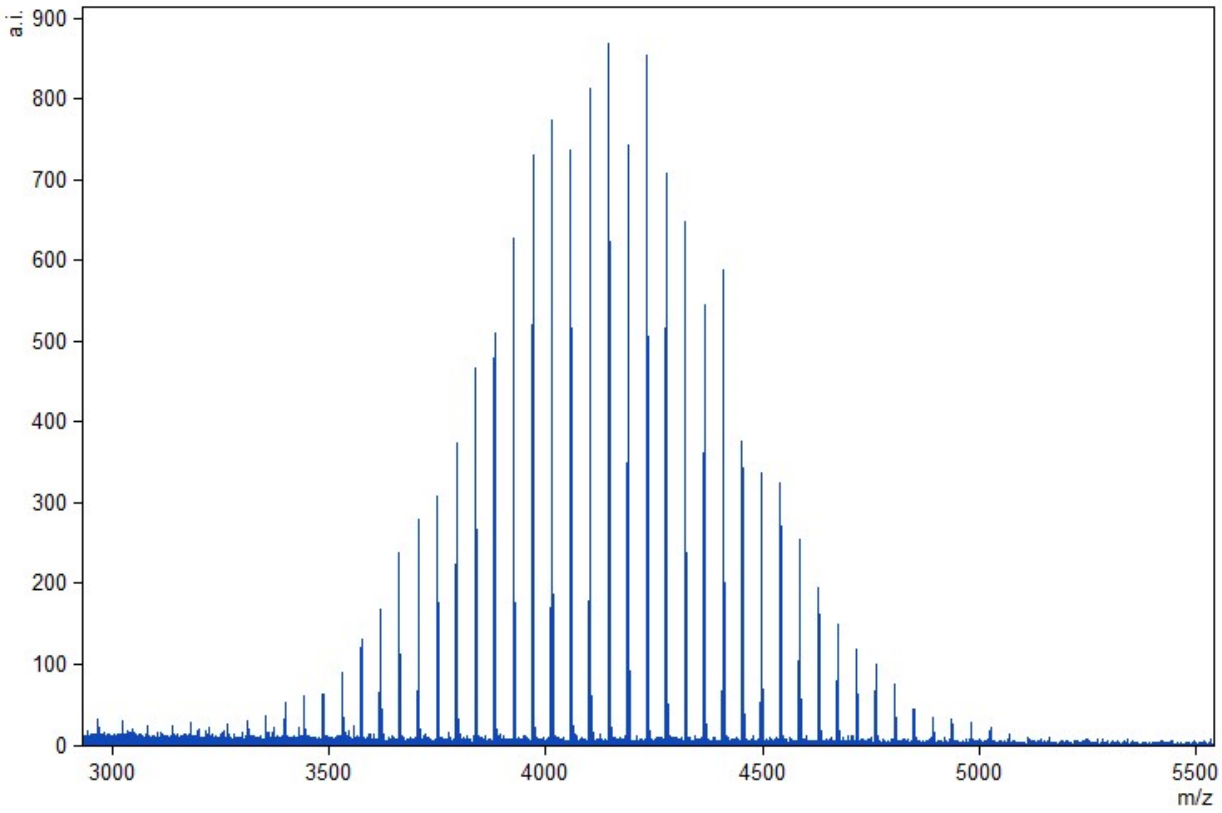

Figure A.26: Maldi of **PEGalkyne, PEO4000,** the one that is part of **Block1000**

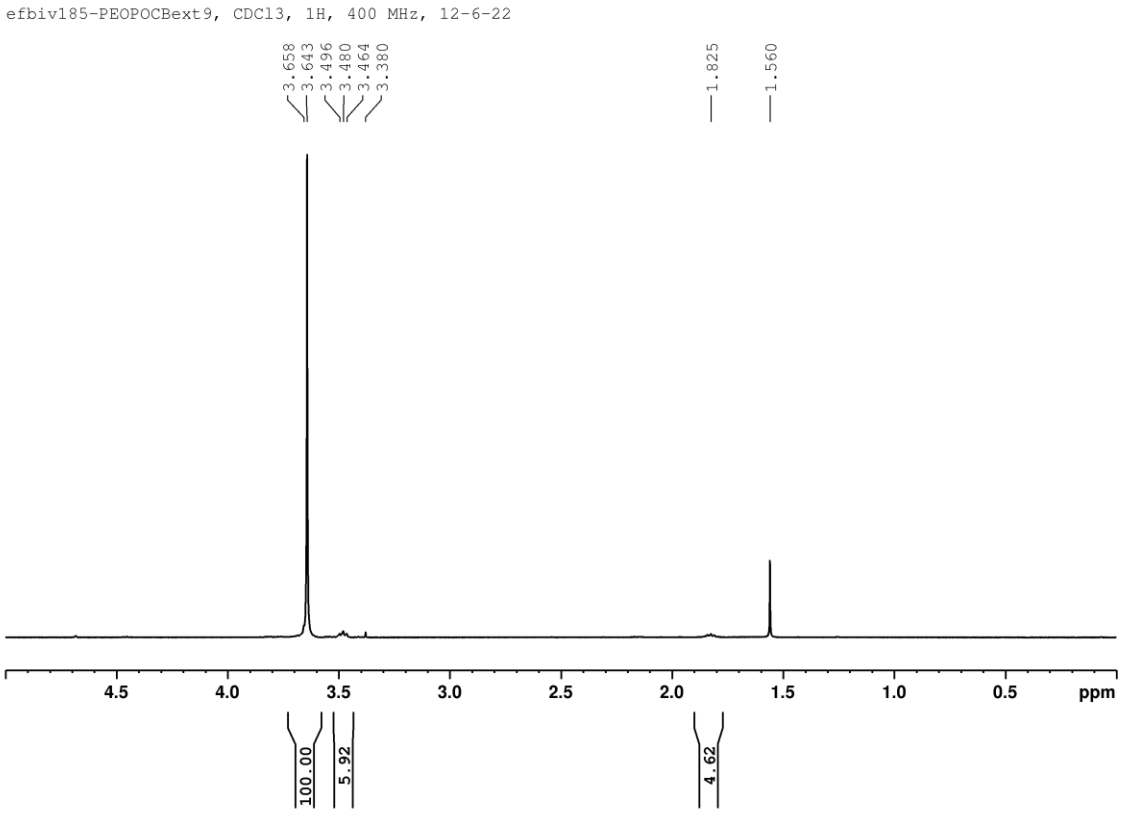

Figure A.27: ^{1}HNMR of **Block1000**

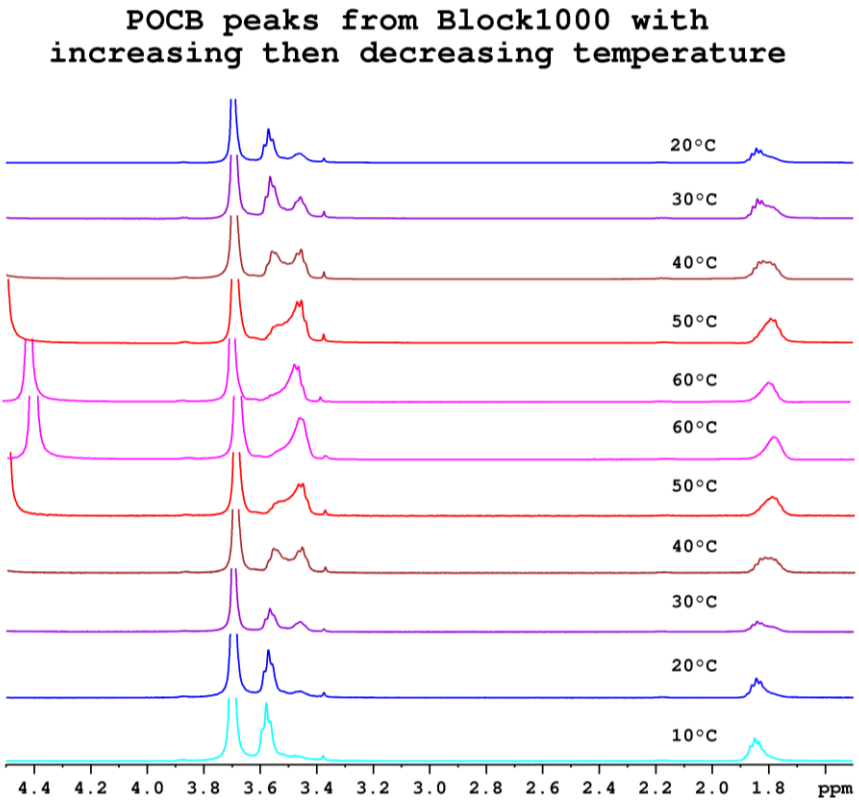

Figure A.28: Block1000 in D_2O, unzoomed

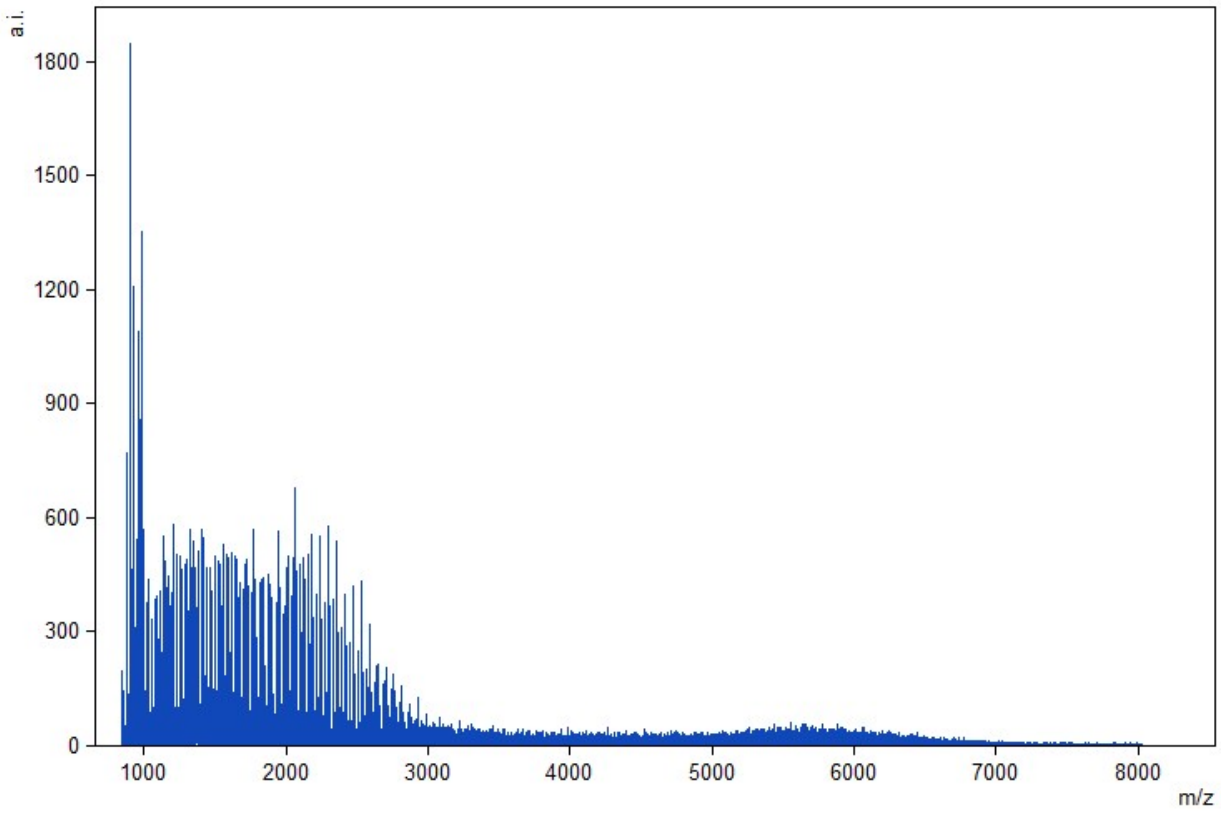

Figure A.29: Bloock1000 Maldi unzoomed

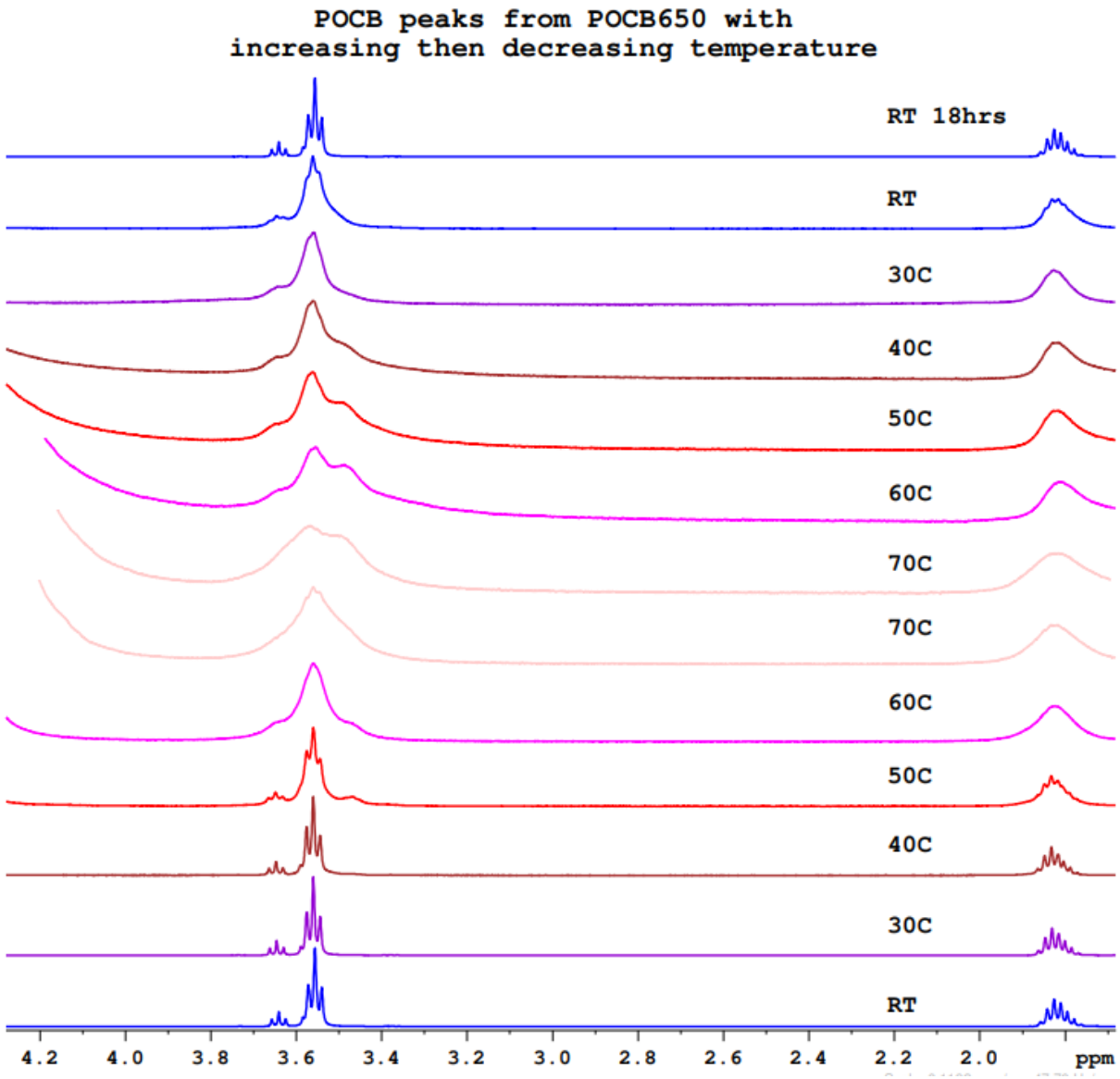

Figure A.30: Cerenol/POCB650 ^{1}HNMR in D_2O

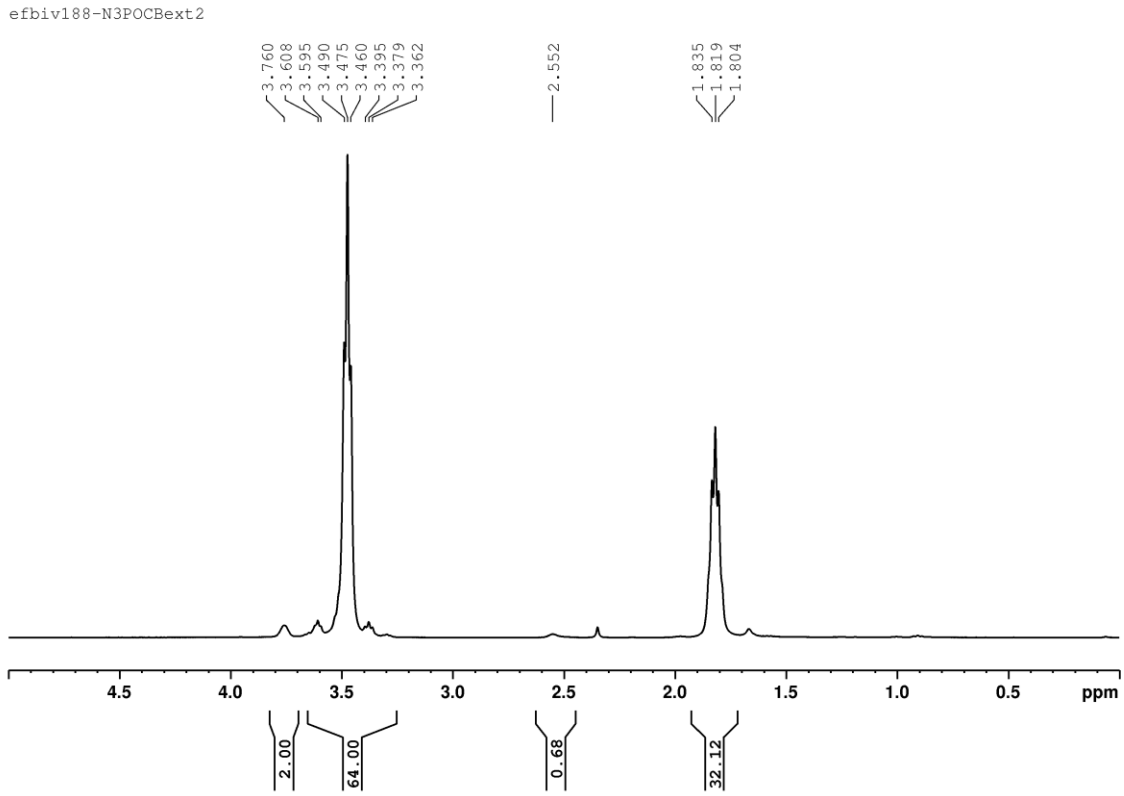

Figure A.31: ^{1}HNMR of **POCB1000** (the one that was not used for the Block1000)

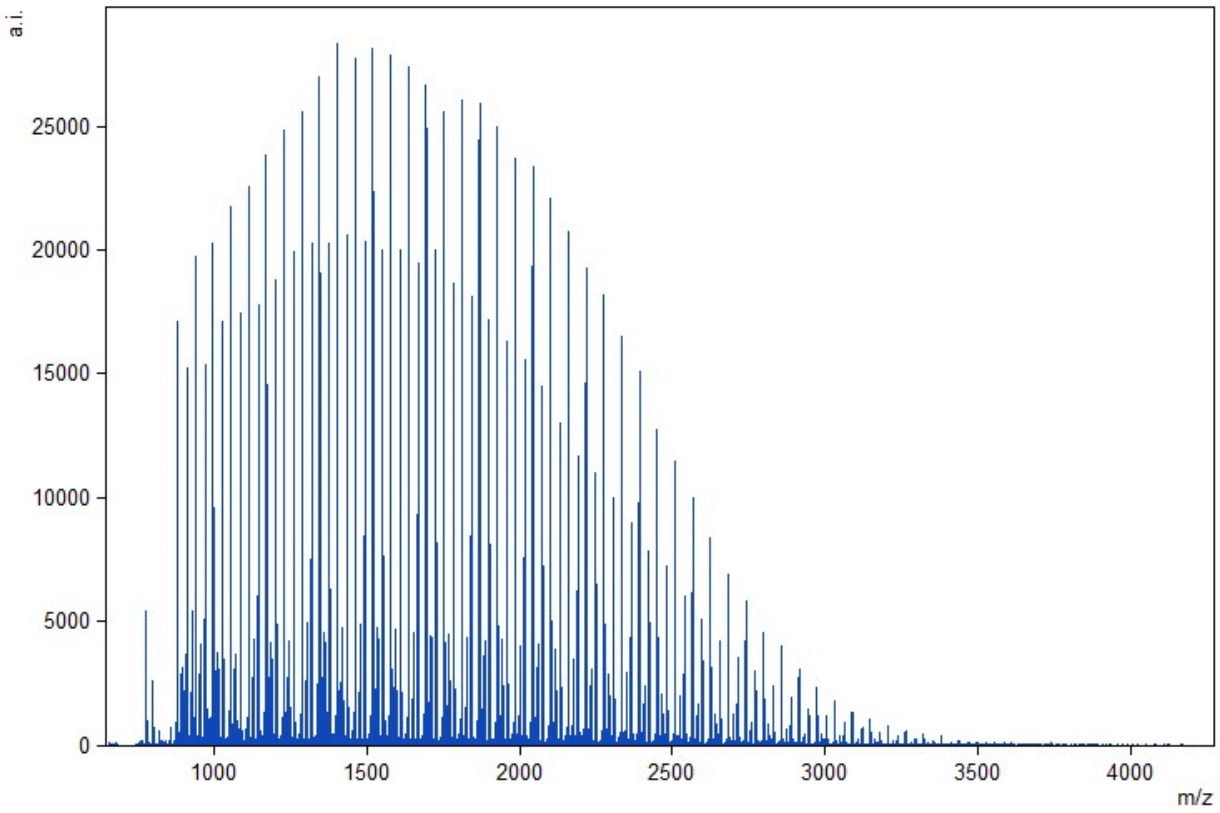

Figure A.32: maldi full N3POCB **POCB1000** (the one that was not used for the Block1000)

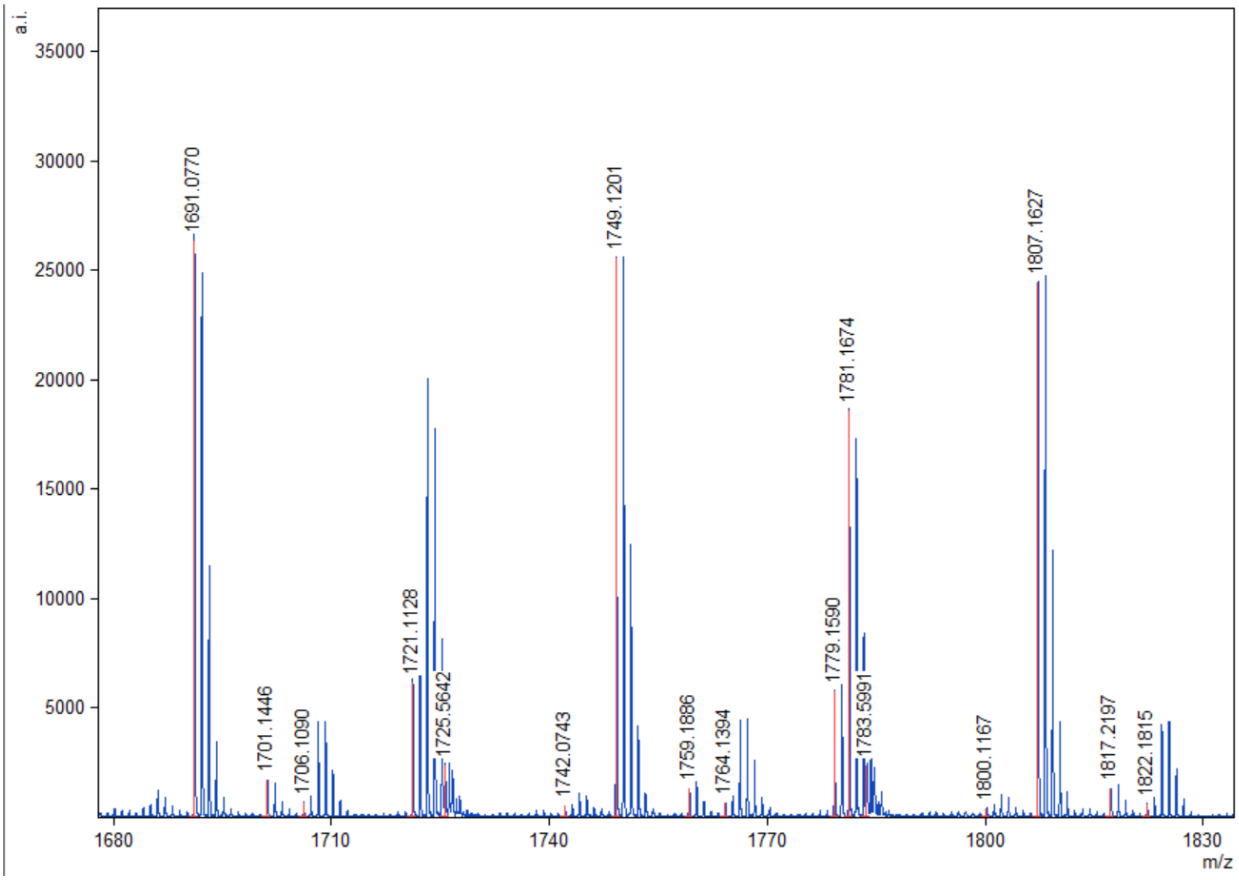

Figure A.33: maldi zoomed N3POCB **POCB1000** (the one that was not used for the Block1000)

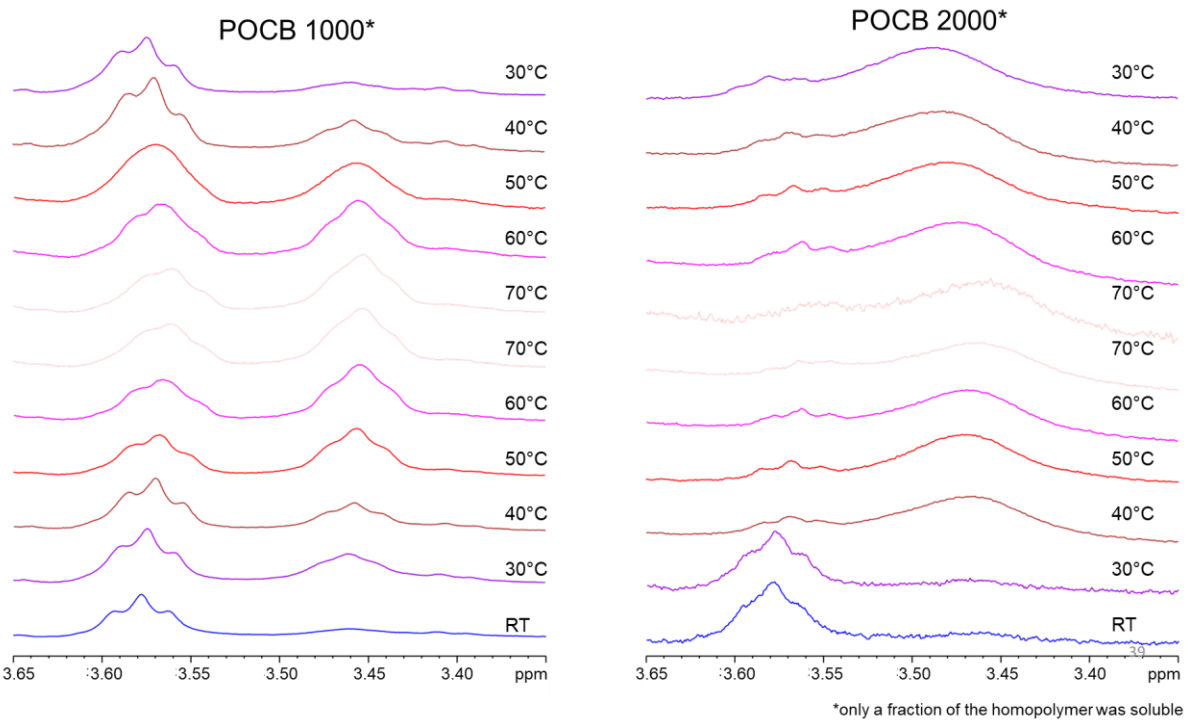

Figure A.34: POCB1000 and POCB2000 ^{1}HNMR in D_2O zoomed

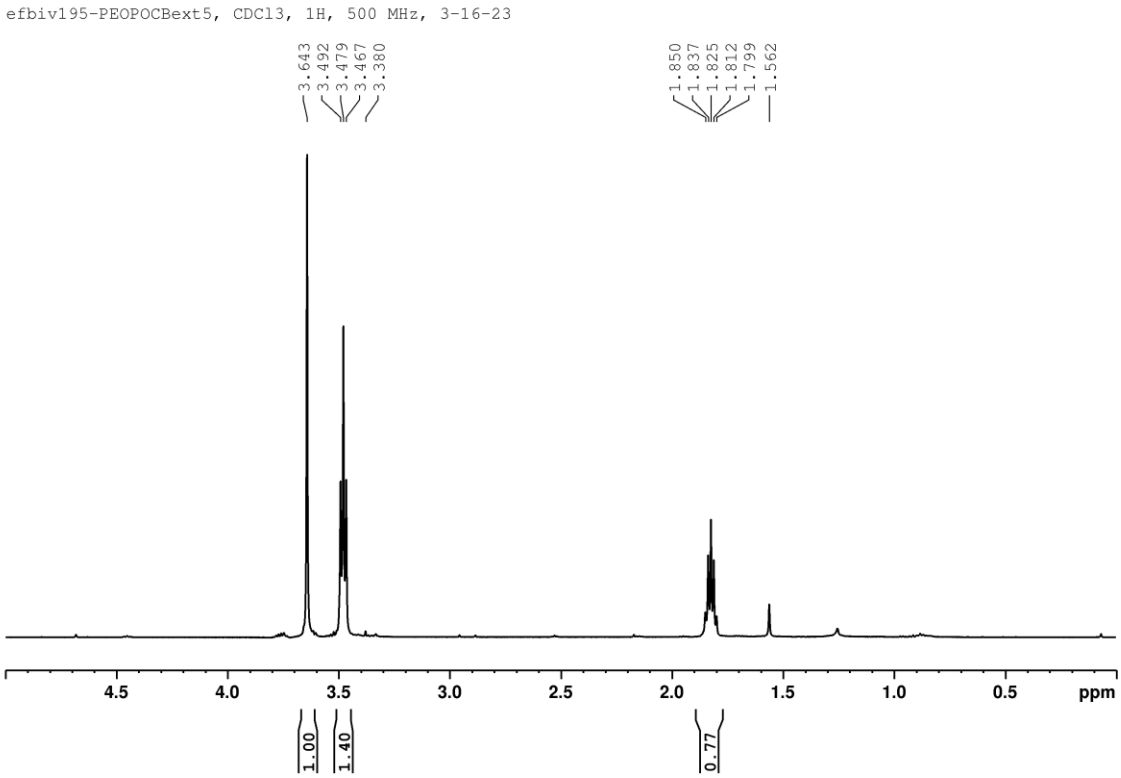

Figure A.35: Block2000 ^{1}HNMR in $CDCl_3$

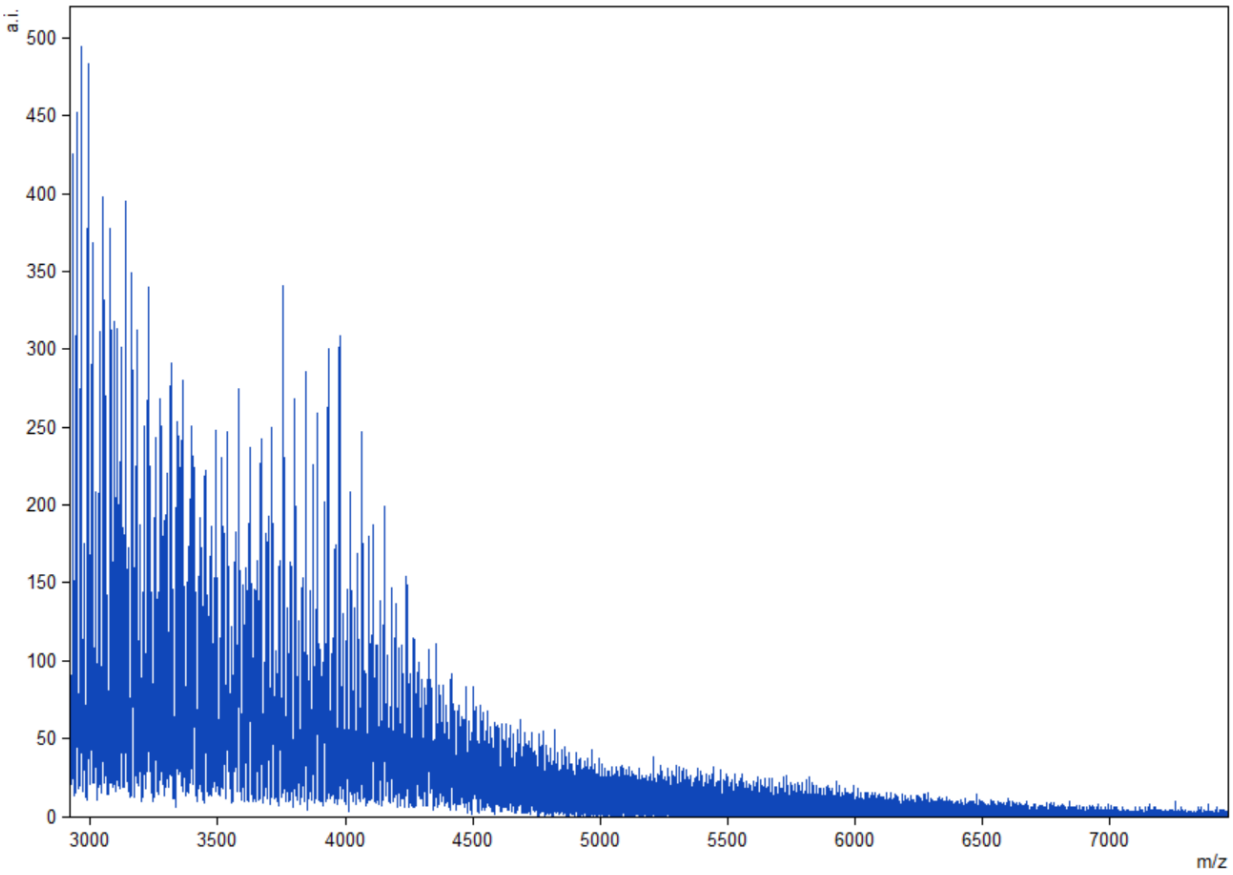

Figure A.36: Full Maldi **Block2000**

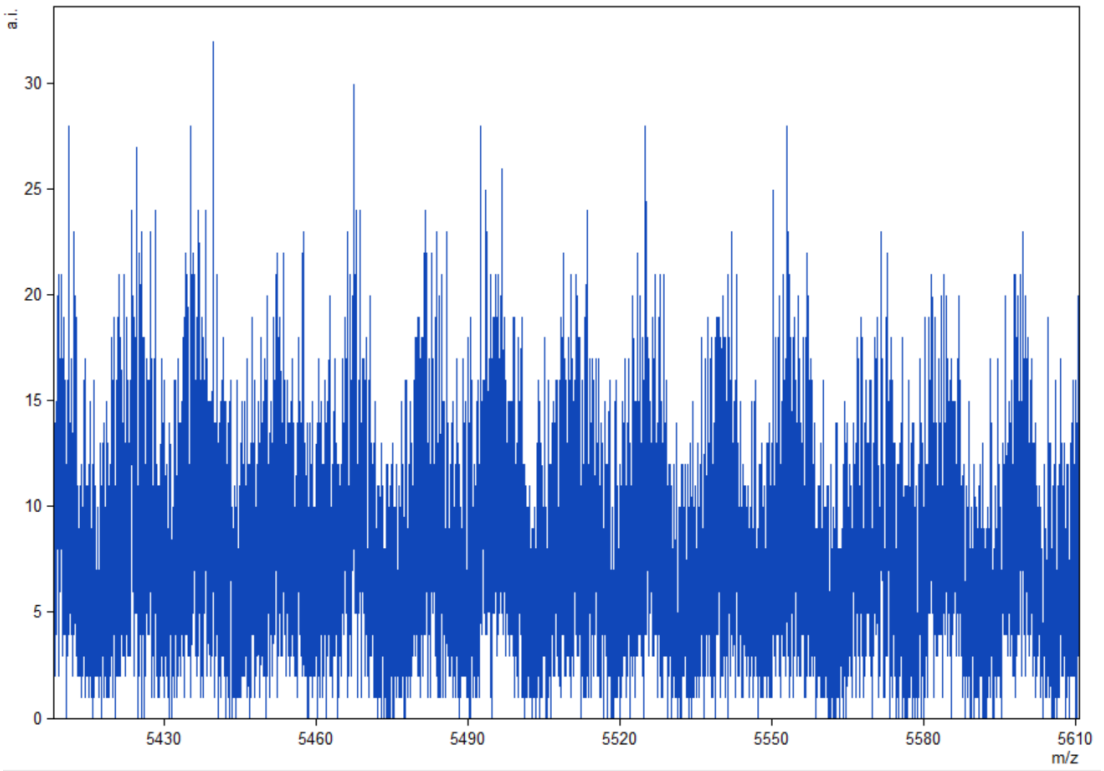

Figure A.37: zoomed Maldi **Block2000**

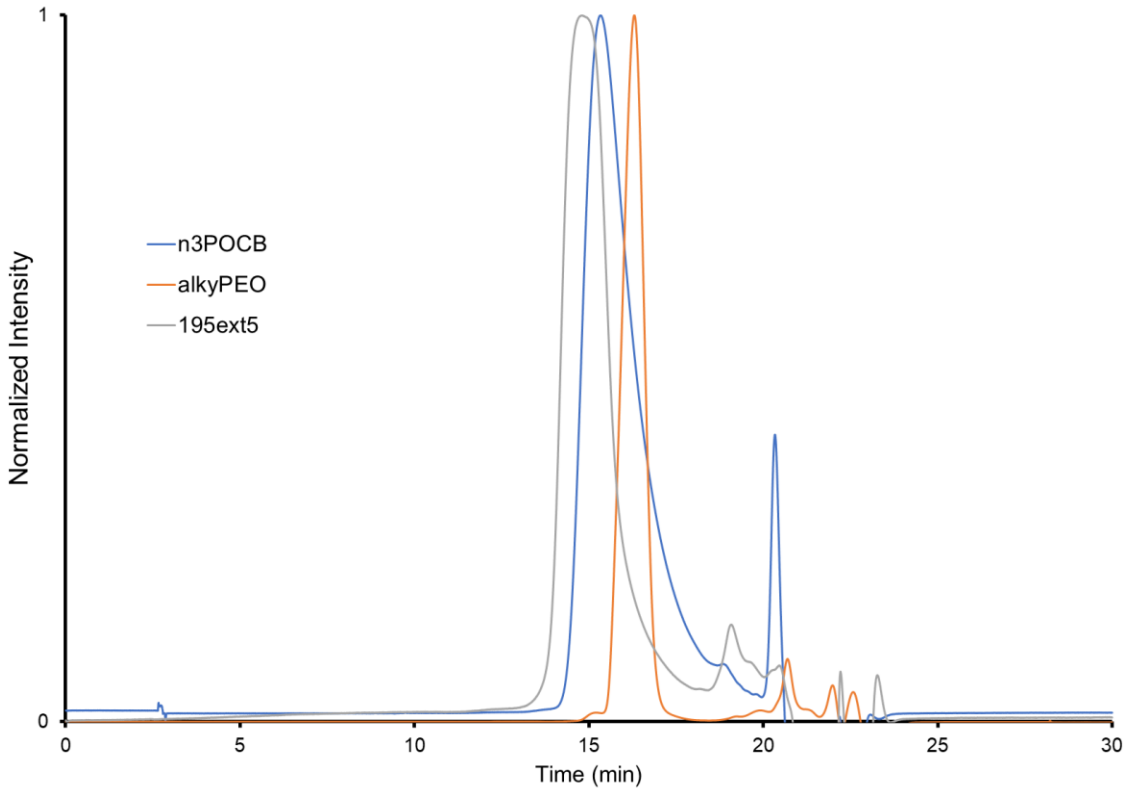

Figure A.38: SEC of 190 (N3POCB/POCB2000), 192 (alkynePEO/PEO4000), and 195 (Block2000)

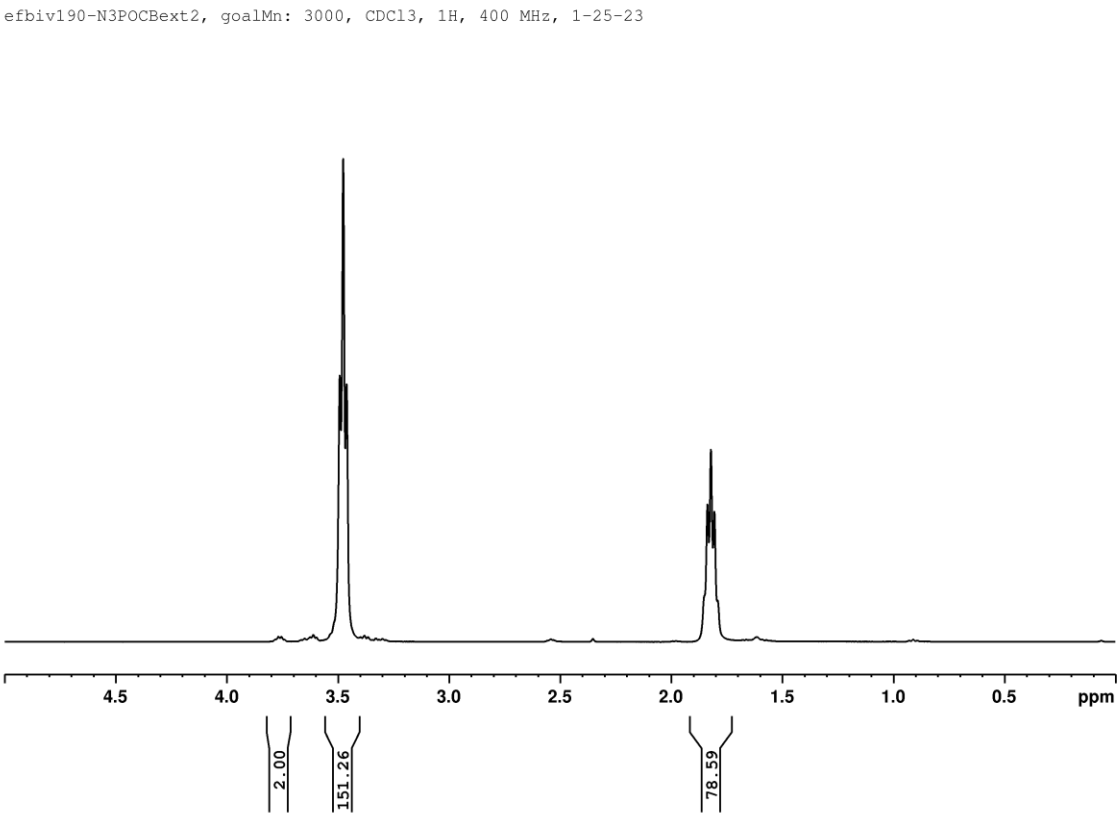

Figure A.39: Block2000 N3POCB ^{1}H NMR

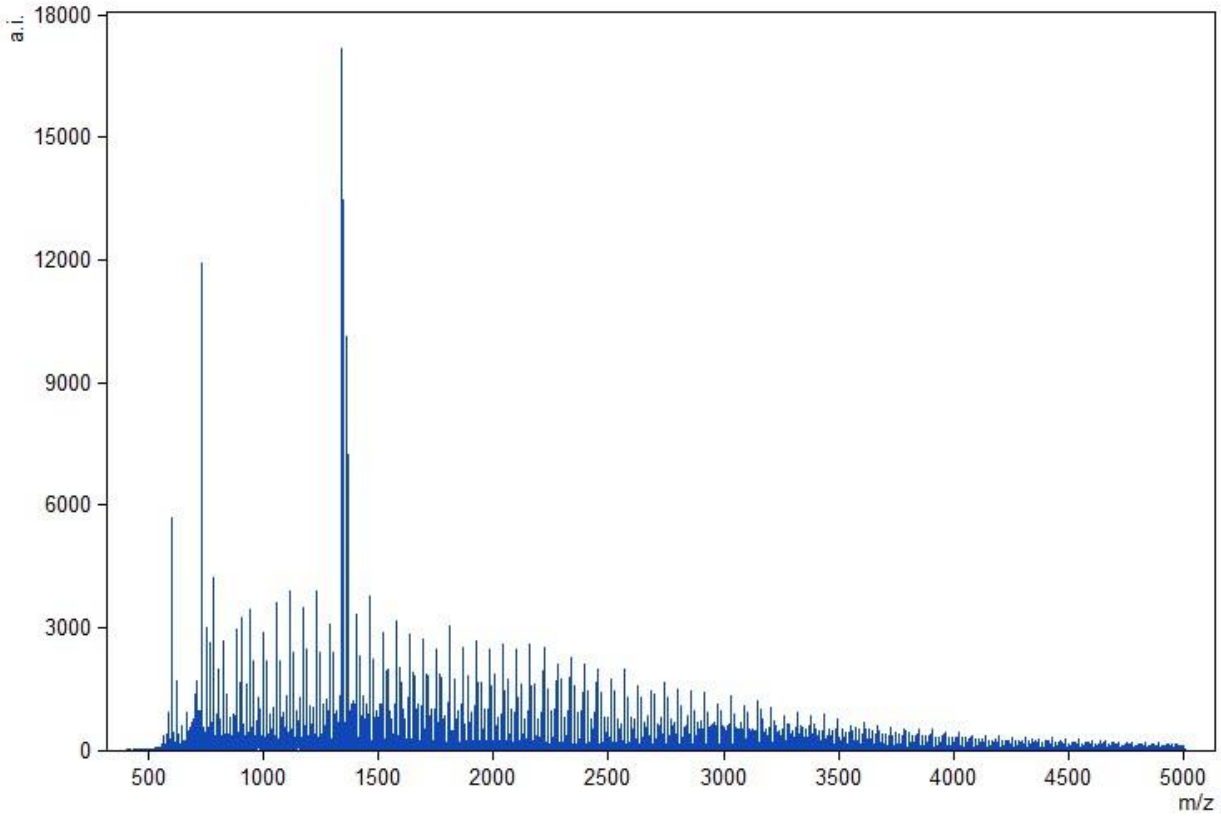

Figure A.40: Block2000 Maldi Full

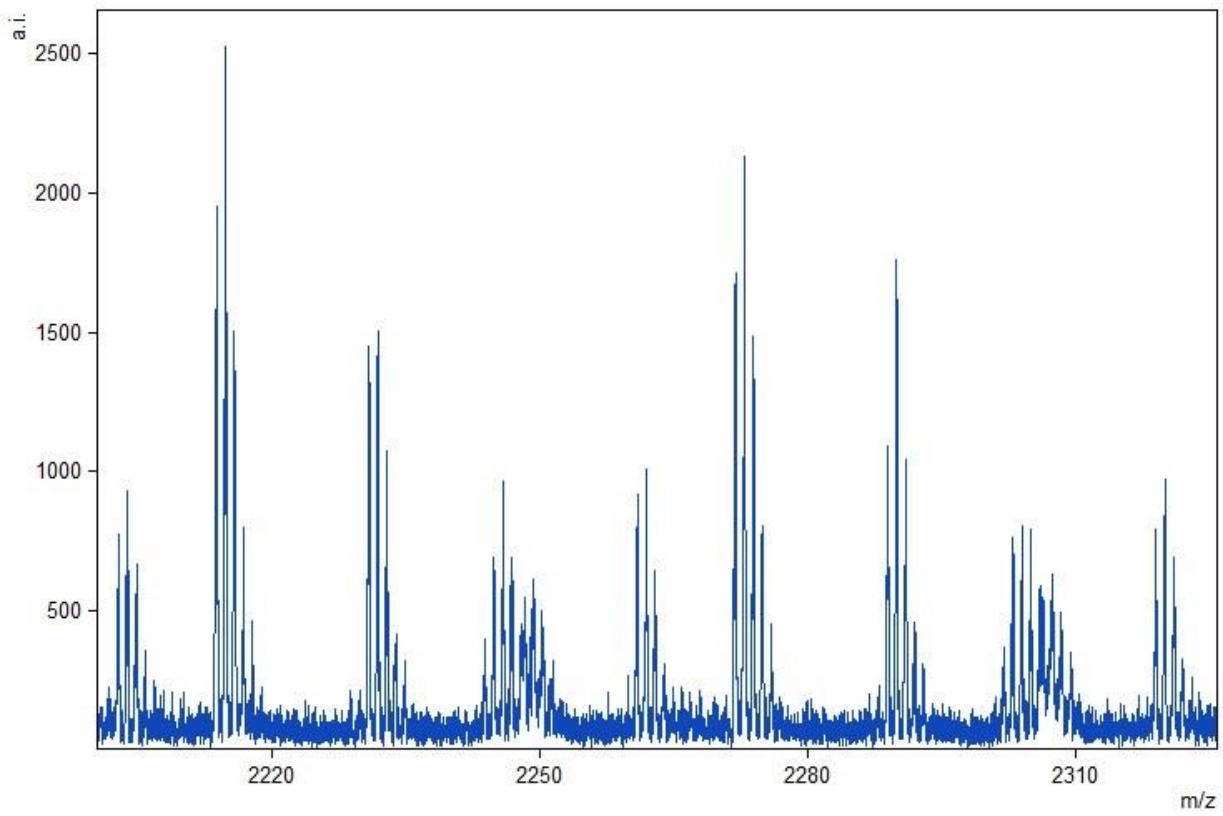

Figure A.41: Block2000 Maldi zoomed

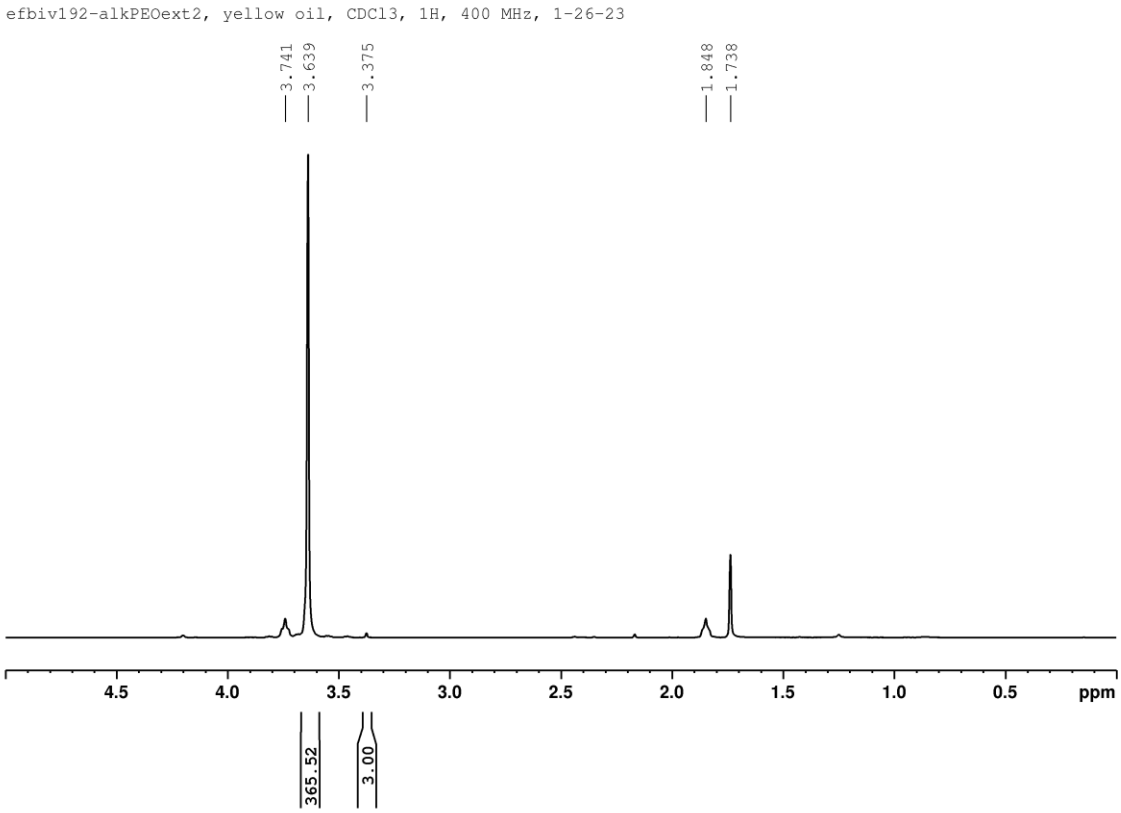

Figure A.42: PEO4000 (the one that was used for Block2000) ^{1}H NMR

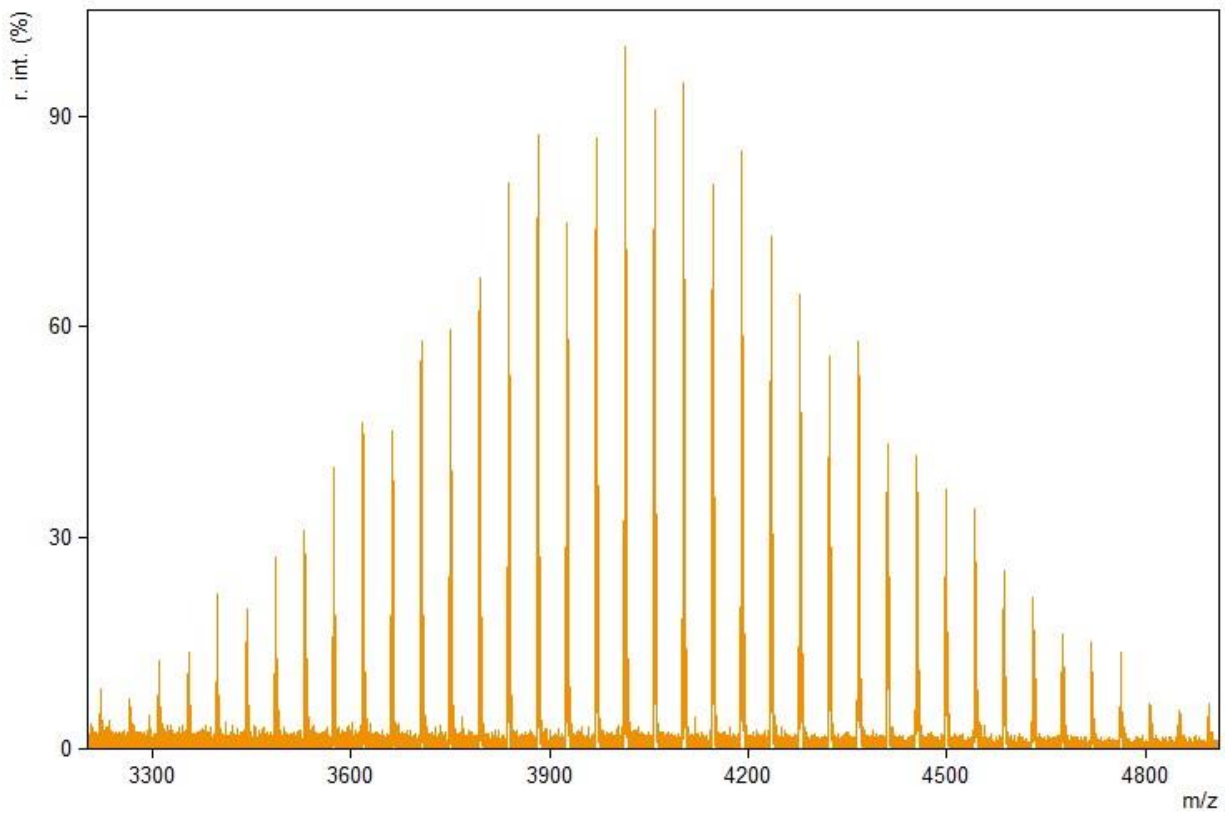

Figure A.43: PEO4000 (the one that was used for Block2000) maldi

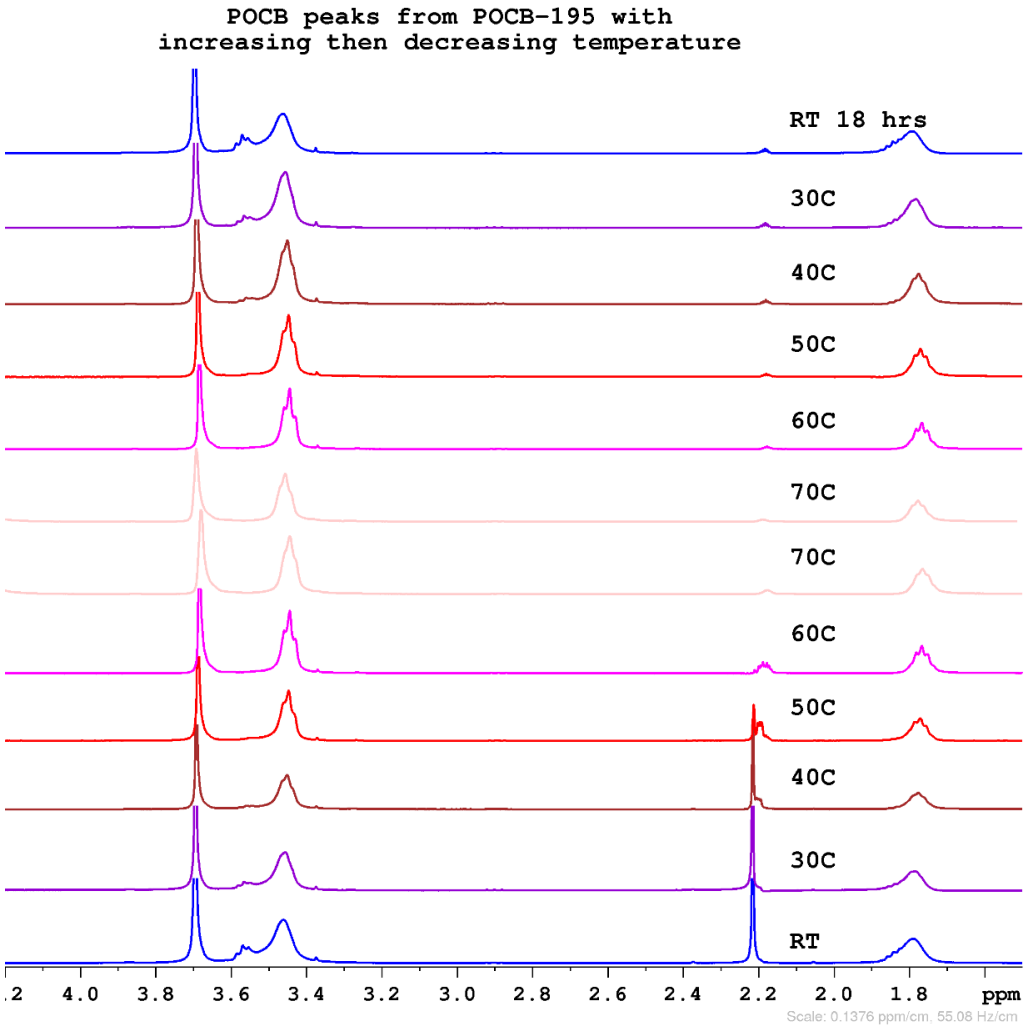

Figure A.44: ^{1}H NMR **Block2000** unzoomed

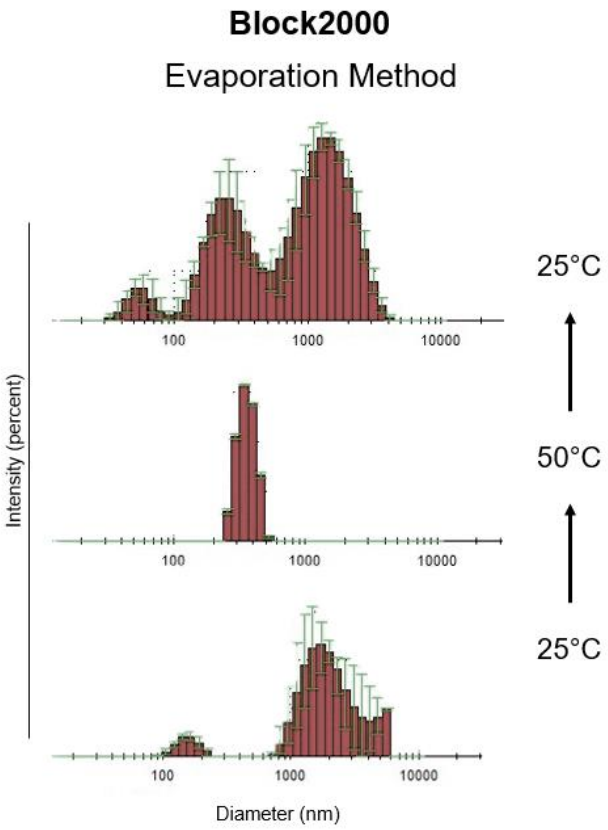

Figure A.45: Block2000 evaporation method DLS

Appendix B Electroadhesion

B1. Derivation of force between two charged capacitor plates

Table B1.1: relevant terms defined

Force between two point charges	$F = k_e \frac{Q_1 Q_2}{4\pi\epsilon_0 \hat{r}^2}$
Q	Charge
r	Distance between charges
ϵ_0	Permittivity of free space
ϵ_r	Relative permittivity (dielectric constant)
Electric field	$E = \frac{F}{Q}$
Charge density of a plane	$\sigma = \frac{Q}{A}$
Potential energy	$\Delta U = W_{field} = F_{field} d = EQd$
d	Distance between charges
Potential	$\Delta V = \frac{\Delta U}{Q}$

$$E = \frac{F}{Q_{point}} = \frac{Q_{point}}{4\pi\epsilon_0\epsilon_r \hat{r}^2} \quad \text{(B1.1)}$$

Electric fields are vectors and can be added. On a plane of charged particles, only the vertical component (z) of electric fields will be non-zero because the x and y components will sum to zero.

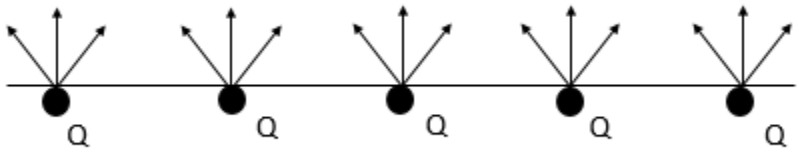

Figure B1.1: charged points on a plane with electric field lines.

Assume a point P that is z height above an electrically charged plane is experiencing an electric field from a point q somewhere on the plane

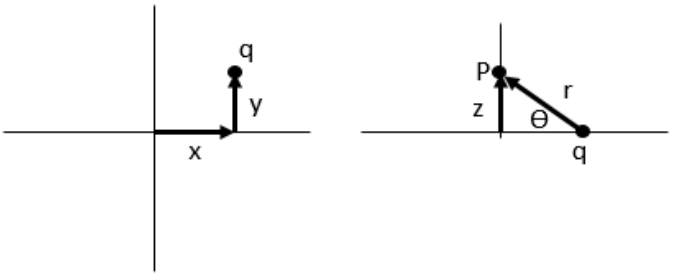

Figure B1.2: a point p above a charged plane.

$$E_P = \frac{Q_{point}}{4\pi\epsilon_0\epsilon_r\hat{r}^2} sin\theta \quad \text{(B1.2)}$$

Since electric fields can be added, you can sum all z components of the electric field that are contributing to the electric field at point P. At this time, it would also be helpful to define the surface charge σ as $\sigma = \frac{Q}{A}$ where now Q is the total charge and A is the area, so that the charge is distributed on the plane continuously and the z component contributions to the field at point P can be summed through integration.

$$E_P = \int_{-\infty}^{\infty}\int_{-\infty}^{\infty} \frac{\sigma}{4\pi\epsilon_0\epsilon_r \hat{r}^2} sin\theta dxdy \quad \text{(B1.3)}$$

$$r = \sqrt{x^2 + y^2 + z^2} \qquad and \qquad sin\theta = \frac{z}{\sqrt{x^2+y^2+z^2}} \quad \text{(B1.4)}$$

$$E_P = \frac{\sigma z}{4\pi\epsilon_0\epsilon_r}\int_{-\infty}^{\infty}\int_{-\infty}^{\infty} \frac{1}{(x^2+y^2+z^2)^{\frac{3}{2}}} dxdy \quad \text{(B1.5)}$$

At this point it simplifies the math to transfer into polar coordinates

$$E_P = \frac{\sigma z}{4\pi\epsilon_0\epsilon_r}\int_{-\infty}^{\infty}\int_{-\infty}^{\infty} \frac{1}{(s^2+z^2)^{\frac{3}{2}}} sd\theta ds \text{(B1.6)}$$

$$E_P = \left(\frac{\sigma z}{4\pi\epsilon_0\epsilon_r}\right) 2\pi \int_0^{\infty} \frac{s}{(s^2+z^2)^{\frac{3}{2}}} ds \text{(B1.7)}$$

$$E_P = \frac{\sigma z}{2\epsilon_0\epsilon_r}\left(\frac{-1}{\sqrt{s^2+z^2}}\right|_0^{\infty} \text{(B1.8)}$$

$$E_P = \frac{\sigma z}{2\epsilon_0\epsilon_r}(-) \text{(B1.9)}$$

$$E_P = \frac{\sigma}{2\epsilon_0\epsilon_r} \text{(B1.11)}$$

$$E_P = \frac{Q}{2A\epsilon_0\epsilon_r} \text{(B1.12)}$$

Between two parallel, oppositely charged plates, the electric field is doubled because there are electric field contributions from both plates pointing in the same direction

$$E_{tot} = \frac{Q}{A\epsilon_0\epsilon_r} \text{(B1.13)}$$

Solving for the force (experienced by one plate)

$$F = EQ = \frac{Q^2}{2A\epsilon_0\epsilon_r} \text{(B1.14)}$$

Solving for the electric potential (commonly written as just V instead of as the potential difference ΔV)

$$\Delta V = \frac{\Delta U}{Q} \quad \text{(B1.15)}$$

$$\Delta U = W_{field} = F_{field} d = EQd \quad \text{(B1.16)}$$

$$\Delta V = V = Ed \quad \text{(B1.17)}$$

$$V = \frac{Q}{A\epsilon_0 \epsilon_r} d \quad \text{(B1.18)}$$

Using the potential to solve for Q

$$Q = \frac{A\epsilon_0 \epsilon_r}{d} V \quad \text{(B1.19)}$$

Solving for force in terms of potential

$$\mathrm{F} = \frac{Q^2}{2A\epsilon_0 \epsilon_r} = \frac{A\epsilon_0 \epsilon_r}{2} \left(\frac{V}{d}\right)^2 \quad \text{(B1.20)}$$

B2. Time dependent force equation

$$\mathrm{V_d(t)} = V_{applied} - V_g(t) \quad \text{(B2.1)}$$

$$I_{Cd}(t) = C_d \frac{dV_d(t)}{dt} \quad \text{(B2.2)}$$

$$I_{Rd}(t) = \frac{V_d(t)}{R_d} \quad \text{(B2.3)}$$

$$I_{Cg}(t) = C_g \frac{dV_g(t)}{dt} \quad \text{(B2.4)}$$

$$I_{Rg}(t) = \frac{V_g(t)}{R_g} \quad \text{(B2.5)}$$

$$I = I_{Cd}(t) + I_{Rd}(t) = I_{Cg}(t) + I_{Rg}(t) \quad \text{(B2.6)}$$

$$C_d \frac{dV_d(t)}{dt} + \frac{V_d(t)}{R_d} = \frac{V_g(t)}{R_g} + C_g \frac{dV_g(t)}{dt} \quad \text{(B2.7)}$$

$$C_d \frac{d[V_{app}-V_g(t)]}{dt} + \frac{V_{app}-V_g(t)}{R_d} = \frac{V_g(t)}{R_g} + C_g \frac{dV_g(t)}{dt} \quad \text{(B2.8)}$$

$$C_d \frac{d[V_{app}-V_g(t)]}{dt} + \frac{V_{app}-V_g(t)}{R_d} = \frac{V_g(t)}{R_g} + C_g \frac{dV_g(t)}{dt} \quad \text{(B2.9)}$$

$$C_d \frac{-dV_g(t)}{dt} + \frac{V_{app}-V_g(t)}{R_d} = \frac{V_g(t)}{R_g} + C_g \frac{dV_g(t)}{dt} \quad \text{(B2.10)}$$

$$C_d \frac{-dV_g(t)}{dt} + C_g \frac{-dV_g(t)}{dt} = \frac{V_g(t)}{R_g} + \frac{-(V_{app}-V_g(t))}{R_d} \quad \text{(B2.11)}$$

$$C_d \frac{dV_g(t)}{dt} + C_g \frac{dV_g(t)}{dt} = \frac{-V_g(t)}{R_g} + \frac{V_{app}-V_g(t)}{R_d} \quad \text{(B2.12)}$$

$$(C_d + C_g) \frac{dV_g(t)}{dt} = \frac{-R_d V_g(t)+R_g V_{app}-R_g V_g(t)}{R_g R_d} \quad \text{(B2.13)}$$

$$(C_d + C_g) \frac{dV_g(t)}{dt} = \frac{-R_d V_g(t)+R_g V_{app}-R_g V_g(t)}{R_g R_d} \quad \text{(B2.14)}$$

$$R_g R_d (C_d + C_g) \frac{dV_g(t)}{dt} = -R_d V_g(t) + R_g V_{app} - R_g V_g(t) \quad \text{(B2.15)}$$

$$R_g R_d (C_d + C_g) \frac{dV_g(t)}{dt} = R_g V_{app} - (R_g + R_d) V_g(t) \quad \text{(B2.16)}$$

$$R_g R_d (C_d + C_g) \frac{dV_g(t)}{dt} + (R_g + R_d) V_g(t) = R_g V_{app} \quad \text{(B2.17)}$$

$$R_d (C_d + C_g) \frac{dV_g(t)}{dt} + \frac{R_g+R_d}{R_g} V_g(t) = V_{app} \quad \text{(B2.18)}$$

Solving for the complementary function (when $V_{app} = 0$)

$$V_g(t) = Ae^{mt} \quad \text{(B2.19)}$$

$$\frac{dV_g(t)}{dt} = Ame^{mt} \quad \text{(B2.20)}$$

$$R_d\big(C_d + C_g\big)Ame^{mt} + \frac{R_g+R_d}{R_g} Ae^{mt} = 0 \quad \text{(B2.21)}$$

$$m = -\frac{R_g+R_d}{R_g R_d (C_d+C_g)} \quad \text{(B2.22)}$$

$$V_g(t) = Ae^{-\frac{R_g+R_d}{R_g R_d (C_d+C_g)} t} \quad \text{(B2.23)}$$

Particular integral (solving for steady state)

$$\frac{R_g+R_d}{R_g} V_g(t) = V_{app} \quad \text{(B2.24)}$$

$$V_g(t) = \frac{R_g}{R_g+R_d} V_{app} \quad \text{(B2.25)}$$

Complete solution (complementary function + particular integral)

$$V_g(t) = \frac{R_g}{R_g+R_d} V_{app} + Ae^{-\frac{R_g+R_d}{R_g R_d (C_d+C_g)} t} \quad \text{(B2.26)}$$

When V = 0 and t = 0

$$0 = \frac{R_g}{R_g+R_d} V_{app} + Ae^{-\frac{R_g+R_d}{R_g R_d (C_d+C_g)} \times 0} \quad \text{(B2.27)}$$

$$0 = \frac{R_g}{R_g+R_d} V_{app} + A \quad \text{(B2.28)}$$

$$\mathrm{A} = -\frac{R_g}{R_g+R_b} V_{app} \quad \text{(B2.29)}$$

Solved equation

$$V_g(t) = \frac{R_g}{R_g+R_d} V_{app} - \frac{R_g}{R_g+R_d} V_{app} \times e^{-\frac{R_g+R_d}{R_g R_d (C_d+C_g)} t} \quad \text{(B2.30)}$$

$$V_g(t) = \frac{R_g}{R_g+R_d} V_{app} \left(1 - e^{-\frac{R_g+R_d}{R_g R_d (C_d+C_g)} t}\right) \quad \text{(B2.31)}$$

Can also be written (1/R = G where G is conductance):

$$V_g(t) = \frac{G_d}{G_d+G_g} V_{app} \left(1 - e^{-\frac{G_g+G_d}{C_d+C_g} t}\right) \quad \text{(B2.32)}$$